Green Catalysts Preparation Using Supercritical CO_2 as an Antisolvent

By

Zi-Rong Tang

School of Chemistry , Cardiff University

February 2007

ProQuest LLC
789 East Eisenhower Parkway
P.O. Box 1346
Ann Arbor, MI 48106-1346

Acknowledgements

I would like to express sincere thanks to my supervisor, Professor Graham J. Hutchings, for offering me this great opportunity to read PhD degree in his research group at Cardiff University. I would like to thank a lot for his constant support and advice during my PhD.

I would like to thank Dr. Stuart Taylor, Dr. Jonathan Bartley, Dr. Albert Carley, and Dr. Wen-Sheng Dong for their valuable suggestions on my thesis and PhD research work. Their help contributes much to my research work and makes me learn a lot. Thanks go to all the members of Professor Hutchings' research group and the technical staff of the School of Chemistry.

I would like to thank Cardiff University for funding of the project. Finally, I would like to express my thanks to my husband, Mr. Yi-Jun Xu, and my family for their strong support.

Abstract

Using rapid supercritical CO_2 antisolvent precipitation, a set of nanoscaled oxide catalyst precursors have been prepared, which were further calcined to give metal oxides, such as $CuMnO_x$(hopcalite), CeO_2, TiO_2 and ZnO etc. $CuMnO_x$(hopcalite) was used as catalyst without further modification and other single metal oxides were used as supports for gold catalysts. These materials have been characterized using a full range of techniques: XRD, Raman, FT-IR, BET surface area, SEM, DTA/TGA and XPS. Element distribution in the as-precipitated materials was evaluated by TEM-EDX. The catalytic activity of our products was evaluated by low temperature (0~25°C) CO oxidation.

For $CuMnO_x$ (hopcalites), an amorphous homogenous precursor mainly composed of acetates has been prepared. Following calcinations, separated copper nanocrystals supported on manganese oxide (Cu/MnO_x) has been obtained. The preliminary catalytic data show the intrinsic activity for CO oxidation of the catalyst derived from this precursor is considerably higher than the conventional $CuMn_2O_4$ catalysts prepared by coprecipitation, and also currently available commercial catalysts. The results clearly show that a catalyst with enhanced activity can be prepared without the presence of intimately mixed copper and manganese oxide components. In addition, using mixed solvents, such as water-ethanol and water-DMF, crystalline heterogeneous precursors have been produced. With the addition of more water to the precursor solution, there appears to be a reaction

between the metal acetates CO_2, and H_2O. Therefore, carbonates of the metals are precipitated instead of the acetate composition. Following calcination, less crystalline or even amorphous phase-separated nanostructure final catalysts retain the high surface area, which leads higher catalytic activities than that of the current commercial hopcalite catalysts. Furthermore, using 30% H_2O_2 as an oxidizer and ethanol as solvent, catalysts have been prepared as well. All the as-prepared catalysts exhibit higher catalytic activities on CO oxidation when compared to those from solvents in the absence of H_2O_2.

Novel nano-polycrystalline CeO_2 was produced. When it was used as a support for gold and gold palladium nanoparticles, the catalytic data show that the activity and catalyst lifetime for CO oxidation of a gold catalyst supported on this material is much greater than that for gold supported on regular CeO_2 derived from the direct calcination of cerium acetylacetonate. In addition, the Au-Pd catalysts supported on CeO_2 prepared using supercritical antisolvent precipitation are amongst the most active catalysts yet reported for the selective oxidation of alcohols and the direct oxidation of hydrogen to hydrogen peroxide. Similarly, TiO_2 has been produced by supercritical process. When using it as a support for gold nanoparticles, the activity and stability for CO oxidation of a gold catalyst supported on this material is much greater than that for gold supported on regular TiO_2 derived from the direct calcination of titanium oxide acetylacetonate. Finally, ZnO was prepared using supercritical process and then was used as supports for gold particles as well. The catalytic data show that it can give very high activity for CO oxidation.

Contents

Chapter 1

Introduction

1.1 Green chemistry

Green Chemistry, also known as sustainable chemistry, is the design, manufacture and application of chemical products that reduce or eliminate the use or generation of substances that are hazardous to human health and the environment [1]. It is a science-based nonregulatory, economically driven approach toward sustainable development that has grown substantially since the concept fully emerged in 1990s [2]. This approach requires an open and interdisciplinary view of materials design, applying the principle that it is better not to generate waste in the first place, rather than disposing or treating it afterwards. Green chemistry is often cross-disciplinary, which means it can involve governments, academic and industrial communities that perform or support research to achieve common goals.

The green chemistry alternative emerged in the early 1990s by informal networks of practitioners. In the early 1990's, the US EPA's Office of Pollution Prevention and Toxics established the development in the USA of the Presidential Green Chemistry Challenge Award Program after the passage of the first environmental law in 1990 which focused on preventing pollution at the source rather than dealing with remediation or capture of pollutants. EPA has since collaborated with academia,

industry and other government agencies to promoted use of chemistry to develop new technologies for pollution prevention and sustainable development. In the first half of 1990s, both the United Kingdom and Italy launched major initiatives in green chemistry. The UK's efforts are largely coordinated by the scientific community. Firstly, several researchers established the research and education programs in green chemistry. In 1998, the Royal Society of Chemistry launched a major initiative to promote green chemistry in a new journal *Green Chemistry*. In Italy, a 30-university consortium funded by the Italian government has been established to pursue research and education in green chemistry. The Italian National Consortium for Chemistry for the Environment has opened three national laboratories that focus on green chemistry and hosts a green chemistry summer school with participation from 23 nations. Nowadays, many countries including Japan, China and Australia, have launched green chemistry research projects. International collaborations and communications are extensively developing and advancing global environmental protection and sustainable development.

The design of environmentally benign chemicals and processes now may be guided by the 12 Principles of Green Chemistry developed by Paul Anastas and John C. Warner [3-5]. These principles cover the concepts such as maximizing the use of raw materials that are transformed to target products, the design of safe and environmental-benign process, the improvement of energy efficiency and the better disposal of waste by-products. Nowadays, these principles have been used as

guideline and criteria by chemical scientists. The 12 principles of green chemistry can be described in detail as follows:

1. Prevention - It is better to prevent waste than to treat or clean up waste after it has been created.

2. Atom Economy - Synthetic methods should be designed to maximize the incorporation of all materials used in the process into the final product.

3. Less Hazardous Chemical Synthesis - Wherever practicable, synthetic methods should be designed to use and generate substances that possess little or no toxicity to human health and the environment.

4. Designing Safer Chemicals - Chemical products should be designed to effect their desired function while minimizing their toxicity.

5. Safer Solvents and Auxiliaries - The use of auxiliary substances (e.g., solvents, separation agents, etc.) should be made unnecessary wherever possible and innocuous when used.

6. Design for Energy Efficiency - Energy requirements of chemical processes should be recognized for their environmental and economic impacts and should be minimized. If possible, synthetic methods should be conducted at ambient temperature and pressure.

7. Use of Renewable Feedstocks - A raw material or feedstock should be renewable rather than depleting whenever technically and economically practicable.

8. Reduce Derivatives - Unnecessary derivatization (use of blocking groups, protection/ deprotection, temporary modification of physical/chemical processes)

should be minimized or avoided if possible, because such steps require additional reagents and can generate waste.

9. Catalysis – Catalytic reagents (as selective as possible) are superior to stoichiometric reagents.

10. Design for Degradation - Chemical products should be designed so that at the end of their function they break down into innocuous degradation products and do not persist in the environment.

11. Real-Time analysis for Pollution Prevention - Analytical methodologies need to be further developed to allow for real-time, in-process monitoring and control prior to the formation of hazardous substances.

12. Inherently Safer Chemistry for Accident Prevention - Substances and the form of a substance used in a chemical process should be chosen to minimize the potential for chemical accidents, including releases, explosions, and fires.

Since green chemistry emerged in 1991, research programs and centers have been focusing efforts around the principles of green chemistry. The research area of green chemistry is very broad and excellent research is being conducted within polymer, solvents, catalysis, renewables, analytical method development, synthetic methodology development as well as the design of safer chemicals. In 2005 Ryoji Noyori (Nobel laureate in chemistry, 2001) identified three key developments in green chemistry [6]: (1) use of supercritical carbon dioxide as green solvent; (2) using aqueous hydrogen peroxide for clean oxidations and (3) use of hydrogen in asymmetric synthesis.

1.2 Green catalysis

1.2.1 Catalysis and heterogeneous catalysis

Catalysis plays a paramount role nowadays in our society. It has an enormous impact on the chemical industry because catalysts enable reactions to take place and make reaction processes both more efficient and environmentally friendly. In addition, a 0.5% to 1% increase in selectivity of reaction that leads bulk chemicals can lead to an up to 1 million dollar increase in operating profit. Therefore, catalysis has become indispensable in chemical industry and will become more important in 21st century.

Catalysis is the acceleration of a chemical reaction by means of a substance, called catalyst. Here, catalyst is one substance that is added to a reaction system to alter the speed of a chemical reaction approaching a chemical equilibrium. It interacts with the reactants in a cyclic manner promoting many reactions at the molecular level, but it is not consumed. Moreover, a catalyst makes a reaction go faster and in a more selective manner. Generally, there are three kinds of catalysis: heterogeneous, homogeneous and biological catalysis.

In heterogeneous catalysis, the catalyst is in a separate phase from the reactants and products. The catalysts provide a surface in which the chemical reaction takes place on active sites of the surface. A representative example as shown in **Figure 1.1** illustrates how a heterogeneous catalyst works.

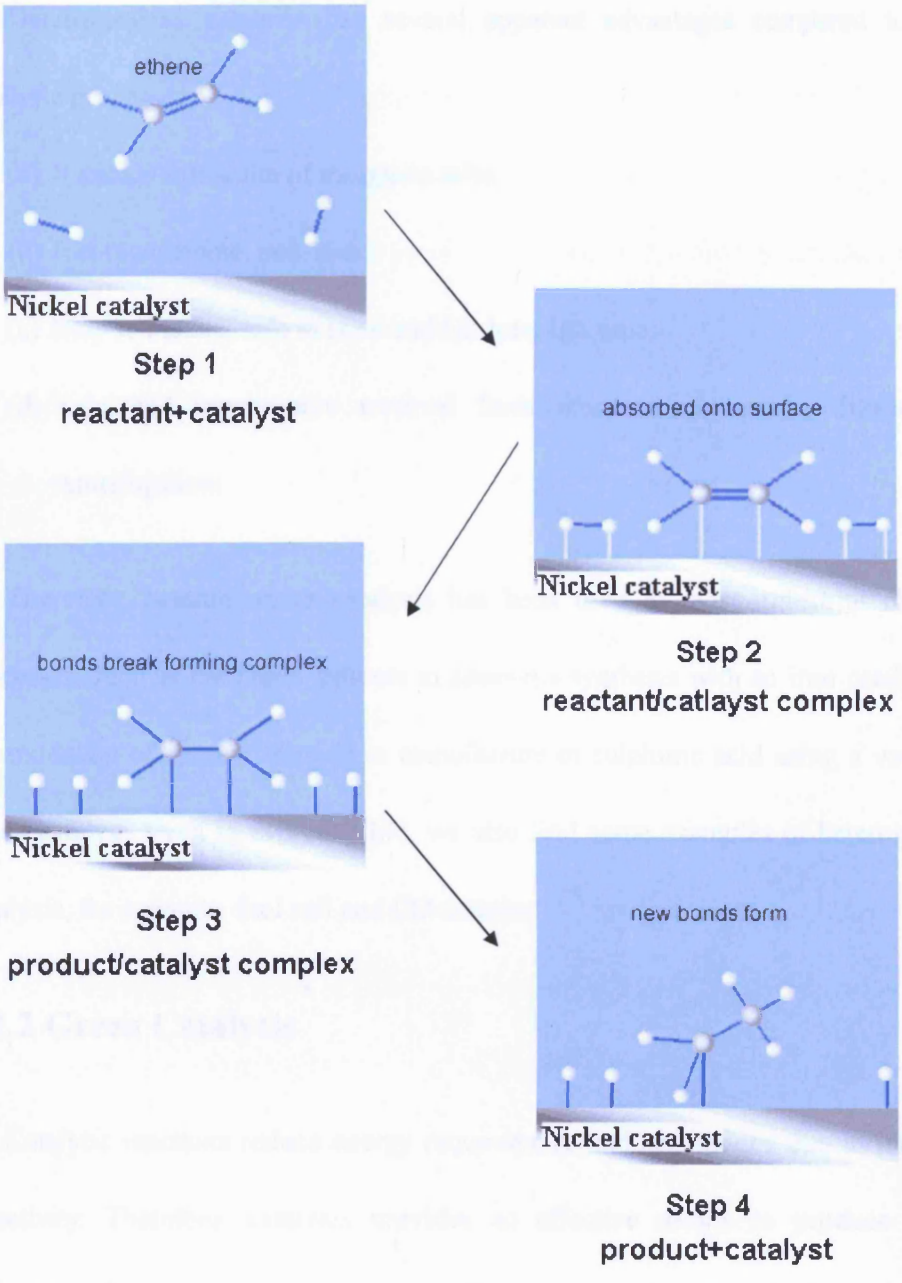

Figure 1.1 An example of heterogeneous catalysis: the hydrogenation of ethene by hydrogen using a nickel catalyst.

Heterogeneous catalysis has several apparent advantages compared to other catalytic processes:

(a) It avoids formation of inorganic salts;

(b) It is regenerable, non-toxic;

(c) Easy to handle, safe to store and has long life time;

(d) Easy and inexpensive removal from reaction mixture by filtration or centrifugation;

Therefore, heterogeneous catalysis has been used in most industrial chemical processes, such as the Haber process in ammonia synthesis with an iron catalyst and the oxidation of sulphur dioxide in manufacture of sulphuric acid using a vanadium oxide catalyst. Even in everyday life, we also find some examples of heterogeneous catalysis, for example, fuel cell and CO detector.

1.2.2 Green Catalysis

Catalytic reactions reduce energy requirements and separations due to increased selectivity. Therefore, catalysis provides an effective means to produce valued compounds from raw materials in a cost-effective and environmentally benign manner. Nowadays, the application of catalysis to reduce toxicity, benign and renewable energy systems, and efficiency makes it a central focus area for green chemistry research.

In recent years the development of catalysts for processes to replace

stoichiometric reactions, which produce large amounts of undesirable waste products, has made a significant contribution to the reduction of environmental pollutants. However, the green of the chemistry industry is offset by other environmental issues: (1) organic solvents, including hazardous chlorinated hydrocarbons, still widely used in many catalytic reactions; (2) traditional procedures for the commercial preparation of catalysts often involve the use of metal nitrates as intermediates, resulting in the generation of waste effluent. Thus, there is an increasing interest on the topic of green catalysis recently. It not only includes developing new catalysts which can offer stable, highly effective catalytic performances, but considers the application of environmentally friendly supercritical fluid on catalysis reactions and catalyst preparations.

Numerous studies have been focused on catalysis using supercritical fluids as solvent. Baiker and Noyori *et al.* have reviewed the works on heterogeneous catalysis and homogeneous catalysis in supercritical fluids, respectively [7-8]. The results in these reviews have shown supercritical fluids have the great potentials in catalytic reactions. At the same time, catalytic materials and supports preparation using supercritical fluids has also been studied [9-11]. The most widely used supercritical fluids in the preparation of catalysts are supercritical water (hydrothermal synthesis) and supercritical CO_2 (antisolvent precipitation).

1.3 Supercritical Fluid (SCF)

1.3.1 Definition

A supercritical fluid is defined as a substance above its critical temperature (T_C) and critical pressure (P_C). The critical point represents the highest temperature and pressure at which the substance can exist as a vapour and liquid in equilibrium.

The phenomenon can be easily explained with reference to a phase diagram in **Figure 1.2**. The curves represent the temperatures and pressures where two phases coexist in equilibrium. The gas-liquid coexistence curve is known as the boiling curve. If we move upwards along the boiling curve, increasing both temperature and pressure, then the liquid becomes less dense due to thermal expansion and the gas becomes denser as the pressure rises. Eventually, the densities of the two phases converge and become identical, the distinction between gas and liquid disappears, and the boiling curve comes to an end at the critical point.

Table 1.1 lists the critical properties of some substances, which usually are used as supercritical fluids [12]. Of all the substances shown by the table, carbon dioxide and water are the most frequently used in a wide range of applications, including extractions, dry cleaning and chemical waste disposal. In polymer systems, ethylene and propylene are also widely used, where they act both as a solvent and as the reacting monomer.

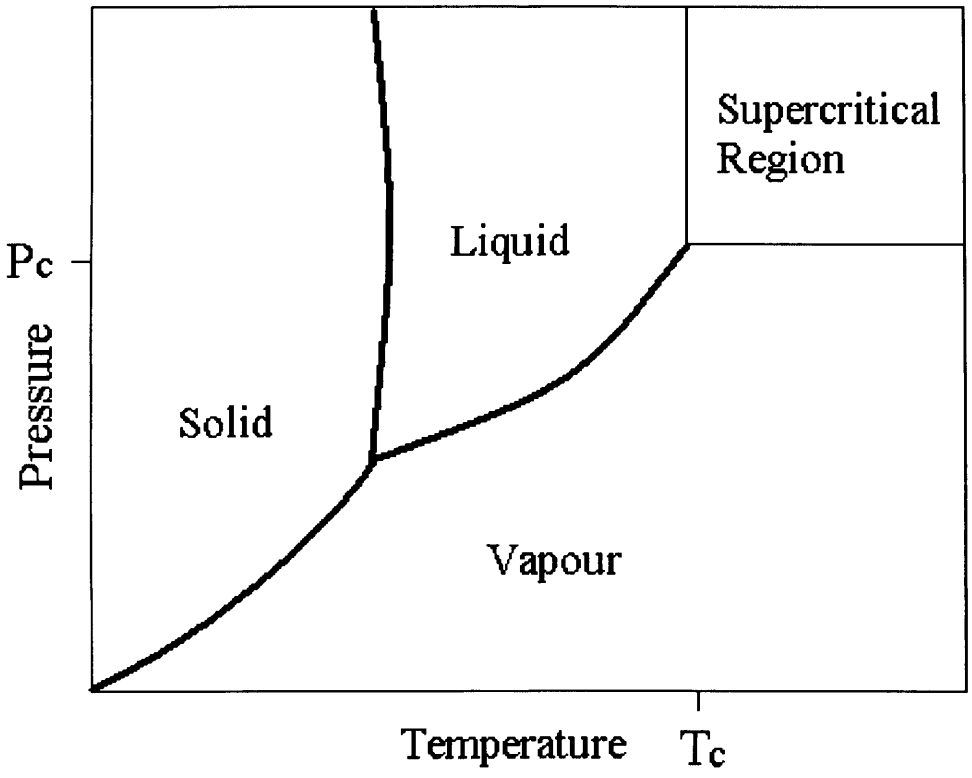

Figure 1.2 P-T phase diagram for a pure substance, which is traditionally used to define the supercritical region.

Table 1.1 Critical data for some substances

Solvent	Molecular Weight	Tc	Pc
	(g/mol)	(K)	(MPa)
Carbon dioxide	44.01	304.1	7.38
Water	18.02	647.3	22.12
Methane	16.04	190.4	4.60
Ethane	30.07	305.3	4.87
Propane	44.09	369.8	4.25
Ethylene	28.05	282.4	5.04
Propylene	42.08	364.9	4.60
Methanol	32.04	512.6	8.09
Ethanol	46.07	513.9	6.14
Acetone	58.08	508.1	4.70

1.3.2 Properties of SCFs

The properties of supercritical fluids are considered to lie between those of a liquid and a gas. They combine the solubility of liquids and the diffusivity of gases [13-14]. However, it should be noted that some of the properties of an SCF are more liquid–like, while others are more gas–like.

Generally, the solubility of a given solute increases with both increasing density of the solvent and increasing vapor pressure of the solute. Consequently, the solubility of a solute in an SCF increases with increasing pressure. It should be noted that solubilities in liquids usually surpass those in SCFs and that the dissolving power of an SCF only approaches that of its liquid solvent. However, SCFs sometimes still can be referred to "supersolvent" because of the unique combination of relatively high solubilities and other gas–like features.

Diffusivities of SCFs are considered as gas-like properties with respect to their order of magnitude. In an SCF, diffusivity decreases as pressure is increased, approaching values of a liquid. Meanwhile, an increase in temperature can lead to the increase of diffusivity.

Furthermore, most properties of supercritical fluids can significantly change with small changes in pressure and temperature, rendering supercritical fluids easily tunable regarding their qualities as a solvent or reactant. It is this mixture of more liquid-like and more gas-like properties together with the easy tunability of those

properties that render SCFs great promising media for chemical processes.

1.3.3 Applications of SCFs

Owing to the specific properties, supercritical fluids have been widely used in various fields including analysis, separation, polymer or material synthesis as well as catalysis. For example:

Supercritical extraction: [15-16] Extraction of solid natural materials, mainly for food ingredients and pharmaceuticals using supercritical fluids has been widely used. So far, there are many large-scale industrial applications on supercritical extraction, for example, coffee decaffeination and hop resin extraction.

Particle formation: [17-22] Extensive efforts have been put on nano- or micro-particles formation using supercritical fluid. Production of the particles mainly comes from hydrothermal synthesis using supercritical water and antisolvent precipitation using supercritical CO_2. So far, particle design has been a major development of supercritical fluids applications, mainly in the pharmaceutical, pigments and catalysts. In particular, the environmentally benign properties of CO_2 make it the most widely used supercritical medium in the particle formation. In the next part, we will focus on the introduction of particle preparation using supercritical CO_2.

1.4 Particles Preparation using Supercritical CO_2 as an antisolvent (SAS)

1.4.1 Supercritical CO_2

Supercritical carbon dioxide (T_C = 31.0 °C, P_C = 73.8 bar) is the most widely used supercritical fluid so far in chemical process due to its "green" properties - it is abundant, inexpensive, nonflammable, nontoxic, and environmentally benign. In addition, CO_2 can be vented to the atmosphere or recycled without harm. Beckman has reviewed on the use of supercritical CO_2 in green chemical synthesis and processing [23]. This literature reveals that the use of CO2 has permeated almost all facets of the chemical industry and that careful application of CO_2 can result in products and processes that are cleaner, less expensive and of higher quality.

During the last decades, there has been an increasing interest in micro- and nano-particles preparation using supercritical CO_2 [9, 17-22]. As we all know, very fine particles are of considerable importance in numerous applications, including pigmental, pharmaceutical, cosmetic and catalytic industries. Several techniques have been used in the past for preparation of very fine particles. However, they suffer from inherent limitations; for example, it is difficult to control particle size and particle size distribution of powder; in addition, liquid crystallization also suffers from the problem of solvent contamination of the precipitate. As an alternative to the traditional techniques, preparation of particles using supercritical CO_2 can potentially overcome some limitations in classical techniques on particle formation.

There have been several methodologies for particle formation using $scCO_2$ according to the literatures, for example, rapid expansion of a supercritical solution (RESS) [24-27], supercritical antisolvent precipitation (SAS) [28-30] and supercritical assisted atomization (SAA) [31-36]. Amongst them, supercritical antisolvent precipitation (SAS) is a technique more recent than the others but already it has become the focus of intense industrial research. Particularly, SAS has much promise for inorganic materials.

1.4.2 Principle of SAS precipitation

The application of the supercritical CO_2 as an antisolvent to precipitate materials from conventional solvents results from the fact that many substances are insoluble in supercritical CO_2. The principle of this technique is quite similar to the well-established use of layering of poor solvents above a solution to result in precipitation or crystallization in synthesis of chemicals. Generally, supercritical antisolvent precipitation succeeds as a method when all the following conditions can be met: (1) The solute is highly soluble in the conventional solvent; (2) The solute has poor solubility in $scCO_2$; (3) $scCO_2$ should have the good miscibility to the conventional solvent. In the SAS technique, essentially, $scCO_2$ is mainly used to reduce the solvent power of a conventional solvent, so that the solute precipitates.

Recently, supercritical antisolvent precipitation process has been considered as an alternative to the liquid antisolvent processes. It has several potential advantages in very fine particle preparation:

(1) The $scCO_2$ has very fast diffusivity which is about two orders of magnitude larger than conventional solvents. This fast diffusion can produce supersaturation immediately prior to precipitation, and thus leads to the formation of nanoparticles not usually accessible by liquid antisolvents or other conventional techniques. At the same time, it is also convnenient for the control of the particle size distribution.

(2) The CO_2 is environmentally benign and it can be vented to the atmosphere or recycled without harm. So the recovery of dry precipitates from the SAS process can be easily done by just a single depressurization. This step of the process is always problematic for other techniques, where complex treatments for the complete elimination of contamination from liquid residues are required.

(3) The temperature and the density of the $scCO_2$ as well as the flow rates of the $scCO_2$ and the solution can be manipulated to control the particle size, shape and the morphology of the precipitated particles. It is known that control of these parameters is quite important for particle design, particularly for the particles used as heterogeneous catalysts.

1.4.3 Experimental apparatus

Particle formation using $scCO_2$ as an antisolvent has been performed using different processes and apparatuses. This induced various acronyms to be used by different authors to indicate the precipitation process, such as GAS(compressed gas antisolvent) [37-39], PCA(precipitation by compressed antisolvent) [40-43],

SEDS(solution enhanced dispersion by superciritical fluids) [45] and SAS(superciritial antisolvent precipitation) [28-30]. However, the principles on these techniques are exactly the same. Amongst all of these acronyms, SAS gives a better description of the process since it points out the supercritical nature of the antisolvent used.

For particle formation using supercritical CO_2 as an antisolvent, two kinds of operations generally are used in the preparation process according to the literature: (a) batch operations, and (b) semi-continuous operation.

1.4.3.1 Batch Operation

Figure 1.2 shows a schematic representation of a batch supercritical antisolvent particle precipitation. In a batch process, the precipitation chamber is loaded with a given quantity of the liquid solution and then the supercritical antisolvent is added until the final pressure is reached. The supercritical antisolvent can be added from the bottom or from the top of the chamber. The batch operation is not generally carried out at a steady state. Therefore, it is difficult to analyze the effect of the process parameters on the precipitated materials.

At the end of the precipitation process, the chamber needs to be washed with the supercritical CO_2 to remove the liquid. This is very important for the achievement of dry and pure precipitates. If the washing is not sufficient, the liquid solvent may resolubilise or contaminate the precipitates during the depressurization of the

apparatus.

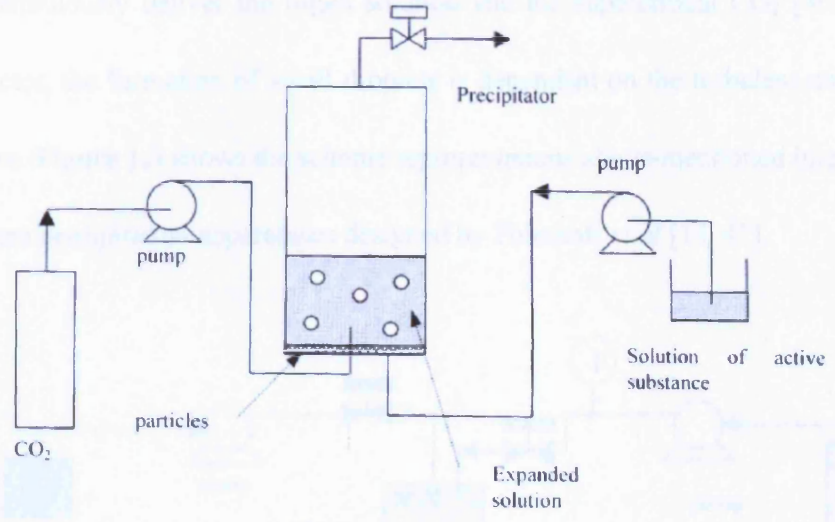

Figure 1.2 Scheme diagram of a SAS batch apparatus [18].

1.4.3.2 Semi-continuous Operation

In the semi-continuous process, the liquid solution and the $scCO_2$ are continuously pumped to the precipitation chamber in co-current mode controlled by back-pressure valve. **Figure 1.3** shows a schematic representation of a batch supercritical antisolvent particle precipitation.

Various parameters can be manipulated to control the continuous precipitation process, such as T, P, the concentration *etc*. One of the key roles is the liquid solution injection into the supercritical media. The injector, also named nozzle, is designed to produce liquid droplet which can be miscible to $scCO_2$, and further form the small particles due to the decrease of solvent power. In order to form the small droplets, small internal diameter capillaries have been used in the literatures [14, 39, 45].

Meanwhile, the coaxial injector devices have also been proposed in which two coaxial tubes continuously deliver the liquid solution and the supercritical CO_2 [46-47]. In this injector, the formation of small droplets is dependent on the turbulent mixing of two flows. **Figure 1.3** shows the scheme representations above-mentioned injectors in antisolvent precipitation apparatuses designed by Poliakoff *et al* [14, 47].

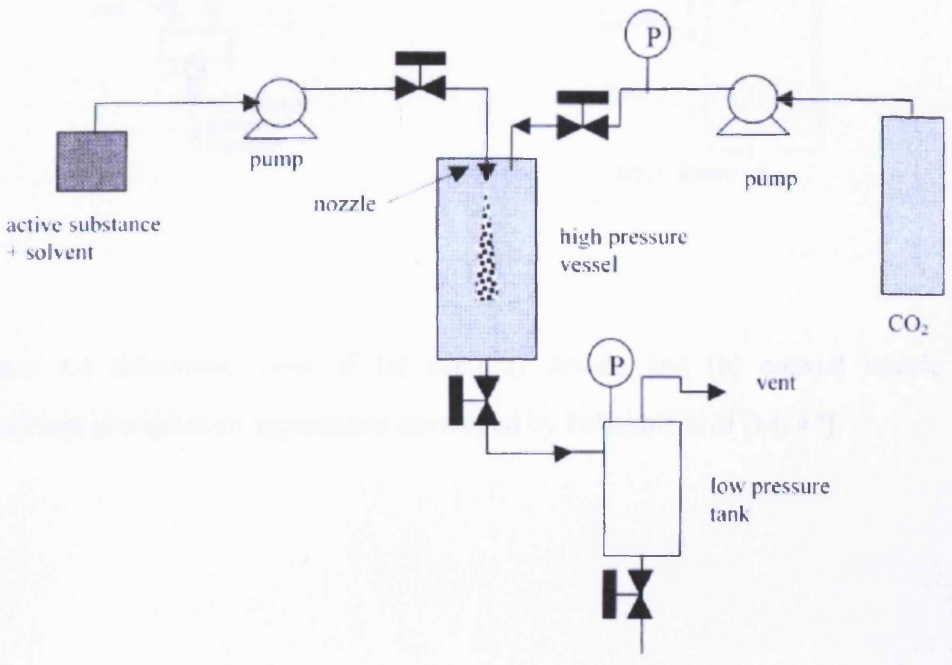

Figure 1.3 A schematic representation of a semi-continuous supercritical antisolvent particle precipitation [18].

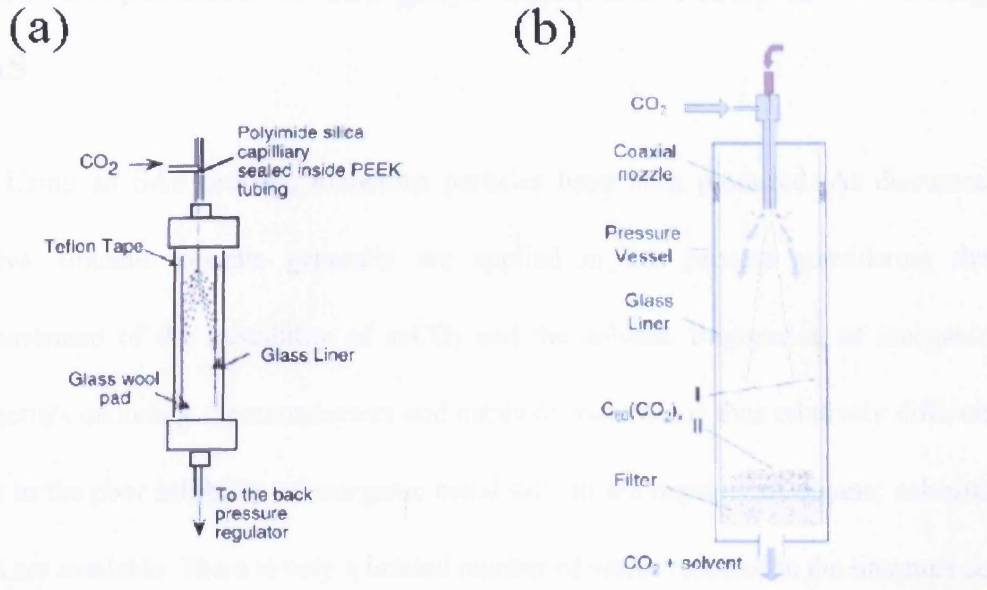

Figure 1.4 Schematic view of (a) capillary nozzle and (b) coaxial nozzle in antisolvent precipitation apparatuses developed by Poliakoff *et al* [14, 47].

1.4.4 Preparation of Inorganic Materials Precipitation Using SAS

Using an SAS process, numerous particles have been produced. As discussed above, organic solvents generally are applied in this process considering the requirement of the miscibility of $scCO_2$ and the solvent. Preparation of inorganic materials including superconductors and catalysis materials is thus relatively difficult due to the poor solubility of inorganic metal salts in the majority of organic solvents that are available. There is only a limited number of works reported in the literature so far, and these are summarized in **Table 1.2**. From the table, it is apparent that DMSO (dimethyl sulfoxide) has been used as solvents in the majority of particle formation of inorganic materials synthesis, which mainly results from the highly solubility of many inorganic metal salts in DMSO [48]. In addition, very fine inorganic particles, down to 50nm, can be obtained using SAS process. It is very promising, particularly in the synthesis of heterogeneous metal oxides catalysts, since catalysts with nanosize have been reported that can greatly exhibit enhanced activity for various catalytic reactions [49-50].

In the following, detailed literature survey, the results classified by the applications will be introduced for a number of inorganic materials prepared by SAS process.

Table 1.2 Particles preparation of inorganic materials using SAS process

Substances	Solvents	Results	References
Ammonium Chloride	DMSO(dimethyl sulfoxide)	crystalline particles; particle size: 0.1-20um	[51]
Barium Chloride	DMSO	cystalline particles ; particle size : 0.5um	[51]
Cobaltous nitrate	acetate	fluffy pink powder with free-flowing	[52]
Europium acetate	DMSO or NMP (N-methylpyrrollidone)	mean diameter of particle: 0.2um	[53]
Gadolinium acetate	DMSO	mean diameter of particle: 0.2um	[53]
Neodymium acetate	DMSO or NMP	mean diameter of particle: 0.1um	[54]
Nickel chloride hexahydrate	absolute ethanol	very fine free-flowing powder	[52]
Samarium acetate	DMSO	particle size:0.1-0.5 um	[10,29,54]
Samarium acetate	water+ethanol	particle size: 0.2 um	[55]
Silver nitrate	methanol	particle size: 0.3um	[55]
TiO_2	ethanol	Anatase TiO_2, average particle size : 200nm	[56]
Vanadium phosphorus oxide	isopropanol	amorphous particles; particle size: 0.075-1um	[57,58,59]
Yttrium acetate	DMSO	particle size: 0.1-1um	[54,60]
Zinc acetate	DMSO or NMP	amorphous particles; mean diameter of particle: 50nm	[11,30]

1.4.5.1 Catalysts preparation

(1) ZnO precursor (ZnAc)

To evaluate the applicability of this new process to the production of controlled size nanoparticles of catalyst precursors, zinc acetate was precipitated using SAS technique[11,30]. The result showed that amorphous zinc acetate nanoparticles down to about *ca.* 30nm were obtained. Surface area was measured by N_2 adsorption using the BET method and was found to be up to about 175m^2/g due to the production of particles with a porous surface. SEM images and the particle size distribution of as-prepared ZnAc particles are shown in **Figure 1.5** and **Figure 1.6**, respectively.

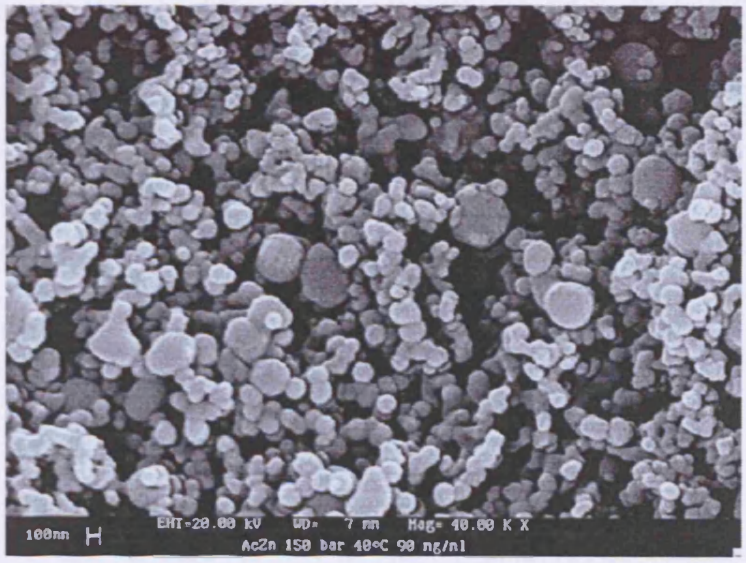

Figure 1.5 SEM image of ZnAc particles obtained at 150bar, 40°C, 90mg/ml DMSO.

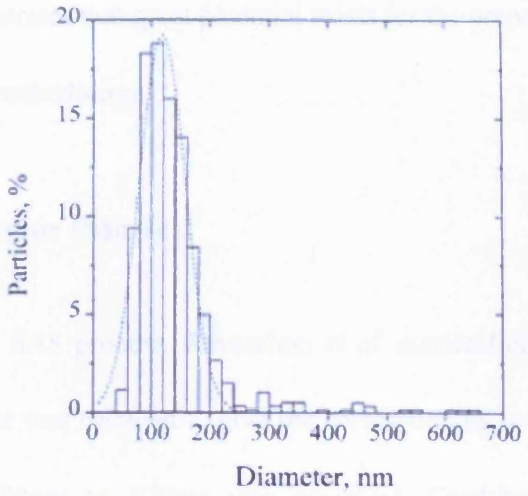

Figure 1.6 Mean particle size and particle size distribution of ZnAc obtained obtained at 150bar, 40°C, 90mg/ml DMSO.

This work explored the influence of the liquid phase concentration of ZnAc in DMSO on particle size and particle size distribution. They found that the particle size and particle size distribution increased with the increasing of liquid concentration. However, the surface areas decreased with the decreasing of liquid concentration. In addition, the effect of pressure and different solvents were further considered. When using NMP as a replacement for DMSO, more aggregated nanoparticles were observed. They attribute this to an interaction between the precipitates and the solution formed by NMP and scCO2. They thought that NMP have a mild coslovent effect to ZnAc particles when solublized in $scCO_2$. However, after one hour calcination at 300 °C, the high surface area of as-precipitated ZnAc dropped to about $55m^2/g$. Further work needs to be done on the optimization of the calcination process. This pioneering work on preparation of catalyst precursors using SAS process and the

new method demonstrates that great potential exists for the preparation of nano-scaled catalysts using the methodology.

(2) SmO_x precursor (SmAc)

Using the same SAS process, Reverchon *el al.* successfully prepared samarium acetate which further was calcined to give the corresponding oxide [10]. The particle size ranged from 50nm to 300nm was observed. Catalytic activity for ethane dehydrogenation on SmOx(SAS) was tested and it showed high selectivity to ethylene (58% at 680°C) in the oxidative dehydrogenation of ethane, which has been shown in **Figure 1.7**.

Furthermore, they compared the ethylene yield obtained with SmOx(SAS) and regular SmOx at a given value of ethane conversion. The result showed that the yield of ethylene on SmOx(SAS) is higher than on regular SmOx. This work gives an exciting information that catalysts derived from supercritical antisolvent precipitation may exhibit better catalytic performance to selective oxidation reaction.

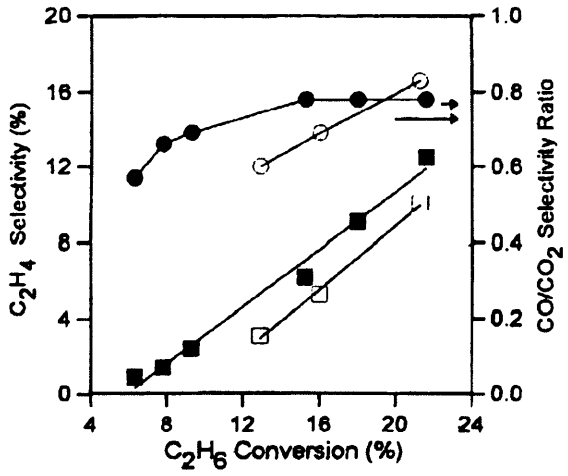

Figure 1.7 Ethylene yield (■,□) and CO/CO_2 selectivity ratio (●,○) versus ethane conversion on SmOx(SAS)(solid symbols) and on regular SmOx(open symbols) catalysts.

(3) VPO

Hutchings and co-workers reported the preparation of vanadium phosphate (VPO_{sc}) using supercritical CO_2 as an antisolvent in 2001[57-59]. The precipitation started from the isopropanol solution of vanadium phosphate and VPO precursor subsequently was obtained which consists of discrete spherical particles ranging between 75nm and 1um in diameter (**Figure 1.8**).

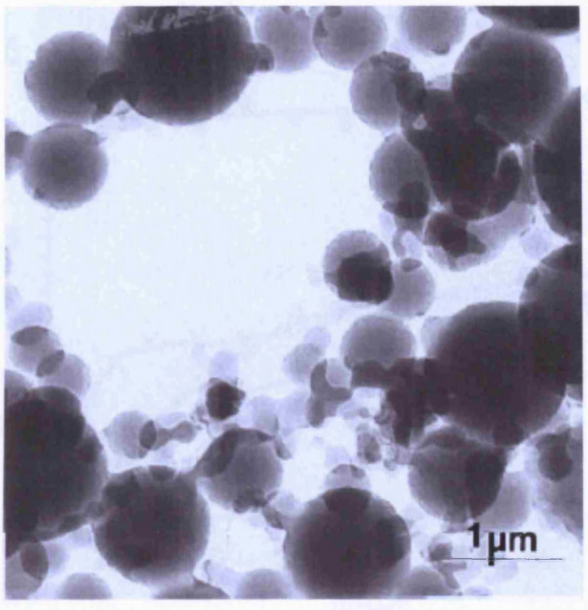

Figure 1.8 TEM image of as-prepared VPO precursor obtained at 110bar, 60°C.

Detailed caltalytic performance on this newly-prepared VPO was investigated on the partial oxidation of butane to maleic anhydride with the comparison of other conventional prepared VPO catalysts (**Figure 1.9** and **Table 1.3**). They found that the new vanadium phosphate catalyst (VPO_{sc}) using SAS process offered two distinct advantages over previous conventional preparation methods. First, compared with other conventional VPO catalysts, VPOsc did not require an extensive pretreatment time in the reactor and stable catalytic performance was attained as soon as the catalyst reached the required operating temperature. Second, the VPOsc was more active than the standard VPO catalysts despite the GHSV being twice that used for the conventional VPO catalysts.

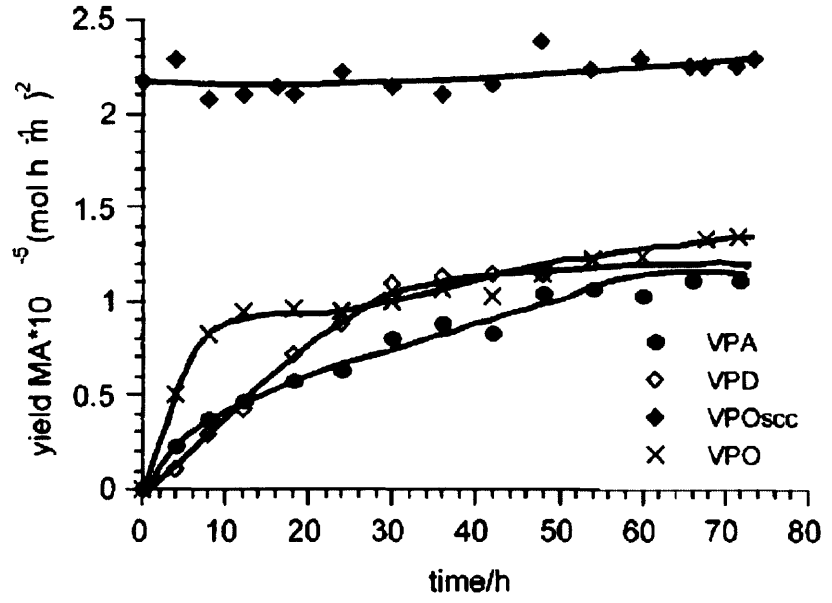

Figure 1.9 The yield of maleic anhydride (mol/h m^2) with time on stream for the VPA, VPO, VPD, and VPOsc catalysts. GHSV=1200^{-1} for the VPO, VPD, and VPA catalysts; GHSV=2400 $^{-1}$ for the VPOsc catalyst. The reaction temperature was 400±°C and the concentration of butane in air was 1.5% by volume for all catalysts.

Table 1.3

The Yield of Maleic Anhydride (mol/h · m^2) for the VPA, VPO, VPD, and VPO_{sc} Catalysts under Steady-State Conditions

Preparation route	*n*-Butane conversion (%)	Selectivity (%)	Surface area ($m^2 g^{-1}$)	Specific activity (mol MA $m^{-2} h^{-1}$)
VPA	11	51	4	1.24×10^{-5}
VPO	27	52	14	1.35×10^{-5}
VPD	62	64	43	1.19×10^{-5}
VPO_{sc}	24	48	6	2.2×10^{-5}

Note GHSV = 1200 h^{-1} for the VPO, VPD, and VPA catalysts; GHSV = 2400 h^{-1} for the VPO_{sc} catalyst. The reaction temperature was 400°C and the concentration of butane in air was 1.5% by volume for all catalysts.

This work has been the first detailed study on the application of catalysts derived from supercritical antisolvent precipitation. It further indicates that preparation of catalysts using supercritical CO_2 as an antisolvent may have a great potential to be an alternative preparation method since better catalytic performance than that of convention catalysts has been obtained in some reactions so far.

1.4.5.2 Superconductor preparation

A set of superconductor precursors including EuAc, GdAc, LaAc, YAc and SmAc have been prepared using SAS process by Reverchon and co-workers [53,54,60]. They systematically studied the effect of different preparation parameters, such as volumetric expansion of solvent, T, P, liquid concentrations, the feed ratio solution/antisolvent and various solvents, have been investigated. This systematic work offered the useful information on tailoring the particle size and morphology of particles in supercritical antisolvent precipitation process.

Taking an example of the preparation of YAc [54], the effects of volumetric expansion of DMSO was mainly investigated. Their results showed that volumetric expansion of DMSO mainly controlled the morphology of particles produced by SAS. SEM images of YAc in **Figure 1.10** clearly exhibited the change of morphology induced by volumetric expansion. When pressure varied from 100 to 160bar, no definite trend on the effect can be identified any more since the maximum value of volumetric expansion has been reached at that region.

Meanwhile, their study suggested the solute concentration mainly controls primary particle size and particle size distribution of precipitated materials, as shown in **Figure 1.11**. The data showed that the observed increase of diameter and particle size distribution correlates very well with the reduced concentration of all the tested solutes. For example, when using the same reduced concentration for various chemicals, the similar mean particle size and particle size distribution were observed. Due to the reduced concentration was defined as the ratio between the concentration of the liquid solution feeding to the SAS system and the concentration at saturation conditions, the distance from the saturation point was considered by the authors as the driving force for the particles formation and can determine their final characteristics.

This work offers a very useful guide for the preparation of inorganic materials with controlled size and morphology, which is quite essential for nanoscaled catalysts preparation.

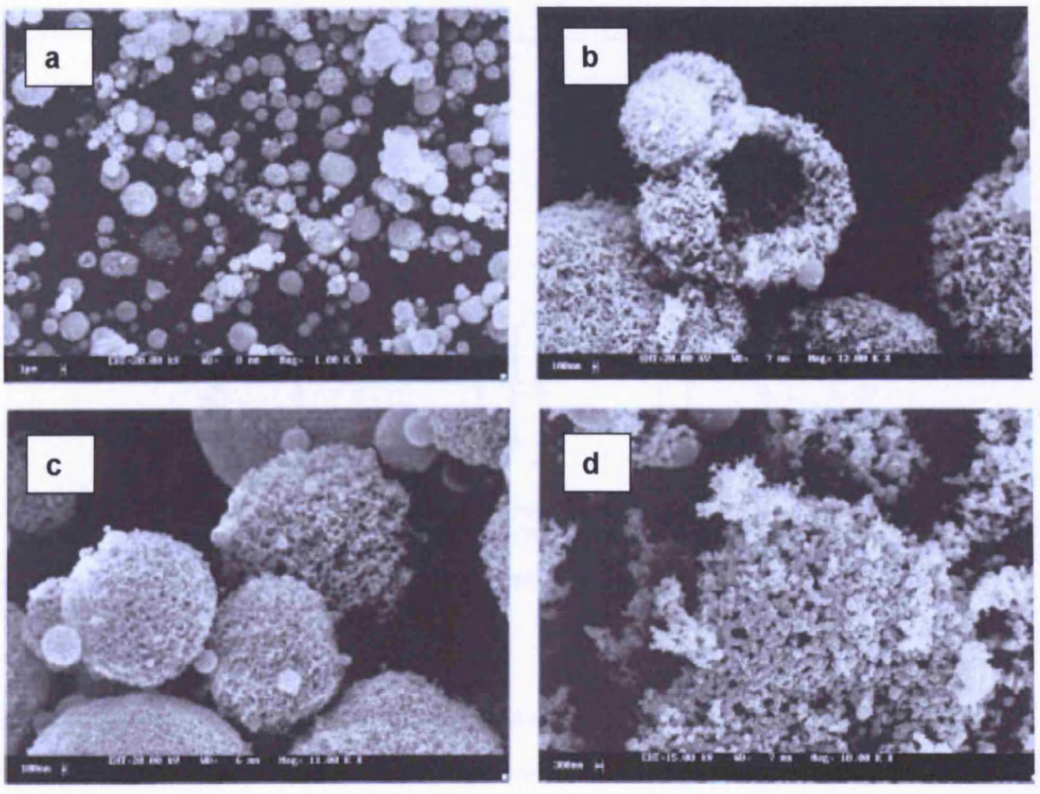

Figure 1.10 (a) SEM image, landscape view of AcY particles produced by SAS at 140 bar, 60 °C, 15 mg of solute/mL of DMSO. In this case very large (up to 20 *u*m diameter) expanded droplets (balloons) have been observed. (b) SEM image at the same conditions as those in Figure 4a. Details of the expanded droplets observed in the previous figure. This image shows the submicronic structure of these large aggregates. (c) SEM image at the same conditions as those in Figure 4a. One of the expanded droplets observed in the previous figures is broken. It is possible to observe that balloons are empty spherical shells. (d) SEM image of AcY at 90 bar, 40 °C, 15 mg of solute/mL of DMSO. Incipient explosion of a balloon.

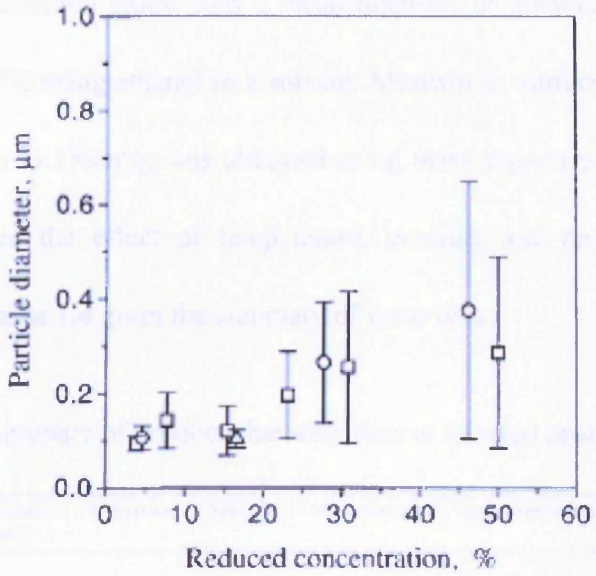

Figure 1.11 Mean diameter of particles against the reduced concentration of Y, Sm, and Nd acetates: □ = AcSm; O = AcY; △ = AcNd.

1.4.5.3 Other Materials

Very recently, Alonso *et al.* reported synthesis of titanium oxide particles using supercritical CO_2 as an antisolvent [56]. Quite different from previous studies, they directly obtained titanium oxide from the SAS process without a calcination procedure. They performed the precipitation at the pressure of 10-20MPa and the temperature of 200-300°C. Both of the pressure and temperature are much higher than previous works. Therefore, their process can be considered the combination of precipitation and decomposition of as-prepared particles.

In their study, the organometallic diisopropoxititanium bis(acetylacetonate) (DIPBAT) has been proposed a new organomatallic precursor for the synthesis of

TiO_2. Anatase titanium oxide with a mean diameter of 200nm, can be obtained at 20MPa and 300°C using ethanol as a solvent. Meanwhile, surface area of as-prepared anatase TiO_2 up to $150m^2/g$ was obtained using these supercritical conditions. They also investigated the effect of temperature, pressure and residence time on the precipitation. **Table 1.4** gives the summary of these data.

Table 1.4 Summary of product characteristics at selected operational conditions

P (MPa)	T (°C)	Residence time (s)	TiO_2 anatase	Yield (%)	Average size (nm)	Product pollution (% C)	Crystallinity	BET area (m^2/g)
Batch process[a]								
10.0	300		Yes	74	200	7.1	Very good	108
20.0	300		Yes	88	450	1.2	Very good	113
20.0	250		Yes	75	300	2.0	Good	160
20.0	200		¿?	-	-	12.0	Poor	350
Semi-continuous process[b]								
20.0	300	120	Yes	85	250	<1	Very good	159
20.0	300	90	Yes	82	125	<1	Very good	152
20.0	300	60	Yes	80	100	<1	Very good	140
20.0	300	30	¿?	-	-	-	Poor	-
20.0	300	20	¿?	-	-	-	Poor	-

[a] Initial concentration = 0.05 g DIPBAT/g reaction medium. Hydrolysis reactant: ethanol. Molar ratio EtOH/DIPBAT = 28.
[b] Hydrolysis reactant: ethanol. Molar ratio EtOH/DIPBAT = 28.

They considered the formation of anatase TiO_2 can be attributed to the hydrolysis of DIPBAT followed by the decomposition of the hydroxide. The reaction mechanism of the hydrolysis and decomposition process in supercritical antisolvent precipitation is described as follows:

$$EtOH \leftrightarrow \text{ethene} + H_2O$$

$$Ti(OR)_2(OR')_2 + H_2O \leftrightarrow Ti(OR)(OR')_2(OH) + ROH$$

$$Ti(OR)(OR')_2(OH) + H_2O \leftrightarrow Ti(OR')_2(OH)_2 + ROH$$

$$Ti(OR')_2(OH)_2 + H_2O \leftrightarrow Ti(OR')(OH)_3 + R'OH$$

$$Ti(OR')(OH)_3 + H_2O \leftrightarrow Ti(OH)_4 + R'OH$$

$$Ti(OH)_4 \leftrightarrow TiO_2 + 2H_2O$$

In this procedure, water for the hydrolysis is generated by decomposition of ethanol in the supercritical process. A molar ratio of at least 28 mol EtOH /mol DIPRAT is required in order to complete the reaction and to form anatase TiO_2. At the same time, high temperature of 300°C is essential to complete decomposition of titanium hydroxides.

This work demonstrates that remarkable progress has been achieved for preparation of metal oxides using supercritical antisolvent precipitation because it successfully solves the problem that the high surface area of the precipitated materials can't be retained after calcinations [11]. This is particularly essential for preparation of nanoscaled oxide catalysts in the future.

1.5 Aim of this project

In recent years the development of catalysts for processes to replace stoichiometric reactions, which produce large amounts of undesirable waste products, has made a significant contribution to the reduction of environmental pollutants. Unfortunately, this 'greening' of the chemical industry at one level is offset by environmental issues at another, issues that we now have to address. Traditional procedures for the commercial preparation of catalysts often involve the use of metal nitrates as intermediates, resulting in the generation of waste effluent. Recent UK regulations concerning the control of nitrate effluent will inevitably place severe restrictions on catalyst production, necessitating the development of new methods for catalyst synthesis. The aim of this project is to develop new preparation methodologies for heterogeneous catalysts currently prepared using nitrates with co-precipitation. Specific objectives will include:

a) The preparation of hopcalite ($CuMnO_x$) using supercritical CO_2 of high activity catalysts for CO oxidation.

b) The study of manipulating the parameters in supercritical antisolvent precipitation process to control and obtain the required material morphology.

c) The study of the synthesis of high activity oxides as supports for gold nanoparticles for CO oxidation as well as alcohol oxidation.

References and Notes

[1] P. T. Anastas and L. G Williamson, *Green chemical syntheses and Processes*, American Chemical Society: Washington, DC, 2000: Chapter 1.

[2] S. K. Ritter, *Chem. Eng. News*, 2001, **79**, 27.

[3] P. T. Anastas, J. C. Warner *Green Chemistry: Theory and Practice*, Oxford University Press: New York, 1998, p.30.

[4] http://www.epa.gov/greenchemistry/pubs/principles.html.

[5] P. T. Anastas and M. M. Kirchhoff, *Acc. Chem. Res.* 2002, **35**, 686.

[6] R. Noyori, *Chem. Com.* 2005, **14**, 1807.

[7] A. Baiker, *Chem. Rev.* 1999, **99**, 453.

[8] P. G. Jessop, T. Ikariya and R. Noyori, *Chem. Rev.* 1999, **99**, 475.

[9] E. Reverchon, *J. Supercrit. Fluid*,1999,**15**,1.

[10] E. Reverchon, G D. Porta, D. Sannino, L. Lisi and P. Ciambelli, *Stud. Surf. Sci. Catal.* 1998, **118**, 349.

[11] E. Reverchon, G Della Porta, D. Sannino and P. Ciambelli, *Powder Technol.*, 1999, **102**, 127.

[12] W. Wagner and A. Kruse, *Properties of Water and Steam*, Springer-Verlag, Berlin, 1998.

[13] R. Wandeler and A. Baiker, Cattech, 2000, **2**, 128.

[14] J. A. Darr and M. Poliakoff, *Chem.Rev.* 1999,**99**,495.

[15] T. L. Chester, J. D. Pinkston and D. E. Raynle, *Anal. Chem.* 1994,**66**, 106R

[16] M. D. Bermejo, F. Fdez-Polanco and M. J. Cocero, *Ind. Eng. Chem. Res.* 2006,

45, 3438.

[17] E. Reverchon and R. Adami, J. of Supercritical Fluids, 2006, **37**, 1

[18] J. Jung and M. Perrut, J of Supercritical Fluids, 2001, **20**,179.

[19] A. I. Cooper, *Adv. Mater.*, 2003,**15**,049.

[20] S. M. Pourmortazavi and S. S. Hajimirsadeghi, *Ind. Eng. Chem. Res.*, 2005, **44**, 6523.

[21] Y. Hakuta, H. Hayashi and K. Arai, *Current Opinion in Solid State and Materials Science*, 2003, 7, 341.

[22] A. I. Cooper, *J. Mater. Chem.*, 2000,**10**, 207.

[23] E. J. Beckman, J of Supercritical Fluids, 2004, **28**,121.

[24] R. D. Smith, U. S. Patent 4,582,732, 1986.

[25] R. D. Smith, U. S. Patent 4,734,451, 1988.

[26] P. G Debenedetti, J. W. Tom, X. Kwauk and S. –D. Yeo, *Fluid Phase Equilib.* 1993, 82, 311.

[27] J. W. Tom and P. G Debenedetti, *J. Aerosol Sci.* 1991, **22**, 555.

[28] E. Reverchon, *In Proc. 5th Meeting on Supercritical Fluids*, Nice, France, 1998, T1, 221.

[29] E. Reverchon, G. Della Porta and A. Di Trolio, *In Proc. 4th Conf. on Supercritical Fluids and Their Applications*, Capri, Italy,1997, 335.

[30] E. Reverchon, A. A. Barba, G. Della Porta, P. Ciambelli and D. Sannino, *In Proc. 4th Conf. on Supercritical Fluids and Their Applications*, Capri, Italy, 1997, 385.

[31] R. E. Sievers, U. Karst, U.S. Patent 5,639,441, 1997.

[32] R. E. Sievers, U. Karst, J. D. Schaefer, C. R. Stoldt, B. A. Watkins, *J. Aerosol Sci.* 1996, **27**, S497.

[33] S. E. Sievers, P. D. Milewski, C. Y. Xu, U. Karst, J. Rusic-Pavletic, K. D. Kusek, T. Mandal, W. C. Anderson, C. R. Stoldt, J. D. Schaefer, B. A. Miles, *In Proc. 5th Meeting on Supercritical Fluids*, Nice, France, 1998, T1, 273

[35] E. Reverchon, *Ind. Eng. Chem. Res.*, 2002, **41**, 2405.

[36] E. Reverchon and A, Spada, *Ind. Eng. Chem. Res.*, 2004, **43**, 1460.

[37] P. M. Gallagher, M. P. Coffey, V. J. Krukonis and W. W. Hillstrom, *J. Supercrit. Fluids* 1992, **5**, 130.

[38] S.-D. Yeo, G.-B. Lim, P. G. Debenedetti and H. Bernstein, *Biotechnol. Bioeng.* 1993,**41**, 341.

[39] T. W. Randolph, A. D. Randolph, M. Mebes and S. Yeung, *Biotechnol. Prog.* 1993,**9**, 429.

[40] D. J. Dixon, K. P. Johnston, *J. Appl. Polym. Sci.* 1993, **50**,1929.

[41] S. Mawson, M. Z. Yates, M. L. O'Neill, K. P. Johnston, *Langmuir* 1997, 13, 1519.

[42] S. Mawson, K. P. Johnston, D. E. Betts, J. B. McClain and J. M. DeSimone, *Macromolecules* 1997, 30, 71.

[43] S. Mawson, S. Kanakia, K. P. Johnston, *Polymer* 1997, **38**, 2957.

[44] S. Palakodaty, P. York, M. Hanna and J. Pritchard, *In Proc. 5th Meeting on Supercritical Fluids*, Nice, France, 1998, **T1**, 275.

[45] D.J. Dixon, K.P. Johnston and R.A. Bodmeier, AIChE J. 1993,**39**,127.

[46] S. Jaarmo, M. Rantakyla, O. Aaltonen, *Proceedings of the 4th International Symposium on Supercritical Fluids*, Tohoku Univ. Press, Sendai (Jap), 1997, 263.

[47] C. N. Field, P. A. Hamley, J. M. Webster, D. H. Gregory, J. J. Titman and M. Poliakoff, *J. Am. Chem. Soc.* 2000, **122**, 2480.

[48] R. P. Vignes, Dimethyl Sulfoxide (DMSO)-A "New" Clean, Unique, Superior Solvent. American Chemical Society, Annual Meeting, August 20-24, 2000.

[49] A. T. Bell, *Science*, 2003, **199**, 1688.

[50] N. Pernicone, *Cattech*, 2003, 7, 196.

[51] S. D. Yeo, J.H. Choi, T.J. Lee, J. of Supercritical Fluids, 2000,**16**,235.

[52] M. Hanna, P. York, Patent WO 95/01221, 1994.

[53] E. Reverchon, I. De Marco and G. Della Porta, J of Supercritical Fluids, 2002, **23**, 81.

[54] E. Reverchon, G. Della Porta, A. Di Trolio and S. Pace, *Ind. Eng. Chem. Res.*, 1998, **37**, 952.

[55] M. Hanna, P. York, Patent WO 98/36825, 1998.

[56] E. Alonso, I. Montequi, S. Lucas and M. J. Cocero, J of Supercritical Fluids, 2007, **39**,453.

[57] G J. Hutchings, J. K. Bartley, J. M. Webster, J. A. Lopez-Sanchez, D. J. Gilbert, C. J. Kiely, A. F. Carley, S. M. Howdle, S. Sajip, S. Caldarelli, C. Rhodes, J. C. Volta and M. Poliakoff, *J. Catal.*, **197**, 232 (2001).

[58] G J. Hutchings, J. A. Lopez-Sanchez, J. K. Bartley, J. M. Webster, A. Burrows, C. J. Kiely, A. F. Carley, C. Rhodes, M. Havecker, A. Knop-Gericke, R. W. Mayer, R. Schlogl, J. C. Volta and M. Poliakoff, *J. Catal.*, **208**, 197 (2002).

[59] J. A. Lopez-Sanchez, J. K. Bartley, A. Burrows, C. J. Kiely, M. Havecker, R. Schlogl, J. C. Volta, M. Poliakoff and G J. Hutchings, *New J. Chem.*, **26**, 1811 (2002).

[60] E. Reverchon, G Caputo and I. De Marco, *Ind. Eng. Chem. Res.*, 2003, **42**, 6406.

Chapter 2
Experimental Details

2.1 Catalysts Preparation

2.1.1 Precursor Precipitation by the SAS process

2.1.1.1 SAS apparatus

The scheme of the SAS apparatus is shown in **Figure 2.1**. It is a semi-continuous precipitation instrument. This apparatus consists of two HPLC pumps (Jasco, PU-980 for solution and PU-1580-CO_2 for CO_2), a back pressure regulator (BPR, Jasco, BP-1580-81), a precipitation chamber and an isothermal oven. Previously, we have successfully precipitated vanadium phosphate catalysts used this apparatus [1,2].

CO_2 is pumped as a liquid using one HPLC pump over the critical pressure (72bar), which is maintained by BPR. It passes through a length of coiled tube in the isothermal oven and is heated through its critical point. The starting solution is pumped through a fine capillary (220um id) into the precipitation vessel by the other HPLC pump. As the solution exits the capillary, the solvent and CO_2 diffuse into each other, reducing the solubility and the solutes precipitate. A stainless steel filter (500nm) is put at the bottom of the vessel. It collects the precipitates but allow the CO_2 and solution to pass though. To avoid clogging the BPR, a second stainless steel filter is set to locate below the first one to collect some particles which passes though the first filter.

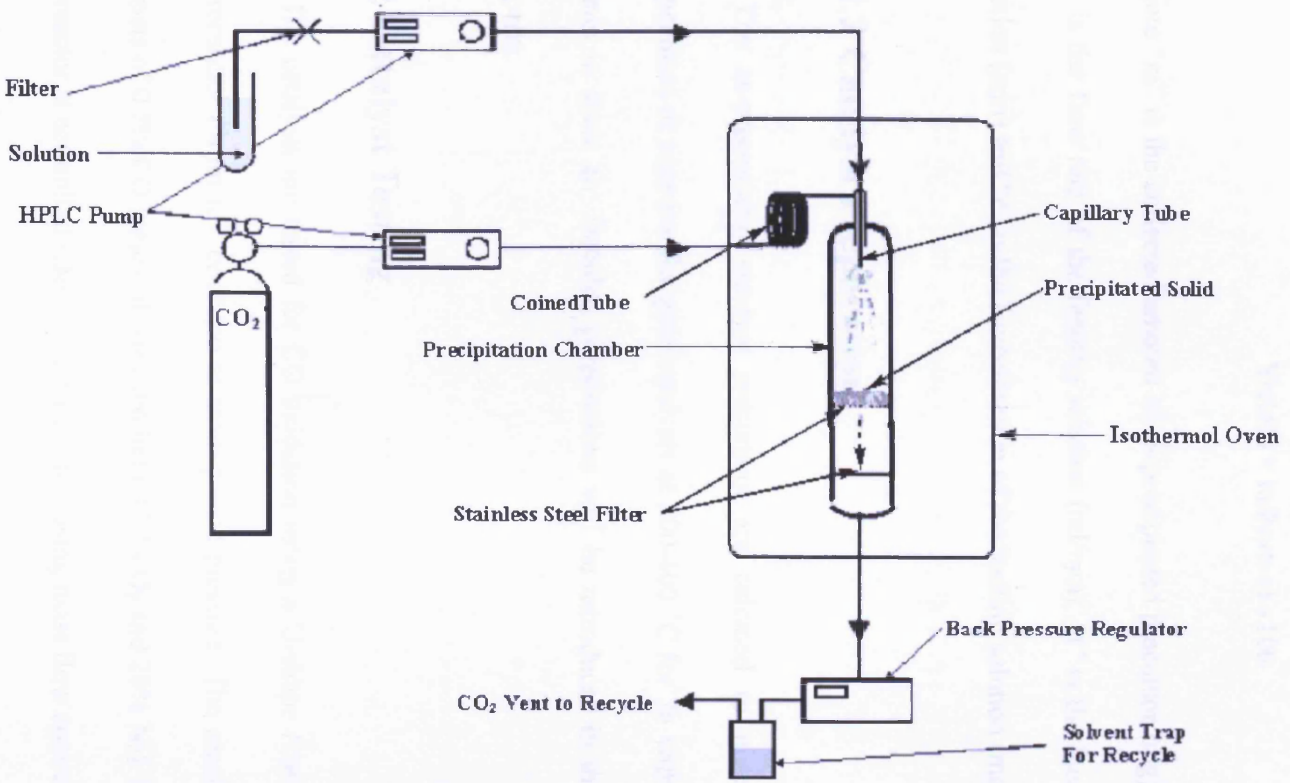

Figure 2.1 Scheme diagram of SAS apparatus in this experiment.

2.1.1.2 Calculation of the yield of as-precipitated precursor

The yield of as-precipitated precursors is approximately calculated as follows:

$$Yield\% = m/(v \times t \times c) \times 100$$

Where "m" is the collected amount of as-precipitated precursor (mg) after operation, "v" is the flow rate of the feeding solution (ml/min), "t" is the feeding time of the solution (min) and "c" is the concentration of the feeding solution (mg/ml).

2.1.2 Catalyst Preparation

The as-precipitated catalyst precursors are calcined to give final catalysts (hopcalites) or supports for gold catalysts at 300-400 °C for 2h with the ramp of 10 °C/min in static air. Detailed preparations will be introduced in the corresponding chapters.

2.2 Catalyst Testing

The catalysts are tested for CO oxidation using a U-shape fixed-bed laboratory microreactor (3mm id), operated at atmospheric pressure. The reaction gas mixture consists of 0.5% CO balanced with synthetic (80% O_2 and 20% N_2). The gas is fed to the reactor at controlled rates of 22.5 ml min^{-1} using mass flow controllers and passed over the catalysts (15 or 50mg). The catalyst temperature is maintained at 25 °C by immersing the quartz bed in a thermostatically controlled water bath. The products are analyzed using on-line gas chromatography.

2.3 Characterization

2.3.1 Characterization of precursors and catalysts

All the as-precipitated precursors and as-calcined catalysts as well as as-prepared gold catalysts have been characterized by XRD, BET, FT-IR, Raman, AAS, TGA, SEM, TEM and XPS. Amongst these characterizations, all the analysis work on gold catalysts was finished by Prof. C. Kiely's group in Lehigh University in USA and all the analysis on hopcalite sample was finished by Prof. M. Rosseinsky's group in Liverpool University. XPS analysis on gold catalysts and hopcalite samples was performed by Dr. A. Carley in Cardiff University

2.3.2 Chatacterization Techniques

2.3.2.1 X-ray powder diffraction (XRD)

X-ray powder diffraction (XRD) is widely used as a common technique in the research study of heterogeneous catalysts. XRD is a non-destructive technique and its most widespread use is for the identification of crystalline compounds by their diffraction pattern [3,4]. This method can be used for phase identification, quantitative analysis and the determination of structure imperfections. When X-rays interact with a crystalline substance, a diffraction pattern will be obtained. Hence, the X-ray diffraction pattern of a pure substance is like a fingerprint of the substance. With regard to pure amorphous solid materials, no phase diffraction patterns appear by XRD analysis. **Figure 2.2** displays a schematic picture of the X-ray tube, the X-ray

detector and the sample during the X-ray scan.

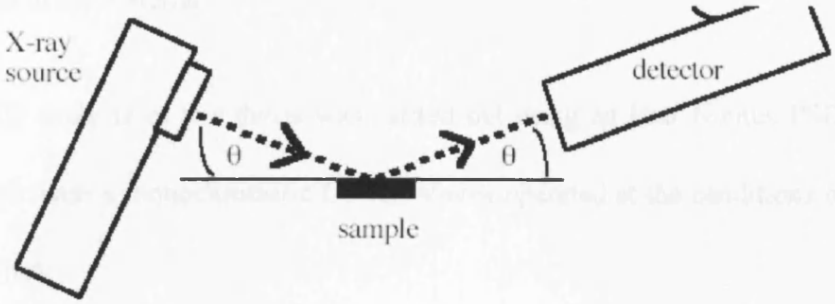

Figure 2.2 Schematic picture of the X-ray tube, X-ray detector and sample (θ: diffraction angle)

The basic theoretical principle that XRD analysis leans against is based on a mathematical formula called Bragg's Law, which is shown in **Figure 2.3**. According to this equation, when X-rays hit a crystalline sample and are diffracted, the distances between the planes of atoms that constitute the sample can be measured.

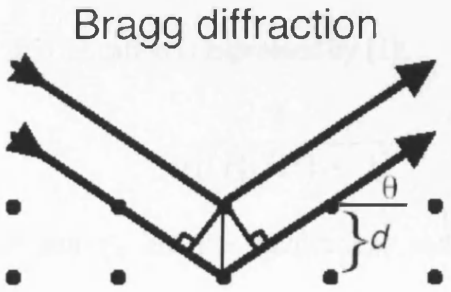

$n\lambda = 2d \sin\theta$
n: the order of the X-ray beam
λ: the wavelength
d: the interplanar spacing generating the diffraction
θ: the diffraction angle

Figure 2.3 Scheme of Bragg's Law of diffraction

The characteristic sets of d-spacings generated in a typical X-ray can be used as a fingerprint of the sample, since each crystalline material has a unique X-ray diffraction pattern. X-rays are diffracted by each material differently depending on what atoms make up the crystal lattice and how these atoms arrange. By comparison

with standard reference patterns and measurements, the XRD pattern allows for identification of the material.

The XRD analysis in this thesis was carried out using an Eraf Nonius PSD120 diffractometer with a monochromatic Cu $K_{\alpha 1}$ source operated at the conditions of 40 keV and 30 mA.

2.3.2.2 BET method

The most widely used technique for determining the surface area is the so-called BET method (Brunauer, Emmet and Teller, proposed in 1938) [5]. Surface area is an important and intrinsic physical property of materials and often plays a significant role in the reactivity of catalysts and sintering behaviour of powdered metals and so on. The concept of the theory is an extension of the Langmuir theory. The resulting BET equation is expressed by (1):

$$\frac{1}{v\left[(P_0/P)-1\right]} = \frac{c-1}{v_m c}\left(\frac{P}{P_0}\right) + \frac{1}{v_m c} \qquad (1)$$

P and P_0 are the equilibrium and the saturation pressure of adsorbates at the temperature of adsorption, v is the adsorbed gas quantity (for example, in volume units), and v_m is the monolayer adsorbed gas quantity.

The basic principle of BET method is to determine the surface area by calculating the amount of gas adsorbed at cryogenic temperatures. According to the amount of gas adsorbed at a given pressure, the BET equation can be used to calculate

the number of adsorbed gas molecules that would be required to form a monolayer on the surface. In the present work, data were treated in accordance with the BET method from the nitrogen adsorption isotherms.

For the BET surface area analysis in this thesis, powder samples were firstly degassed for approximately 30 minutes. After that, the sample was placed in a sample vessel connected to a gas inlet (liquid N_2 at 77K used to cool the vessel), a vacuum pump and an electronic barometer. The initial step of the analysis involved evacuation of the chamber in order to remove adsorbed molecules from the surface followed by the deposition step where N_2 was allowed into the chamber and the pressure was measured. All the analysis of samples were performed using the Micromeritics Gemini 2360 Analyzer, which is a fully automatic, single- or multi-point surface area analyzer.

2.3.2.3 Thermo gravimetric analysis (TGA)

Thermo gravimetric analysis (TGA) is a useful thermal analysis technique, which can be employed to measure the amount of weight change of a material, either as a function of increasing temperature, or isothermally as a function of time, in an atmosphere of nitrogen, helium, air, other gas, or in vacuum. Inorganic materials, metals, polymers and plastics, ceramics, glasses, and composite materials can be analyzed.

During the current work in this thesis, TGA analysis is mainly applied to

determine temperature and weight change of decomposition reactions, which in turn allows us to get a quantitative composition analysis of the material that was studied. All of the TGA analysis in the current work was carried out in N_2 flow with the ramp of 10°C/min using the SETARAM'S Labsys thermogravimetric analyzers.

2.3.2.4 X-ray photoelectron spectroscopy (XPS)

X-ray photoelectron spectroscopy (XPS) is among the most frequently used techniques in catalysis. It can yield information on the elemental composition, the oxidation state of the elements, chemical species that exist on the surface of samples, and in favorable cases on the dispersion of one phase over another [6]. This technique usually consists of a fixed X-ray energy source and an electron energy analyzer. Routinely, used X-ray sources are Al K_α (1486.6eV) or Mg K_α (1253.6eV). XPS analysis should be performed under a ultra high vacuum (UHV) environment.

The basic principle of XPS is based on the photoelectric effect proposed by Einstein [6], in which an atom absorbs a photon of energy hν; next a core or valence electron with binding energy E_b is ejected with kinetic energy E_k. In XPS, measuring the E_k and calculating the E_b will produce the fingerprint of the atom because for each and every element, there will be a characteristic binding energy associated with each core atomic orbital. Thus, the XPS spectra are able to provide information on the electronic state, elemental composition and chemical species that exist on the surface samples.

XPS analysis in this thesis X–ray photoelectron spectra were measured on a

Kratos Axis Ultra DLD spectrometer using a monochromatic AlK_{α} X-ray source (75 W) and an analyser pass energy of 40 eV. Samples were mounted using double-sided adhesive tape, and binding energies are referenced to the C(1s) binding energy of adventitious carbon contamination taken to be 284.7 eV.

2.3.2.5 Scanning electron microscopy (SEM)

Scanning electron microscopy (SEM) is a kind of electron spectroscopy capable of producing high resolution images of a sample surface, which involves using electrons rather than light to form an image [7]. Consequently, SEM allows a greater depth of focus than optical microscopy and is able produce an image that is a good illustration of a three-dimensional sample. SEM images have a characteristic three-dimensional appearance and are useful for judging the surface structure of the sample.

The basis principle of SEM can be simply described as the following: when electron beam hits the sample, two sorts of electrons, namely secondary electrons and backscatter electrons are produced . These two kinds of electrons are collected by the detector and converted to a signal that is transferred to a viewing screen, thus forming the SEM image. SEM images will show a quite natural looking on what the surface looks like. **Figure 2.4** gives SEM images of human hair and P25-TiO_2 powder.

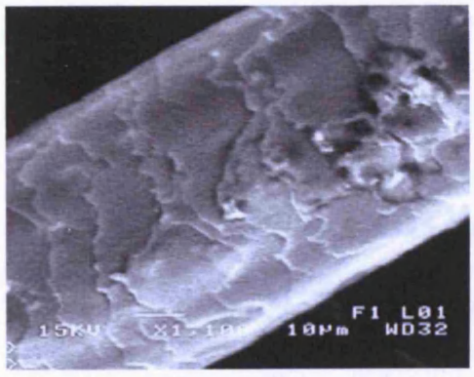

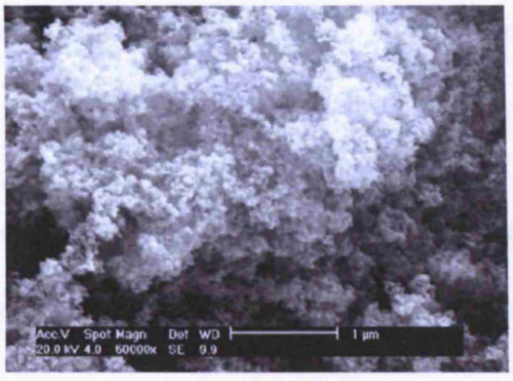

Human hair **TiO_2(P25) powder**

Figure 2.4 SEM images of human hair and TiO_2 (P25) powder

During the research in this thesis, SEM images were primarily used to provide the following information, including surface topography and surface morphology (i.e. the shape and size of particles making up the sample). All of the SEM analysis was carried out using a Hitachi S-246ON instrument operating at 25KV on gold coated powder samples.

2.3.2.6 Transmission electron microscopy (TEM)

Transmission electron microscopy (TEM) is another type of electron microscopy using electrons as source to image the sample, which is similar to SEM [7]. In catalysis, TEM is widely used to characterize the microscopic structure of catalysts, such as particle size and the shape of particles at an atomic scale. The main difference between SEM and TEM is the resolution power. The spatial resolution of the SEM depends on the size of the electron spot. The resolution is as well limited by the size of the interaction volume and the extent of material which interacts with the electron beam. The spot size and the interaction volume are both very large as compared to the

distances between atoms. As a result, the resolution of the SEM is not high enough to image down to the atomic scale.

However, TEM can detect the sample down to an atomic scale. This is because TEM uses electronmagnetic lenses to focus the electrons into a very thin beam and this electron beam will travel through the specimen. At the bottom of microscopy, the transmitted (unscattered electrons) hit a fluorescent screen, forming the so-called TEM image. The high contrast TEM image is formed by blocking electrons deflected away from the optical axis of the microscope by placing the aperture to allow only unscattered electrons through. In addition, another type of TEM is scanning transmission electron microscopy (STEM), where the beam can be rastered across the sample to form the image. **Figure 2.5** gives TEM images of multi-walled carbon nanotube and Al_2O_3-suppoted gold catalyst.

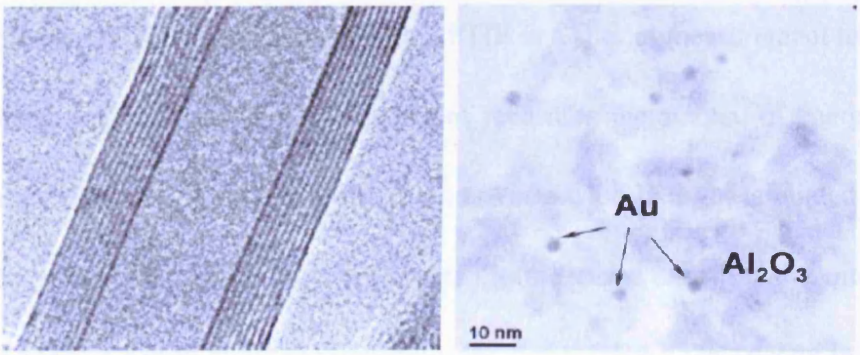

Figure 2.5 TEM images of multi-walled carbon nanotube and Au/Al_2O_3 catalyst

In this thesis, samples of each catalyst were prepared for transmission electron microscopy characterization by dispersing the powder in ethanol. A drop of the suspension was then placed on a 300 mesh lacey carbon TEM grid and allowed to dry.

Bright-field imaging experiments were carried out in a JEOL 2000 FX TEM operating at 200kV. Annular dark-field (ADF) imaging and x-ray energy dispersive spectroscopy (XEDS) analyses were carried out at 300kV using a VG HB 603 dedicated scanning transmission electron microscope (STEM) fitted with a Nion spherical aberration corrector and an Oxford Instruments INCA 300 system for XEDS spectrum imaging. All the analysis work on gold catalysts was finished by the group in Lehigh University in USA and all the analysis on hopcalite sample was finished by the group in Liverpool University. In particular, in this thesis, the joint-use of SEM and TEM was adopted since both of them can provide complementary information.

2.3.2.7 Fourier transform infrared spectroscopy (FTIR)

Fourier transform infrared spectroscopy (FTIR) is a powerful tool for identifying types of chemical bonds in a molecule by producing an infrared absorption spectrum that is like a molecular fingerprint [8,9]. FTIR is a special measurement technique for collecting infrared spectra (IR). Instead of recording the amount of energy absorbed when the frequency of the infra-red light is varied, the IR light is guided through an interferometer. After passing the sample, the measured signal is the interferogram. Since FTIR is a kind of IR spectroscopy, the signal from FTIR spectra is identical to that from conventional infrared spectroscopy. The theoretical principle of FTIR is the same as IR.

IR is one of the most common spectroscopic techniques. Simply, it is the absorption measurement of different IR frequencies by a sample positioned in the path

of an IR beam. IR works because chemical bonds have specific frequencies at which they vibrate corresponding to energy levels [8,9]. Consequently, IR is a spectroscopy that uses the information of molecular vibration. Since different functional groups absorb characteristic frequencies of IR radiation, IR spectra will give us the information that what kinds of functional groups exist in the material that is analyzed. **Figure 2.6** shows an example of FTIR spectrum of silicone. By adopting various sampling accessories, IR spectrometers can accept a wide range of sample types such as gases, liquids, and solids.

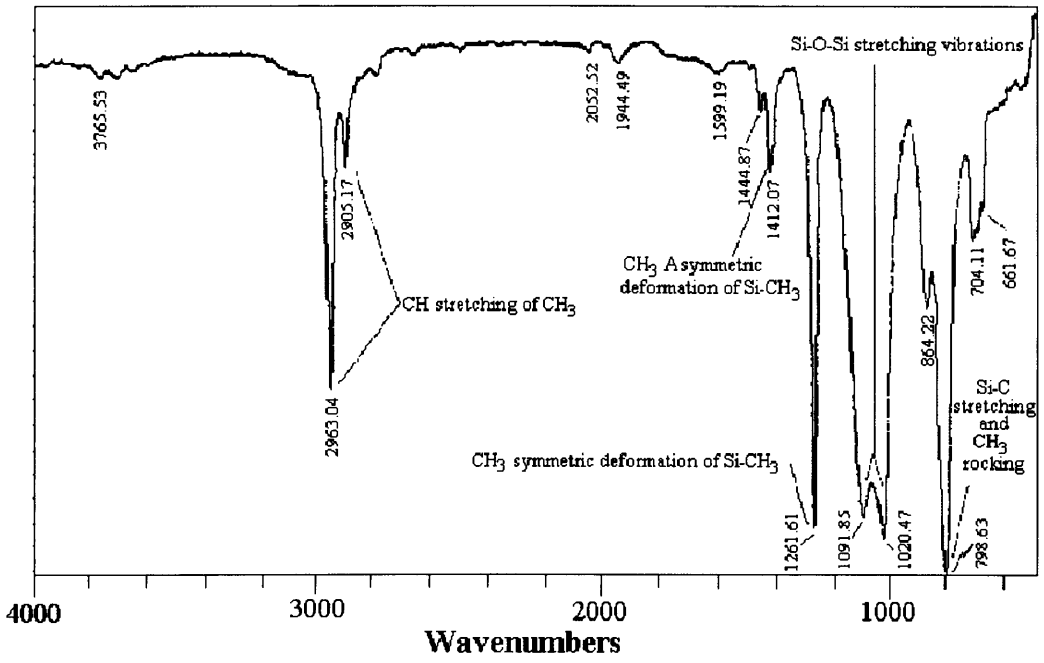

Figure 2.6 FTIR spectrum of silicone (polydimethylsiloxane)

In this thesis, the main goal of FTIR analysis is to determine the chemical functional groups in the sample, which is able to help structural elucidation and compound identification. All the analysis of FTIR was carried out on a Perkin Elmer series 2000 FT-IR spectrometer.

2.3.2.8 Raman spectroscopy

Similar to Infrared spectroscopy (IR), Raman spectroscopy also measure the vibrational energies of molecules but these methods rely only different selection rules [8,9]. For a vibrational motion to be IR active, the dipole moment of the molecule must change. For example, the symmetric stretch in carbon dioxide is not IR active because there is not change in the dipole moment whereas the asymmetric stretch is IR active due to a change in dipole moment. For a transition to be Raman active, a change in polarizability of the molecule must be happened with the vibration motion. From this viewpoint, Raman spectroscopy complements IR spectroscopy. Some chemical functional groups that IR can not detect can be analyzed by Raman spectroscopy analysis. The relationship and difference between the spectroscopy lines that IR and Raman detect can be seen in **Figure 2.7**.

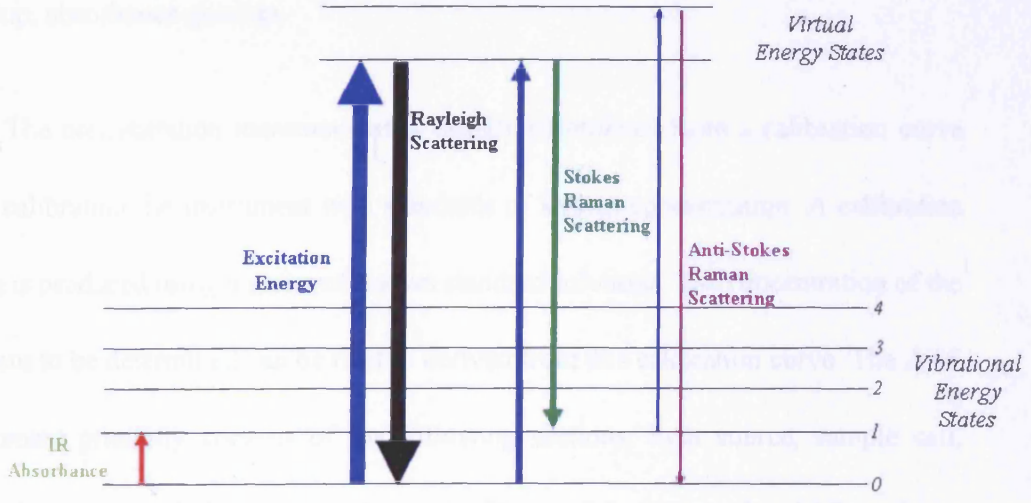

Figure 2.7 Comparisons of energy levels in Raman and IR spectra

All of the Raman analysis in this thesis was carried out on a Renishaw Ramanscope spectrograph fitted with a green Ar+ laser (λ=514.532nm).

2.3.2.9 Atomic Absorption Spectrophotometry (AAS)

Atomic absorption spectroscopy (AAS) is a technique for determining the concentration of a particular metal element within a sample [10]. In their elemental form, metals are able to absorb ultraviolet (UV) light when they are excited by heat. Each metal has a characteristic wavelength that will be absorbed. AAS looks for a particular metal by focusing a beam of UV light at a specific wavelength through a flame and into a detector. The sample of interest is aspirated into the flame. If that metal is present in the sample, it will absorb some of the light, thus reducing its intensity. The AAS instrument measures the change in intensity. Then, a computer data system converts the change in intensity into an absorbance. As concentration goes up, absorbance goes up.

The concentration measurement is usually determined from a calibration curve after calibrating the instrument with standards of known concentration. A calibration curve is produced using a series of known standard solutions. The concentration of the element to be determined can be readily derived from this calibration curve. The AAS instrument primarily consists of the following sections: light source, sample cell, monochromator and detector, as shown in **Figure 2.8**. During the AAS analysis, successful operation of AAS often depends on the correct choice of flame, suitable

preparation of samples and standards, careful optical alignment of the lamp with the monochromator and careful alignment of the burner with the light path.

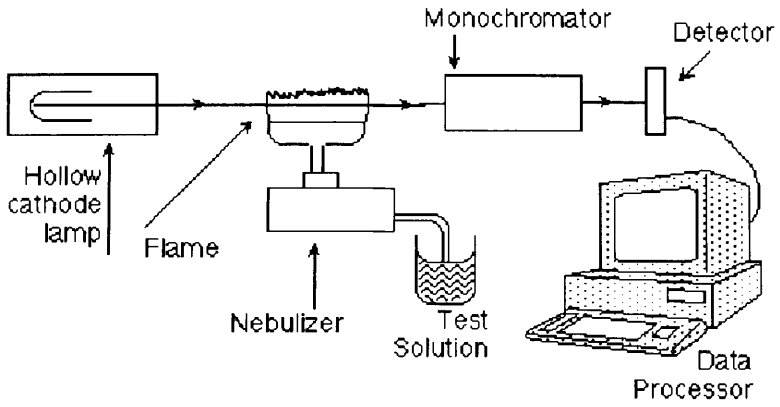

Figure 2.8 Sketch of atomic absorption spectrophotometer

In this thesis, AAS is mainly used to determine the loading of metal on a support and the ration of composition of metal elements in a compound. All the analysis of AAS was carried out with a Perkin-Elmer 2100 Atomic Absorption spectrometer using an air-acetylene flame.

References and Notes

[1] G J. Hutchings, J. K. Bartley, J. M. Webster, J. A. Lopez-Sanchez, D. J. Gilbert, C. J. Kiely, A. F. Carley, S. M. Howdle, S. Sajip, S. Caldarelli, C. Rhodes, J. C. Volta and M. Poliakoff, *J. Catal.* 2001,**197**,232.

[2] G J. Hutchings, J. A. Lopez-Sanchez, J. K. Bartley, J. M. Webster, A. Burrows, C. J. Kiely, A. F. Carley, C. Rhodes, M. Havecker, A. Knop-Gericke, R. W. Mayer, R. Schlogl, J. C. Volta and M. Poliakoff, *J. Catal.* 2002, **208**,197.

[3] R. Jenkins, R. L. Snyder, *Introduction to X-ray Powder Diffractiometry* John Wiley, 1996.

[4] B. D. Cullity, S. R. Stock, *Elements of X-ray Diffraction* 3rd Ed. Addison-Wesley, 2001.

[5] S. Brunauer, P. H. Emmett, E. Teller, *J. Am. Chem. Soc.* 1938, **60**, 309.

[6] J. F. Watts, J. Wolstenholme, *An Introduction to Surface Analysis by XPS and AES* John Wiley & Sons, 2003.

[7] S. L. Flegler, J. W. Heckman, K. L. Klomparens, *Scanning and Transmission Electron Microscope*, Oxford University Press, 1993.

[8] J. W. Niemantsverdriet, *Spectroscopy in Catalysis*, Wiley, 1993.

[9] B. Schrader, *Infrared and Raman Spectroscopy*, VCH Publishers Inc, New York, 1995.

[10] J. W. Robinson, R. Robinson, *Atomic Spectroscopy*, Marcel Dekker, 1996.

Chapter 3

Preparation and Catalytic Evaluation of $CuMnO_x$ for CO Oxidation

3.1 Introduction

The mixed copper manganese oxide (CuMnOx), also called hopcalite, is a well-known oxidation catalyst at room temperature. It can effectively remove deadly carbon monoxide from breathing air, destroy Volatile Organic Compounds (VOC) in ambient environment, as well as destruct toxic and corrosive emission of ozone. Since its first reported use in 1921, this catalyst system has been successfully used as a commercial catalytic material for over 80 years in respiratory protection in military, mining and space application.

During the last decades, to investigate its activity-structure correlation and achieve higher catalytic activity, the studies of hopcalite have been carried out on synthesis methods, characterization, adsorption and physical properties, mechanism of catalytic activity as well as applications. So far, it is suggested that the high activity of the hopcalite catalyst is due to the resonance system $Cu^{2+}+Mn^{3+}\Leftrightarrow Cu^{1+}+Mn^{4+}$ and the unique adsorption properties of CO on Cu^{2+}/Mn^{4+} as well as of oxygen on Cu^{1+}/Mn^{3+}.The purpose of the resonance system is thought as the regeneration of the

catalyst in an active state after chemisorption of CO and O_2 and formation of CO_2 [1-4]. In addition, the activity of hopcalite also depends on its morphology since many studies have showed that the hopcalite is highly active in the amorphous state,[1-2] even at room temperature, and the activity is lost if the material is calcined at temperatures above *ca.* 500°C when a crystalline spinel phase is formed. On the other hand, the studies of the synthesis methods indicated that the activity of $CuMn_2O_4$ is known to depend on the structure of the catalyst precursor [5] and, in general, this is in turn controlled by the preparation method. Recently, Hutchings and co-workers have investigated the effect of the parameters in the coprecipitation procedures on the catalyst performance [5-7]. Their results showed that the ageing time in the precipitate process is of crucial importance in the preparation of active hopcalites and the most active catalyst was aged for 12 hours and the phase prepared was the stoichiometric $CuMn_2O_4$. The modified approach has led to the preparation of the hopcalite with better catalytic activity [5-7] .

It is well known that active hopcalites are currently prepared by coprecipitation of a basic carbonate from a solution of the nitrates using sodium carbonate. Recently, the UK government has issued new regulations [8] concerning the control of nitrate effluent that will place severe restrictions on catalyst production, as nitrates are standard starting point for the preparation of many large-scale heterogeneous catalysts. Therefore, there is an urgent need to develop a new catalyst preparation methodology that avoids the use of nitrates. This is particularly important for hopcalite thinking that it is widely used in breathing apparatus, smoke hoods and other personal protection

applications. Using supercritical fluids in catalyst preparation provides an important possibility of a nitrate-free path to catalysts and catalyst precursors, thereby providing a new green route for catalyst manufacture.

In this chapter,it was focused on the preparation of nanostructured $CuMnO_x$ using supercritical CO_2 as an antisolvent and acetates as starting precursors. Different solvents for metal acetates including pure solvents and cosolvents contained water as well as hydrogen peroxide have been investigated and catalysts with high activity for CO oxidation at room temperature have been obtained.

3.2. Experimental

3.2.1 Catalyst Preparation

The synthesis of $CuMn_2O_4$ was performed using the apparatus shown schematically in Chapter 2 (**Figure 2.1**). A mixed solution of copper acetate and manganese acetate (1:2 in molar ratio) in solvent (i.e. dimethyl sulfoxide) was prepared. Supercritical CO_2 was pumped in at pressures of up to 110bar with the flow rate of 10 ml min^{-1}. The whole system was held at 40 °C. Initially, pure solvent was pumped through a fine capillary into the precipitation vessel at a flow rate around 0.1 ml min^{-1} for 25 min in co-current mode with supercritical CO_2 in order to obtain steady-state conditions in the vessel. After the initial period, the flow of liquid solvent was stopped and the mixed acetate solution was delivered at 0.1 ml min^{-1} flow rate.

The system pressure and temperature was maintained constantly during the course of feeding the solution and CO_2. As the solution exited the capillary, the droplet and $scCO_2$ rapidly diffused into each other, causing expansion, simultaneously reducing the solvent power. The solute was precipitated rapidly. When all the solution had been processed, $scCO_2$ was pumped for a further hour to wash the vessel in case the residual dimethyl sulfoxide (DMSO) condensed during the depressurization and partly solubilized the precipitated powder modifying its morphology. When the washing process was completed, the CO_2 flow was stopped and the vessel was depressurized to atmospheric pressure and the light green as-precipitated precursor was collected. The precursor was calcined at a certain temperature in air to produce the final catalyst-copper manganese oxide which was further used to the oxidation of CO under ambient temperature.

To investigate the influence of various precipitation environments in supercritical process, I explored different pressure from 110 to 150bar and different temperatures from 40 to 60 °C. In addition, various kinds of solvents were applied, which range from single solvents, including DMSO, DMF and NMP etc, to mixed solvents, such as water-ethanol, water-DMF and H_2O_2-ethanol etc.

All these as-prepared precursors were characterized by the analysis of XRD, BET FT-IR, TGA, SEM, and in selected samples, by TEM and XPS.

3.2.2 Materials

All the materials were used as supplied. **Table 3.1** lists the details on all these materials including solvents, metal salts and CO_2 gas.

Table 3.1 Specification of materials used in the supercritical antisolvent precipitation

Materials *	Grade	Company
CO_2	SFC, 99.99%	BOC
Cupric acetate monohydrate	ACS reagent, ≥98%	Sigma-Aldrich
Manganese(II) acetate tetrahydrate	≥99%	Aldrich
Dimethyl sulfoxide (DMSO)	ACS reagent, ≥99.9%	Aldrich
ethanol	Analytical reagent, absolute	Fisher
Dimethylformamide (DMF)	HPLC grade	Acros
N-Methyl-2-pyrrolidone (NMP)	Spectrophotometric grade, 99%	Aldrich
methanol	HPLC Grade	Fisher
H_2O_2	30% H_2O_2 in water	Aldrich

3.3. Results and Discussion

3.3.1 Using pure DMSO as a solvent

DMSO is a clean, low toxic and dipolar aprotic solvent which widely functions as a reaction solvent in pharmaceutical, agricultural, polymer processes and sugar esters [9]. Due to its high solubility of inorganic metal salts and complete miscibility with $scCO_2$, DMSO has been considered the best solvent to produce metal oxide precursors in supercritical antisolvent precipitation process. Recently, Reverchon and co-workers have successfully produced a variety of metal oxides applying DMSO as a solvent in supercritical process [10-11]. Their results showed well-defined nanoparticles of metal oxides precursors have been obtained with high yield due to the excellent miscibility between DMSO and supercritical CO_2 as well as the good dissolve power of DMSO to metal acetates.

In view of these pioneer works, our initial synthesis of CuMnOx in supercritical antisolvent process was performed using pure DMSO as a solvent. Experiments were conducted over about 6h, which resulted in the synthesis of approximately 0.5g of light green solid. The yield was calculated approximately around 45% based on the starting materials of CuAc of 10 mg/ml and MnAc of 24.5 mg/ml in DMSO.

3.3.1.1 Characterization of the precursor

The precursor obtained from supercritical antisolvent process was characterized by the analysis of XRD, FT-IR, SEM and TEM. The results are showed as follows

The XRD patterns of as-prepared precursor and the starting materials (CuAc and MnAc) are shown in **Figure 3.1**. The hopcalite precursor produced from supercritical process is clearly amorphous, in contrast with the crystalline CuAc and MnAc before supercritical process. The result is in full agreement with the literature reports, in which amorphous materials were always obtained in supercritical antisolvent process when using pure DMSO as a solvent [10]. Due to the prompt precipitation induced by the rapid mix between $scCO_2$ and DMSO in supercritical process, it is easy to understand that the amorphous precursor can be obtained using this method.

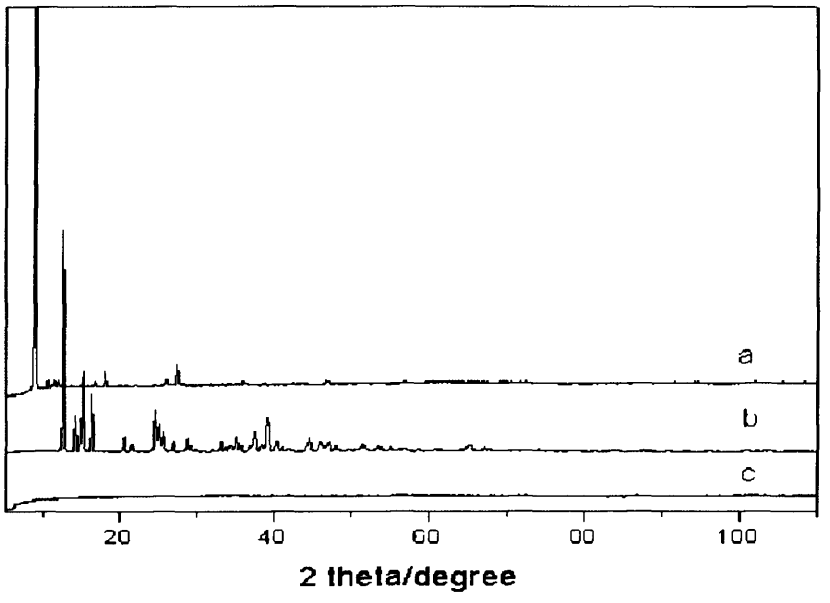

Figure 3.1 XRD patterns of untreated manganese acetate (a), copper acetate (b) and $CuMnO_x$ precursor from supercritical process (c).

The FT-IR spectrum of the precursor (**Figure 3.2**) shows the main bands of the acetate salts at 1561 and 1415 cm^{-1}, corresponding to the asymmetric and symmetric stretching of carboxyl groups, respectively. There are also bands observed at 1471 cm^{-1} as a shoulder, and at 842cm^{-1}, which may be attributed to the presence of a little bit basic carbonate salts. The presence of carbonate salts can be attributed to the exposing of the materials to CO_2 atmosphere in the supercritical process.

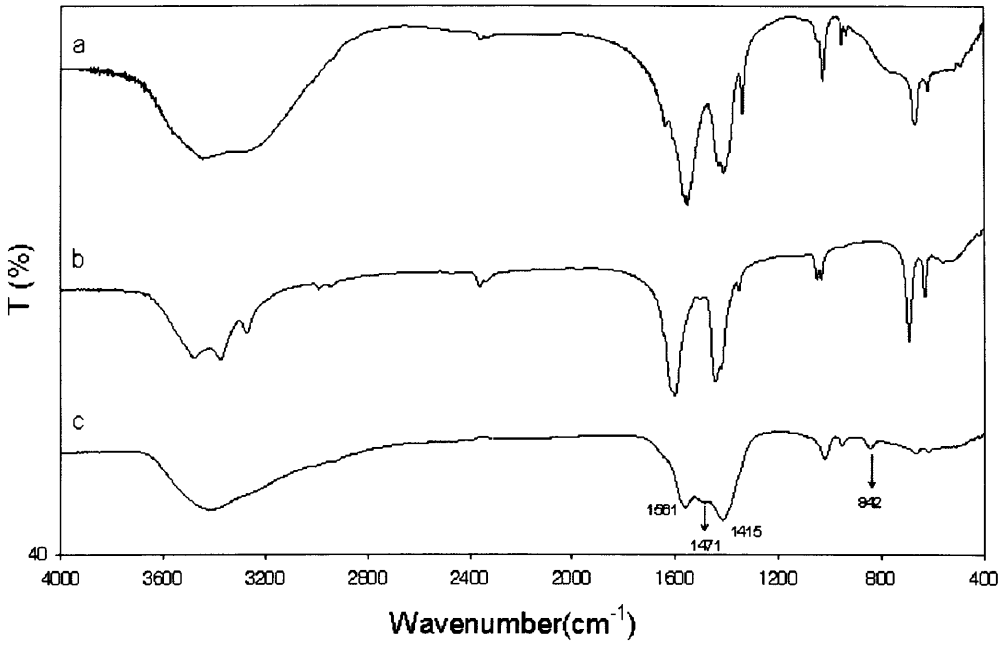

Figure 3.2 The FT-IR spectra of untreated manganese acetate (a), copper acetate (b) and $CuMnO_x$ precursor from supercritical process (c).

BET surface area measurements show that precursors made using this process exhibit exceptionally high surface area, up to *ca.* 300 m^2g^{-1}. The ratio of [Cu]:[Mn] in the precursor prepared was found to be 0.51 by the analysis of AAS, indicating that the copper acetate and manganese acetate were precipitated stoichiometrically.

The SEM images of the precursor (**Figure 3.3**) show that almost no well defined particles can be observed. The material is highly aggregated with each other and the particle size is quite small from the images and the average size of the material is around 20nm.

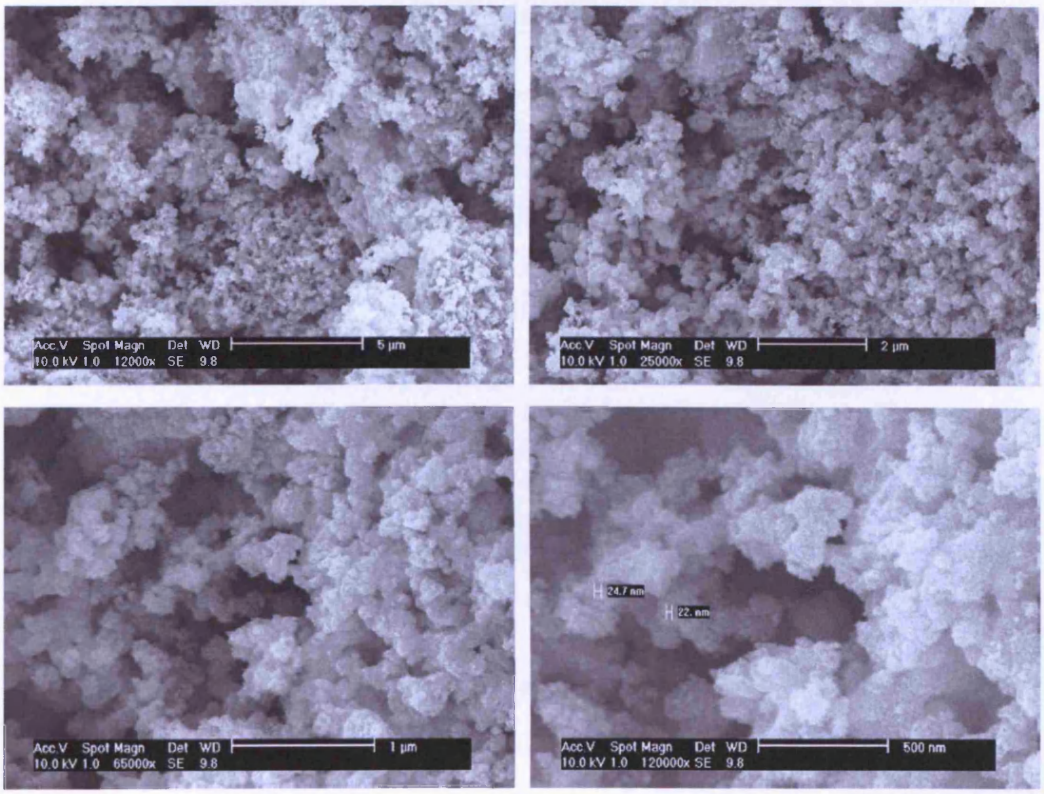

Figure 3.3 SEM images of CuMnOx Precursor from supercritical process

In order to investigate the morphology of particles, the analysis of TEM on the precursor has been performed. The TEM image of the precursor (**Figure 3.4**) reveals very little contrast, consistent with the lack of crystalline order. Furthermore, the image shows that the material has slightly aggregated quasi-spherical non-faceted particles of relatively uniform size and dimensions (10-20 nm with some particles as

large as 50 nm), which are smaller in comparison with those afforded by other precipitation routes.

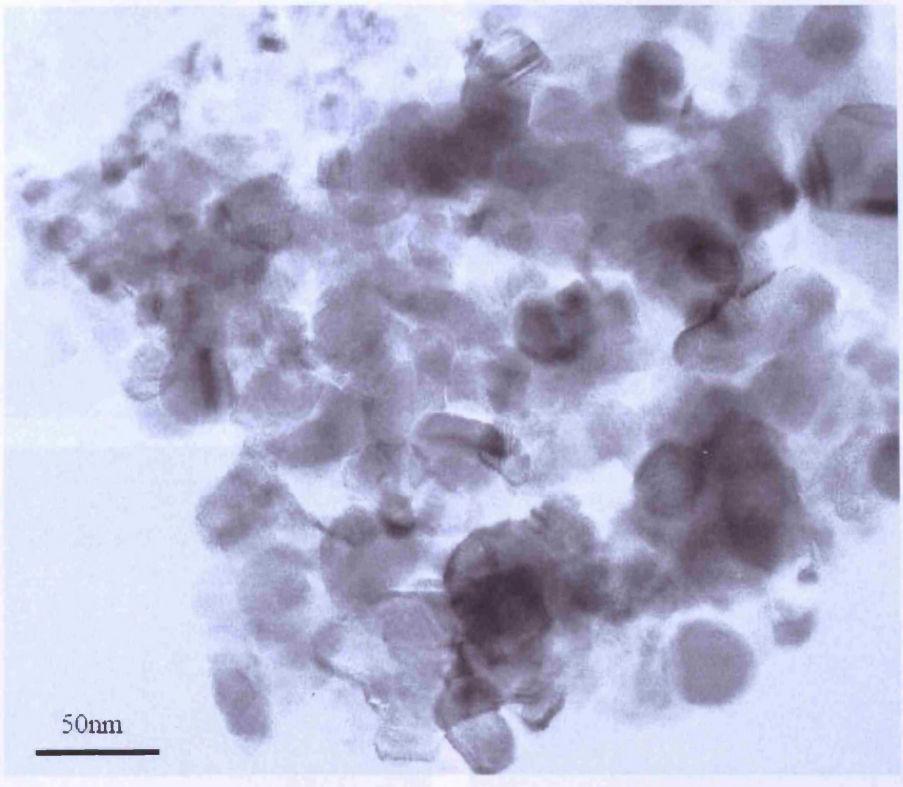

Figure 3.4 TEM image of $CuMnO_x$ precursor prepared using DMSO as solvent

The elemental distribution within the precursor particle assemblage is highly homogeneous even when probed with the high spatial resolution for chemical analysis (8 Å) of the STEM (**Figure 3.5**) – there is nanoscale intermixing of Cu, Mn and O within the precursor although even the STEM cannot resolve individual particles within these highly aggregated assemblies. Hence, we conclude that the precursor comprises amorphous compositionally homogeneous nanocrystals of mixed copper and manganese acetates, together with some basic carbonate salts.

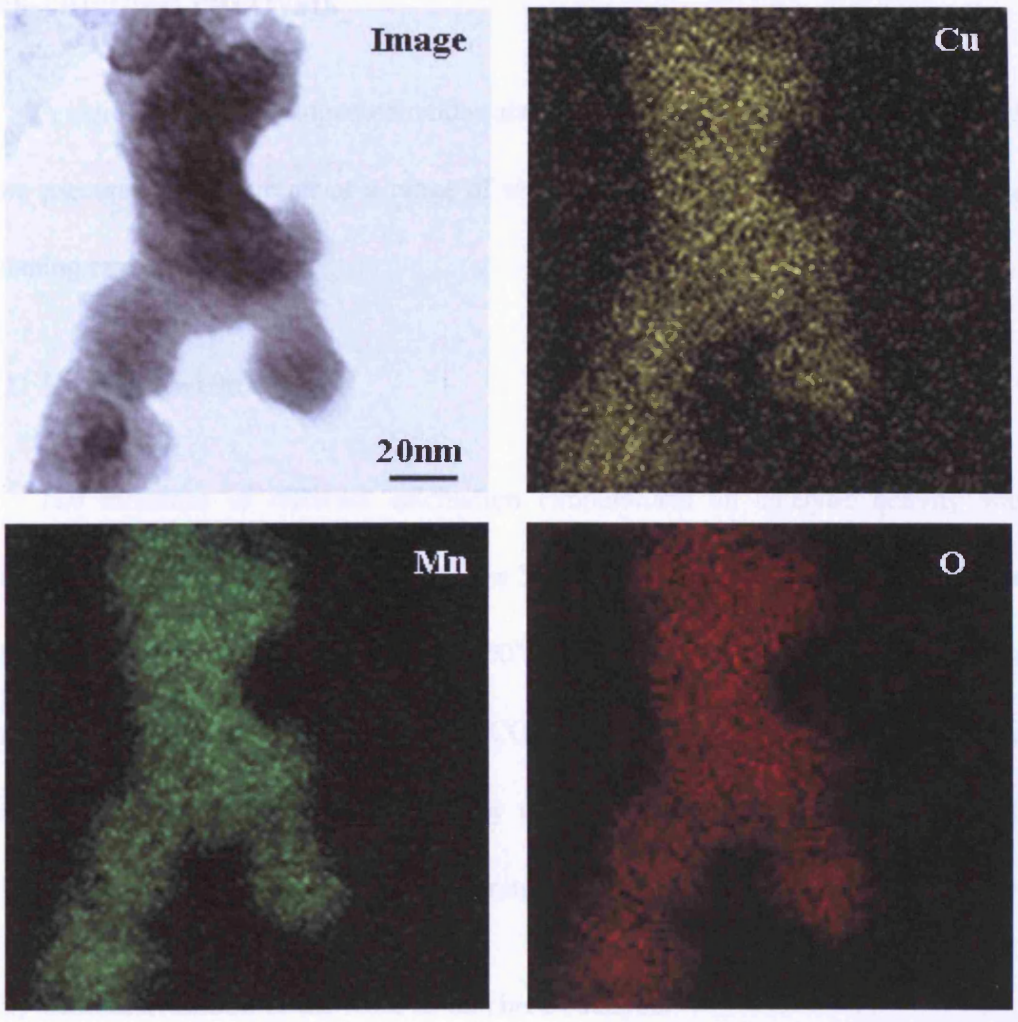

Figure 3.5 STEM dark field image of nanoparticles from the precursor material prepared using DMSO as solvent. The element distribution across this area is mapped by EDX and the different maps shown correspond to Mn, Cu and O edges.

3.3.1.2 Characterization and catalytic performance of as-calcined catalysts

A series of copper manganese oxide catalysts were then obtained by calcination of the precursors in static air at a range of temperatures (250-500 °C) for 2 h, with a heating rate of 20 °C min^{-1}.

(1) Catalytic performance

The influence of different calcination temperatures on catalytic activity was investigated. The result is shown in **Figure 3.6**. Clearly, when calcination temperature is quite low (< 300°C) or quite high (= 500°C), the catalysts exhibit the poor catalytic performance with the conversion on CO oxidation down to 3%. The highest conversion up to around 14% is given by the catalyst calcined at 300°C. The result illustrates the optimum calcination temperature is *ca.* 300 °C.

(2) Characterization of the final as-calcined catalysts

From the XRD analysis shown in **Figure 3.7**, it can be seen that the catalysts exhibit almost the same crystallinity after calcination in static air, even at a low calcination temperature (250 °C). Moreover, the crystallinity of the material increased with increasing calcination temperature. For the catalyst with calcination at 300°C, the diffraction patterns show that there is not typical $CuMn_2O_4$ phases and only some MnO_x phase is observed. With the increase of calcinations temperature, the main

phases are a little different. When calcined at 500°C, the catalyst shows two phases: $Cu_{1.4}Mn_{1.6}O_4$ and MnO_x.

The FT-IR spectrum of the final catalyst calcined at 300 °C is tested. As shown in **Figure 3.8**, the spectrum does not exhibit the bands of the carboxyl groups, indicating the precursor was decomposed completely at this temperature. In addition, the band at *ca.* 600 cm^{-1} can be attributed to the vibration of Mn-O bonds. Furthermore, we do not observe the bands from Cu-O bonds. This result is in greatly consistent with the observation from XRD characterization, in which only some manganese oxide appears.

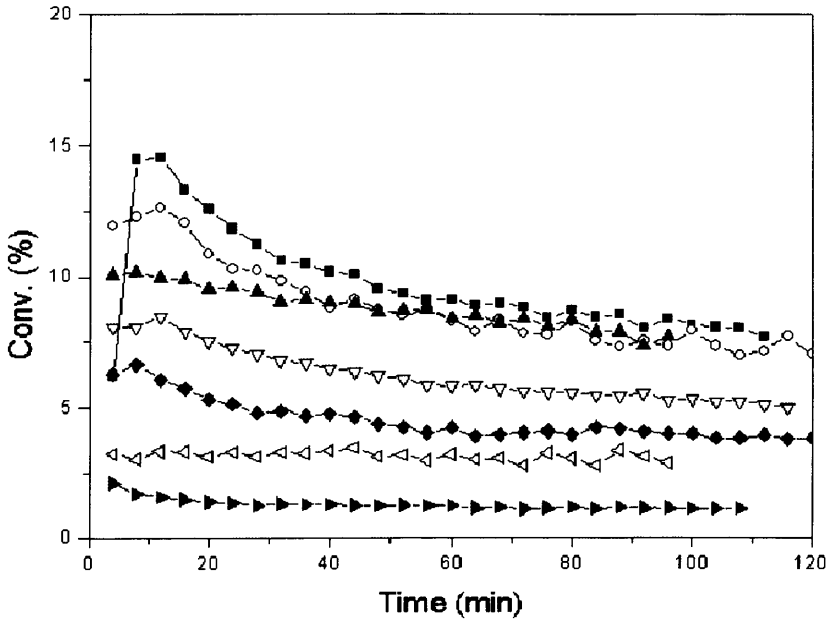

Figure 3.6 Catalytic performance of the CuMnOx precursor (▶) and the final catalysts calcined at 250°C (◆), 275°C (▽), 300°C (■), 350°C (○), 415°C (▲) and 500°C (◁). Test conditions: 298K, 0.5% CO in synthetic air, 50mg catalyst, GHSV=17000h^{-1}.

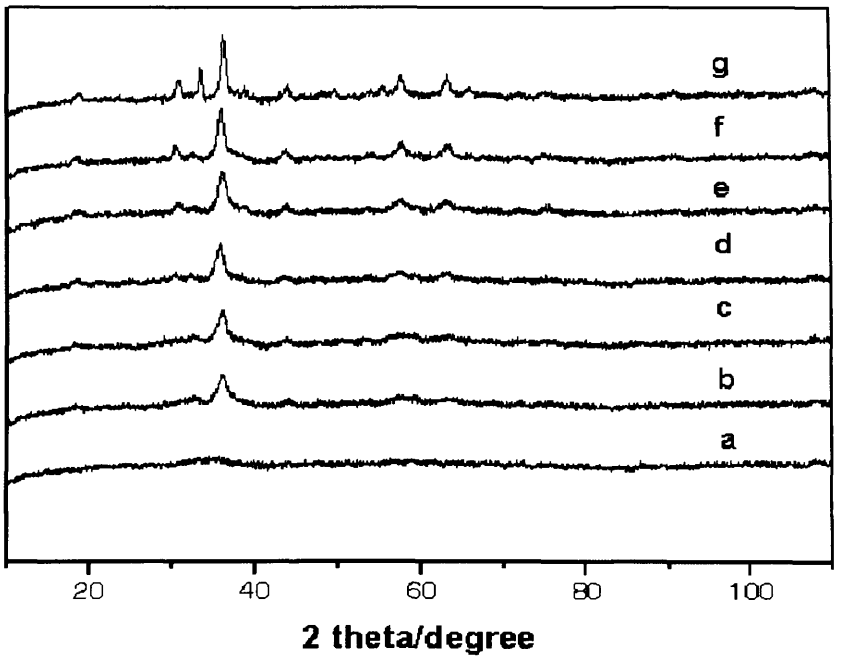

Figure 3.7 XRD patterns of precursor (a) and the final catalysts calcined at (b) 250°C, (c) 275°C, (d) 300°C, (e) 350°C, (f) 415°C and (g) 500°C.

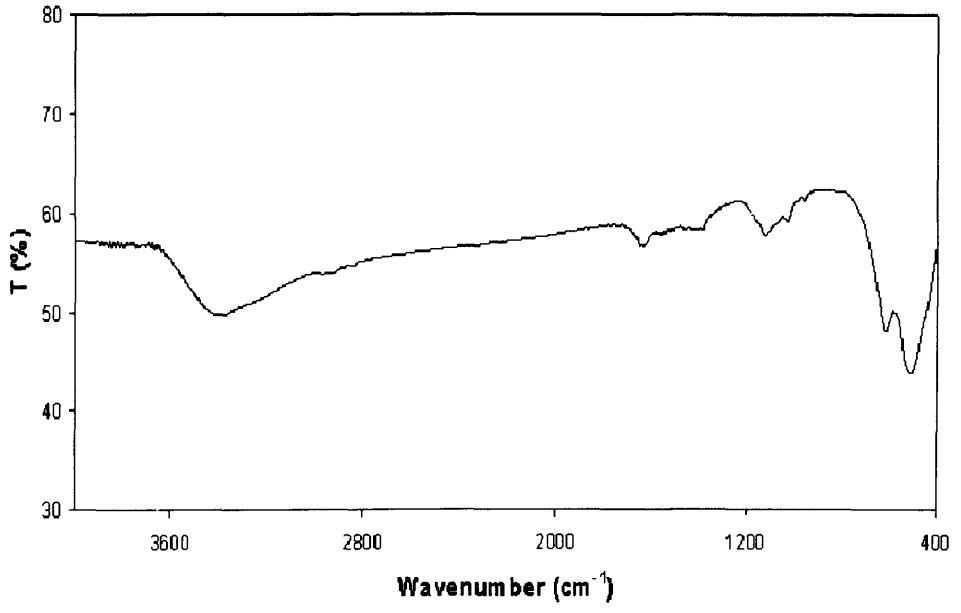

Figure 3.8 FT-IR spectrum of the catalyst calcined at 300°C

The TEM images of the catalyst calcined at 300 °C are shown in **Figure 3.9a**. Following calcination, the material remains agglomerated and only a few single particles are observed. However, the particle size of the material is in the range of 10 to 20 nm with the larger particles visible in the precursor no longer apparent. This overall particle shrinkage is consistent with the loss of carbonaceous matter on annealing observed by FT-IR spectrum. These observations demonstrate that calcination does not induce grain growth as the thermal input is insufficient to drive long-range mass transport. Importantly, the observation of regular contrast in the HRTEM images indicates that the material is now crystalline and qualitatively different from the amorphous precursor.

Furthermore, detailed examination with the high chemical analysis spatial resolution of the STEM (**Figure 3.10**) reveals that there has been a transition to a nanoscale phase-separated material where the distribution of Cu and Mn differs across the assembly. Due to the aggregated nature of the nanoparticles it is difficult to analyse single particles, but by comparison of the elemental maps from the STEM, it is apparent that calcination produces a phase-separated material consisting of intimately mixed nanoparticles of copper metal and manganese oxides. The differences from the element maps for the precursor are striking – although the particle sizes are not significantly changed by calcination, atomic mobility is sufficient to permit the formation of two distinct metallic and metal oxide phases. Thus, we observe discrete spherical Cu particles, which can be seen clearly from the

HR-TEM image (**Figure 3.9b**) and rectangular MnO_x particles (**Figure 3.9c**). Of particular importance is the observation that the catalyst treated at 300 °C does not contain any $CuMn_2O_4$ or similar ternary oxide phases associated previously with active hopcalite catalysts, yet still exhibits high activity for CO oxidation.

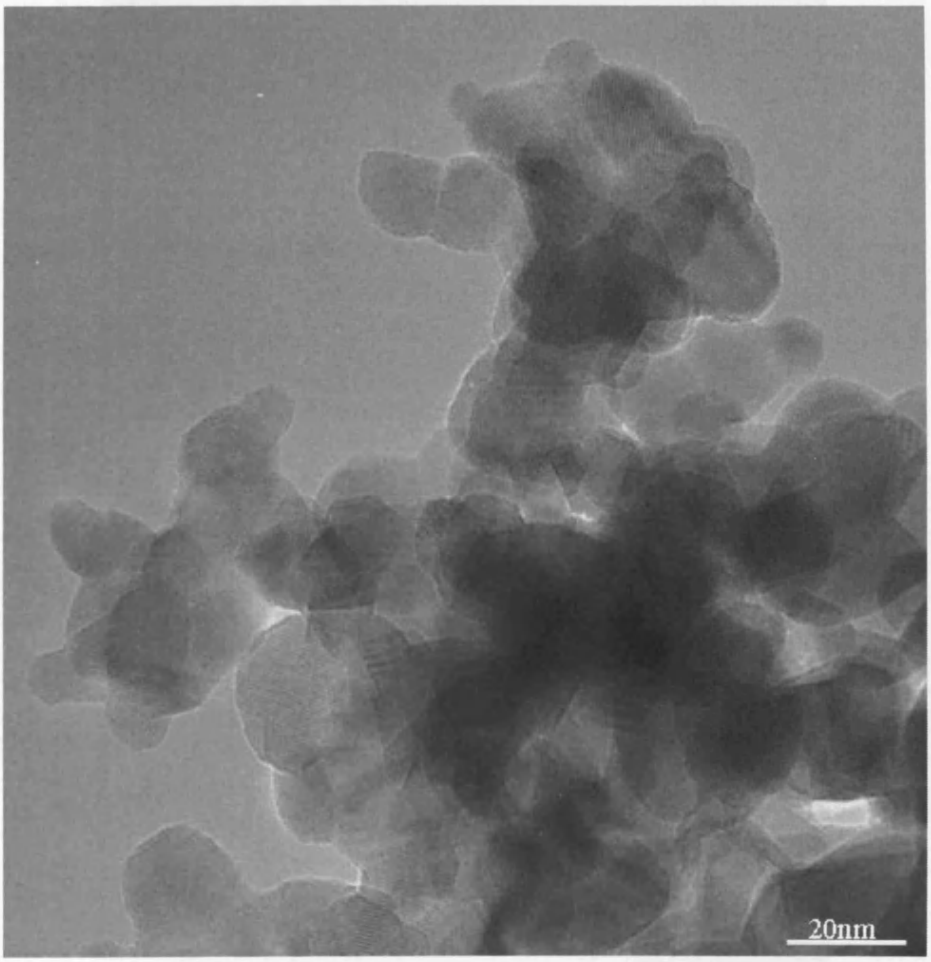

Figure 3.9a TEM image of the catalyst prepared using DMSO as solvent calcined at 300°C. crystallised Cu/MnO_X particles formed during calcination of the precursor. Cu particles appear circular/spherical whereas the MnO_X particles appear rectangular.

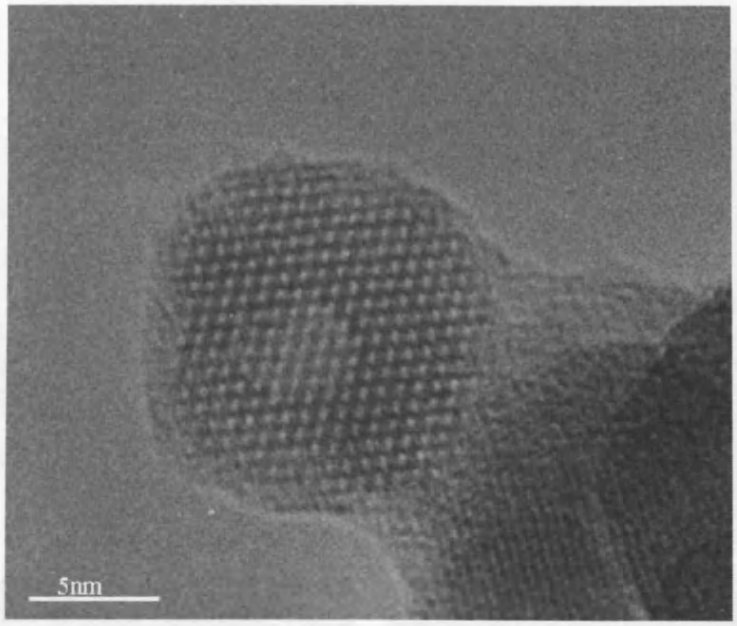

Figure 3.9b The lattice images for Cu particles in HR-TEM

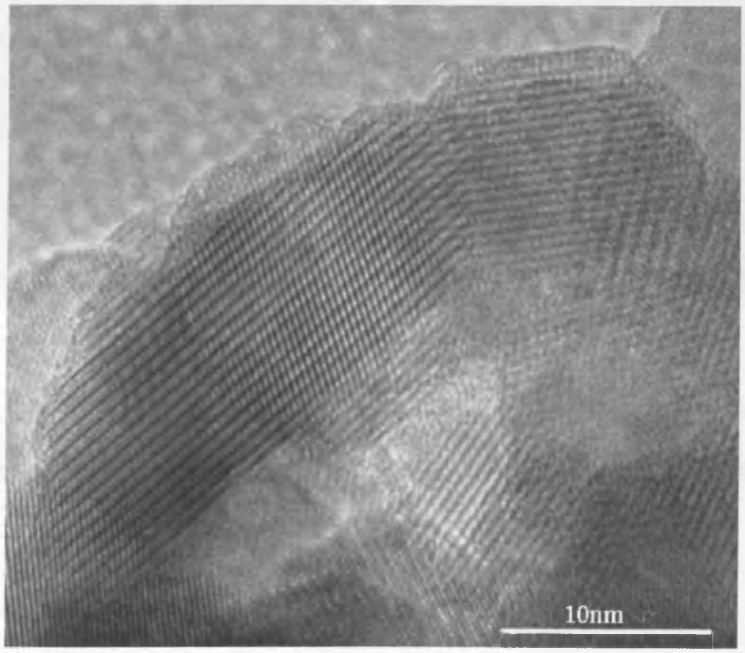

Figure 3.9c The lattice images for MnO_x particles in HR-TEM

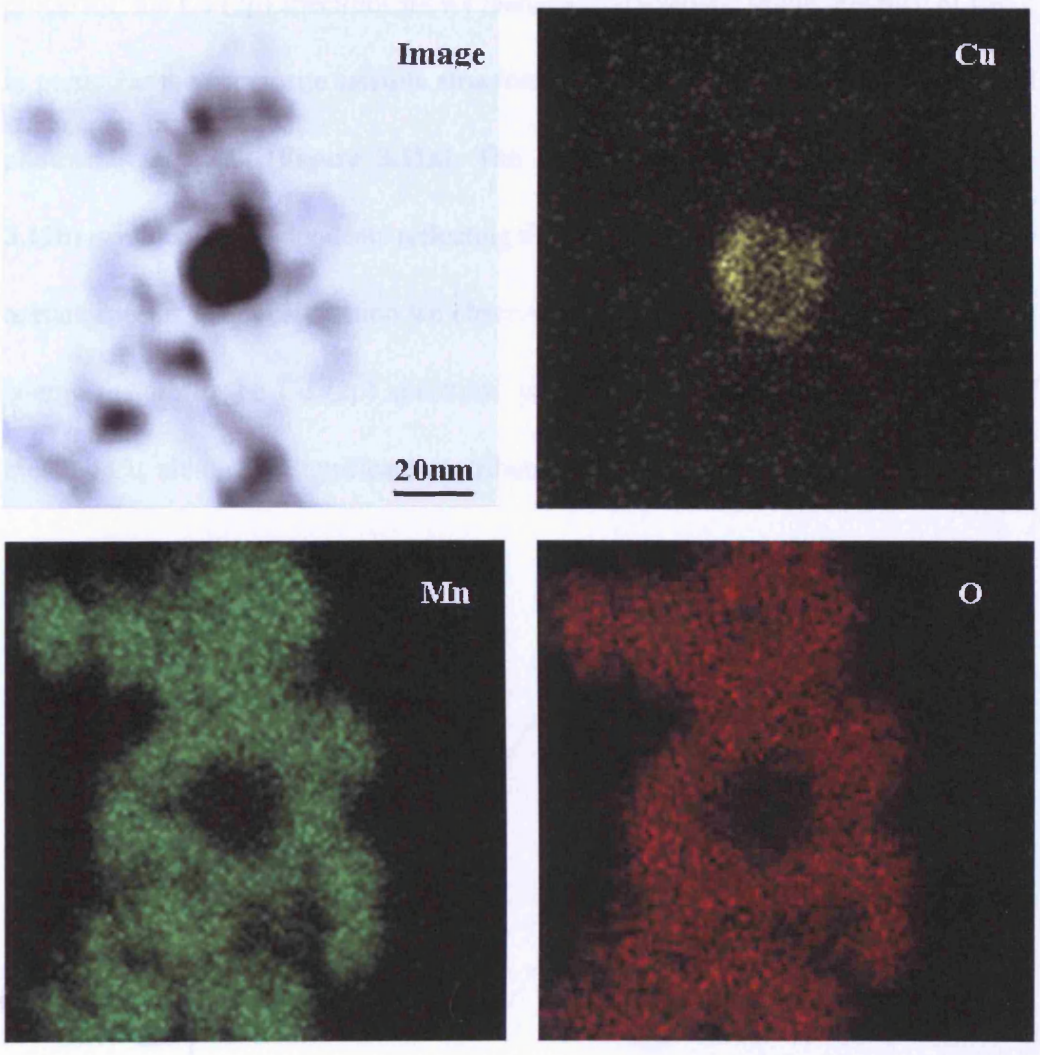

Figure 3.10 STEM dark field image of nanoparticles from the 300°C calcined material. The element distribution across this area is mapped by EDX and the different maps shown correspond to Mn, Cu and O edges.

Detailed X-ray photoelectron spectroscopy analysis has also revealed striking differences between the precursor and the calcined material (**Figure 3.11a-c**). For the precursor, the Cu (2p) spectrum shows features characteristic of the presence of Cu^{2+}, in particular the composite satellite structure separated by *ca* 6-8 eV from the primary photoemission peak (**Figure 3.11a**). The corresponding C (1s) spectrum (**Figure 3.11b**) exhibits two components reflecting the two non-equivalent carbon atoms in the acetate species. After calcination we observe the development of a new lower binding energy feature in the Cu (2p) spectrum, which is consistent with the formation of metallic Cu, although a significant contribution from a Cu^{2+} phase remains.

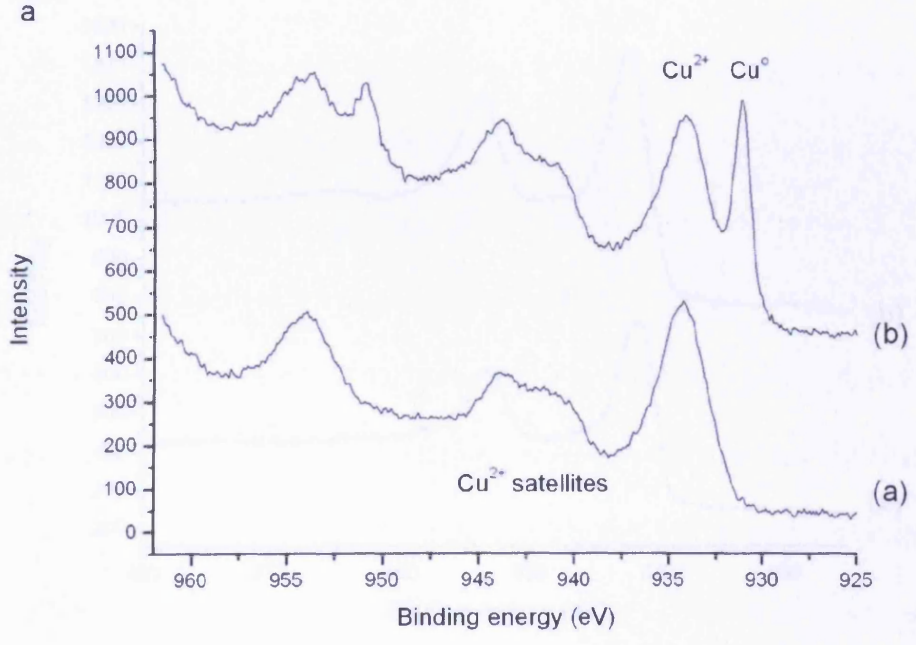

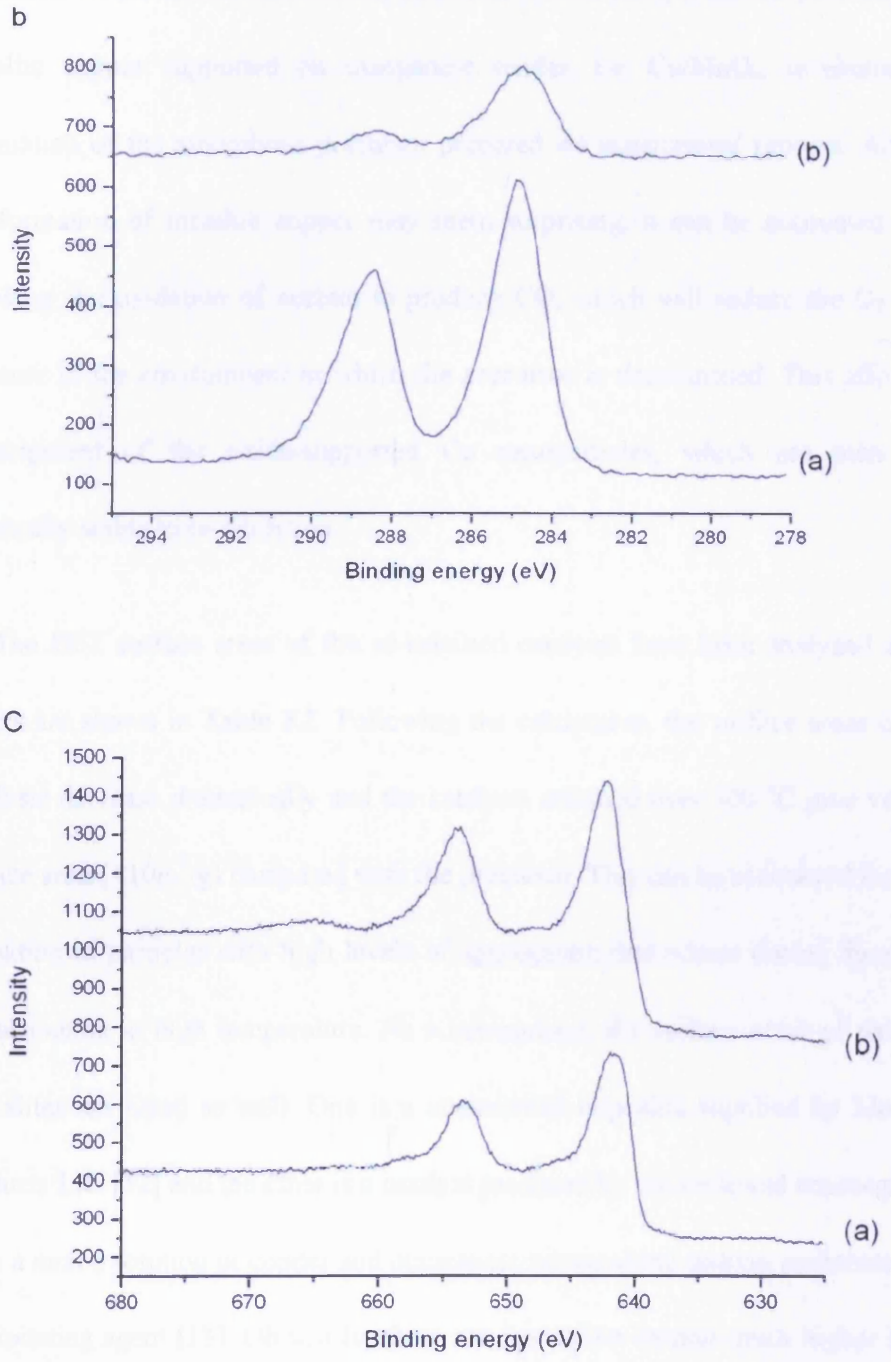

Figure 3.11 X-ray photoelectron spectra for (a) the precursor and (b) after calcination at 300 °C. **a**, Cu (2p) spectra; **b**, C(1s) spectra and **c**, Mn(2p) spectra.

Based on the results from TEM, STEM as well as XPS, it can be concluded that metallic copper supported on manganese oxides, i.e. Cu/MnO_x, is obtained by calcination of the amorphous precursor prepared *via* supercritical process. Although the formation of metallic copper may seem surprising, it can be accounted for by invoking the oxidation of acetate to produce CO, which will reduce the O_2 partial pressure in the environment in which the precursor is decomposed. This affords the development of the oxide-supported Cu nanoparticles, which are then rather kinetically stable to re-oxidation.

The BET surface areas of the as-calcined catalysts have been analyzed and the results are shown in **Table 3.2**. Following the calcination, the surface areas of these catalysts decrease dramatically and the catalysts calcined over 300 °C give very low surface areas($<10 m^2/g$) compared with the precursor. This can be accounted for by the formation of particles with high levels of aggregation that occurs during the process of calcination at high temperature. As a comparison, the surface areas of two other hopcalites are listed as well. One is a commercial hopcalite supplied by Molecular Products Ltd. [12] and the other is a catalyst produced by conventional coprecipitation from a mixed solution of copper and manganese nitrate using sodium carbonate as the precipitating agent [13]. Obviously, these two hopcalites exhibit much higher surface areas up to $164 m^2/g$ than that of the catalyst produced from supercritical process.

Table 3.2 The surface areas of as-calcined catalysts

Catalysts (calcination temperature)	Surface area (m^2/g)
$CuMnO_x$ (250°C)	45
$CuMnO_x$ (275°C)	36
$CuMnO_x$ (300°C)	10
$CuMnO_x$ (350°C)	11
$CuMnO_x$ (415°C)	8
$CuMnO_x$ (500°C)	6
Commercial hopcalite	164
Hopcalite prepared by coprecipitation	117

(3) Specific catalytic activity of the newly prepared hopcalite

In order to compare the specific catalytic activity of the new catalyst with currently available hopcalites, the commercial catalyst supplied by Molecular Products and the catalyst prepared by conventional coprecipitation have been tested. The data normalized for surface area to show the intrinsic activities of the catalyst surfaces are presented in **Figure 3.12**.

Based on the results, it is clear that the new catalyst prepared using supercritical antisolvent precipitation exhibit the highest catalytic activity, which is about two times higher than that of the conventionally prepared sample and the commercial catalyst as well when compared under steady state conditions; furthermore, the increase in activity is much more pronounced during the initial time on stream, which

is an important factor for respiratory protection devices. This enhanced catalytic activity can be ascribed to the nanocrystalline nature of the calcined materials, which brings the active components together without requiring them to be present in the same phase. These results strongly suggest that there is an intrinsically intimate relationship between the structure of catalyst and the catalytic activity. Importantly, it demonstrates that supercritical carbon dioxide antisolvent process provides a new green route to preparation of catalysts with novel structures, which may lead to the unexpected catalysts with higher activity.

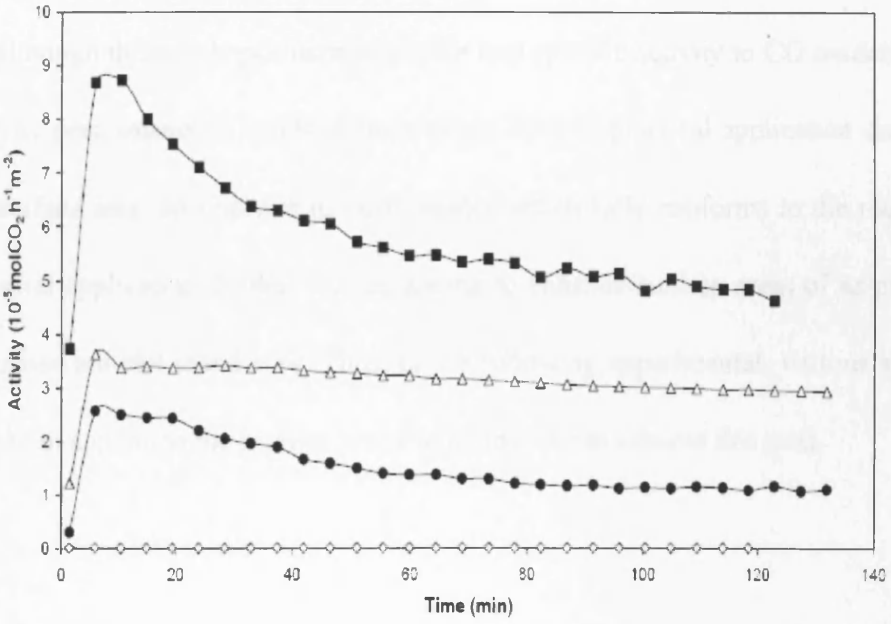

Figure 3.12 Specific catalytic activities of the Cu/MnO_x precursor from the new supercritical process(◇), the Cu/MnO_x catalyst from the new supercritical process (■), conventional hopcalite prepared from coprecipitation (△) and commercial hopcalite (●).

3.3.1.3 Conclusion

New separated nanostructured hopcalite (Cu/MnOx) with high specific catalytic activity has been obtained using DMSO as a solvent in supercritical antisolvent precipitation process. The results clearly show that a catalyst with enhanced activity can be prepared without the presence of intimately mixed copper and manganese oxide components; this opens up the possibility of designing further improved catalysts, since previous design approaches have been based on the need to obtain homogeneous mixtures, with ternary oxide phases as the major active components.

Although the new hopcalite exhibits the best specific activity to CO oxidation, the catalytic performance in terms of mass is not ideal to practical application due to its low surface area. To improve its performance which fully conforms to the request of industrial application, further studies aiming to enhance surface areas of as-prepared hopcalites are still mandatory. Thus, in the following experimental, various solvents have been applied to the catalyst preparation in order to achieve this goal.

3.3.2 Preparation of $CuMnO_x$ using water as cosolvent

3.3.2.1 5% water-contained solvents

In this section, 5% water-contained cosolvents, including water-DMSO, water-NMP, water-ethanol, water-methanol and water-DMF, are applied as solvents of acetates. Following the preparation procedure shown in Section 2.1, the preparation of catalysts in the supercritical system is performed using the mixed starting solution of CuAc(5mg/ml) and MnAc(12.25mg/ml) in these cosolvents under the pressure of 110bar and temperature of 40°C. The flow rate of 0.1ml/min is for starting solutions and 7ml/min for $scCO_2$. All the experiments are conducted around 8h and precursors are produced consequently with the approximate yield of 45 ~ 50%. In addition, as a comparison, corresponding precursors using pure solvents under the same conditions are also produced. All the precursors are calcined at 300°C for 2h and 20h, respectively, in static air to give the final catalysts.

The BET surface areas test are performed on all the precursors and final catalysts and the results are listed in the **Table 3.3**. As can be clearly seen, the surface areas of precursors produced from water-contained cosolvents exhibit the general decreasing tendency compared with the precursors obtained from pure solvents. Following the calcination, however, all the final catalysts produced from cosolvents show unexpected higher surface areas up to *ca.* $100m^2/g$ than those of catalysts produced from pure solvents. Furthermore, the surface areas of these catalysts are even higher when the calcination time is prolonged from 2h to 20h if using water-NMP,

water-MeOH and water-DMF as cosolvents. This is an exciting result because it offers us a possible solution to improve the surface area of the hopcalite prepared using supercritical CO_2 as an antisolvent, thereby achieving the better catalytic performance to CO oxidation.

Table 3.3 BET surface areas of as-prepared precursors and final catalysts

Cosolvent	Surface area (m^2/g)		
	Precursor	As-calcined catalyst	
		300°C for2h	300°C for 20h
5% H_2O in DMSO	115	58	51
5% H_2O in NMP	243	57	83
5% H_2O in EtOH	200	65	85
5% H_2O in MeOH	176	47	51
5% H_2O in DMF	242	70	95
0% H_2O in DMSO	268	21	13
0% H_2O in NMP	258	33	26
0% H_2O in EtOH	264	33	20
0% H_2O in MeOH	202	40	34
0% H_2O in DMF	241	30	26

To see if the catalytic activities of hopcalites produced from cosolvents can be enhanced with the increase of their surface areas, the reaction of CO oxidation at room temperature is tested on these as-prepared hopcalites. **Figure 3.13a~e** list all the results respectively. Based on the results shown in figures, some important conclusions can be drawn as follows.

(a) All the catalysts obtained from pure solvents are active for CO oxidation and the conversions to this reaction are around 10~15%. When prolonging the calcination time from 2h to 20h, all the activities show slight decrease. This phenomenon may be attributed to the overall reduction of surface area derived from calcination process with longer time.

(b) Except the catalysts produced by the 5%water- contained DMSO, all the catalysts show the better catalytic activities on the reaction of CO oxidation. Particularly for the catalysts obtained from 5% water-contained EtOH and 5% water-contained DMF, the clear enhancement of the activity for CO oxidation can be observed. Furthermore, the catalysts after calcination for 20h exhibit better catalytic performance compared with those after calcinations for 2h. This result is fully consistent with the observations on the data of surface areas, that is, the catalytic activities of as-prepared hopcalites improve with the increase of their surface areas.

(c) The catalyst produced from 5% water-contained DMSO shows no activity to CO oxidation.

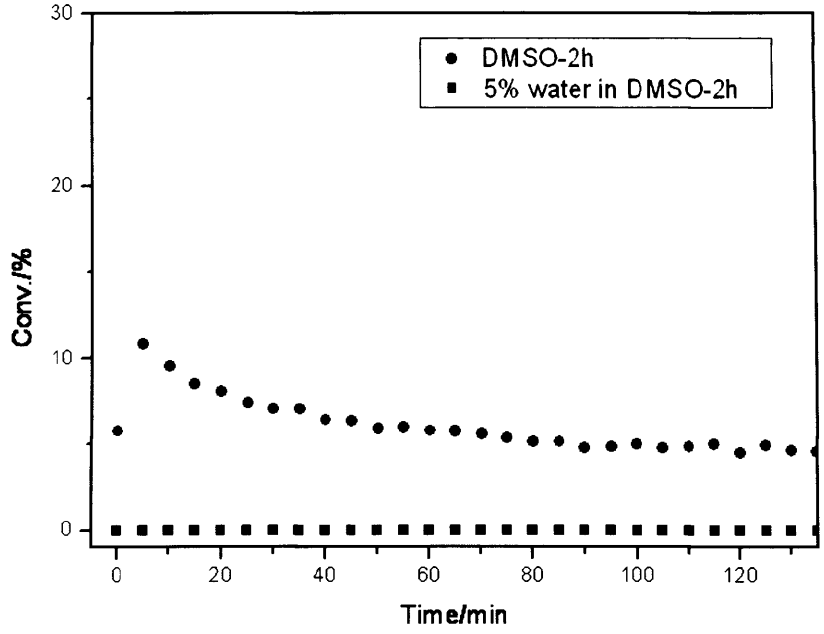

Figure 3.13a catalytic performance of hopcalites produced from DMSO and 5% water-contained DMSO. Test conditions: 298K, 0.5% CO in synthetic air, 50mg catalyst, GHSV=17000h^{-1}.

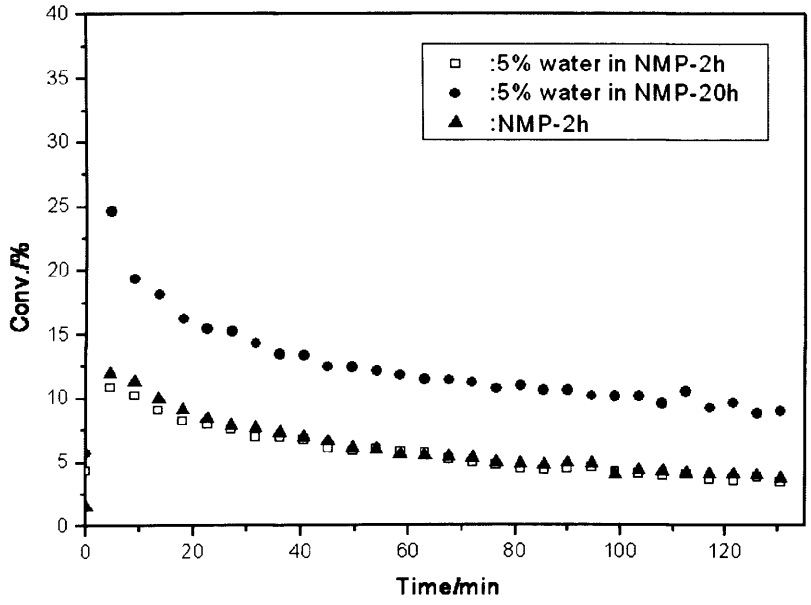

Figure 3.13b catalytic performance of hopcalites produced from NMP and 5% water-contained NMP. Test conditions: 298K, 0.5% CO in synthetic air, 50mg catalyst, GHSV=17000h^{-1}.

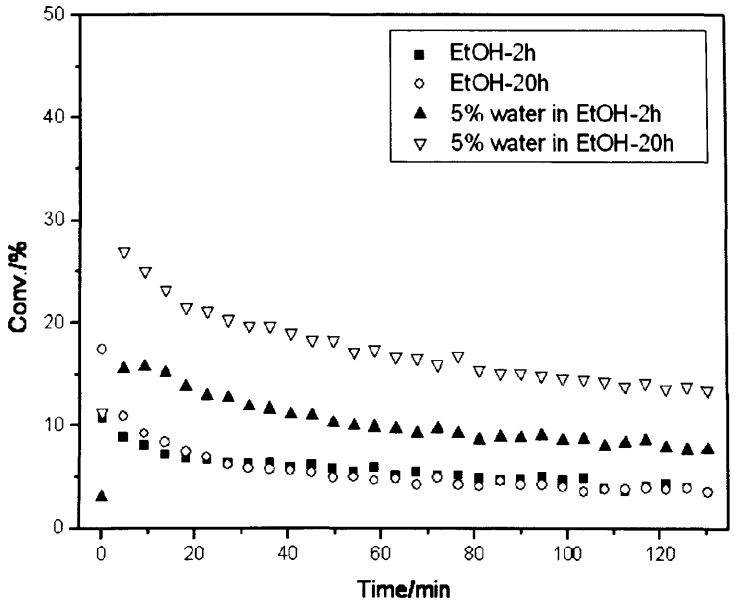

Figure 3.13c catalytic performance of hopcalites produced from pure EtOH and 5% water-contained EtOH. Test conditions: 298K, 0.5% CO in synthetic air, 50mg catalyst, GHSV=17000h^{-1}.

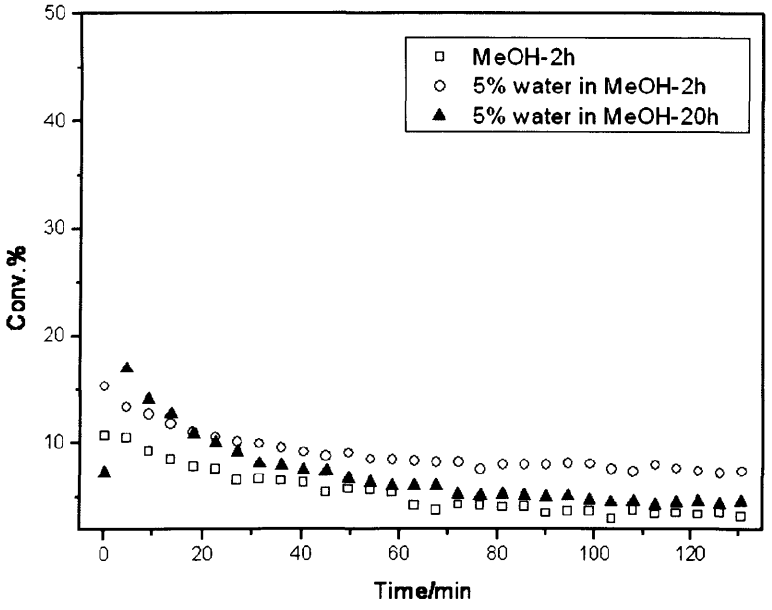

Figure 3.13d catalytic performance of hopcalites produced from pure MeOH and 5% water-contained MeOH. Test conditions: 298K, 0.5% CO in synthetic air, 50mg catalyst, GHSV=17000h^{-1}.

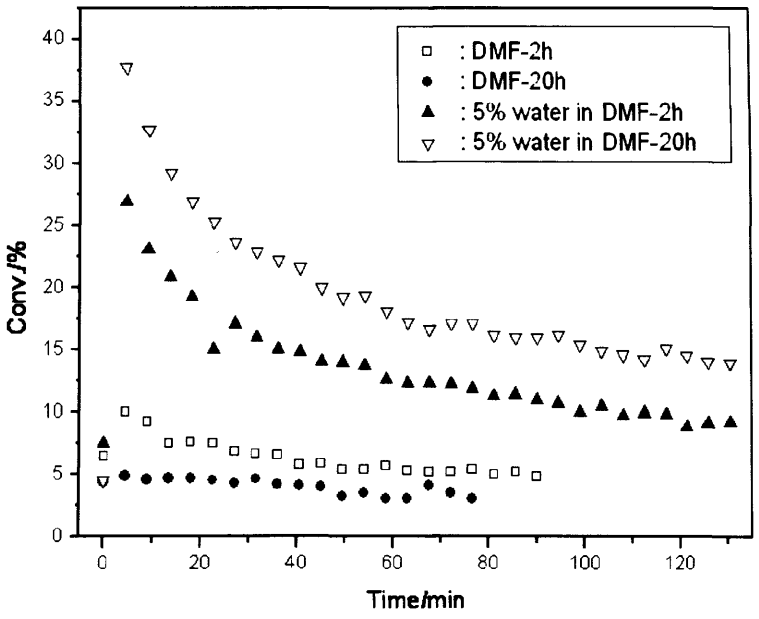

Figure 3.13e catalytic performance of hopcalites produced from pure DMF and 5% water-contained DMF. Test conditions: 298K, 0.5% CO in synthetic air, 50mg catalyst, GHSV=17000h^{-1}.

At this stage, encouraged by the much higher catalytic activity derived from the catalysts prepared from 5% water-contained cosolvents, are systematically investigate the effect of water as a cosolvent in this supercritical preparation process. Two water-contained solvents, water- EtOH and water-DMF, are chosen as candidates for further systematic experiments due to their excellent performance in the primary experiments shown in this section.

3.3.2.2 water-ethanol as a co-solvent

To investigate systematically the effect of water-ethanol as a co-solvent, we have explored the different volume ratio solvents by adding different amounts of water to the ethanol from 0 to 100 vol%. The preparations of precursors are carried out using the mixed starting solution of CuAc(5mg/ml) and MnAc(12.25mg/ml) in the water-ethanol cosolvents under the control condition of 110bar and 40°C with the flow rate of 0.1ml/min for starting solutions and 7ml/min for $scCO_2$. The experiments are conducted for around 8h and precursors are produced consequently with the approximate yield of 45%. The final catalysts are obtained by the calcination at 300°C for 2h and 20h, respectively, in static air with the ramp of 10°C /min.

(1) Characterization of as-prepared precursors

The detailed experimental results on precursors are shown in Table 3.4. As shown clearly, no precipitates can be achieved when there is more than 25% water in ethanol. This is reasonably understandable because water is not miscible with $scCO_2$ in supercritical antisolvent precipitation process and therefore cannot be easily carried outside from the preparation system if there is high water content in the solution. For the four precursors obtained, their surface areas decrease with the increasing addition of water in ethanol. In addition, the color of the products changes from green to yellow by adding more water to ethanol.

Table 3.4 The experimental results of precursors produced from water-EtOH solvents

Precursor	Solvent	Precipitates	Surface area(m^2/g)
a	0% H_2O	green	264
b	5% H_2O	dry powder	200
c	10% H_2O	↓	152
d	15% H_2O	yellow (not quite dry)	140
--	25% H_2O	wet precipitates	------
--	50% H_2O	No dry products	------
--	100% H_2O	No product	-------

XRD analysis was performed on these products and the results are shown in **Figure 3.14**. In the absence of water the material obtained is absolutely amorphous as indicated by the X-ray diffraction. However, the precursors which are obtained from the solutions containing water, i.e. 5%, 10% and 15%, show crystalline carbonates. In addition, with the increase of water content in ethanol, the crystallinity of materials increases. Thus, it obviously indicates the formation of more carbonates.

The FT-IR spectra (**Figure 3.15**) are in agreement with the results of XRD determination. It confirms the presence of large amount of carbonates when more water is added in ethanol. As shown by the figure, the precursor obtained in the absence of water (a) exhibits bands of the acetate salts, with main bands at 1561 and 1418 cm^{-1}, indicating the presence of acetates when using pure ethanol as a solvent. As water is added, the bands associated with carbonate species at 1485 and 862cm^{-1}, start to appear until almost complete carbonates are observed when using 15%

H_2O/85% ethanol as a solvent.

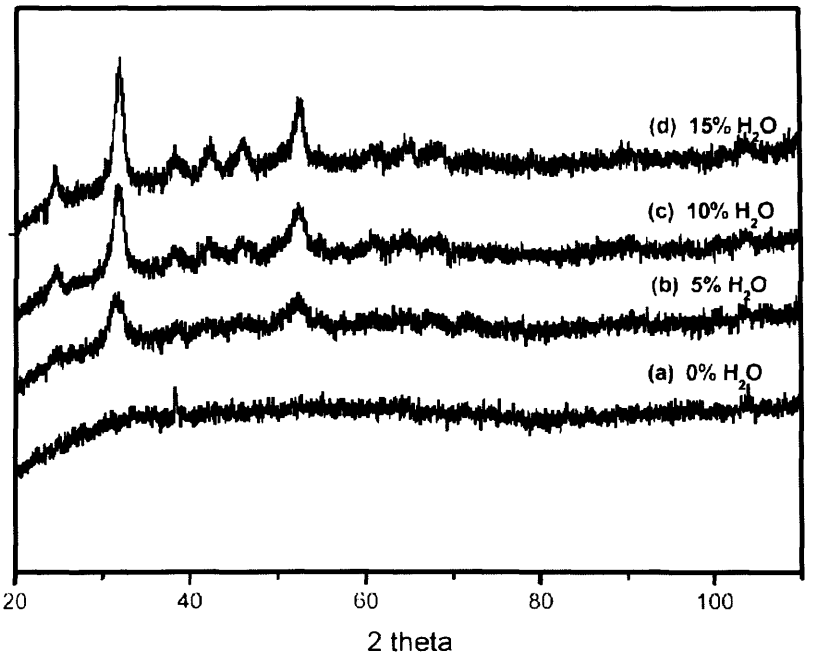

Figure 3.14 XRD patterns of precursors produced from water-EtOH solvents

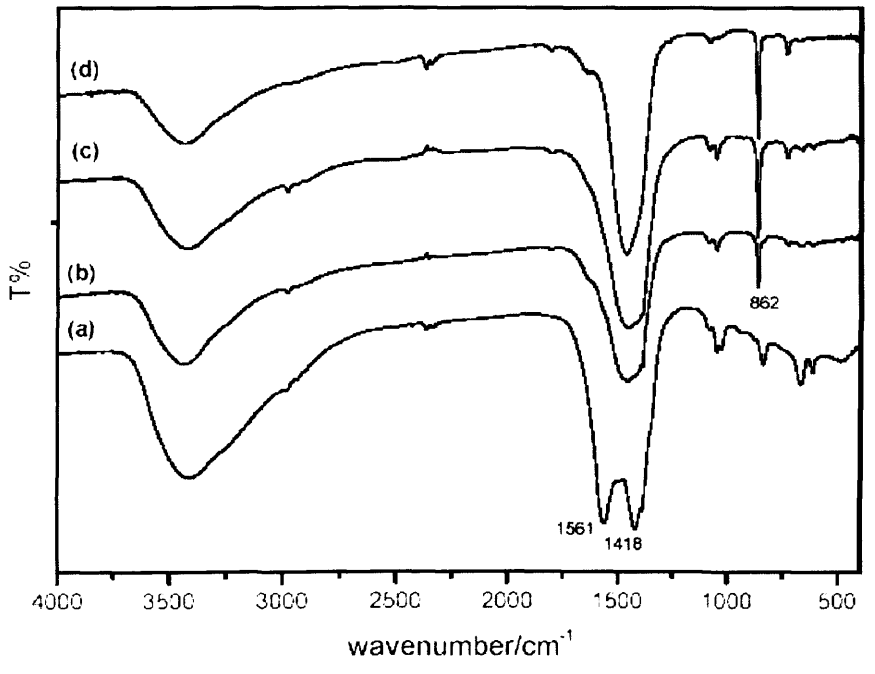

Figure 3.15 FT-IR spectra of precursors produced from water-EtOH solvents

The results of TGA analyses performed on the four as-prepared products and the results are shown in **Figure 3.16a-d**. The differences of components with these 4 precursors can be found accordingly. As shown by **Figure 3.16a**, the precursor produced from pure ethanol has four-stage weight losses which appear at 72°C, 200°C, 236°C and 297°C respectively, corresponding to the loss of absorbed solvent, copper hydroxide, copper acetate and manganese acetate [14]. These results indicate that copper hydroxide has been obtained in this supercritical antisolvent process when using pure ethanol as a solvent. With the adding of water to ethanol, all the precursors show three-stage weight losses. No copper hydroxide has been observed any more. The loss in the first stage (<100°C) is attributed to the physical-absorbed solvent. The second stage at about 250°C is corresponding to the loss of mixed copper acetate and copper carbonate [14] and the third stage at 300°C belongs to the loss of mixed manganese acetate and manganese carbonate [15]. With the increase of water content in ethanol, the second stage shifts from 245°C to 269°C and the third stage shifts from 297°C to 332°C (see Figure3.16b-d), indicating almost complete carbonates exist when using 15% H_2O/85% ethanol as solvent. The results are in full agreement with the analysis of XRD and FT-IR.

SEM testing has been conducted on the four precursors. From the images (see **Figure 3.17a-d**), some detailed information on the morphology of particles is obtained. When using pure ethanol as solvent, small particles around 50~100nm are observed. However, the particle size increases to about 0.5~1um dramatically with the adding water to ethanol. It can be explained as follows: the $scCO_2$ can not diffuse with

the cosolvent completely since it is not miscible with water, thereby resulting in the presence of large-size particles. Interestingly, cauliflower-like structures can be observed when we magnify the images of the precursors produced from water-ethanol cosolvents. A large number of particles down to 20nm are observed to be aggregated closely with each other to form large cauliflower-like structures. It further indicates partial miscibility between $scCO_2$ and the cosolvent.

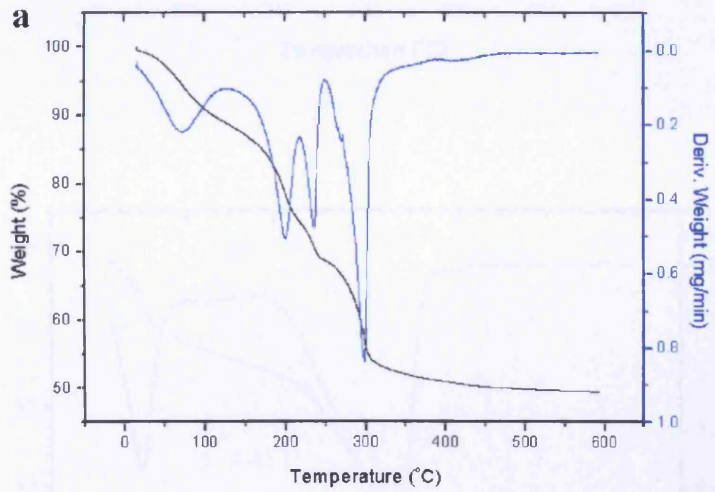

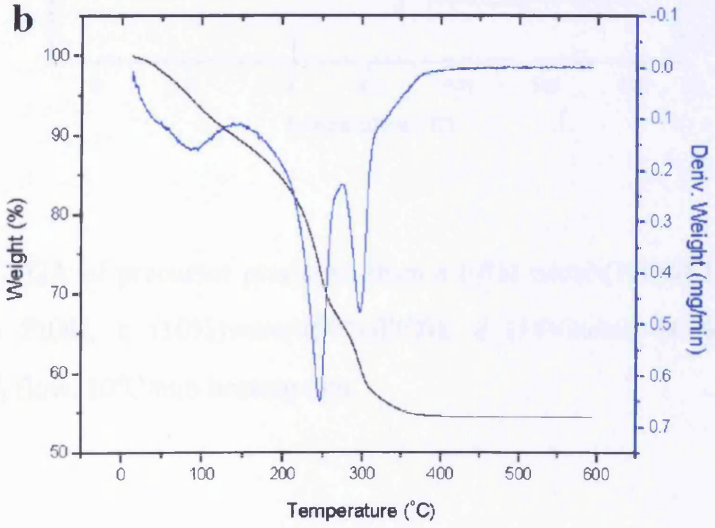

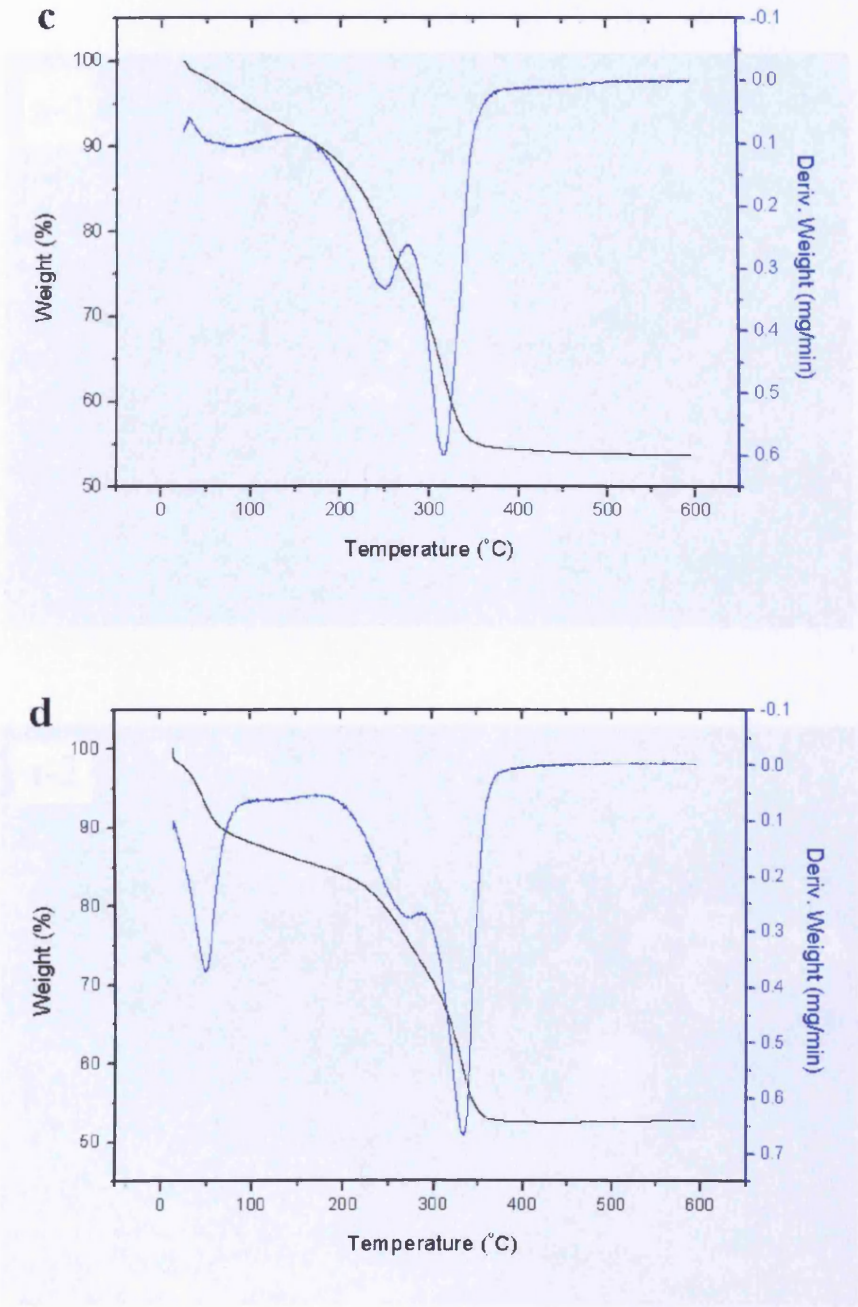

Figure 3.16 TGA of precursor produced from a (0%) water-(100%) EtOH, b (5%) water-(95%) EtOH, c (10%)water-(90%)EtOH, d (15%)water-(85%)EtOH. Test condition: N_2 flow, 10°C/min heating rate.

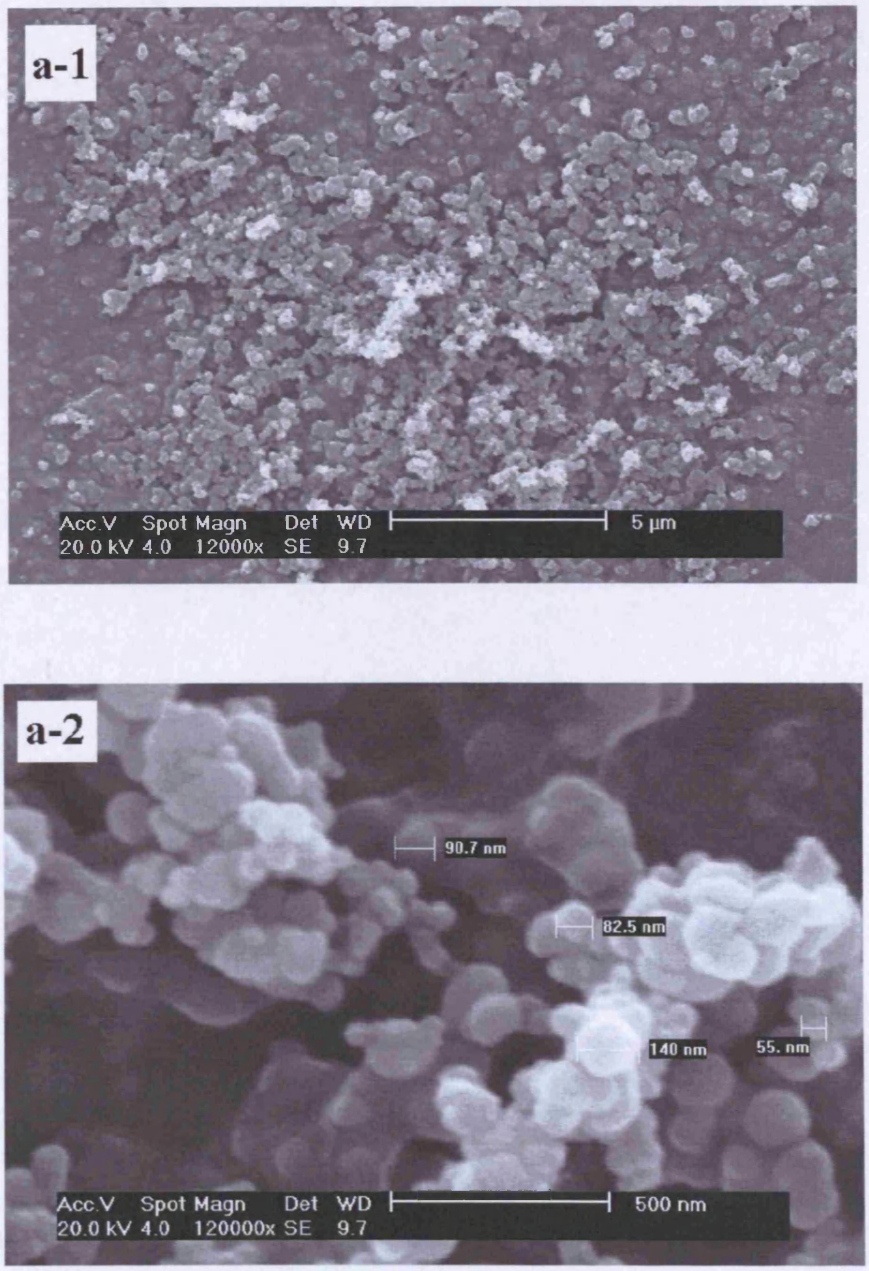

Figure 3.17a SEM images of precursor produced from 0%water-100%EtOH

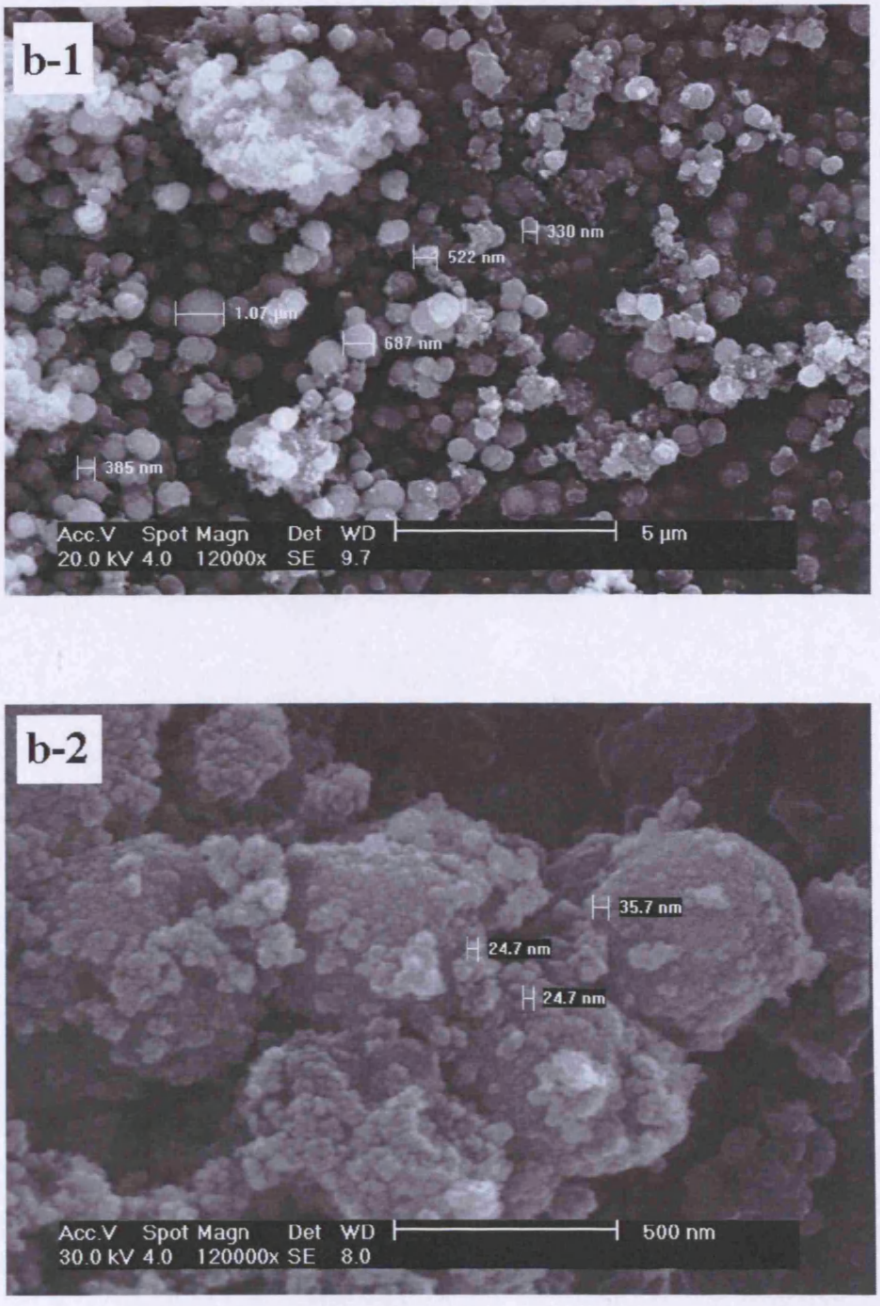

Figure 3.17b SEM images of precursors produced from 5%water-95%EtOH

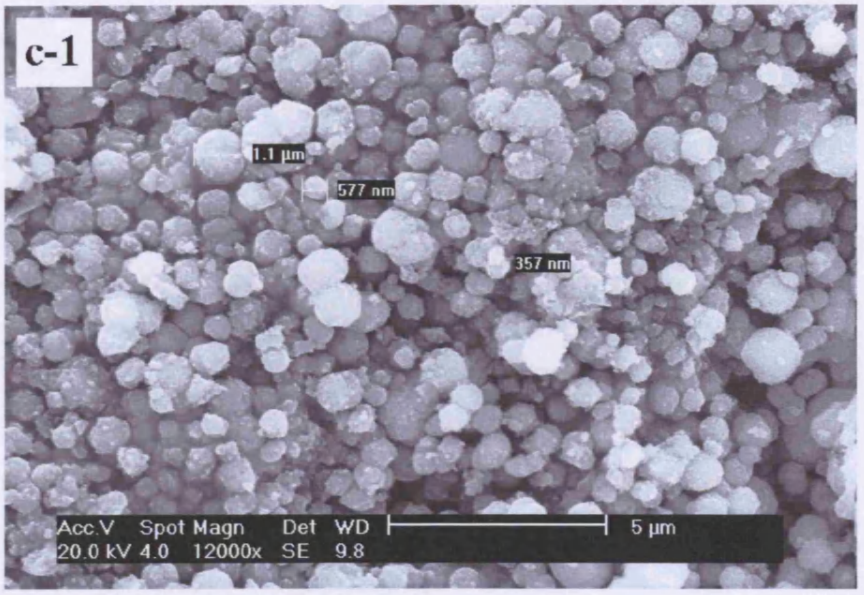

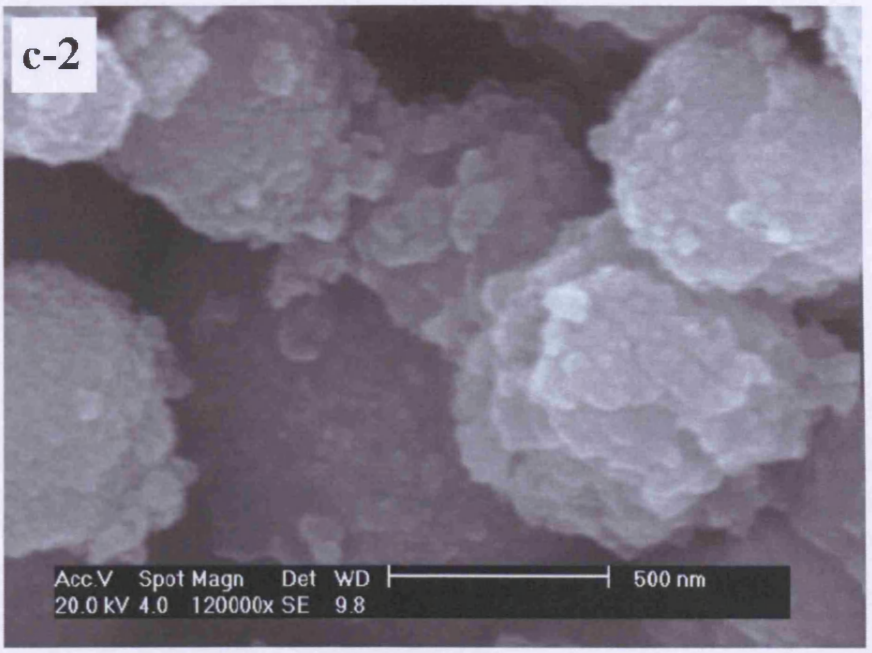

Figure 3.17c SEM images of precursors produced from 10%water-90%EtOH

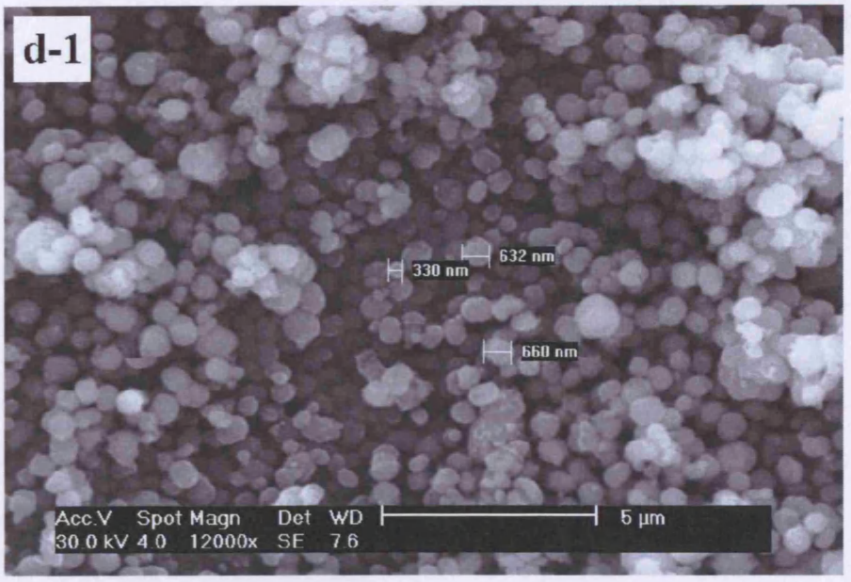

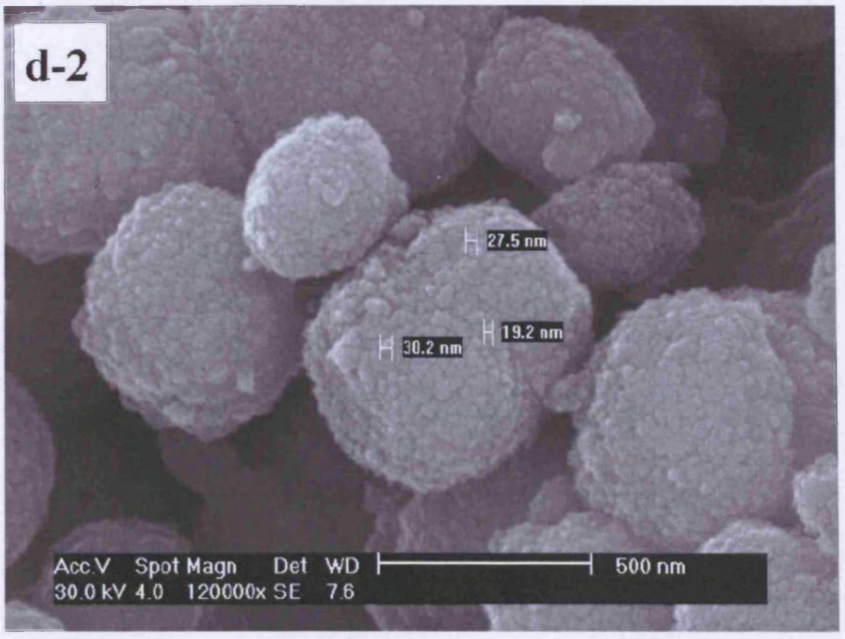

Figure 3.17d SEM images of precursors produced from 15%water-85%EtOH

(2) As-calcined catalysts

Table 3.5 lists the surface areas of these as-calcined catalysts. The surface areas are retained following the calcination, when using water-ethanol as a solvent. Particularly, the surface areas of catalyst **c** and **d** are retained or even higher than those of corresponding precursors. In addition, the increase of surface areas of these catalysts is observed when the calcination time is extended from 2h to 20h, which is in agreement with the previous observation as has been discussed in **Section 3.3.2.1**,

Table 3.5 The surface areas of as-calcined products under 300°C for 2h and 20h

catalysts	Surface area(m^2/g)	
	300°C for 2h	300°C for 20h
a	33	20
b	65	83
c	136	142
d	175	179

Figure 3.18a-b show XRD patterns of the catalysts calcined at 300°C for 2h and 20h, respectively. Combined with the XRD results of precursors, it is interesting to find that the more crystalline the precursor appears the more amorphous the calcined catalyst is. For example, the amorphous precursor (a) crystallises on calcinations, while for the catalyst **d** which is produced from 15% water-85% ethanol, complete amorphous morphology is obtained. In addition, no change is observed for the morphology of the catalysts obtained from water-contained ethanol when prolonging

the calcination time from 2h to 20h. It is different from catalyst **a**, in which the extension of calcination time results in the presence of more crystalline materials. The XRD patterns of crystalline materials exhibit the diffraction lines of $CuMn_2O_4$.

SEM images of these materials are exhibited in **Figure 3.19a-d**. The results indicate that the morphology and the size of most particles are retained in the final catalysts. However, many separated small particle down to 10~30nm are observed when magnifying the images. Moreover, the longer the calcination time, the more the small particles. Importantly, this result gives a good explanation to the maintenance of high surface areas of catalysts produced from water-ethanol, as well as the achievement of higher surface areas when prolonging the calcinations time.

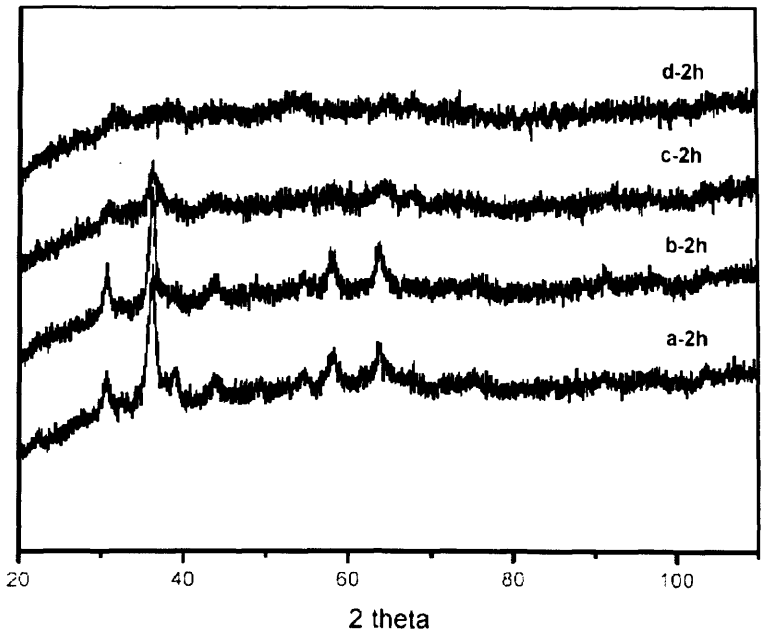

Figure 3.18a XRD patterns of the catalysts calcined at 300°C for 2h

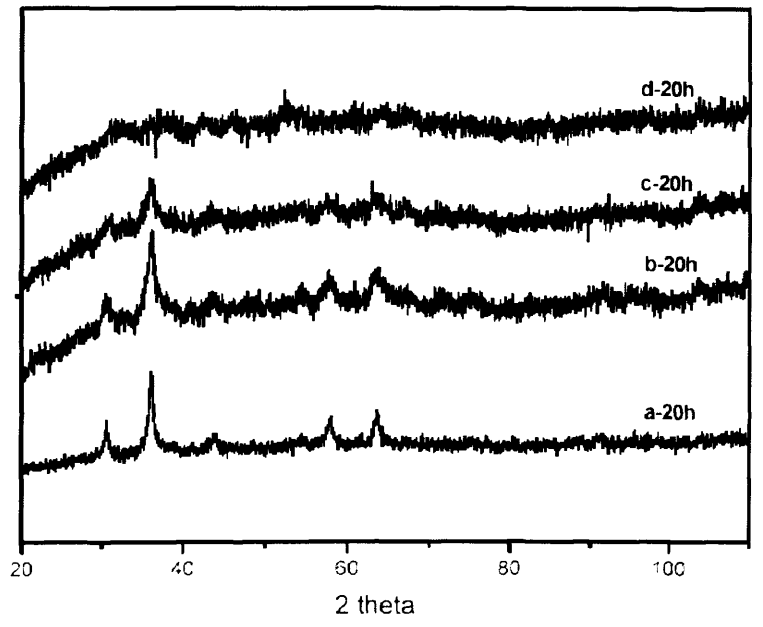

Figure 3.18b XRD patterns of the catalysts as-calcined at 300°C for 20h

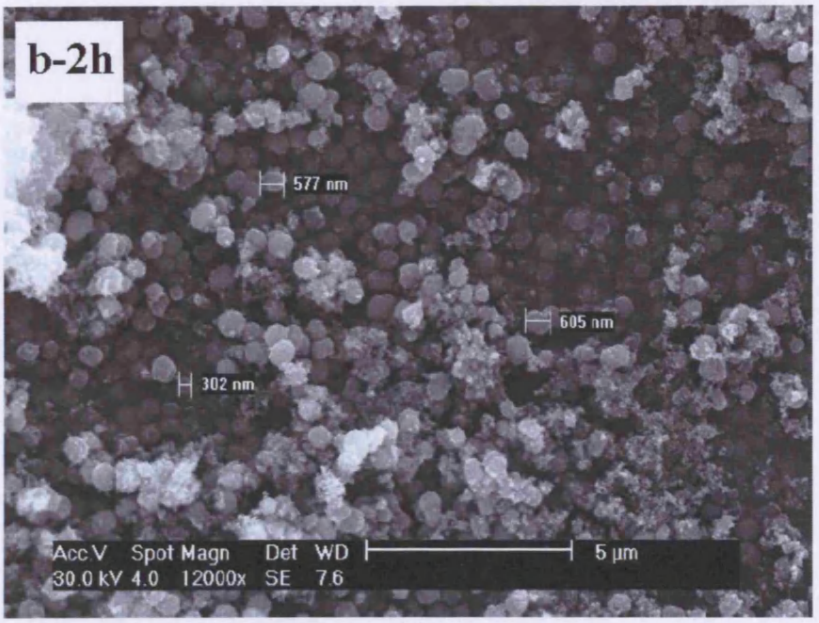

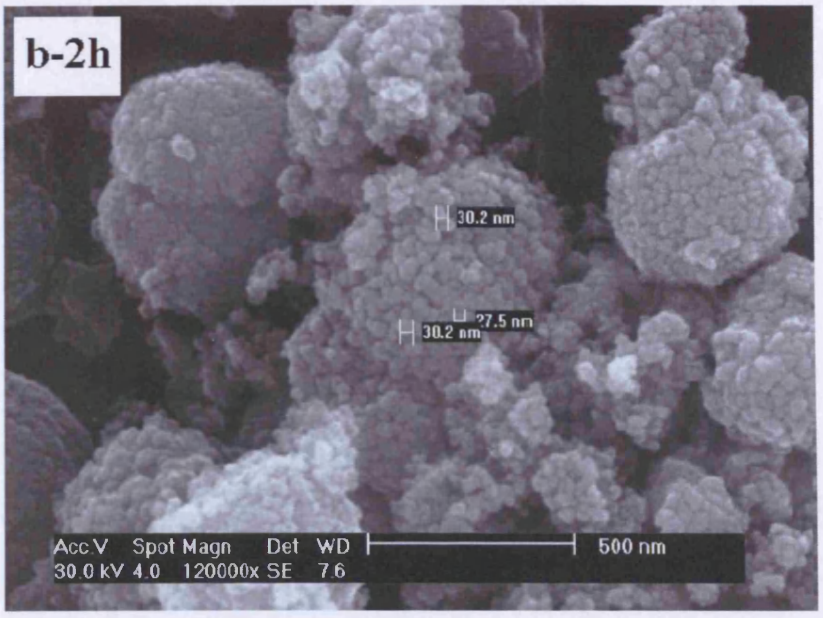

Figure 3.19a SEM images of as-calcined catalyst produced from (5%)water-(95%)EtOH (after calcination at 300°C for 2h).

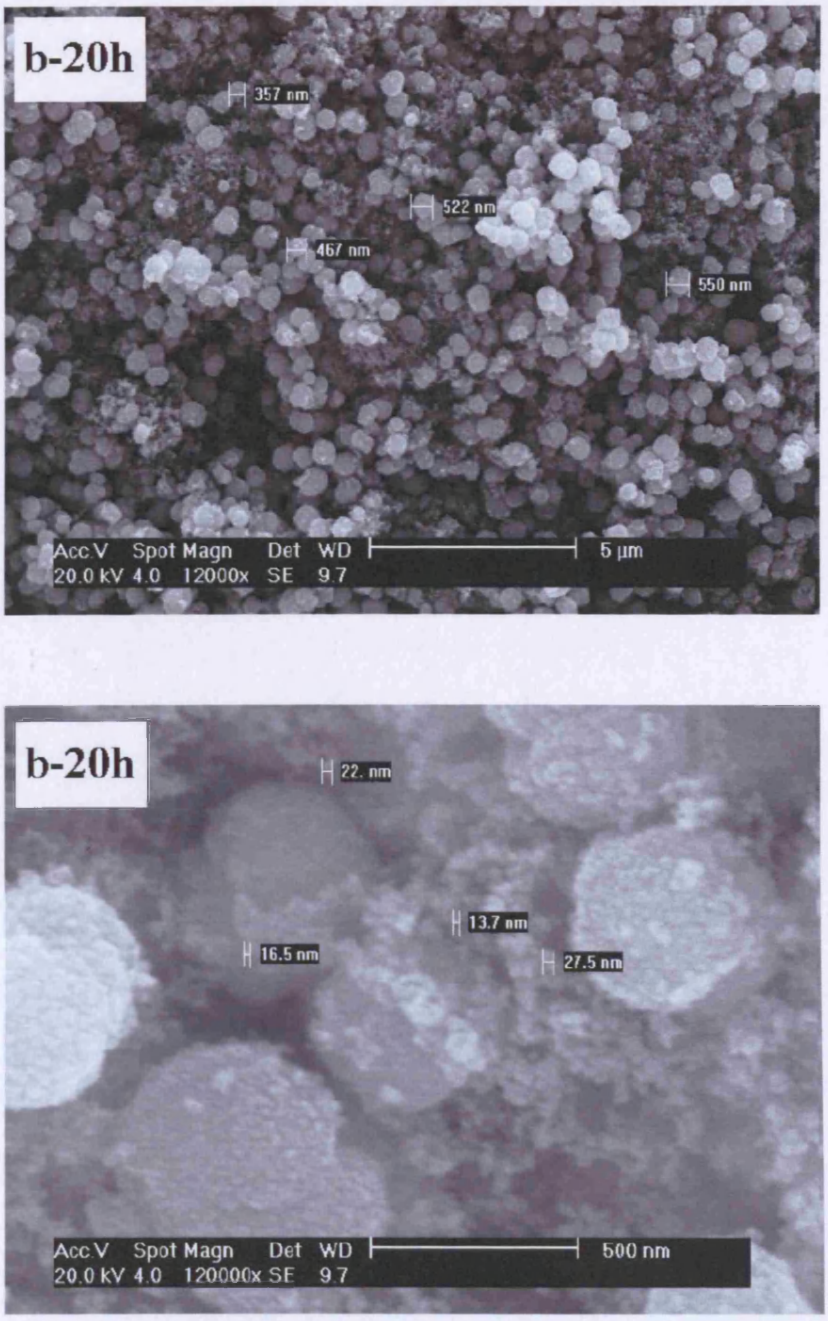

Figure 3.19b SEM images of as-calcined catalyst produced from (5%)water -(95%) EtOH (after calcination at 300°C for 20h).

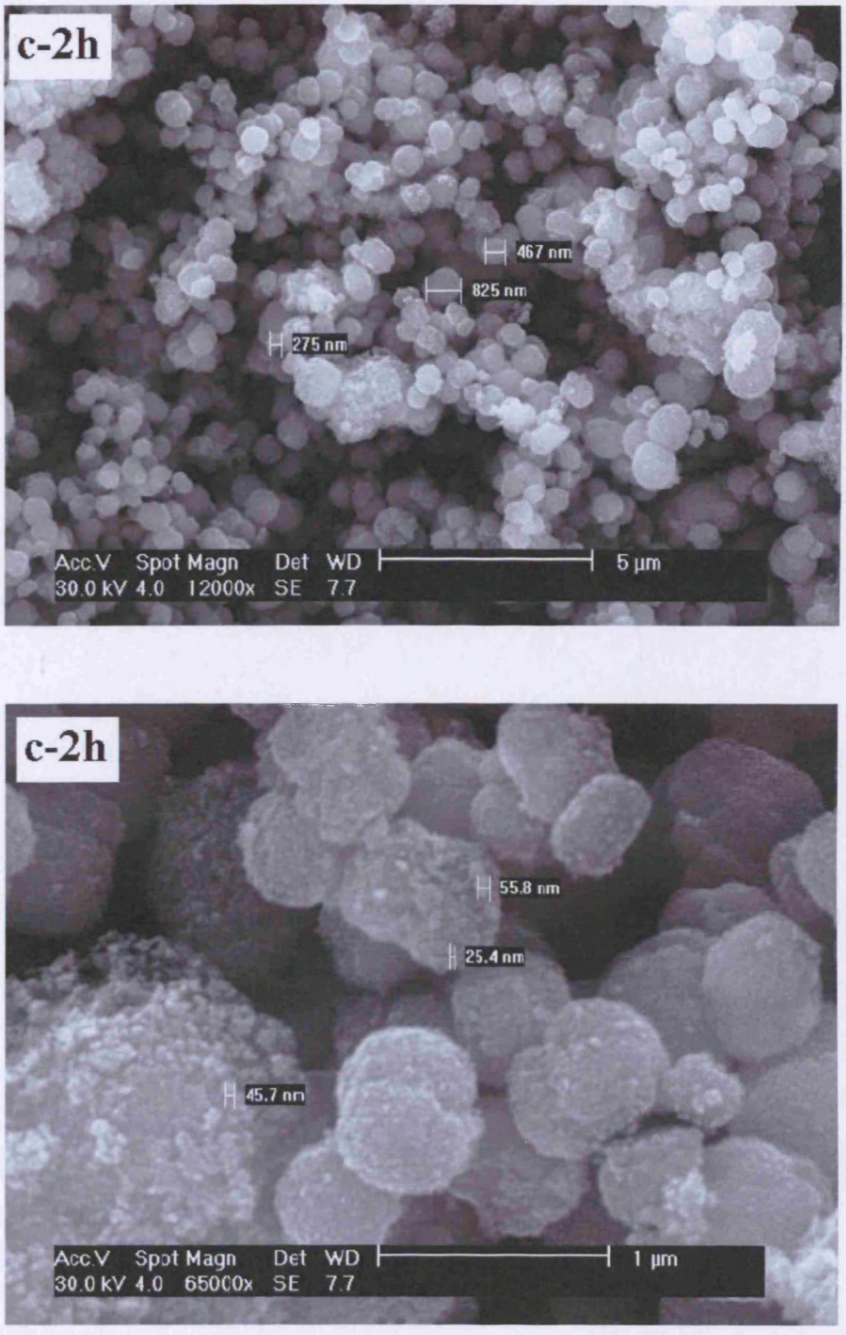

Figure 3.19c SEM images of as-calcined catalyst produced from (10%)water-(90%) EtOH (after calcination at 300°C for 2h).

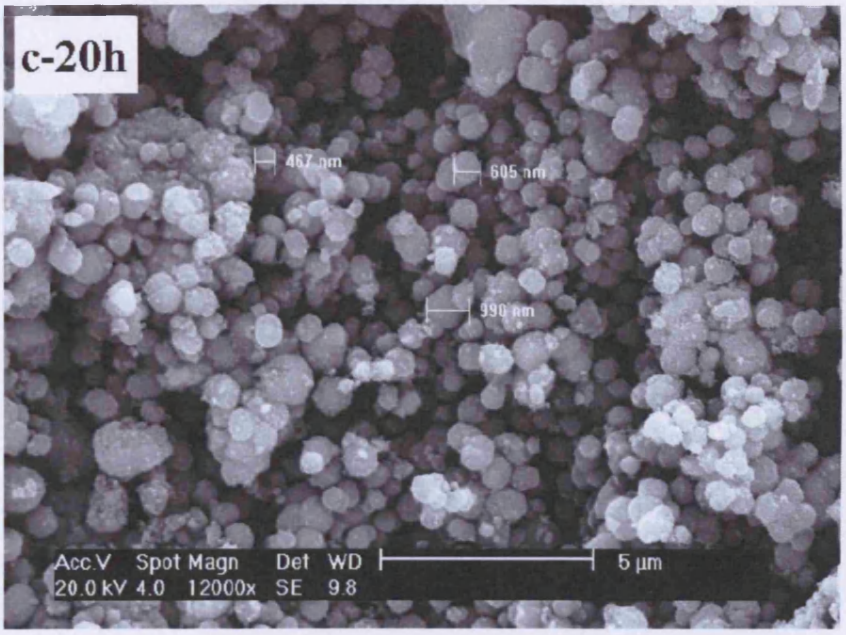

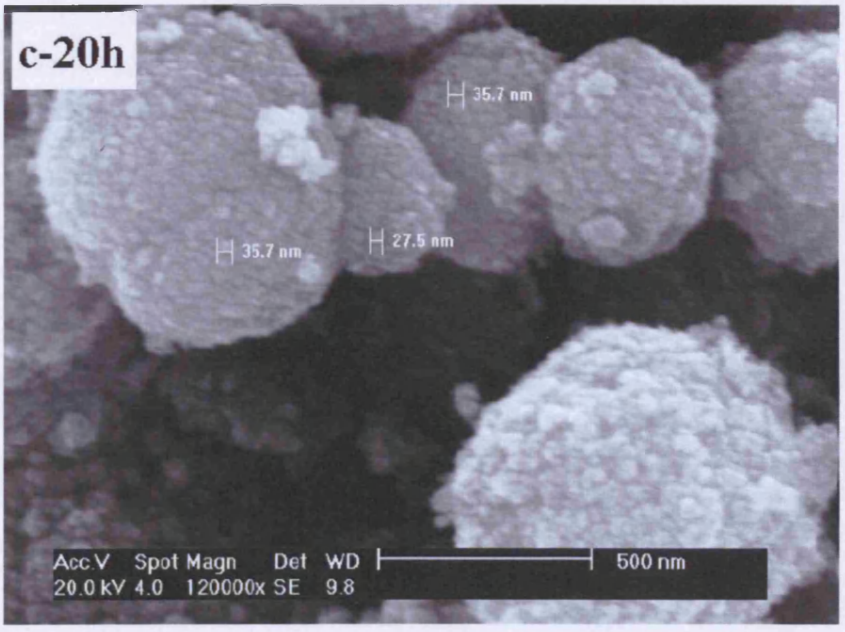

Figure 3.19d SEM images of as-calcined catalyst produced from (15%)water-(85%) EtOH (after calcination at 300°C for 2h).

The reaction of CO oxidation at room temperature on these as-prepared hopcalites has been tested. **Figure 3.20a-b** list all the catalytic performances on the catalysts calcined at 300°C for 2h and 20h. Based on the results shown in figures, some interesting conclusions can be obtained:

(a) Firstly, it is apparent that the catalytic activities are enhanced when using water-ethanol as solvent. All of these three catalysts derived from water-contained ethanol give higher conversion than the one produced from pure ethanol.

(b) Secondly, the most active catalyst for CO oxidation is the one derived from 10% water-contained ethanol, which is much better than the others. This suggests that it is of importance to control the volume ratio of water versus ethanol. The catalytic performance of these four catalysts shows in the following order: c>b>d>a, no matter how long the calcination time is.

(c) The calcination time has an important effect on the catalytic activity, particularly for the catalyst c. The conversion up to 65% can be obtained when the catalyst is derived from calcinations for 2h. However, only the conversion about 42% is observed when calcination time is prolonged to 20h.

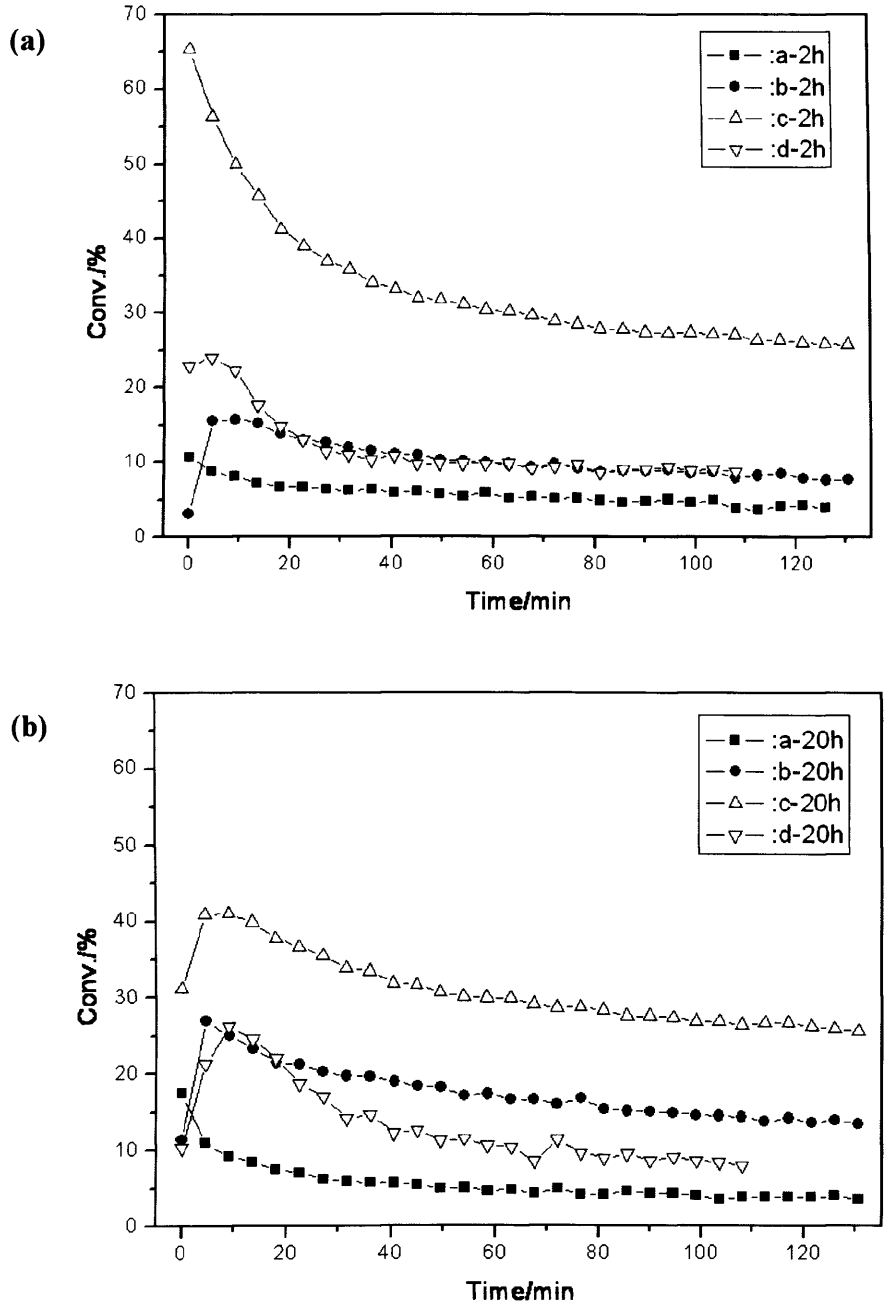

Figure 3.20 Catalytic performance of **(a)** the catalysts as-calcined at 300°C for 2h and **(b)** the catalysts as-calcined at 300°C for 20h: **a**: 0%H_2O-100%EtOH product; **b**: 5%H_2O-95%EtOH product ; **c**: 10% H_2O-90%EtOH product; **d**: 15%H_2O-85% EtOH product. Test conditions: 298K, 0.5% CO in synthetic air, 50mg catalyst, GHSV=17000h^{-1}.

To further investigate the relationship of structure and activity of the as-prepared hopcalite with the best catalytic performance, a detailed TEM analysis on the precursor prepared from 10% water-90% ethanol, as well as its calcined product which is obtained with calcination at 300°C for 2h, has been performed. Detailed TEM analysis (**Figure 3.21a**) shows that the precursors are crystalline, and furthermore, STEM analysis (**Figure 3.21b**) shows them to be less homogeneous than those prepared using dimethyl sulfoxide as solvent (**Figure 3.5**). But, the final catalysts following calcination give a phase-separated material consisting of intimately mixed nanoparticles of copper and manganese oxides (**Figure 3.21c**), which is very similar to that observed for the catalyst prepared using DMSO (**Figure 3.10**). This result indicates, similar to the catalyst derived from DMSO, mixed Cu/MnOx nanophase plays a main role on the catalytic activity of CO oxidation.

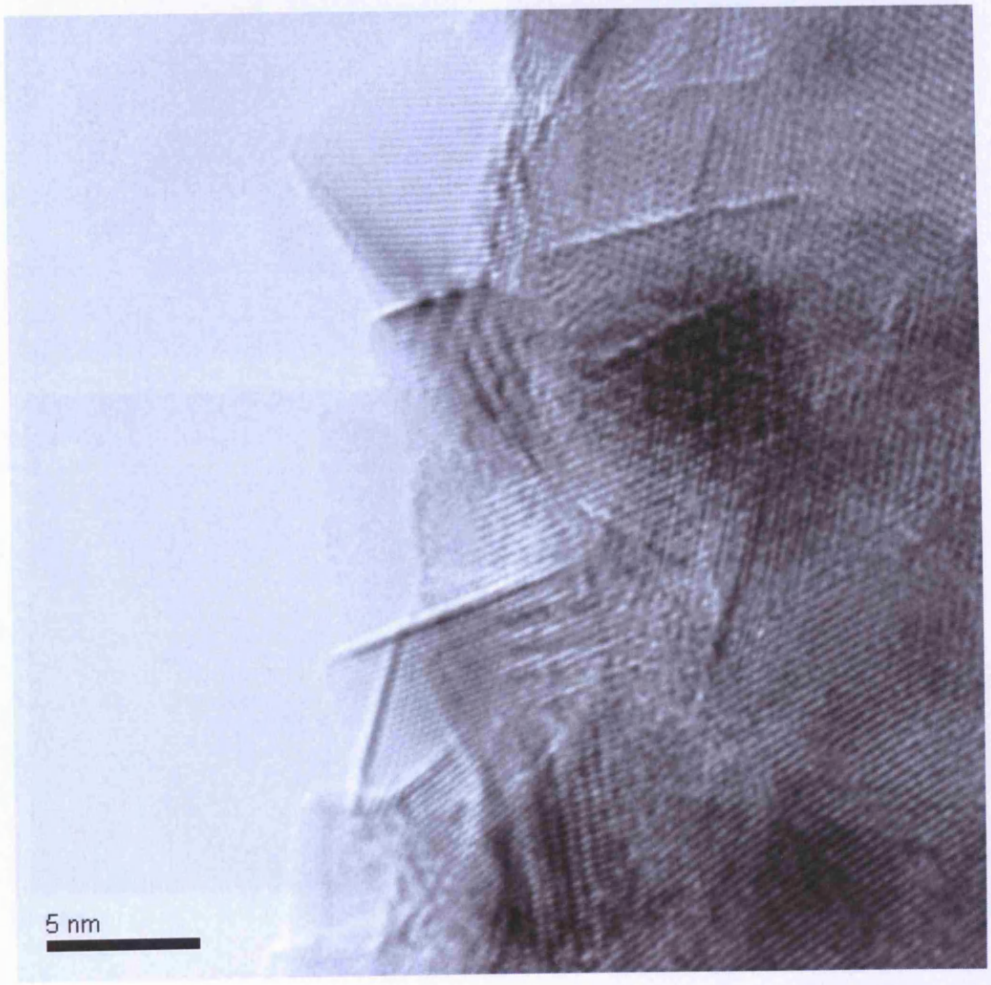

Figure 3.21a TEM image of Cu/MnO_x precursor prepared using ethanol (90%)-water (10%) as solvent

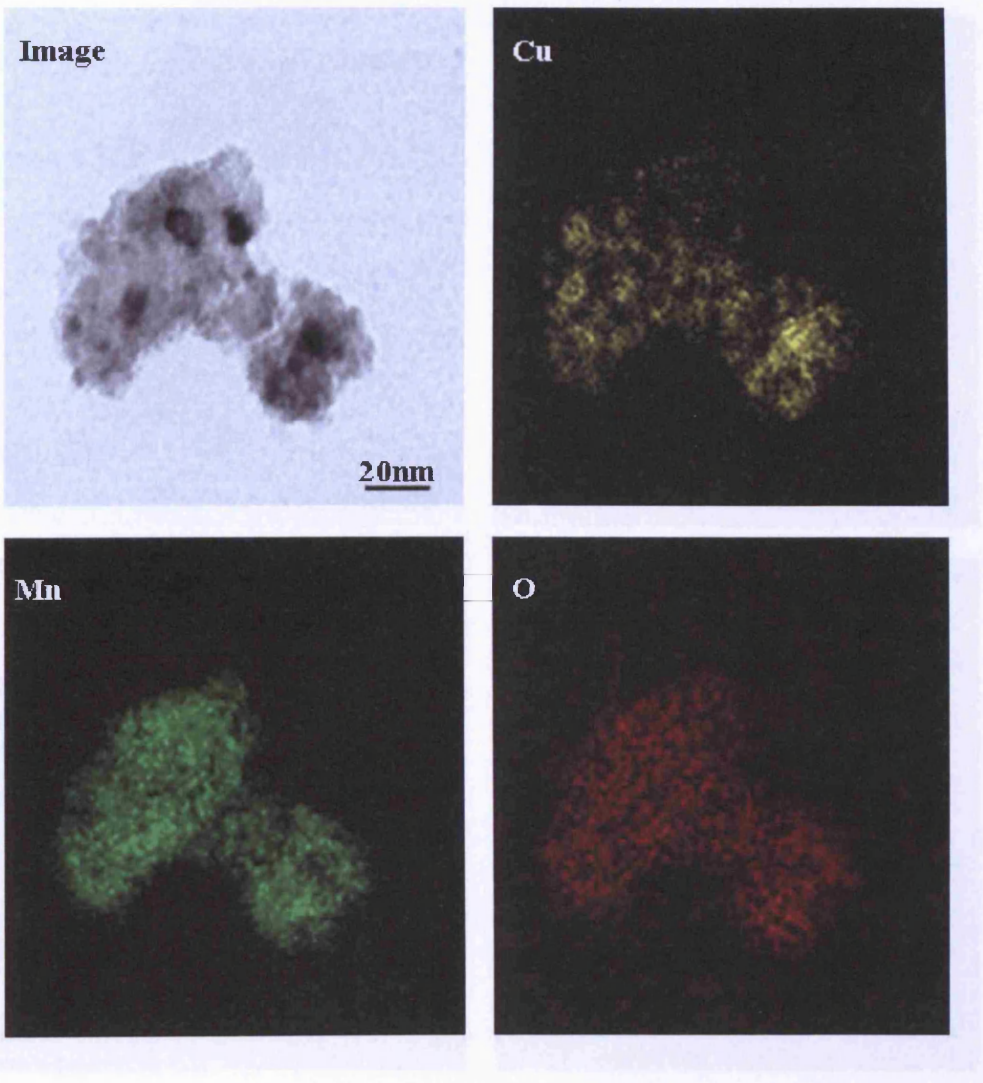

Figure 21b TEM of the precursor produced from 10% water-90% ethanol

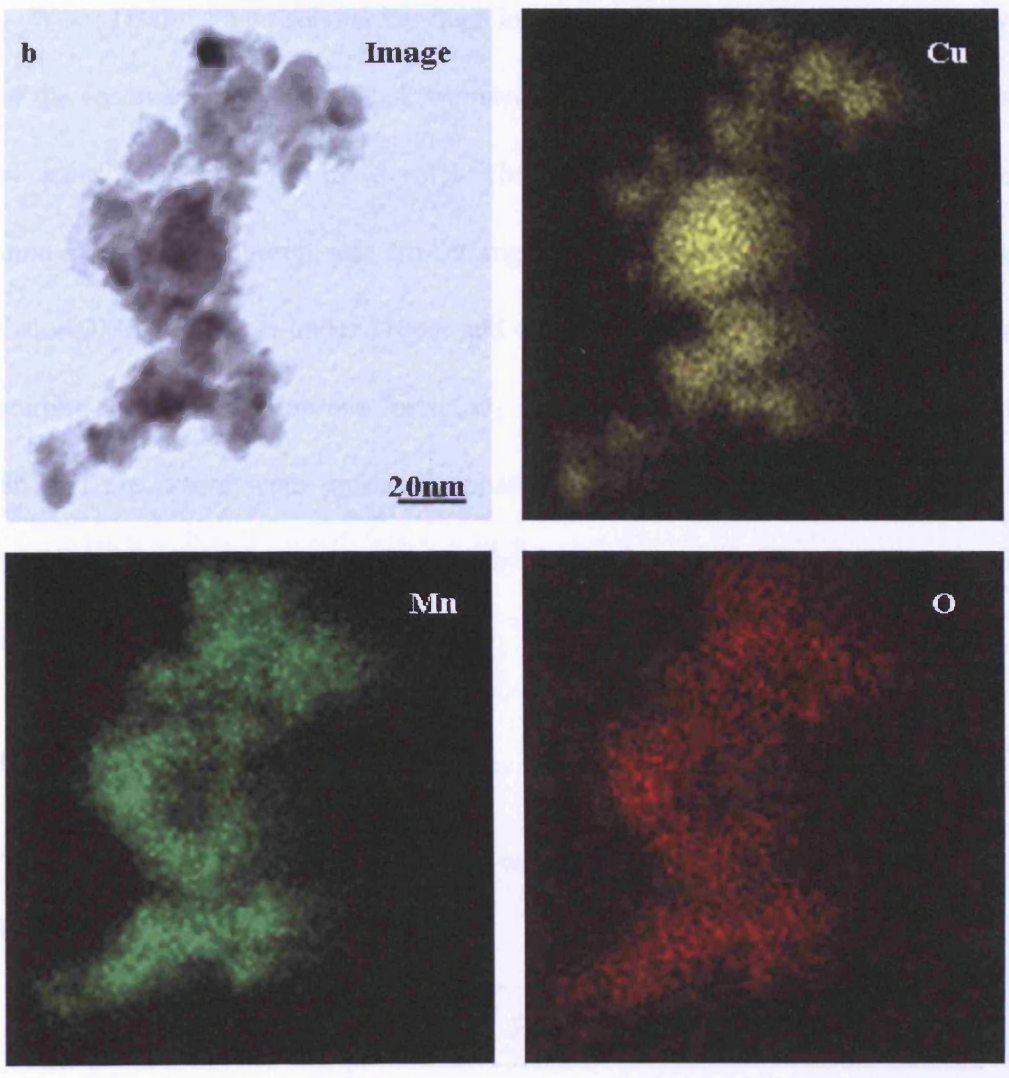

Figure 3.21c TEM of the corresponding catalyst calcined at 300 for 2h

3.3.2.3 water-DMF as a co-solvent

Water-DMF as a co-solvent has been investigated in this section. Like the study of the cosolvent of water-ethanol, we have also explored adding different amounts of water to DMF from 0 to 15 vol%. The preparations were performed using the mixed starting solution of CuAc(5mg/ml) and MnAc(12.25mg/ml) in the water-DMF cosolvents under 110bar and 40°C with the flow rate of 0.1ml/min for starting solutions and 7ml/min for $scCO_2$. The experiments were conducted around 8h and precursors were produced consequently with the approximate yield of 40-50%. The final catalysts were given by the calcination at 300°C for 2h and 20h in static air with the ramp of 10°C /min.

(1) Characterization of Precursors

Table 3.6 Effect of water as a co-solvent with DMF for the supercritical antisolvent preparation method.

Precursor	Solvent	Precipitates	surface area(m^2/g)
a	0% H_2O	Brown powders	241
b	5% H_2O		242
c	10% H_2O		113
d	15% H_2O		106

As shown in **Table 3.6**, brown precipitates have been achieved. In addition, similar to the products from water-ethanol cosolvent, the precursors' surface areas decrease with the addition of more water in DMF.

The XRD analysis is performed on these materials and the results are shown in **Figure 3.22**. The XRD patterns of these as-prepared precursors are similar to the products prepared from water-contained ethanol. In the absence of water, the material obtained is completely amorphous. The precursors which are obtained from the solutions containing water, i.e. 5%, 10% and 15%, show crystalline carbonates. In addition, with the increase of water content in ethanol, the materials crystallinity increases. It obviously indicates the formation of more carbonates. The carbonates most likely are produced from the reaction of carbonic acid and metal acetates in the supercritical environment of high pressure.

FT-IR spectra of the precursors (**Figure 3.23**) also show the similar trend to the products prepared from water-ethanol. The precursor prepared from pure DMF exhibits bands of the acetate salts, with main bands at 1561 and 1418 cm^{-1}, indicating the presence of acetates. As water is added, the bands associated with carbonate species start to appear until almost complete carbonates are observed when using 15% H_2O/85% DMF as solvent.

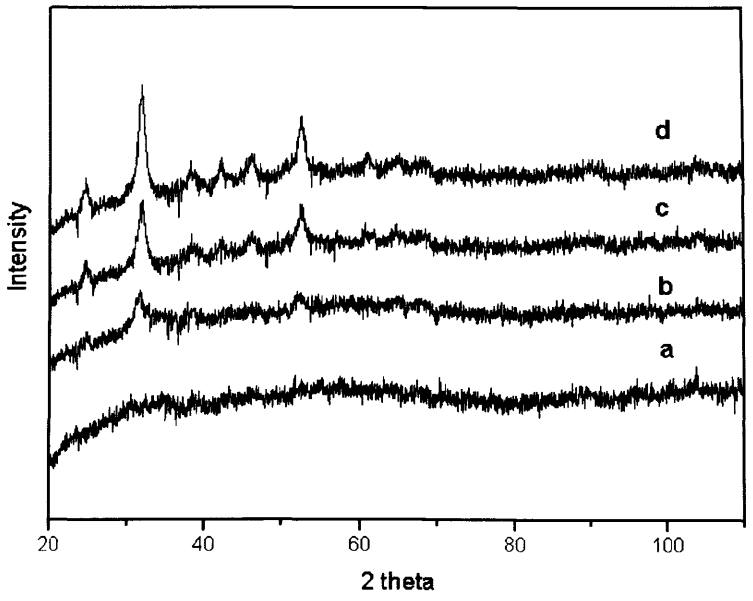

Figure 3.22 XRD patterns of the precursors prepared from water-DMF solvents

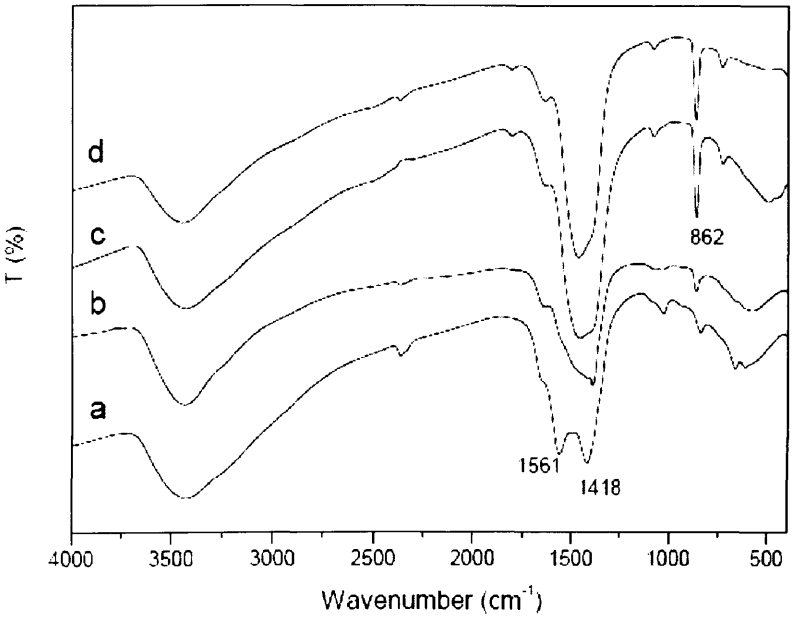

Figure 3.23 FT-IR spectra of the precursors prepared from water-DMF solvents

TGA analyses have been performed on the four as-prepared products and the results are showed in **Figure 3.24**. The results show the differences of components with these 4 precursors. As shown by **Figure 3.24a**, as observed with the product prepared from pure EtOH, the precursor produced from pure DMF has similar four-stage weight losses which appear at 100°C, 192°C, 232°C and 300°C respectively, corresponding to the loss of absorbed solvent, copper hydroxide, copper acetate and manganese acetate [14-15]. With the adding of water to DMF, the components of the precursors will change. For the precursor prepared from 5% water-contained DMF(**Figure 3.24b**), the component is close to the precursor produced from pure DMF since their weight losses are very similar. With the increase of more water content (>5%), only two main weight losses can be observed since a majority of carbonates were obtained. The losses at the first stage (<100°C) are attributed to the physical-absorbed solvent. The second stages at 350-370°C are corresponding to the loss of complete carbonates (**Figure 3.24c-d**).

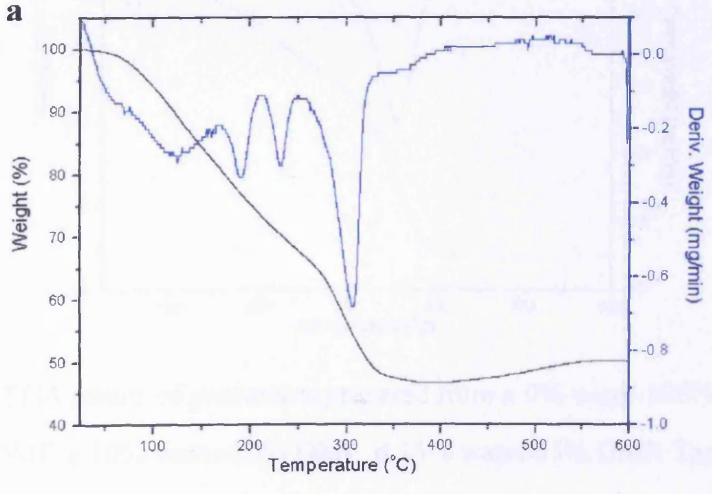

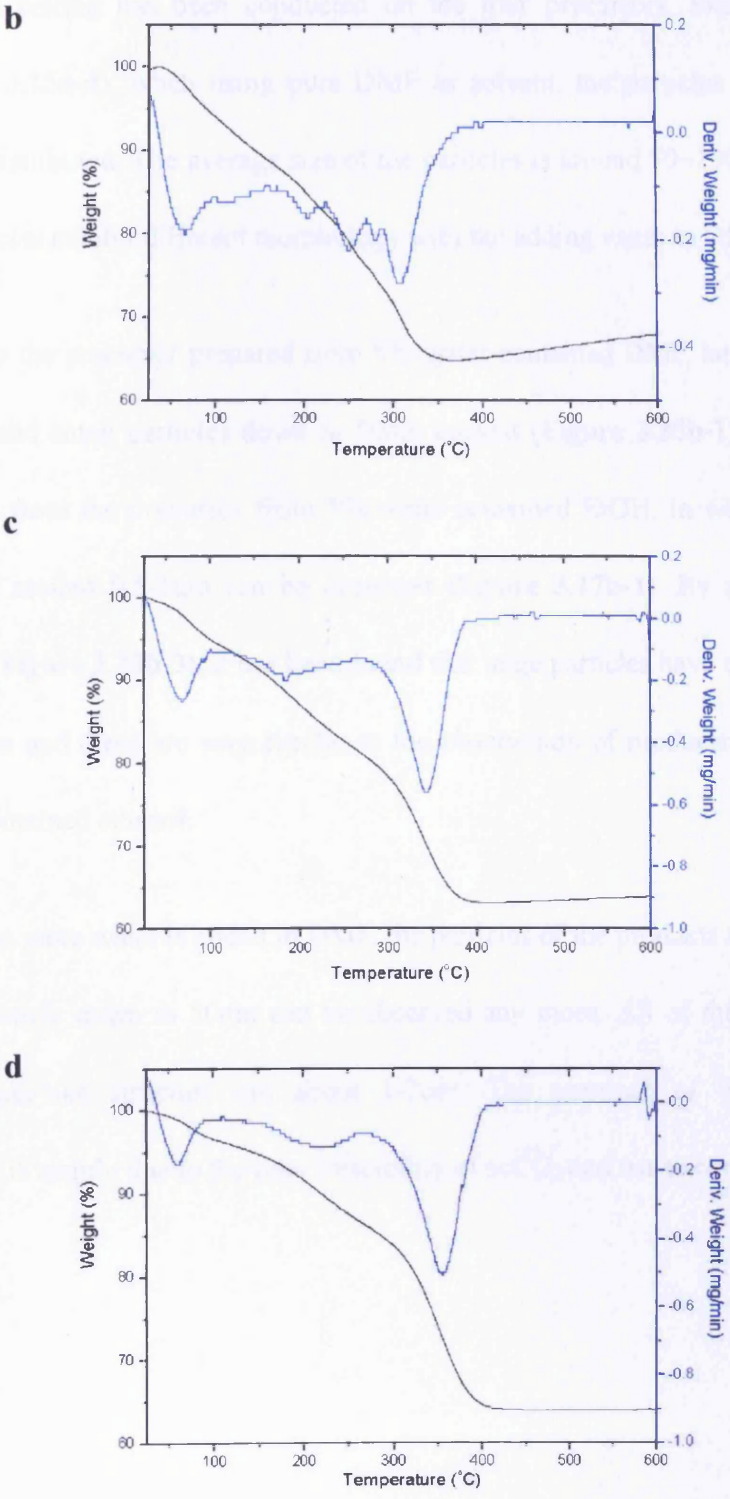

Figure 3.24 TGA results of precursors prepared from **a** 0% water-100% DMF, **b** 5% water-95% DMF, **c** 10% water-90% DMF, **d** 15% water-85% DMF. Test conditions: N_2 flow, 10°C/min heating rate.

SEM testing has been conducted on the four precursors. From the images (**Figure 3.25a-d**), when using pure DMF as solvent, the particles are small and evenly distributed. The average size of the particles is around 50~100nm. However, the particles exhibit different morphology with the adding water to DMF.

As to the precursor prepared from 5% water-contained DMF, large particles up to 3um and small particles down to 50nm coexist (**Figure 3.25b-1**). This is quite different from the precursor from 5% water-contained EtOH, in which only large particles around 0.5-1um can be observed (**Figure 3.17b-1**). By magnifying the images (**Figure 3.25b-3**), it has been found that large particles have cauliflower-like structures and these are very similar to the observation of products prepared from water-contained ethanol.

When more water is added in DMF, the particles of the products are even and no small particle down to 50nm can be observed any more. All of the particles with cauliflower-like structure are about 1-2um. The presence of these large-size particles is mainly due to the poor miscibility of $scCO_2$ and water-contained solvent.

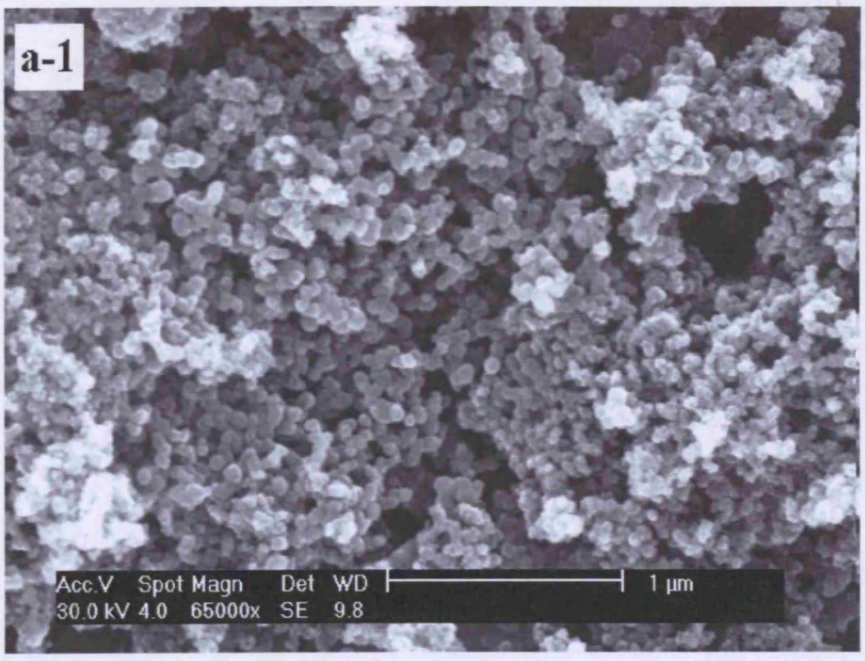

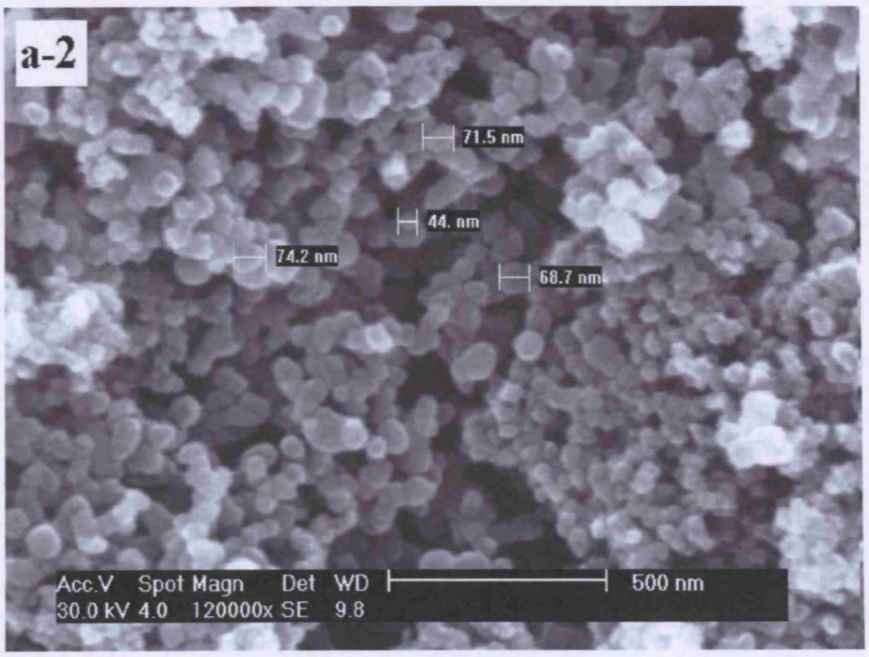

Figure 3.25a SEM images of the precursor prepared from 0% water-100% DMF

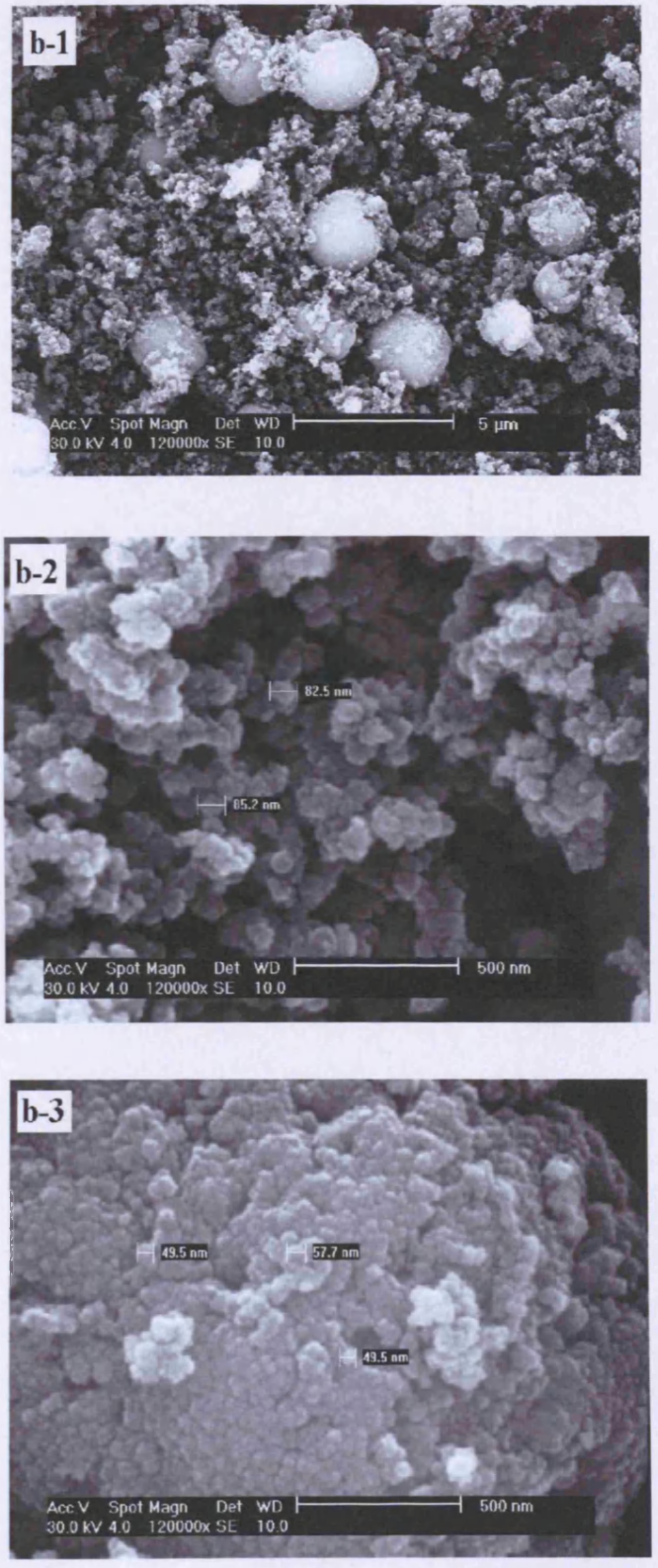

Figure 3.25b SEM images of the precursor prepared from 5% water-95% DMF

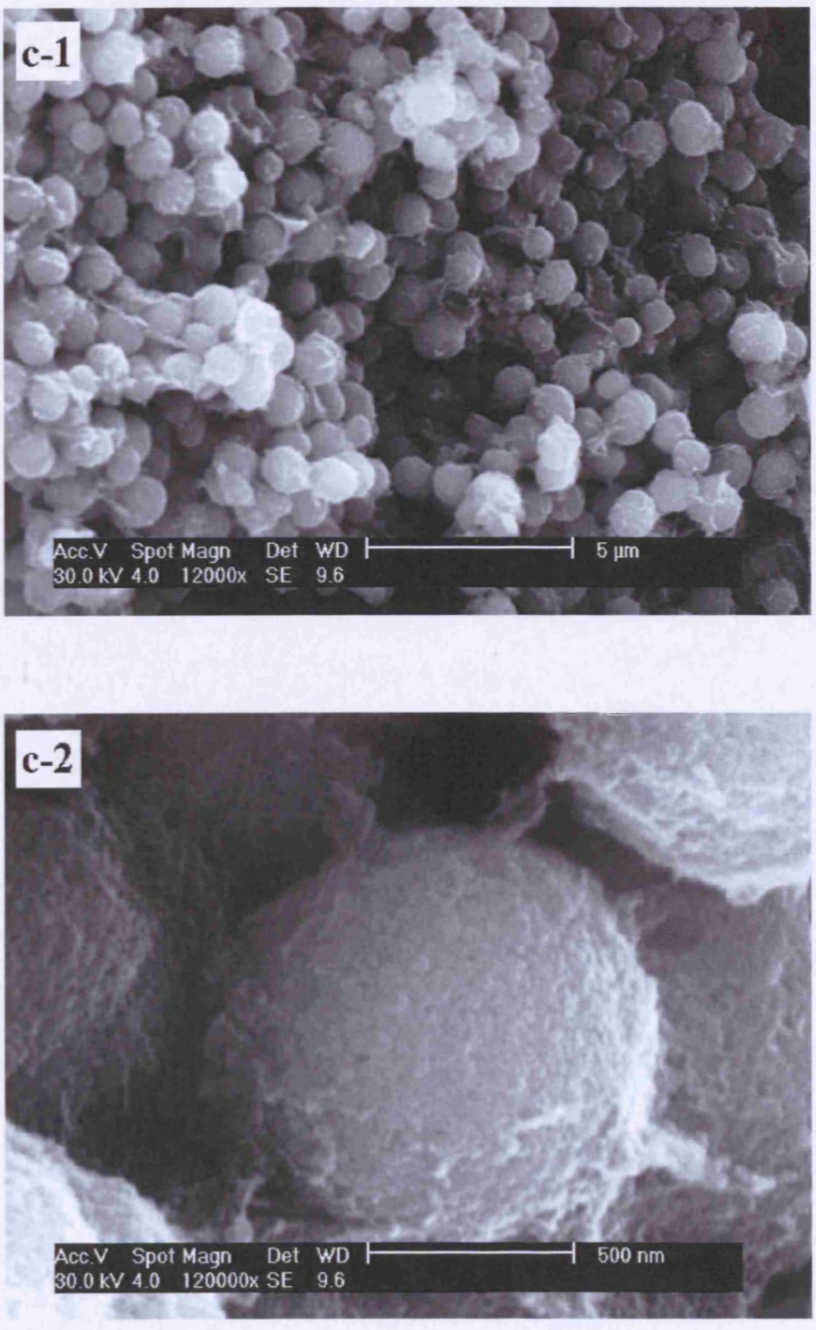

Figure 3.25c SEM images of the precursor prepared from 10% water-90% DMF

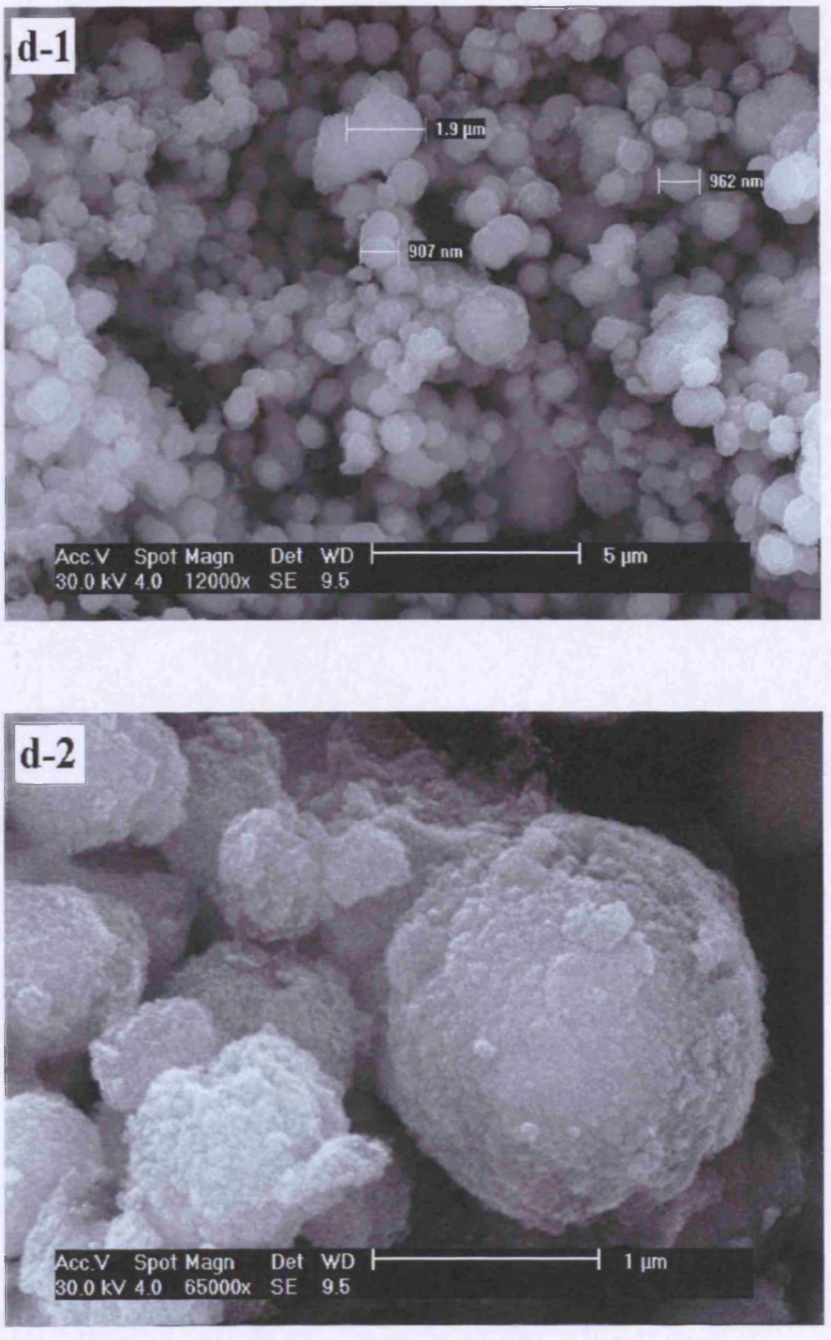

Figure 3.25d SEM images of the precursor prepared from 15% water-85% DMF

(2) Characterization and catalytic performance of as-calcined catalysts

Table 3.7 lists the surface areas of as-calcined catalysts. Similar to previous results derived from water-contained solvents, the surface areas are retained or improved dramatically following the calcination when using water-DMF as a solvent. This result further indicates that the addition of water to solvent can highly increase the surface areas of final hopcalites.

Table 3.7 The surface areas of as-calcined products under 300°C for 2h and 20h

catalysts	Surface area(m^2/g)	
	300°C for 2h	300°C for 20h
a	21	20
b	70	95
c	222	206
d	210	142

Figure 3.25 show XRD patterns of the catalysts calcined at 300°C for 2h and 20h, respectively. Similar to the XRD results of precursors derived from water-contained EtOH, it has been found that the more crystalline the precursor appears the more amorphous the calcined catalyst is. The XRD patterns of crystalline materials exhibit the diffraction lines of $CuMn_2O_4$. Different from its water-EtOH counterpart, the catalyst derived from 10% water-contained DMF shows complete amorphous no matter how long it is calcined. These indicate the components and morphology of products can be strongly tailored by the application of different solvents.

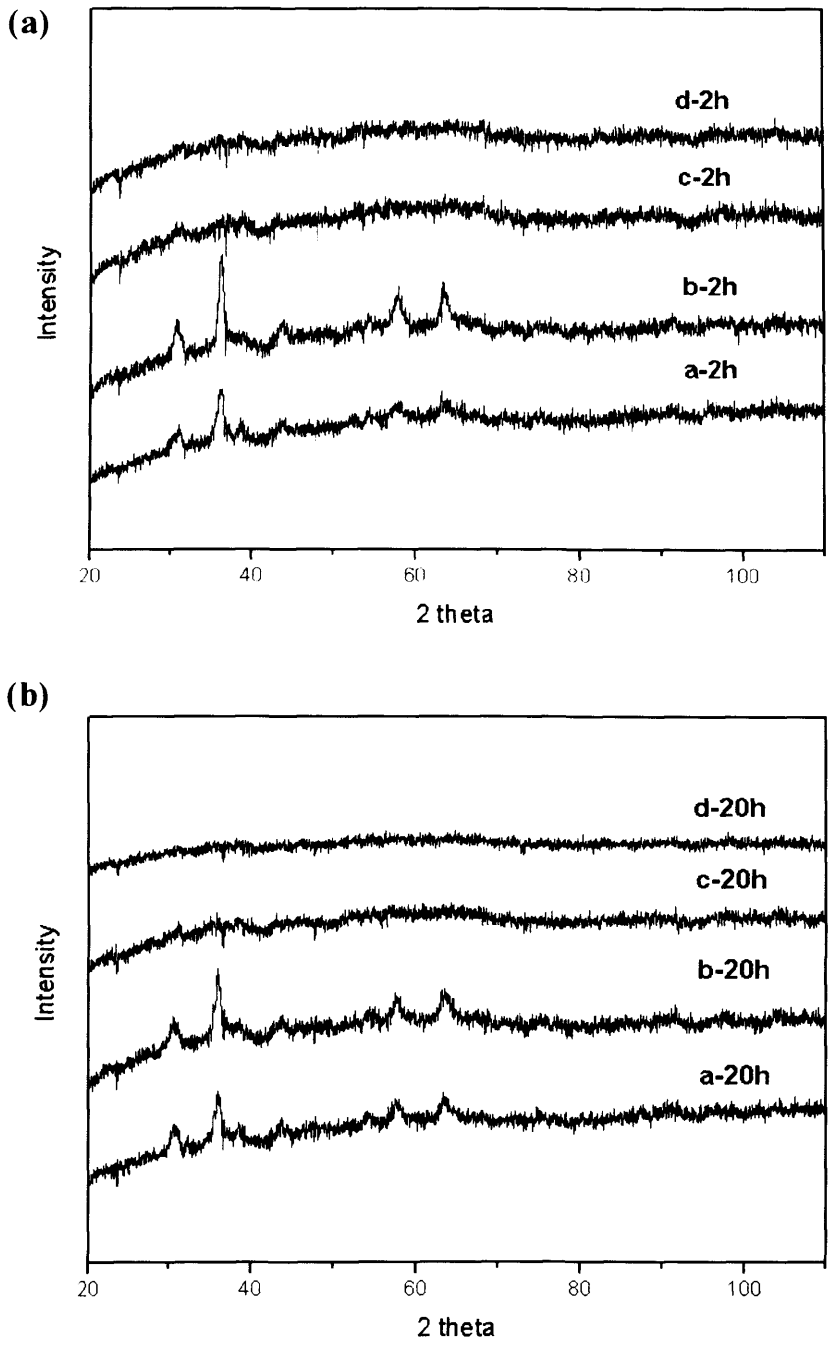

Figure 3.25 XRD patterns of **(a)** catalysts calcined at 300°C for 2h and **(b)** XRD patterns of catalysts calcined at 300°C for 20h. **a**: 0%H_2O-100%DMF product; **b**: 5%H_2O-95%DMF product ; **c**: 10%H_2O-90%DMF product; **d**: 15%H_2O-85% DMF product.

The catalytic activities on ambient CO oxidation of these as-prepared hopcalites derived from water-DMF solvent have been tested. **Figure 3.26a-b** list all the catalytic performances on these catalysts calcined at 300°C for 2h and 20h, respectively. A detailed inspection of these data can lead to the following conclusions:

(a) Firstly, when compared with the catalyst prepared from pure DMF, the overall enhancement on catalytic activities of the hopcalites derived from water-contained DMF has been observed.

(b) Secondly, it is unexpected to see that the catalysts derived from 10%~15% water-contained DMF exhibit extremely high conversion for CO oxidation at the very beginning stage of test process. Up to nearly 90% of conversion can be obtained as shown by **Figure3.26b**. This is still an exciting result although the high conversion can not be maintained for a long time.

(c) Thirdly, the calcination time influences catalytic activity as well. Generally, regarding the catalysts calcined from the same precursors, the longer the calcination time is, the better their catalytic activity is. The catalytic performance of these catalysts (except Catalyst d-20h) roughly shows in the following order: d>c>b>a, no matter how long the calcination time is.

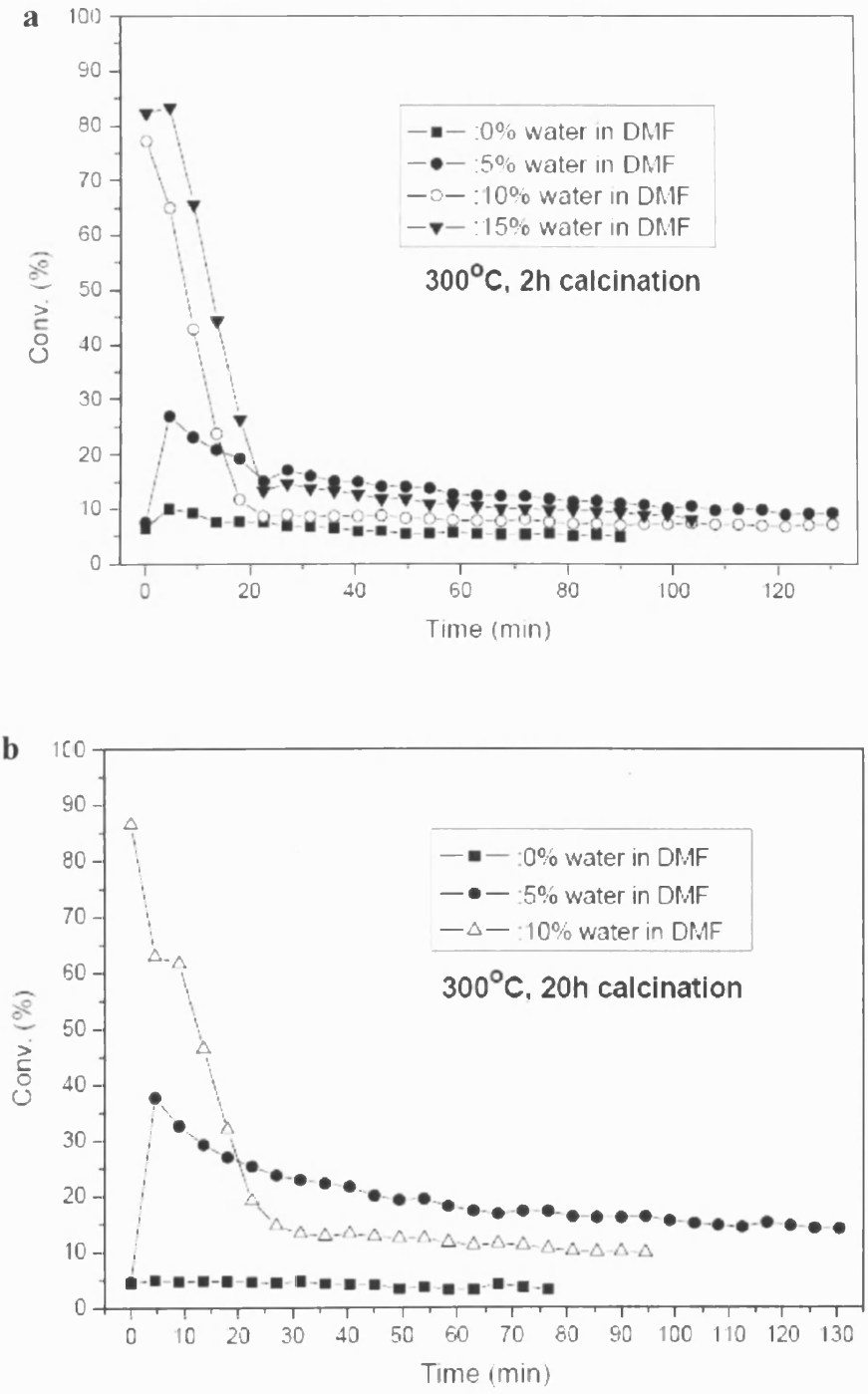

Figure 3.26a-b Catalytic performances of the as-calcined hopcalites derived from water-DMF cosolvent. Test conditions: 298K, 0.5% CO in synthetic air, 50mg catalyst, GHSV=17000h^{-1}.

To investigate the structure of as-prepared hopcalites in more detail, the XPS analysis were performed on the hopcalite derived from 10% water-contained DMF (i.e. Precursor **d** and Catalyst **d-2h**) and the results show in **Figure 3.27**. For the precursor, the Cu (2p) spectrum shows features characteristic of the presence of Cu^{2+}, in particular the composite satellite structure separated by *ca* 6-8 eV from the primary photoemission peak (**Figure 3.27a**). The corresponding C(1s) spectrum (**Figure 3.27b**) exhibits two components reflecting the two non-equivalent carbon atoms in the acetate species. After calcination we didn't observe the metallic Cu in the catalyst and the Cu(2p) spectrum only shows features characteristic of the presence of Cu^{2+}.

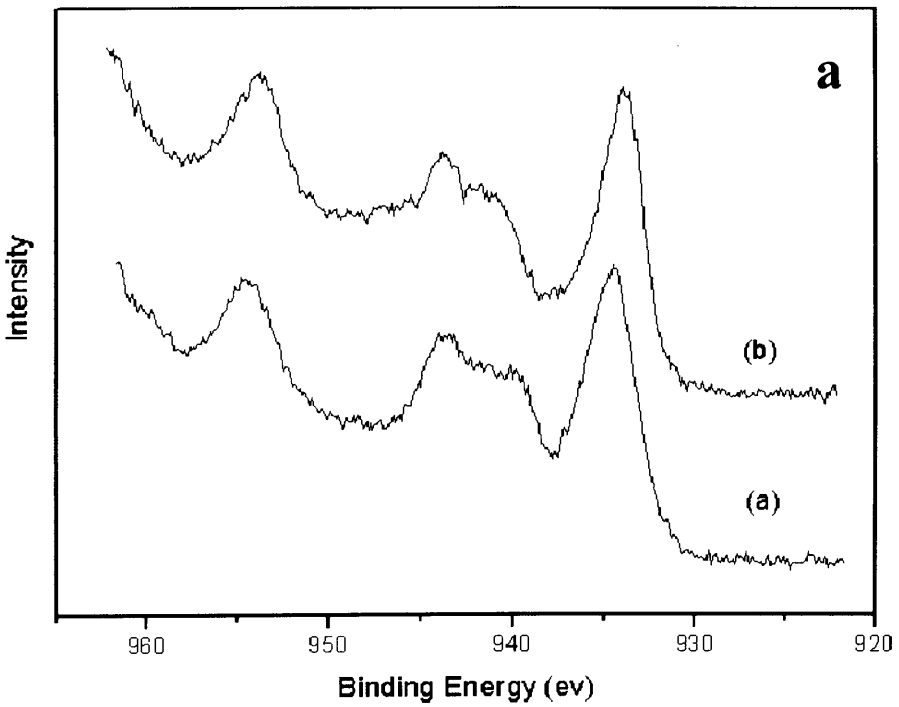

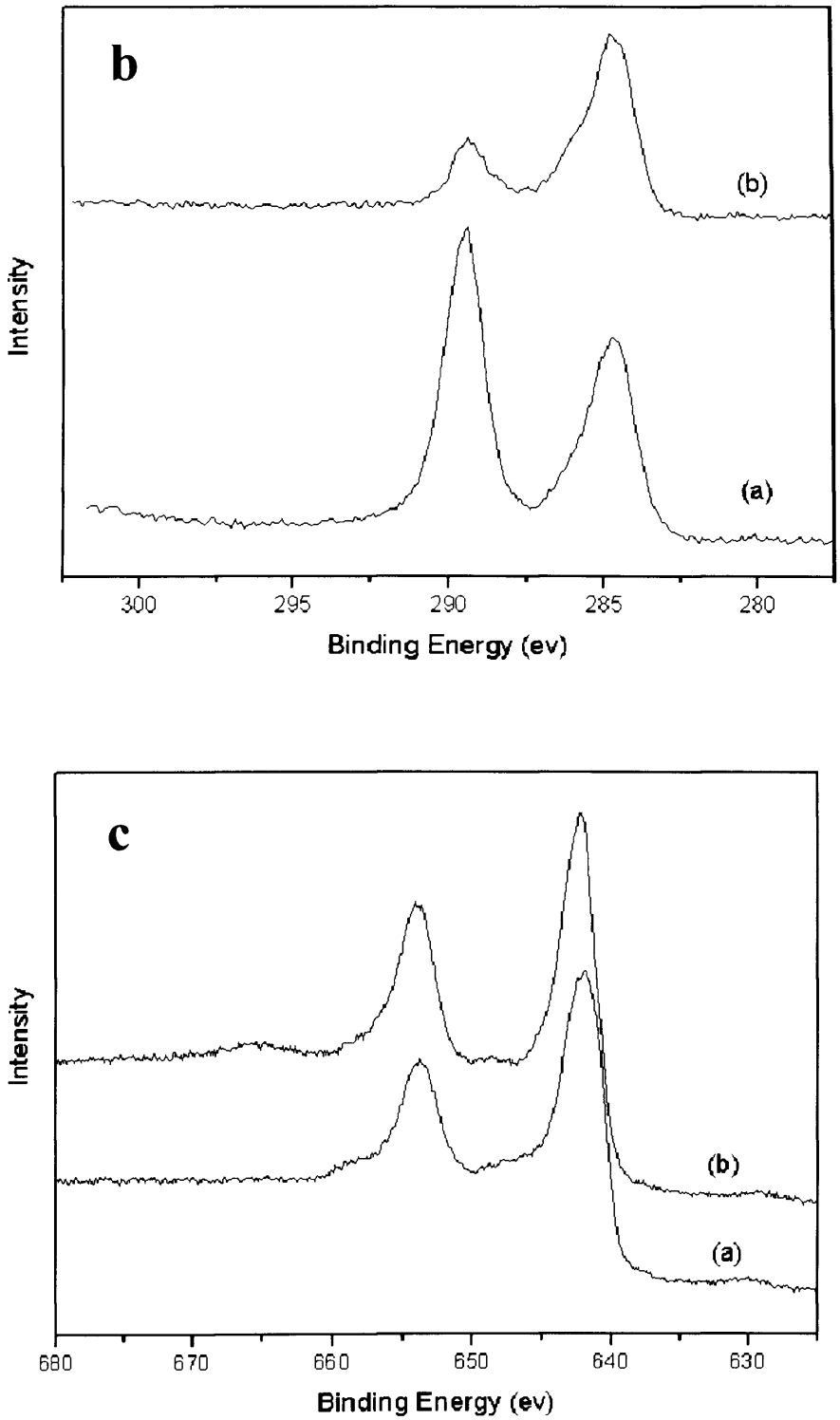

Figure 3.27 X-ray photoelectron spectra for (a) the precursor and (b) after calcination at 300 °C for 2h. **a**, Cu (2p) spectra; **b**, C(1s) spectra and **c**, Mn(2p) spectra.

process. Recently, there has been an increasing interest using H_2O_2 in supercritical system. For instance, H_2O_2 has been used as primary oxidant of heterogeneous catalytic oxidation in supercritical CO_2 [16-18]. In addition, most recently, H_2O_2 has also been successfully used in supercritical deposition process and materials preparation with supercritical system. For example, Gougousi *e. al.* reported a novel method for deposition of a variety of metal oxides thin films directly using metal-organic precursors soluble in supercritical CO_2 and H_2O_2 [19]. In this work, H_2O_2 worked as oxidizer and offered a viable source of oxygen for oxide deposition process. Their results showed that metal oxides combined with minor carbonates and hydroxides have been produced under supercritical process at low temperature. This study inspires us to consider applying H_2O_2 as an oxidizer in the preparation of hopcalite using supercritical antisolvent precipitation.

To investigate systematically the effect of H_2O_2-contained ethanol, we explored adding different amounts of H_2O_2 solution to the ethanol from 0 to 10 vol%. H_2O_2 solution (30 wt% in water) was used as received. With the adding of more H_2O_2 solution to ethanol, the green Cu/Mn acetate solution became dark grey owing to the oxidation of manganese acetate by H_2O_2. The preparations were performed using the mixed starting solution of CuAc (5mg/ml) and MnAc(12.25mg/ml) in the

H_2O_2-ethanol co-solvents under 110bar and 40°C with the flow rate of 0.1ml/min for starting solutions and 7ml/min for $scCO_2$. The experiments were conducted around 8h and precursors were produced consequently with the approximate yield of 50%. The final catalysts were given by the calcination at 300°C for 2h and 20h, respectively, in static air with the ramp of 10°C /min.

3.3.3.1 Characterization of precursors

The detailed experimental results on precursors are shown in **Table 3.8**. As shown clearly, with the addition of more H_2O_2 solution, the colour of the products changes from green to brown and then dark gray. The appearance of dark colour might be attributed to the formation of Mn (+3) due to the addition of H_2O_2 in starting solution. In addition, like all the previous precursors derived from water-contained cosolvents, the surface areas of these precursors also decrease with the addition of more H_2O_2 to ethanol. Since we applied 30% H_2O_2 solution in water, most likely, the reduction of the surface areas is mainly attributed to the adding of some water.

The XRD analysis has been performed on these products and the results are shown in **Figure 3.28**. The materials obtained from 0%-5% H_2O_2 solution are absolutely amorphous as illustrated by the patterns of X-ray diffraction. Nevertheless, when 10% H_2O_2 solution is added to ethanol, the product exhibits its crystallinity which can be ascribed to the diffraction patterns of carbonates.

Table 3.8 The experimental results of precursors produced from H_2O_2-EtOH

Precursor	Solvent	Precipitates	surface area (m^2/g)
a	0% H_2O_2	Green	264
b	1% H_2O_2	↓ dry powder	261
c	5% H_2O_2		249
d	10% H_2O_2	dark grey	160

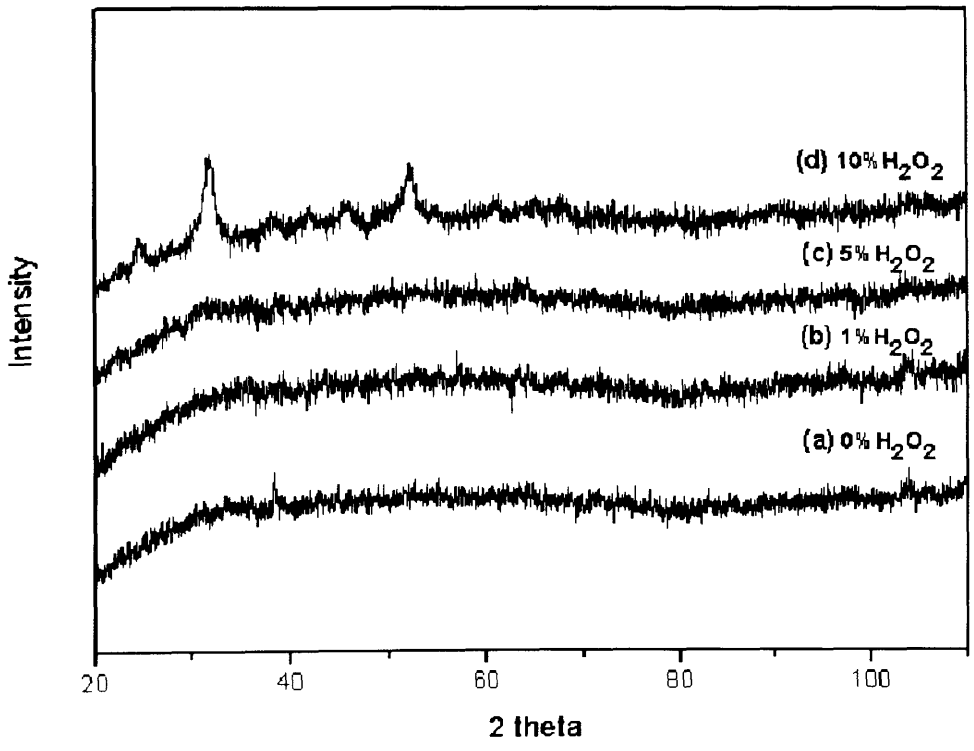

Figure 3.28 XRD patterns of precursors produced from H_2O_2-contained EtOH

The FT-IR spectra (**Figure 3.29**) are in agreement with the results of XRD determination. It confirms the presence of large amount of carbonates when 10%

H_2O_2 solution is added in ethanol, whereas the precursors derived from 0%-5% H_2O_2-contained solution only exhibit the characteristic of acetates. It is worthwhile to be mentioned that the precursor derived from 5% H_2O_2-95% ethanol, is quite different from the product prepared from 5% water-95% ethanol. The former exhibits bands of almost complete acetate salts (only a little bit carbonates appear), whereas the latter mainly shows major carbonate salts (see **Figure 3.15**).

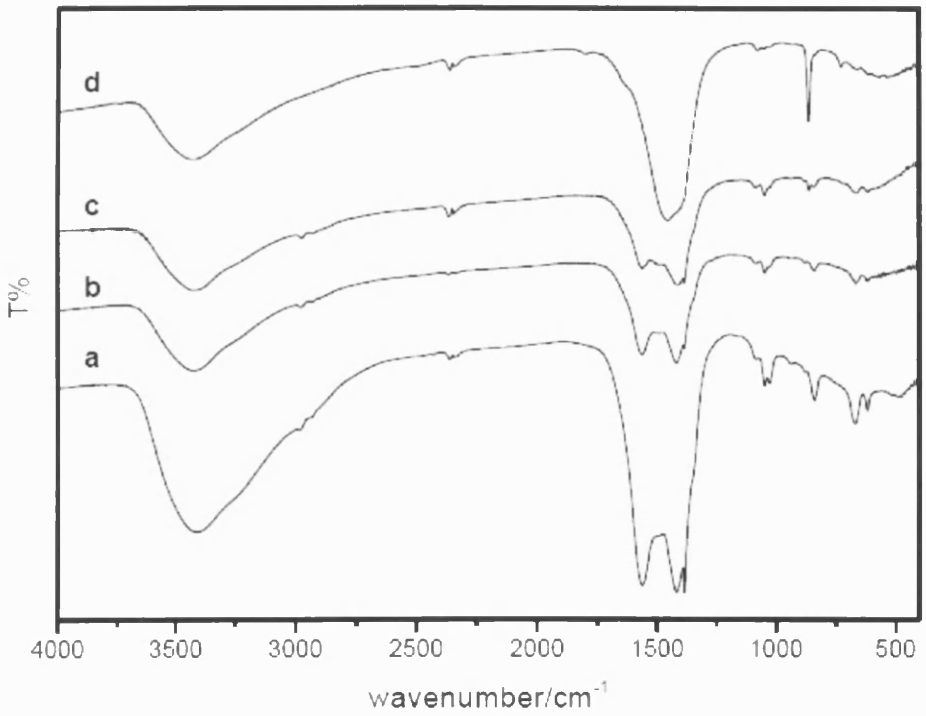

Figure 3.29 FT-IR spectra of precursors produced from **a** 0% H_2O_2-100% EtOH, **b** 1% H_2O_2-95% EtOH, **c** 5% H_2O_2-95% EtOH, **d** 10% H_2O_2-90% EtOH.

TGA analyses have been performed on the four as-prepared products and the results are showed in **Figure 3.30a -d**. In particular, these results are in excellent accordance with the observations from XRD and FT-IR. The precursor produced

from pure ethanol has four-stage weight losses which appear at 72°C, 200°C, 236°C and 297°C, respectively. The adding of 1% H_2O_2 solution to ethanol doesn't affect the component of as-prepared precursor and the same four-stage weight losses can be observed clearly. In a similar way, precursor c which prepared from 5%H_2O_2-95% ethanol also keeps approximate four-stage weight losses. With respect to the product prepared from 10%H_2O_2-95% ethanol, it shows three-stage weight losses and very similar to the precursor produced from 10% water-95% ethanol. The loss at the first stage (<100°C) can be attributed to the physical-absorbed solvent. The second stage at *ca.* 260°C is corresponding to the loss of mixed copper acetate and copper carbonate and the third stage at 330°C belongs to the loss of mixed manganese acetate and manganese carbonate.

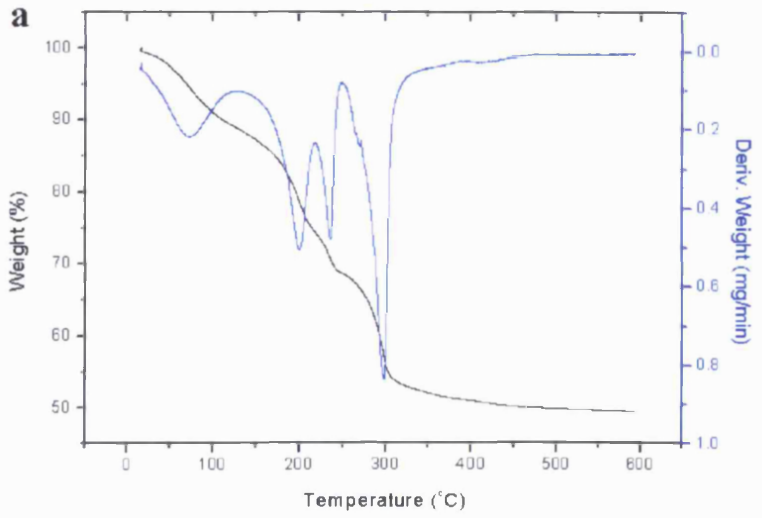

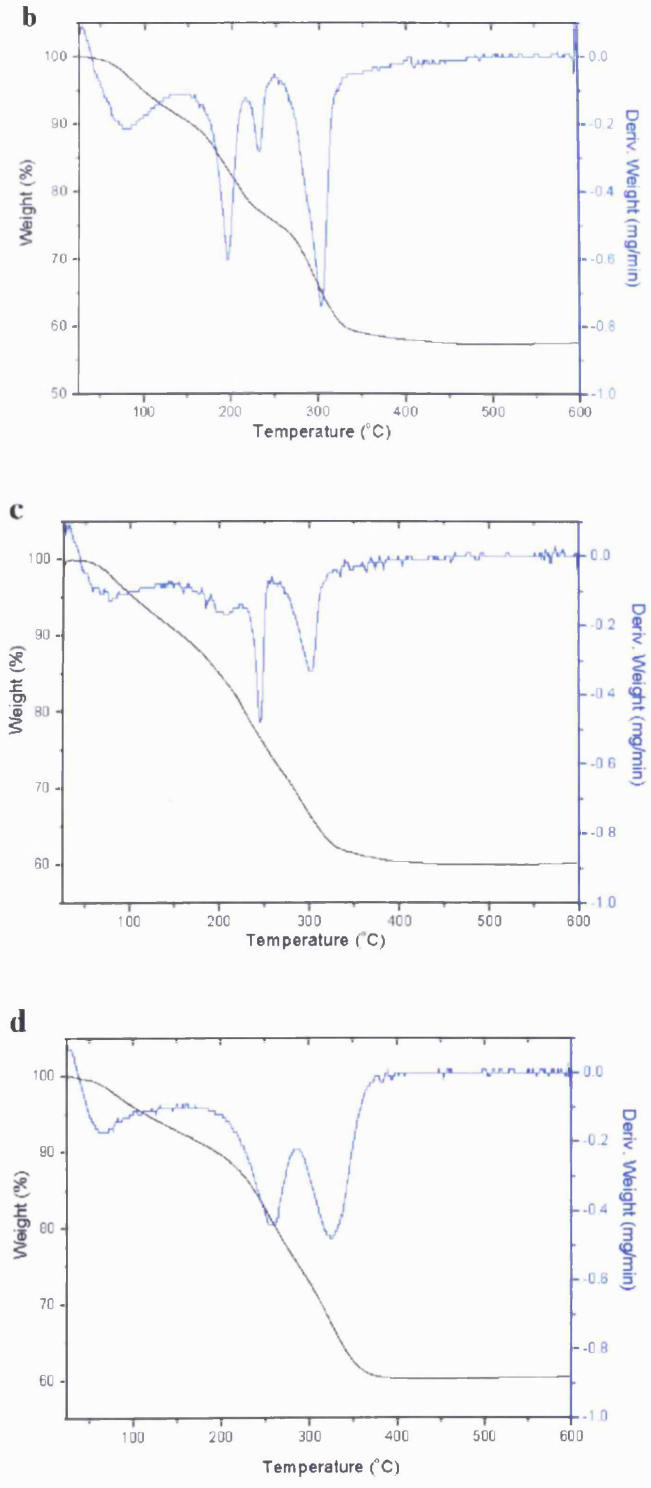

Figure 3.30a-d TGA results of precursors produced from **a** 0% water-100% EtOH, **b** 1% H_2O_2-95% EtOH, **c** 5% H_2O_2-95% EtOH, **d** 10% H_2O_2-90% EtOH. Test conditions: N_2 flow and 10°C heating rate.

SEM testing has been conducted on the four precursors. From the images (see **Figure 3.31a-d**), some detailed information on the morphology of particles is obtained. When using pure ethanol as solvent, small and defined particles around 50~100nm are observed. With the adding 1%-5% H_2O_2 solution to ethanol, the particles aggregate with each other largely. However, many defined particles around 50~100nm can still be detected. When using 10%H_2O_2-90% ethanol as a solvent, many large particles (0.5nm-1um) with cauliflower-like structure appear again. These particles are very similar to those prepared from 10% water -90% ethanol. The formation of these particles is mainly due to partial miscibility between $scCO_2$ and 10%H_2O_2-90% ethanol.

In view of the characterizations of BET, XRD, FT-IR, TGA and SEM, it can be concluded that the application of 10%H_2O_2-90% ethanol gives the hopcalite precursor composed of carbonates with the similar structure to that of the precursor prepared from 10% water-90% ethanol. Whereas, the application of 5%H_2O_2-90% ethanol gives rise to the production of hopcalite precursor composed of acetates.

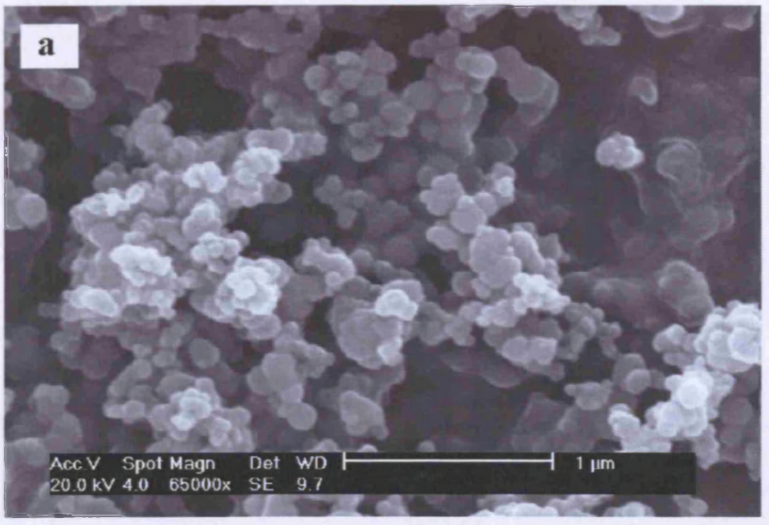

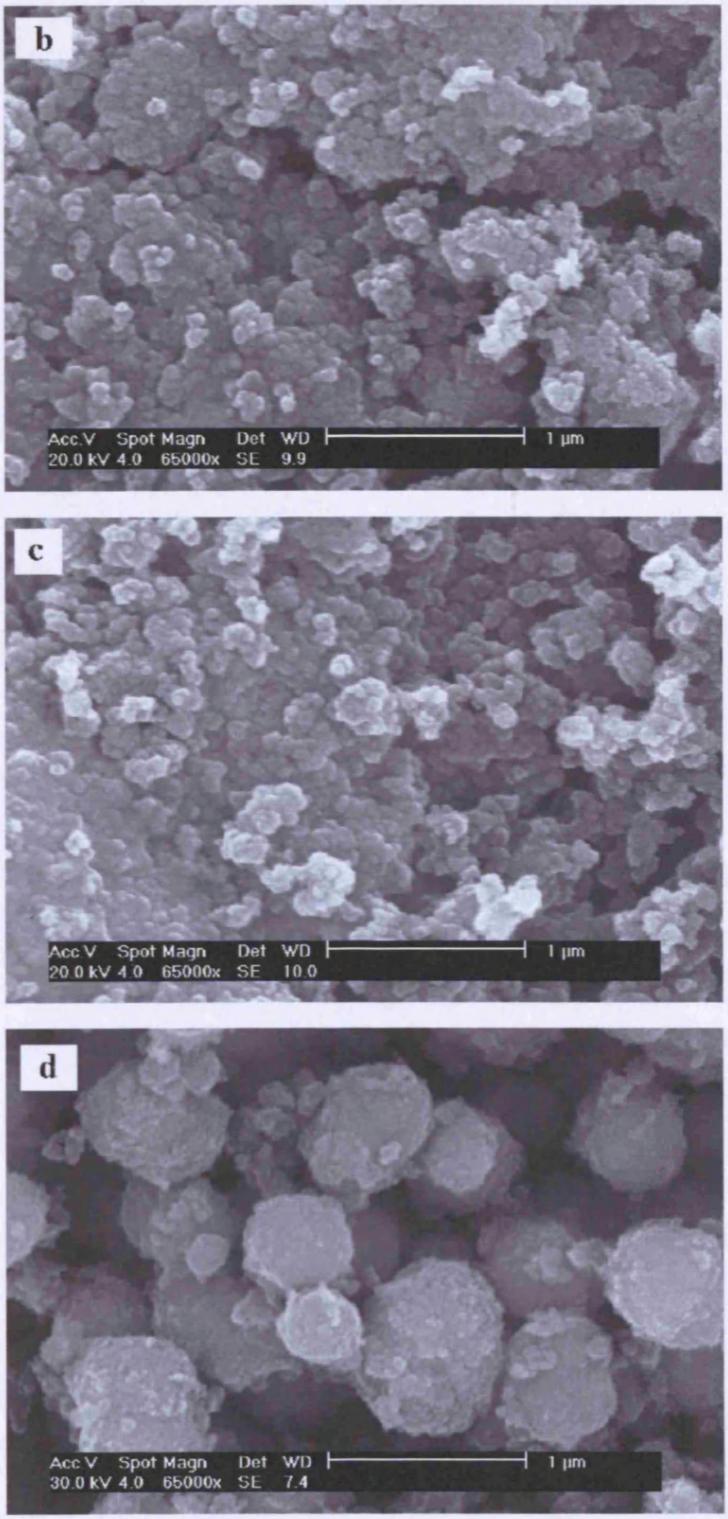

Figure 3.31a-d SEM images of precursors produced from **a** 0% water-100% EtOH, **b** 1% H_2O_2-95% EtOH, **c** 5% H_2O_2-95% EtOH, **d** 10% H_2O_2-90% EtOH.

3.3.3.2 As-calcined catalysts

Table 3.9 lists the surface areas of as-calcined catalysts. Similar to previous results derived from water-contained solvents, the surface areas are retained or improved dramatically following the calcination when using H_2O_2-EtOH as a solvent. This result further indicates that the addition of H_2O_2 solution to solvent can increase the surface areas of final hopcalites as well. Of course, the increase of surface areas most likely is owing to the 70wt%water contained in the H_2O_2 solution.

Table 3.9 The surface areas of as-calcined products under 300°C for 2h and 20h

catalysts	Surface area(m^2/g)	
	300°C for 2h	300°C for 20h
a	33	20
b	37	61
c	52	83
d	184	142

XRD patterns of the catalysts calcined at 300°C for 2h and 20h are shown in **Figure 3.32**. Following calcinations, crystalline catalysts have been obtained when their precursors are amorphous (i.e. catalysts a-c prepared from 0%-5% H_2O_2 contained solvents), and vice versa (i.e. catalyst d produced from 10% H_2O_2 contained solvent). The XRD patterns of crystalline materials exhibit the diffraction lines of $CuMn_2O_4$. These diffraction peaks show no big change no matter how long the calcinations time is, although BET determinations exhibit large difference.

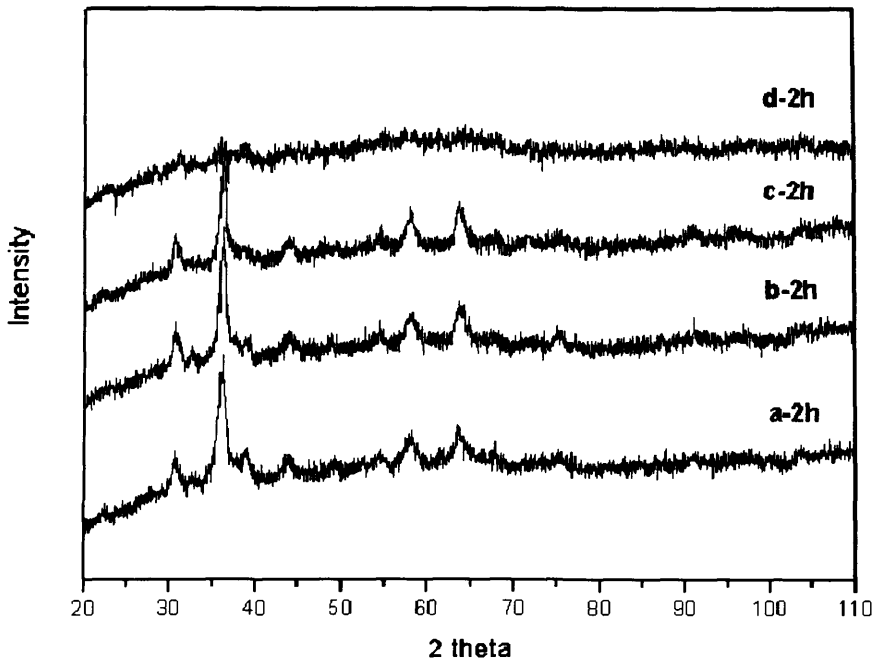

Figure 3.32a XRD patterns of catalysts calcined at 300°C for 2h: **a** 0% H_2O_2-100% EtOH, **b** 1% H_2O_2-95% EtOH, **c** 5% H_2O_2-95% EtOH, **d** 10% H_2O_2-90% EtOH.

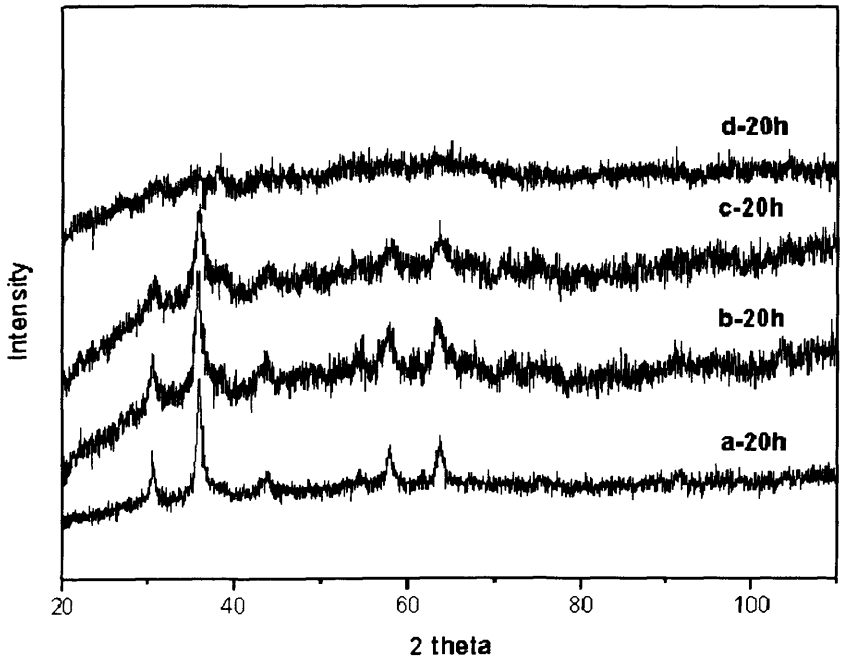

Figure 3.32b XRD patterns of catalysts calcined at 300°C for 20h: **a** 0% H_2O_2-100% EtOH, **b** 1% H_2O_2-95% EtOH, **c** 5% H_2O_2-95% EtOH, **d** 10% H_2O_2-90% EtOH.

The catalytic performances on ambient CO oxidation for these as-produced catalysts have been tested. All the results are shown in **Figure 33a-b**. The following conclusions have been drawn from these data.

(a) The addition of H_2O_2 solution effectively enhances the catalytic activities of final catalysts. All the catalysts prepared from 1%-10% H_2O_2 contained solvents exhibit higher conversion on CO oxidation no matter how long the calcination time is, when compared to those from solvents in the absence of H_2O_2.

(b) In general, the longer the calcination time is, the better the catalytic activity is. The best catalytic performance has been given by catalyst b calcined in air for 20h (which is derived from 5%H_2O_2-95% ethanol) and the conversion for CO oxidation up to 54% has been observed.

(c) For the catalysts prepared from 10%H_2O_2-95% ethanol, their performances are different from their water-ethanol counterparts which always show the best catalytic activities after different calcinations time. This catalyst calcined for 2h only gives 30% conversion for CO oxidation although it is the most active catalyst amongst all the others under the same conditions. Besides, the catalyst calcined for 20h doesn't exhibit enhanced activity at all. In contrast, catalyst c-20h prepared from 5%H_2O_2-95% ethanol shows a great potential on the catalytic conversion of CO to CO_2.

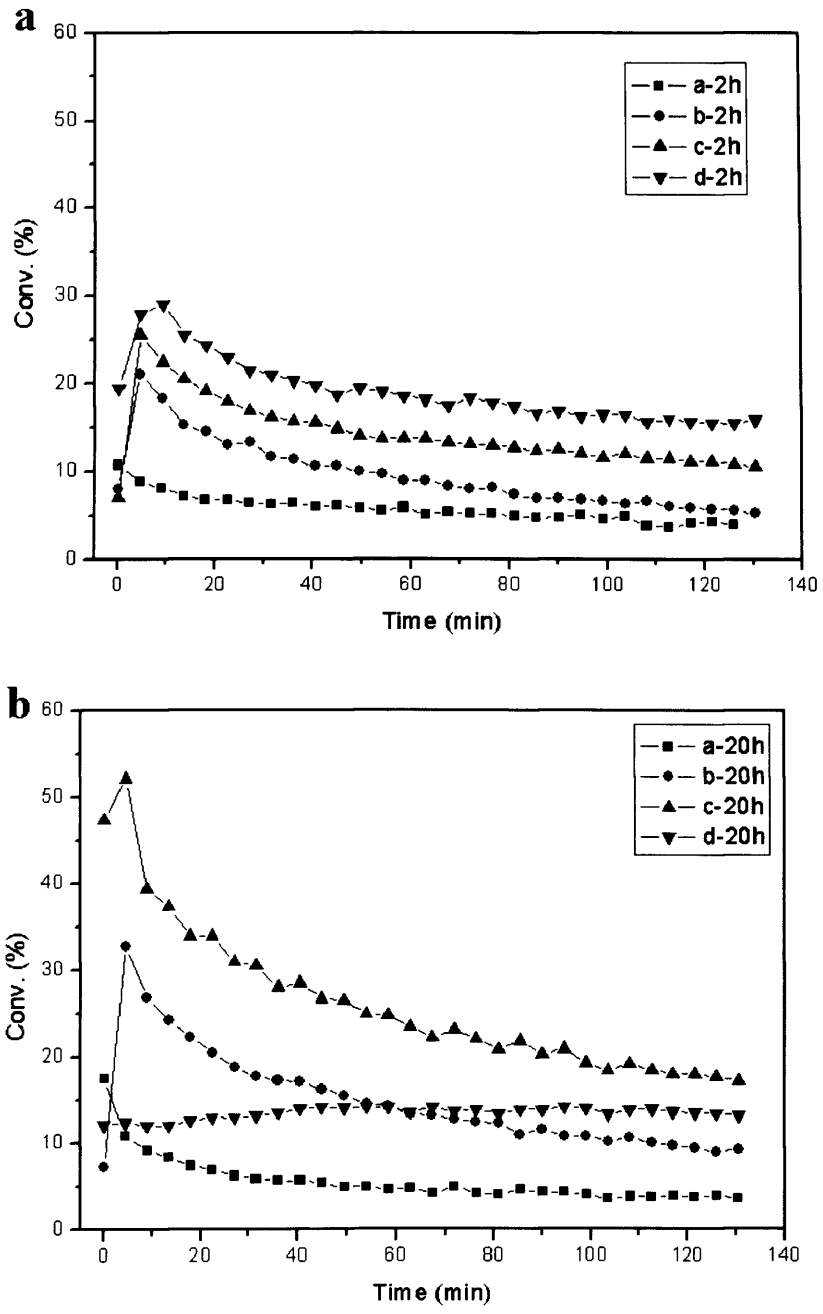

Figure 3.33 Catalytic performance of **(a)** the catalysts calcined from 300°C for 2h and **(b)** the catalysts calcined from 300°C for 20h: **a**: 0%H_2O-100%EtOH product; **b**: 5%H_2O-95%EtOH product ; **c**: 10% H_2O-90%EtOH product; **d**: 15%H_2O-85% EtOH product. Test conditions: 298K, 0.5% CO in synthetic air, 50mg catalyst, GHSV=17000h^{-1}.

To investigate the structure of as-prepared hopcalites in more detail, the XPS analysis were performed on the hopcalite derived from 5% H_2O_2-contained EtOH (i.e. Precursor **c** and Catalyst **c-20h**) and the results show in **Figure 3.34**. For the precursor, the Cu (2p) spectrum shows features characteristic of the presence of Cu^{2+}, in particular the composite satellite structure separated by *ca* 6-8 eV from the primary photoemission peak (**Figure 3.34a**). The corresponding C(1s) spectrum (**Figure 3.34b**) exhibits two components reflecting the two non-equivalent carbon atoms in the acetate species. After calcinations a new lower binding energy feature in the Cu (2p) spectrum, which is consistent with the formation of metallic Cu, is observed. However, a significant contribution from a Cu^{2+} phase remains.

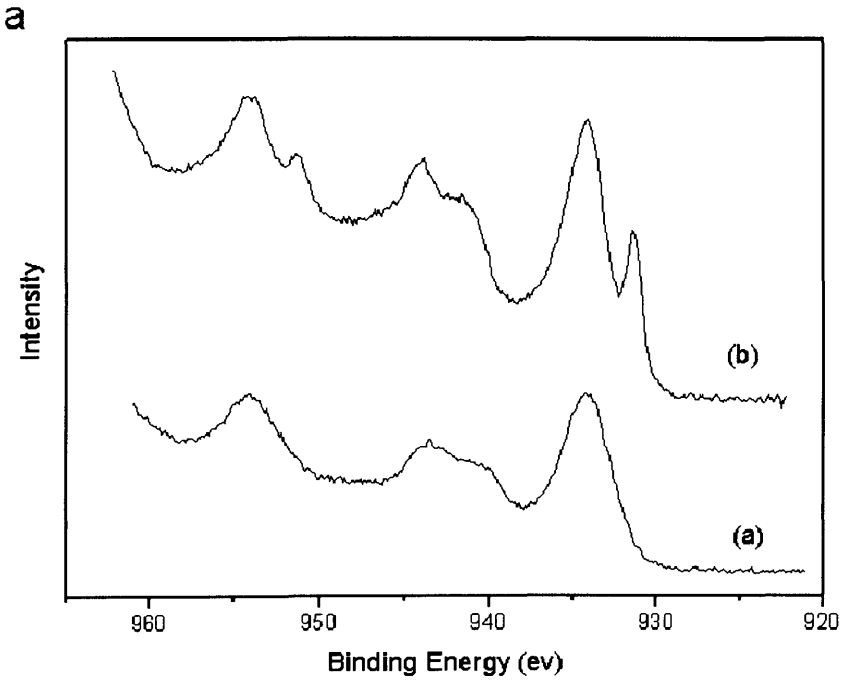

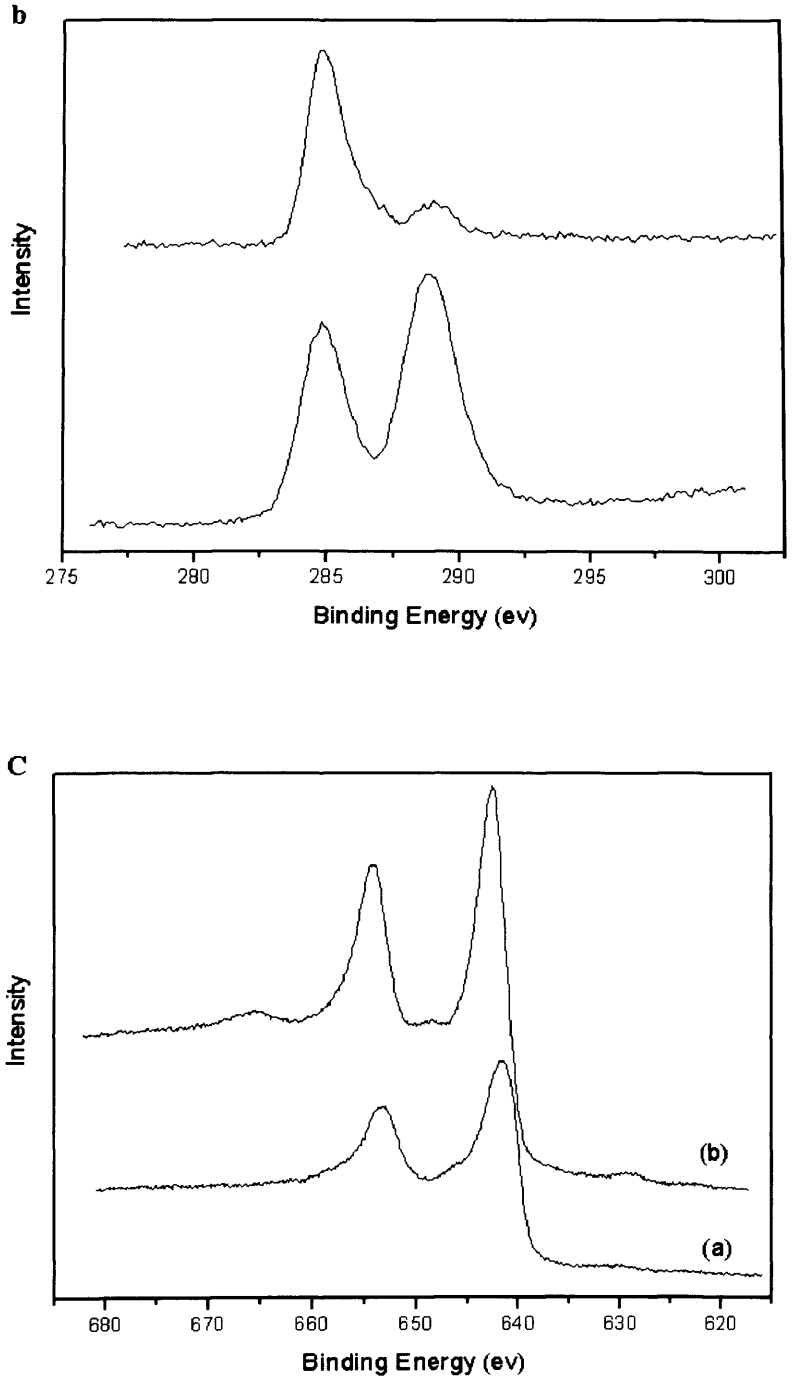

Figure 3.34 X-ray photoelectron spectra for (a) the precursor and (b) after calcination at 300 °C for 20h. **a**, Cu (2p) spectra; **b**, C(1s) spectra and **c**, Mn(2p) spectra.

3.4 Conclusions

A series of copper manganese oxides (hopcalites) have been prepared using supercritical CO_2 as an antisolvent and acetates as starting precursors. We have tried various solvents, such as DMSO, DMF, EtOH as well as some co-solvents, and explored these as-prepared catalysts systematically. The preliminary results show that hopcalites with high activity for CO oxidation have been obtained using this novel particle formation technique. Some primary conclusions are shown as follows.

(a) When using pure DMSO as a solvent, amorphous homogenous precursor mainly composed by acetates have been prepared. This precursor has a very high surface area up to *ca.* $300m^2/g$. The material has slightly aggregated quasi-spherical non-faceted particles of relatively uniform size and dimensions (10-20 nm with some particles as large as 50 nm). Following calcinations, the phase-separated nanocrystalline Cu/MnO_x has been produced. Although its surface area drops dramatically compared with that of the precursor, the preliminary catalytic data show the intrinsic activity for CO oxidation of the catalyst derived from this precursor is considerably higher than the conventional $CuMn_2O_4$ catalysts prepared by coprecipitation, and also currently available commercial catalysts.

(b) By using mixed solvents, such as water-ethanol, water-DMF and H_2O_2-ethanol, crystalline heterogeneous precursors have been produced. With the adding of more water or H_2O_2 to the precursor solution, there seems to be a reaction between the

metal acetates CO_2, and H_2O. Therefore, carbonates of the metals are precipitated instead of the acetate composition. Following calcinations, less crystalline or even amorphous final catalysts retain the high surface area and, furthermore, higher surface areas have been obtained when prolonging the calcination time. As a consequence, this leads a catalyst with higher catalytic activity in terms of surface area than that for the current commercial hopcalite catalysts prepared using standard procedures. In this point, the adding of water or H_2O_2 effectively enhances the catalytic performances of as-prepared hopcalite for CO oxidation reaction.

References and notes

1. S. B. Kanungo, *J. Catal.* 1979, **58**, 419.
2. S. Veprek, D. L. Cocke, S. Kehl and H. R. Oswald, *J. Catal.* 1986, **100**,250.
3. B. Gillot, S. Buguet and E. Kester, *J. Mater. Chem.* 1997, **7(12)**, 2513.
4. B. L. Yang, S. F. Chan, W. S. Chang and Y. Z, Chen, *J. Catal.* 1991, **130**, 52.
5. G J. Hutchings, A. A. Mirzaei, R. W. Joyner, M. R. H. Siddiqui and S. H. Taylor, *Catal. Lett.* 1996, **42**, 1.
6. G J. Hutchings, A. A. Mirzaei, R. W. Joyner,M. R. H. Siddiqui and S. H. Taylor, *Appl. Catal. A: General* 1998, **166**, 143.
7. A. A. Mirzaei, H. R. Shaterian, M. Habibi, G J. Hutchings and S. H. Taylor, *Appl. Catal. A: General* 2003,**253**,499.
8. http://www.defra.gov.uk/environment/water/quality/uwwtd/default.htm
9. R. P. Vignes, Dimethyl Sulfoxide (DMSO)-A "New" Clean, Unique, Superior Solvent. American Chemical Society, Annual Meeting, August 20-24, 2000
10. E. Reverchon, G D. Porta, D. Sannino, L. Lisi, P. Ciambelli, *Studies in Surface Science and Catalyst* 1998, **118**, 349.
11. E. Reverchon, G D. Porta, D. Sannino, P. Ciambelli, *Powder Technology* 1999, **102**, 127.
12. http://www.molecularproducts.com/products_detail.php?id=7
13. Conventional precipitated hopcalites were prepared by Christopher Jones in our groups. The preparation procedure is as follows: 0.25M copper nitrate and 0.5M manganese nitrate were premixed at 80°C and pumped into the precipitation

vessel using peristaltic pump. Precipitation was induced while stirring at 800rpm by the simultaneous addition of 2M sodium carbonate to the nitrate solution while maintaining the pH at 8.3 (+/- 0.1 unit). The mixture was left to age for 6h at 80 °C, after which the precipitates were filtered off and washed subsequently with warm distilled water to remove the remaining Na^+ ion. The resulting solid was dried at 110 °C overnight to give the catalyst precursor. The final hopcalite was obtained by calcination of the precursor at 415 °C for 2h.

14. Z. Ding, R. L. Frost and J. T. Kloprogge, *J. Mater. Sci. Lett.* 2002, **21**, 981.

15. V. Berbenni and A. Marini, *J. Anal. Appl. Pyrol.* 2001, **62**,45

16. S. Campestrini and U. Tonellato, *Adv. Synth. Catal.* 2001, **8**, 343.

17. W. M. Nelson and I. K. Puri, *Ind. Eng. Chem. Res.* 1997, **36**, 3446.

18. E. J. Beckman, *Green Chemistry* 2003, **5**, 332.

19. T. Gougousi, D. Barua, E. D. Young and G. N. Parsons, *Chem. Mater.* 2005, **17**, 5093.

Chapter 4

Preparation of Oxides as Support for Gold Catalysts

4.1 Introduction

Gold has proven to be a versatile catalyst when gold nanoparticles are appropriately supported on various metal oxides, such as TiO_2, CeO_2, Al_2O_3, and SiO_2 etc. To date, highly dispersed gold nanoparticles deposited on oxide supports have exhibited excellent catalytic activity in various important catalytic reactions, for example, CO oxidation[1,2], epoxidation of propene[3], selective oxidations of alkenes and cyclohexane[4,5] and the purification of hydrogen in fuel cells[6,7].

So far, although the mechanism of the catalytic activity of gold nanoparticles is still the subject of debate, a number of publications have clearly shown that the nature of the oxide support is one of the key factors affecting the activity and stability of supported gold catalysts[8-13]. For instance, Corma and co-workers demonstrated that nanocrystalline oxide supports (CeO_2 and Y_2O_3) increase the activity of gold catalysts for CO oxidation in comparison with the regular CeO_2 and Y_2O_3 supports[11,12]. Particularly, when gold is dispersed on nanocrystalline CeO_2, an increase of two orders of magnitude in catalytic activity for CO oxidation has been achieved

compared to the Au/CeO_2 prepared by Au deposition on regular cerium oxide support. More recently, Yan *et al.* reported a significant improvement of the stability of gold nanoparticles against sintering due to the use of a novel modified TiO_2 support[13]. Their study showed that gold nanoparticles can resist sintering to form large particles after calcination at 500°C when using TiO_2 (P25) modified with amorphous aluminum-oxide surface layers as a support, and also its catalytic activity was not affected. In contrast, Au nanoparticles supported on the surface-unmodified P25 exhibited significant sintering and large deactivation was also observed following calcination. Therefore, to achieve the high activity of gold, it is of great importance to synthesize the oxide support with unique surface properties *via* effective preparation procedures.

Supercritical CO_2 antisolvent precipitation has been successfully used recently in the novel preparation of nanoparticles. In this chapter, the preparation of a series of nanoscaled oxide supports for gold catalyst, such as CeO_2, TiO_2 and ZnO, has been investigated. We find that the support obtained from the supercritical process can greatly enhance the catalytic activity of gold nanoparticles for CO oxidation at ambient temperature. In addition, different parameters (such as T, P) in supercritical precipitation have been manipulated to control the particle size and morphology of the as-prepared products.

4.2. Experimental

4.2.1 Materials

All the materials are used as supplied. **Table 4.1** lists all these materials including solvents, metal salts and CO_2 gas.

Table 4.1 Specification of materials used in the preparation of gold catalysts

Materials	Grade	Company
CO_2	SFC, 99.99%	BOC
cerium acetylacetonate	ACS reagent, ≥98%	Sigma-Aldrich
titanium oxide acetylacetonate	≥99%	Aldrich
zinc acetate	ACS reagent, ≥98%	Sigma-Aldrich
dimethyl sulfoxide(DMSO)	≥99.6%	Aldrich
methanol (MeOH)	HPLC Grade	Fisher
chloroauric acid($HAuCl_4$)	ACS reagent, ≥49% as Au	Aldrich
Sodium hydroxide	ACS reagent, ≥97.0%	Aldrich
Sodium carbonate	≥99.5%, ACS reagent	Sigma-Aldrich
Hydrochloric acid	reagent grade, 37%	Fisher
Au/Fe_2O_3	5%wt	World Gold Council

4.2.2 Catalyst preparation

4.2.2.1 Preparation of oxide supports

Cerium acetylacetonate and titanium oxide acetylacetonate have been used to produce CeO_2 and TiO_2 precursors in this supercritical antisolvent process. They are two kinds of coordination compounds bearing a positive cerium or titanium ion in the centre and 2 or 3 acetylacetone (acac) ligands coordinated to the cerium ion. The molecular structures are shown in **Figure 4.1**.

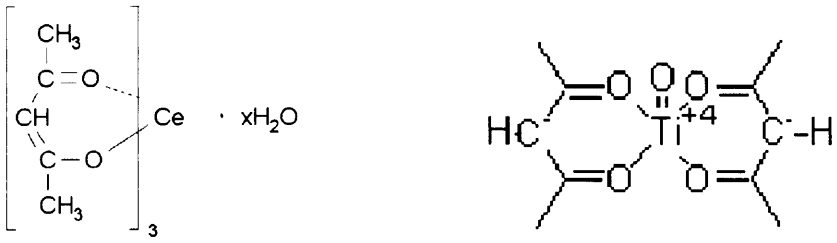

Figure 4.1 Molecular structures of cerium acetylacetonate and titanium oxide acetylacetonate

The solubility of $Ce(acac)_3$ and $TiO(acac)_2$ in different solvents, such as DMSO, DMF, water, methanol and THF, has been tested. The result shows that these two acetylacetonate salts only are soluble in methanol. Therefore, methanol was chosen as a starting solvent for $Ce(acac)_3$ and $TiO(acac)_2$ in supercritical antisolvent process. Since some insoluble complexes appeared after the cerium salt was dissolved in methanol, the methanol solution of $Ce(acac)_3$ was stirred for 24h and then used by filtration.

With respect to the solution of $TiO(acac)_2$ in methanol, it was used directly when all the solids were dissolved because $TiO(acac)_2$ can be completely dissolved in the solvent of methanol.

For the production of ZnO precursors, zinc acetate was used as the starting metal salt and DMSO was used as solvent based on reports in the literature work [14].

The synthesis of precursors was carried out using the methodology described in **Chapter 2**. Solutions of acetylacetonate or acetate in solvents were pumped into the system and mixed with supercritical CO_2 at a fixed temperature and pressure. Precursors were collected from the precipitated vessel and the rough yield calculated is about 60%. These precursors were calcined at 400 °C for 2 h in static air so as to form the oxide supports. To investigate the influence of different precipitation environments, we have explored different pressures from 110 to 150 bar and temperatures from 40 to 60 °C on the precipitation of CeO_2 precursor. As a comparison, untreated oxides were produced by the direct calcination of as-received metal acetylacetonate or metal acetate under the same conditions. **Scheme 4.1** shows the detailed preparation procedures of $scCeO_2$, $scTiO_2$ and scZnO.

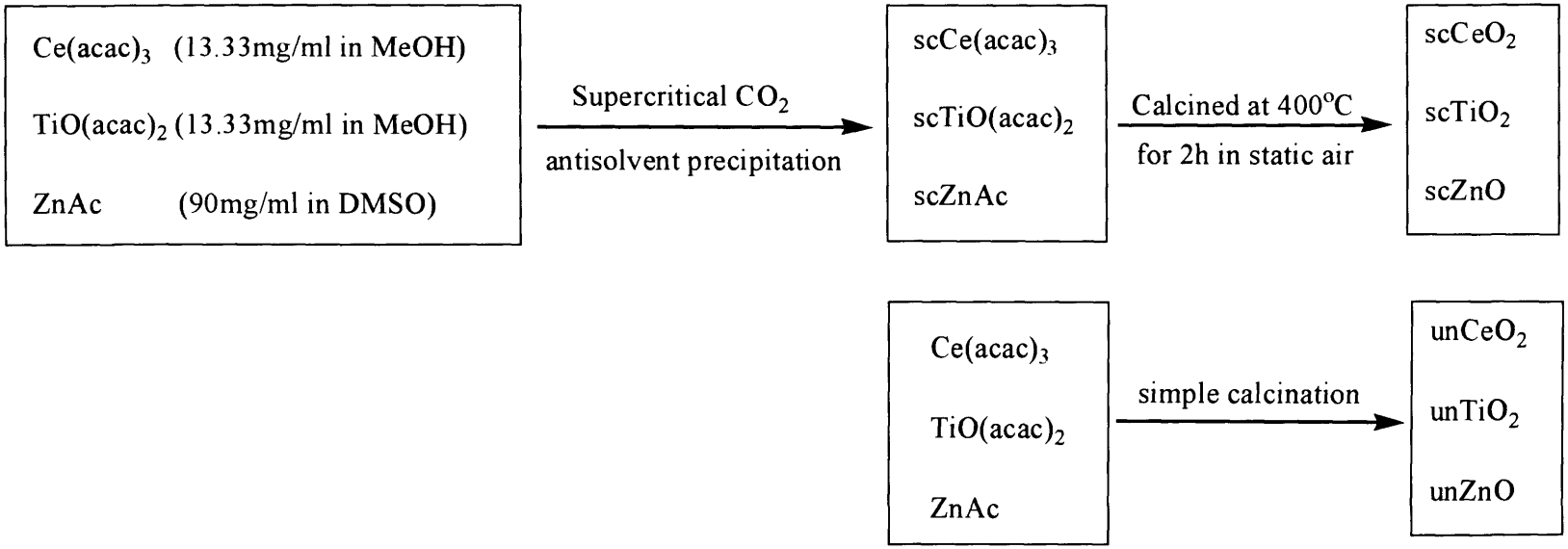

"sc" denotes products which are prepared from supercritical antisolvent precipitation
"un" denotes products which are obtained from simple calcination

Scheme 4.1 Detailed preparation process of oxide supports using supercritical antisolvent precipitation

4.2.2.2 Preparation of gold catalysts

Gold was deposited on the surfaces of oxide supports by the following deposition-precipitation procedures:

(1) Gold/CeO_2

Gold was deposited on $scCeO_2$ and $unCeO_2$ using the following procedure: A solution of $HAuCl_4$ (28mg) in distilled water was adjusted to pH 10 by the addition of 0.2M NaOH. When the pH value was stable, it was added into a slurry containing CeO_2 (200mg) in water (10ml). After adjusting the slurry to pH 10 with 0.2M NaOH, it was stirred for 20h. The solid was then collected by filtration and washed and dried overnight at 373K.

(2) Gold/TiO_2

Gold was deposited on $scTiO_2$, $unTiO_2$, P25 and commercial anatase TiO_2 by the following procedure: A slurry containing TiO_2 (250mg) in distilled water (10ml) was adjusted to pH 2~3 by diluted HCl. When the pH value was stable, a solution of $HAuCl_4$ (30mg) in distilled water (5ml) was added. The pH value was then adjusted to 10 using 2M $NaCO_3$ solution. After that, the slurry was stirred for 20h at room temperature. The solid was then collected by filtration and washed, and dried overnight at 373K.

(3) Gold/ZnO

Gold was deposited on scZnO and unZnO by the following procedure: A slurry containing ZnO (250mg) in distilled water (15ml) was stirred and heated to 80°C. After a solution of H_4AuCl_4 (30mg) in distilled water (5ml) was added, the pH value was then adjusted to 10 using 2M $NaCO_3$ solution. The solution was stirred at 80°C for 1h. The solid was then collected by filtration and washed and dried overnight at 373K.

All the materials, including precursors, supports and gold catalysts were characterized by the analysis of XRD, SEM, BET surface area measurement, and in selected cases, by TEM and XPS. The catalytic performances of these as-prepared gold catalysts were tested for CO oxidation at ambient temperature.

4.2.2.3 Catalyst Testing

(1) CO oxidation

The catalysts were tested for CO oxidation using a fixed-bed laboratory microreactor (3mm id), operated at atmospheric pressure. Typically CO (0.5% CO in synthetic air) was fed to the reactor at a controlled rate of 22.5 ml min^{-1} using mass flow controllers, and passed over the catalyst (15mg for gold/CeO_2 and 50mg for other gold catalysts). The catalyst temperature was maintained at 25 °C by immersing the quartz bed in a thermostatically controlled water bath. The products were analyzed using on-line gas chromatography.

(2) Synthesis of H_2O_2 [15]

Hydrogen peroxide synthesis was performed using a Parr Instruments stainless steel autoclave with a nominal volume of 50 ml and a maximum working pressure of 14 MPa. The autoclave was equipped with an overhead stirrer (0 – 2000 rpm) and had provision for measurement of temperature and pressure. Typically, the autoclave was charged with catalyst (0.05 g unless otherwise stated) and solvent (5.6 g MeOH and 2.9 g H_2O) and purged three times with CO_2 (3 MPa). It was then filled with 5% H_2/CO_2 and 25% O_2/CO_2 to give a hydrogen to oxygen ratio of 1 : 2, at a total pressure of 3.7 MPa at 2 °C. Stirring (1200 rpm unless otherwise stated) was started on reaching the desired temperature, and experiments were run for 30 min unless otherwise stated. H_2O_2 yield was determined by titration of aliquots of the final

filtered solution with acidified $Ce(SO_4)_2$ (7×10^{-3} mol/l). $Ce(SO_4)_2$ solutions were standardized against $(NH_4)_2Fe(SO_4)_2.6H_2O$ using ferroin as indicator.

(3) Alcohol oxidation [16]

Alcohol oxidation was carried out in a 100 ml scale batch stirred reactor (Autoclave Engineers Inline MagneDrive III). The vessel was charged with alcohol (40 ml) and catalyst. The autoclave was then purged 5 times with oxygen leaving the vessel at the desired pressure. The pressure was maintained constant throughout the experiment; as the oxygen was consumed in the reaction it was replenished. The stirrer speed was set at 1500 r.p.m. and the reaction mixture was raised to the required temperature. Samples from the reactor were taken periodically *via* a sampling pipe, ensuring that the volume purged before sampling was higher than the tube volume, and analysed by GC using a DB-Wax column.

4.3. Results and discussion

4.3.1 Gold on CeO_2 support

4.3.1.1 Precursors and supports

Initially, the precursor that was used to generate the support CeO_2 was synthesized by supercritical antisolvent precipitation process. Light brown $Ce(acac)_3$ was obtained from supercritical antisolvent precipitation and calcinations in static air at 400 °C gave light yellow CeO_2 powder. **Table 4.2** lists the detailed results on the preparation conditions of the as-prepared precursors and the corresponding final ceria oxides as well as their BET surface areas. Based on these results, it is interesting to find the following:

(a) The surface areas of precursors prepared from supercritical process are not as high as our previous copper manganese precursors shown in **Chapter 3**. In addition, they vary with the density of supercritical CO_2. The surface areas decrease with the increase of temperature and pressure in the supercritical process. However, the three supercritical precursors still have the larger surface areas than the as-received $Ce(acac)_3$, which only has $4m^2/g$.

(b) Following the calcinations, all the final CeO_2 show an enhancement of surface areas. The surface area of unCeO_2 increases dramatically to $115m^2/g$, which is, most likely, related to the possible presence of a large amount porous structure on the support after calcinations.

Table 4.2 – Detailed information of precursors, ceria supports and the corresponding gold catalysts

Sample	Preparation conditions	BET surface area (m^2/g)
$Ce(acac)_3$	Used as received	4
$unCeO_2$	Direct calcination of $Ce(acac)_3$ at 400 °C	115
$scCe(acac)_3$-1	SAS process (110 bar,40 °C)	31
$scCeO_2$-1	Calcination of $scCe(acac)_3$-1 at 400 °C	34
$scCe(acac)_3$-2	SAS process (150 bar,40 °C)	25
$scCeO_2$-2	Calcination of $scCe(acac)_3$-2 at 400 °C	31
$scCe(acac)_3$-3	SAS process (110 bar,60 °C)	10
$scCeO_2$-3	Calcination of $scCe(acac)_3$-2 at 400 °C	33

X-ray diffraction patterns of $scCe(acac)_3$, and $scCeO_2$ are shown in **Figure 4.2a-c**. It has been found the precursors precipitated from the supercritical process are largely amorphous, in contrast with the crystalline $Ce(acac)_3$ before supercritical processing. Following calcination, the XRD patterns of $scCeO_2$ and $unCeO_2$ (**Figure 4.2b**) are exactly the same and fully consistent with the characteristic diffraction pattern of cubic CeO_2 with fluorite structure.

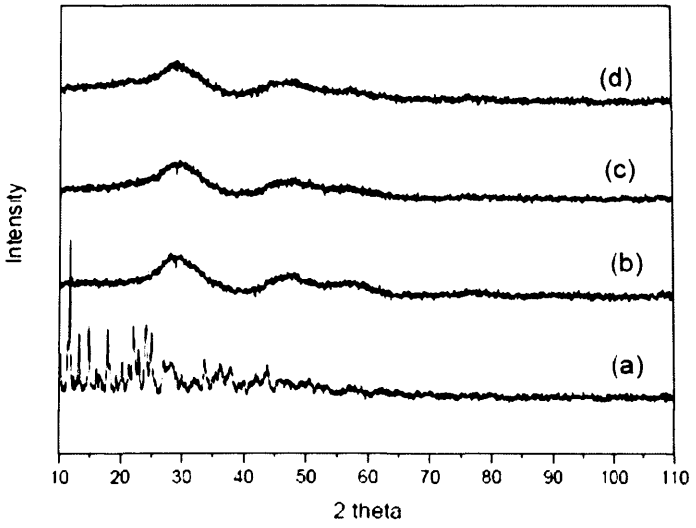

Figure 4.2a XRD patterns of (a) $Ce(acac)_3$, (b) $scCe(acac)_3$-1, (c) $scCe(acac)_3$-2 and (d) $scCe(acac)_3$-3

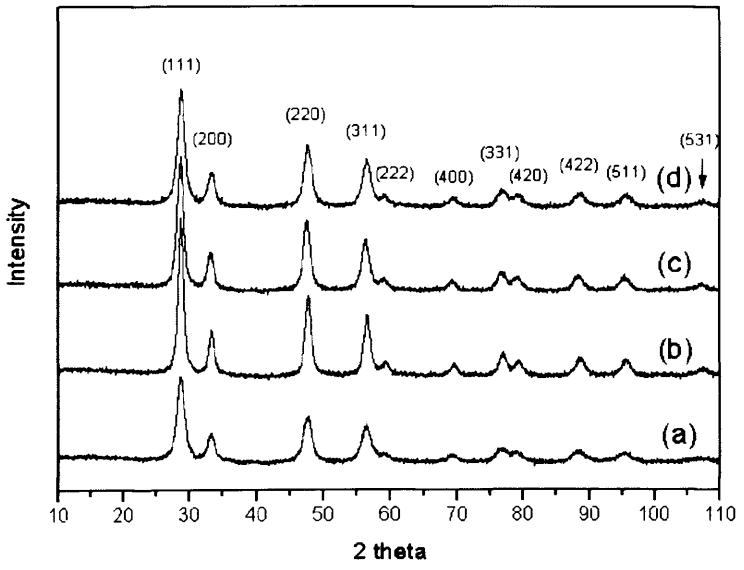

Figure 4.2b XRD patterns of (a) $unCeO_2$, (b) $scCeO_2$-1, (c) $scCeO_2$-2 and (d) $scCeO_3$-3

The SEM images of precursors and as-calcined oxides are shown in **Figure 4.3-5**. From the images of precursors, we found that the individual particles precipitated at 110 bar and 40 °C have spherical shapes with slight degree of aggregation and the average particle size is around 100 nm (**Figure 4.3a**). When the pressure is increased to 150 bar, the material has more uniform particles of around 100nm, and the particle size distribution is narrower than scCe(acac)$_3$-1(**Figure 4.4a**). However, as the temperature is increased to 60 °C, the particle size distribution becomes broader, with small particles of 50nm and larger particles up to 250nm being observed (**Figure 4.5a**).

Following calcination, the SEM images of scCeO$_2$ (**Figure 4.3a-5a**) show the particles are still in spherical shape but aggregate with each other greatly. The particle sizes appear to decrease slightly, compared to the precursors, with small particles of 30-40nm observed. This overall particle size reduction is, most likely, due to the loss of carbonaceous matter during the calcination process.

As a comparison, the SEM images of commercial Ce(acac)$_3$ and its oxide-unCeO2 are shown in **Figure 4.6**. Cerium acetylacetonate without supercritical treatment is a kind of bulk crystalline material with regular shape. After calcination, unCeO$_2$ was obtained. In particular, numerous pores can be easily detected on the surface, which is consistent with the above-mentioned remarkable increase of its surface area after calcination.

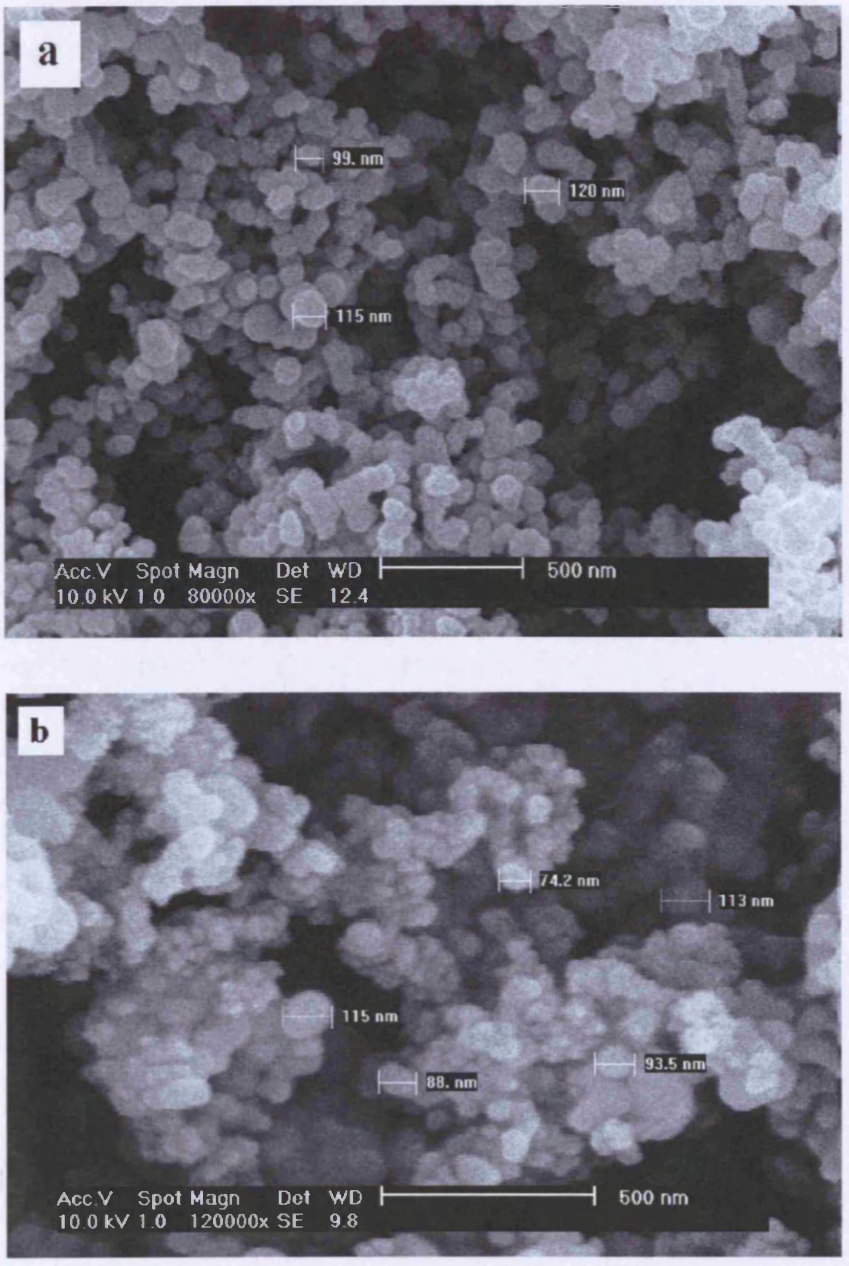

Figure 4.3 SEM images of (a) scCe(acac)$_3$-1 and (b) scCeO$_2$-1

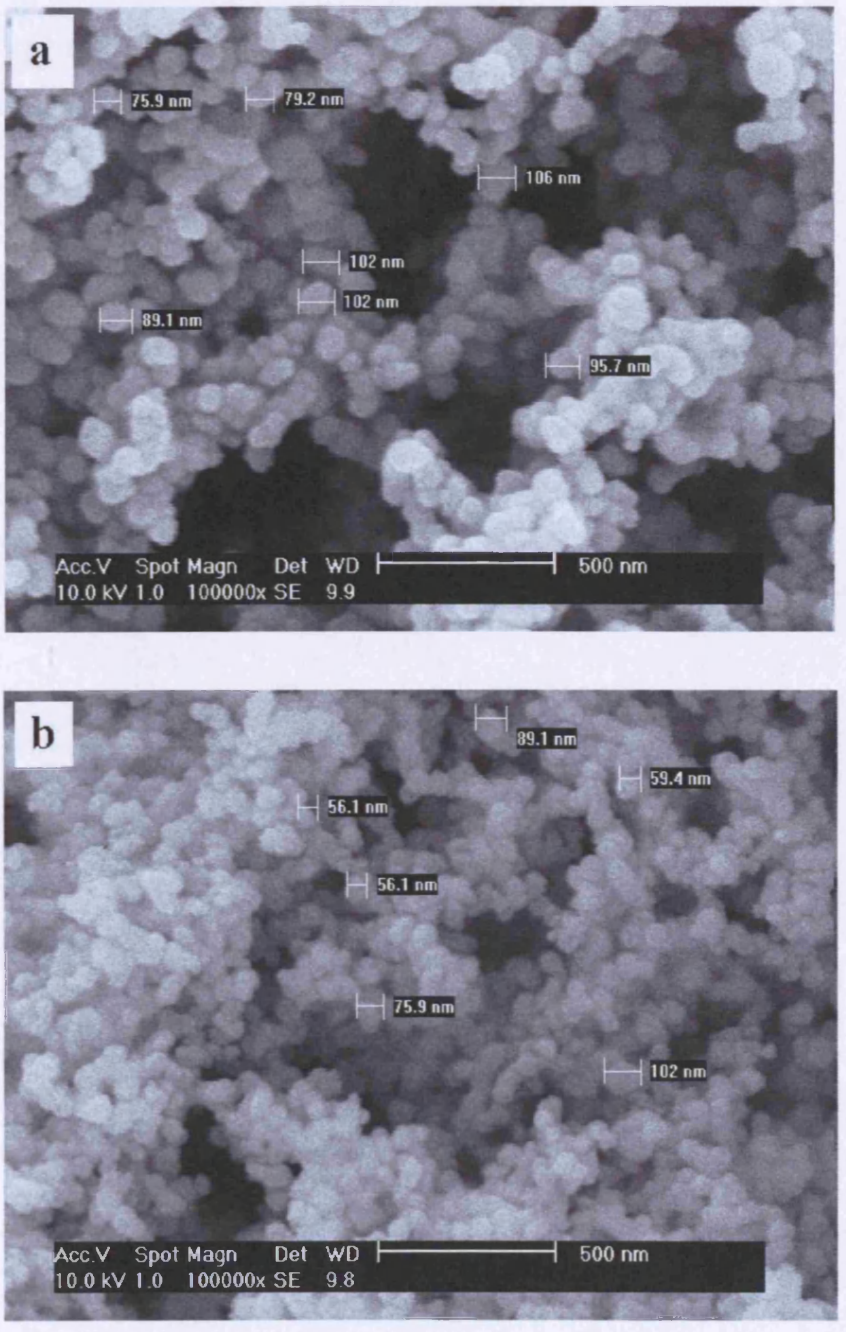

Figure 4.4 SEM images of (a) $scCe(acac)_3$-2 and (b) $scCeO_2$-2

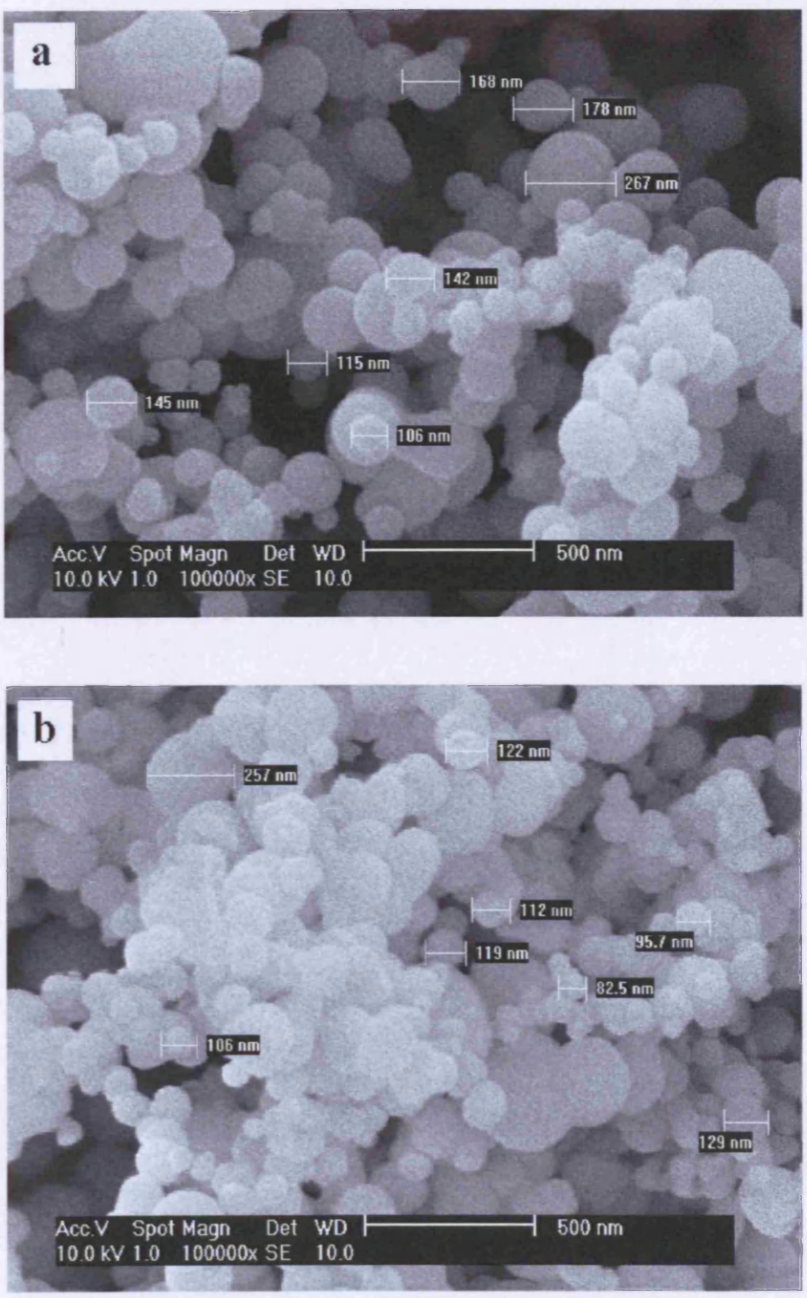

Figure 4.5 SEM images of (a) $scCe(acac)_3$-3 and (b) $scCeO_2$-3

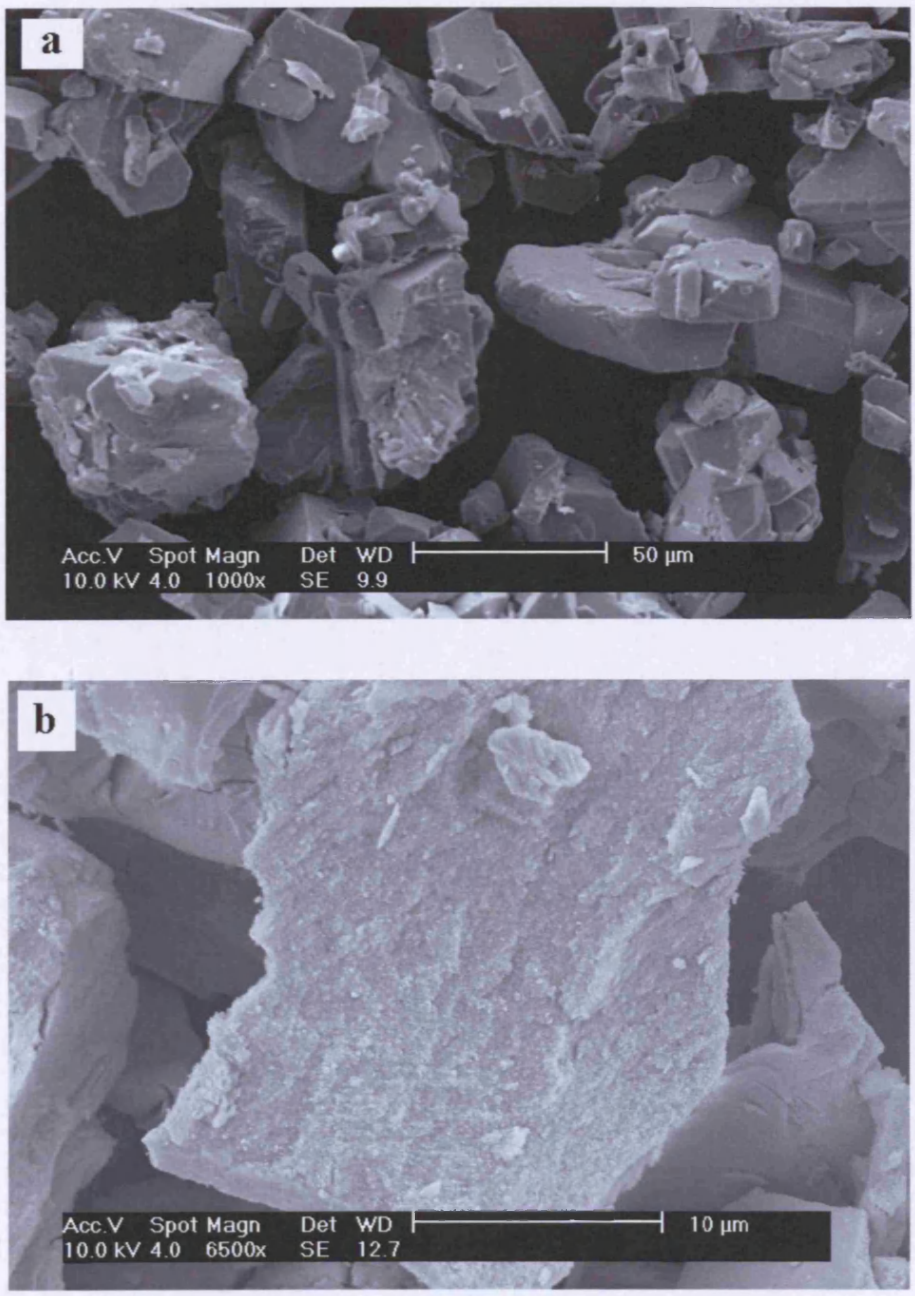

Figure 4.6 SEM images of (a) commercial $Ce(acac)_3$ and (b) $unCeO_2$

To further investigate the microscopic morphologies of as-prepared precursor and as-calcined oxides, TEM analysis was performed on these samples. The TEM images of $scCe(acac)_3$-2, untreated $Ce(acac)_3$ as well as $scCeO_2$-2 are shown in **Figure 4.7-9**. From the result, $scCe(acac)_3$-2 consists of disordered and amorphous sphere-like structures (see **Figure 4.7**). Meanwhile, the particles with unsmooth surface aggregate heavily and even no individual particles can be observed. This is very different from its starting material without supercritical treatment as is shown in **Figure 4.8**.

Upon calcination at 400°C, each sphere crystallizes to form a pseudo-spherical agglomerate of CeO_2 nanocrystals (**Figure 4.9**), and there is some tendency for neighbouring spheres to sinter and form bridging "necks". It is also interesting to note that there is a noticeable drop in contrast in the central region of each sphere which suggests that it may be hollow. This was subsequently confirmed using STEM-ADF imaging and XEDS mapping. As shown in the ADF image in **Figure 4.10**, the contrast change from the perimeter to the center of the sphere is quite large and clearly suggests the presence of a central pore within the spherical agglomerate. Similarly, the XEDS maps of the Ce-L_α and O-K_α signals, shown in **Figure 4.10(b)** and **(c)** respectively, show that far less of the signal of each element is generated from the central region of the particle. This hollow sphere morphology is most likely due to the increase in density that occurs upon crystallization from the initial amorphous uncalcined precursor to the more efficiently packed (i.e denser) polycrystalline form in the calcined catalyst. Since the outer diameter of the spheres is approximately the same size both before and after calcination, densification from the outside inwards

would result in the formation of a pore within the sphere interior.

Similar morphologies were observed for all the other supercritically treated samples. The major structure difference between the CeO_2 support materials treated under differing supercritical conditions of pressure or temperature was found to be in the size distribution of the polycrystalline spheres resulted after calcination.

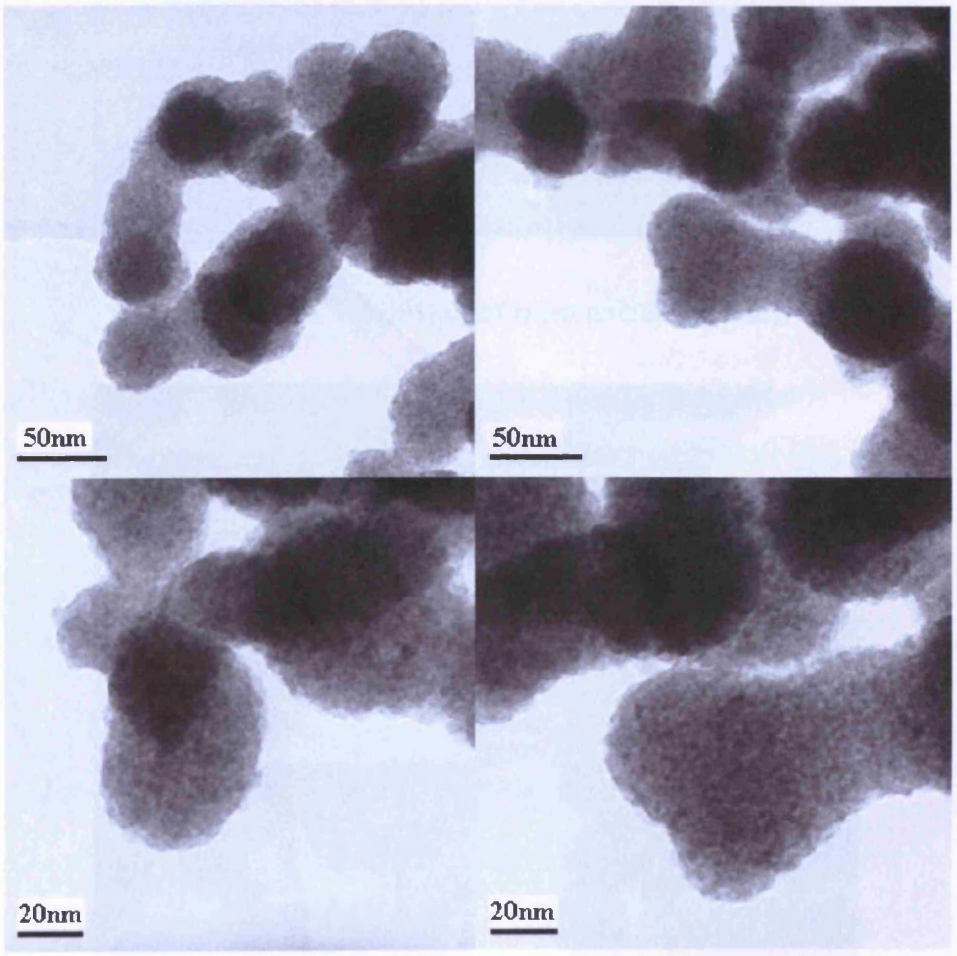

Figure 4.7 TEM images of $scCe(acac)_3$-2

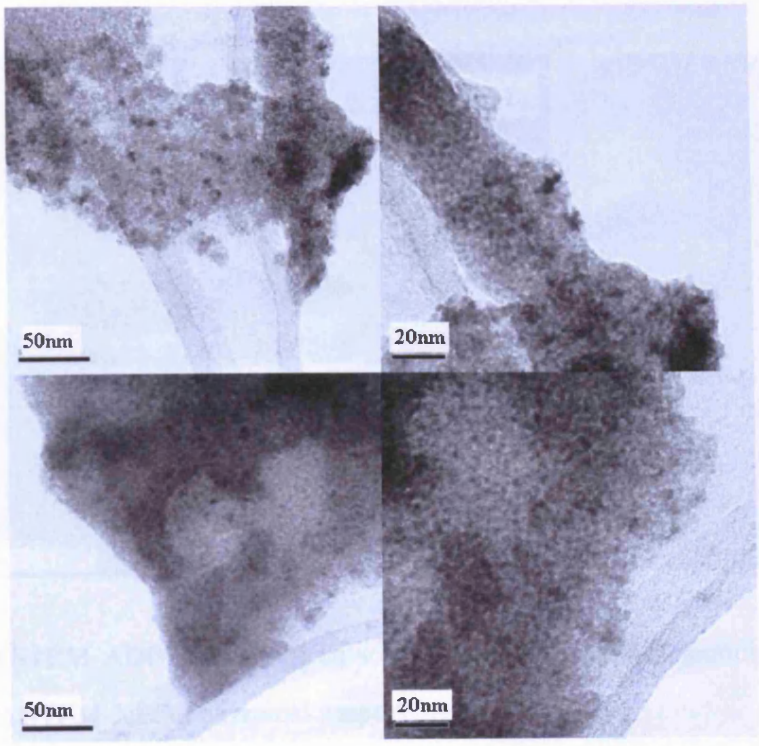

Figure 4.8 TEM images of commercial $Ce(acac)_3$

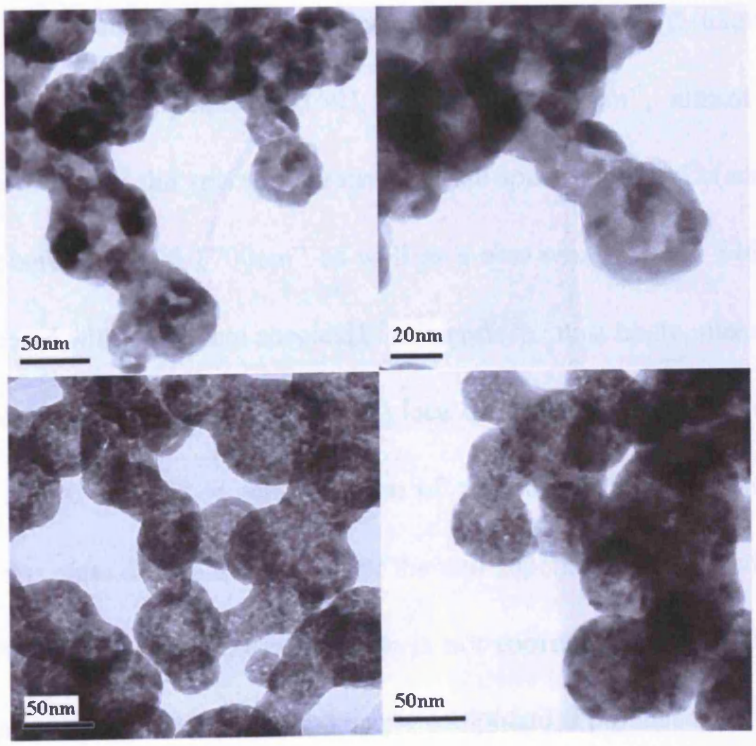

Figure 4.9 TEM images of $scCeO_2$-2

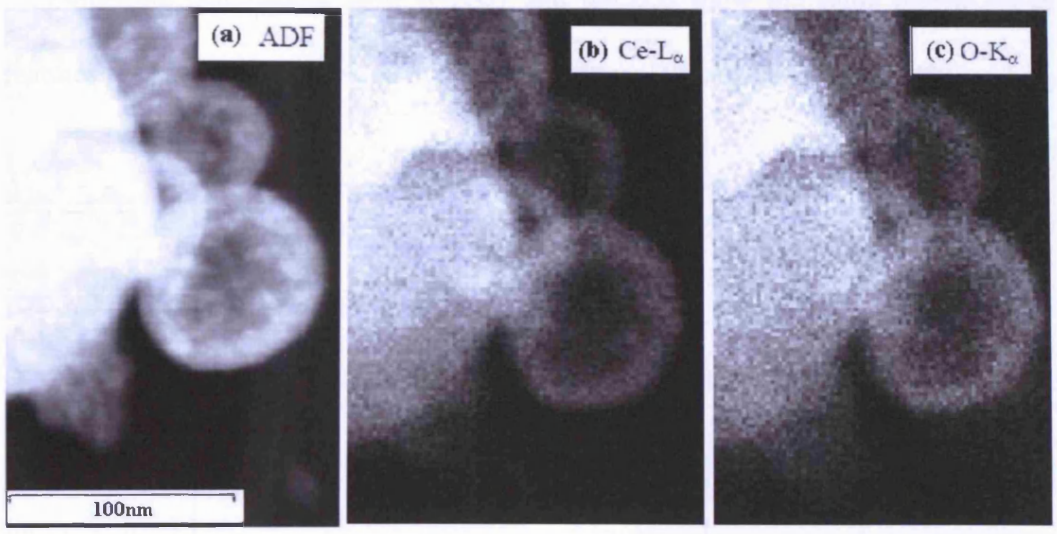

Figure 4.10 STEM-ADF micrograph of $scCeO_2$-2(a) and the corresponding Ce-L_α (b) and O-K_α (c) STEM-XEDS chemical maps.

The FT-IR spectra of commercial $Ce(acac)_3$ and $scCe(acac)_3$-2 are exhibited in **Figure 4.11**. After supercritical treatment, the typical bands of β-diketones of this cerium salt, with main peaks at 1603, 1515 and 1391cm^{-1}, almost completely disappear according to the spectra. Meanwhile, the spectrum of $scCe(acac)_2$ exhibits broad bands between 1200-1700cm^{-1} as well as a new weak band at 846cm^{-1}, which are all associated with carbonate species[17]. Therefore, most likely, major carbonates dominate the supercritical cerium salts in place of acetylacetonates. In addition, the broad peak at 500-700cm^{-1} in the spectrum of $scCe(acac)_3$ indicates Ce-O bonding and this bond is quite different from that of the non-supercritically treated cerium salt. This gives further evidence that cerium ion is not coordinated with β-diketones any more after the supercritical process and a new compound is produced.

Following calcination, both $scCeO_2$ and $unCeO_2$ show the same typical oxide features [18] as clearly reflected in their comparative IR spectra (**Figure 4.12**).

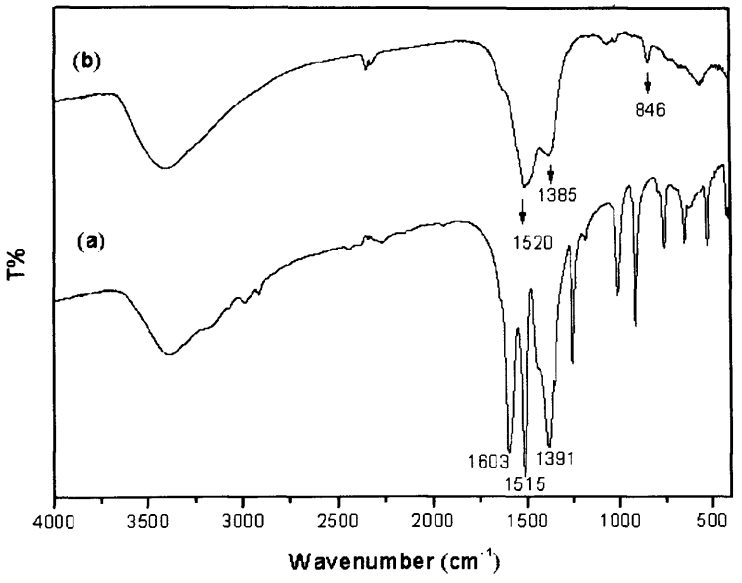

Figure 4.11 FT-IR spectra of (a) $Ce(acac)_3$ and (b) $scCe(acac)_3$

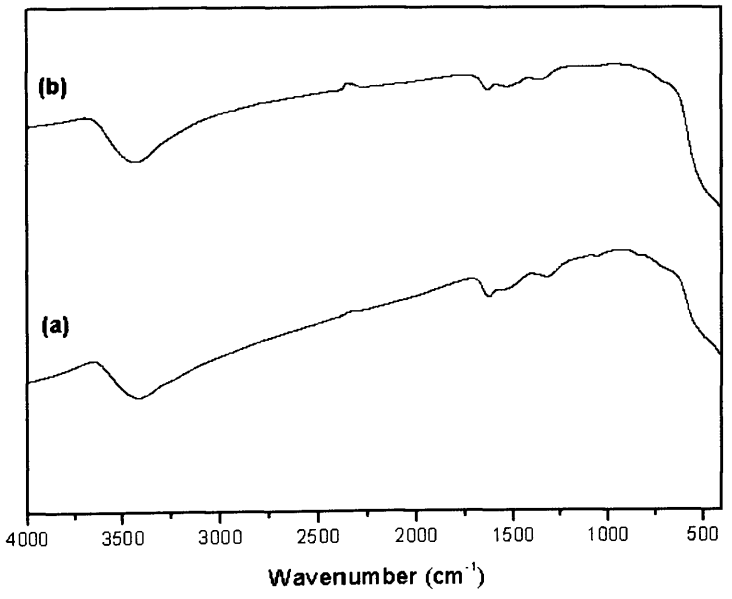

Figure 4.12 FT-IR spectra of (a) $unCeO_2$ and (b) $scCeO_2$

To further determine the composition of as-prepared precursors derived from the supercritical process, Raman analysis was performed on these as-prepared precursors and the result is shown in **Figure 4.13**. Following the supercritical process, the typical bands of cerium salts almost completely disappear which reflects the change of composition before and after supercritical treatment. However, some small peaks can still be detected in the range of 200-2000cm^{-1}. The inset picture in **Figure 4.13** shows this enlarged spectrum. In this spectrum, the broad peak appearing at 1200-1700cm^{-1} can be attributed to carbonates. Surprisingly, a sharp peak at 464cm^{-1} appears, and it is the typical band of CeO_2 [19-20]. It means a minor amount of CeO_2 was produced directly from the supercritical antisolvent process.

Following calcination, the Raman spectra show that complete cerium oxides have been obtained from both commercial $Ce(acac)_3$ and $scCe(acac)_3$ as shown in **Figure 4.14**.

TGA analysis was performed on the as-prepared precursors and the commercial cerium salts. The results further confirm the change of composition before and after the supercritical process. For commercial $Ce(acac)_3$, around 50% weight loss can be seen, while 70% weight loss is observed on the supercritically treated cerium salts. The former indicates the decomposition of $Ce(acac)_3$, while the latter approximately conforms to the decomposition of carbonates.

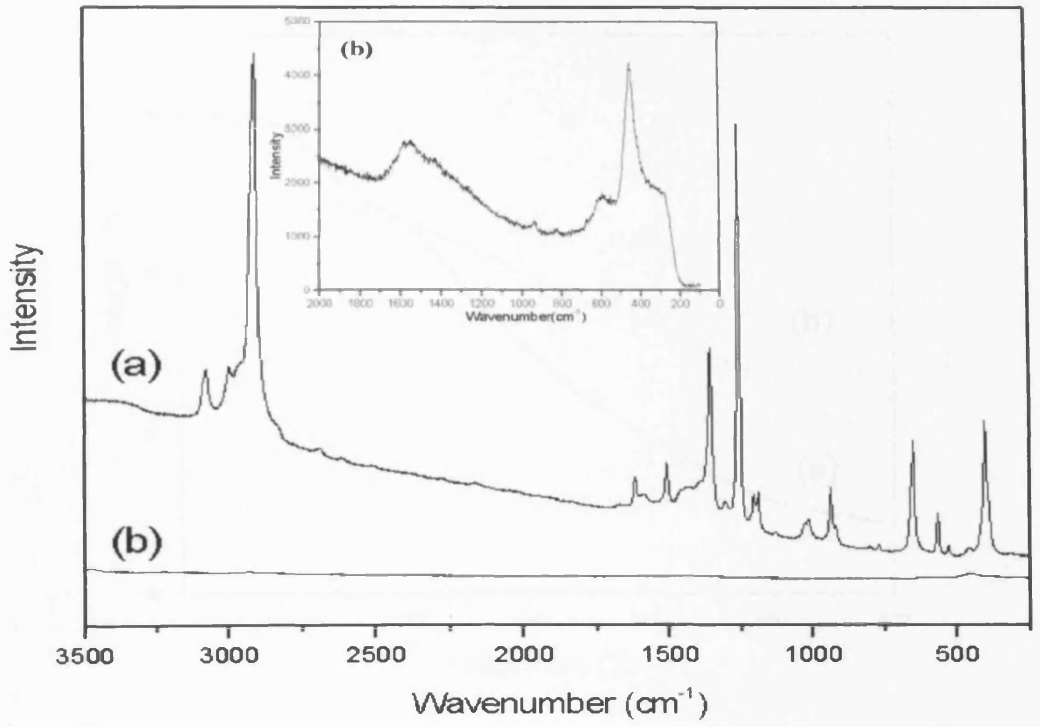

Figure 4.13 Raman spectra of (a) $Ce(acac)_3$ and (b) $scCe(acac)_3$

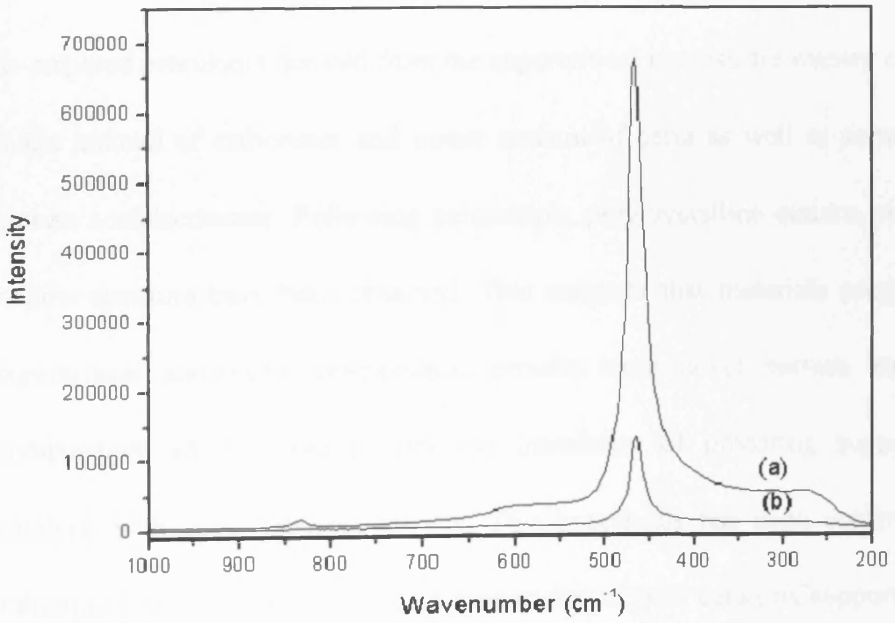

Figure 4.14 Raman spectra of (a) $unCeO_2$ and (b) $scCeO_2$

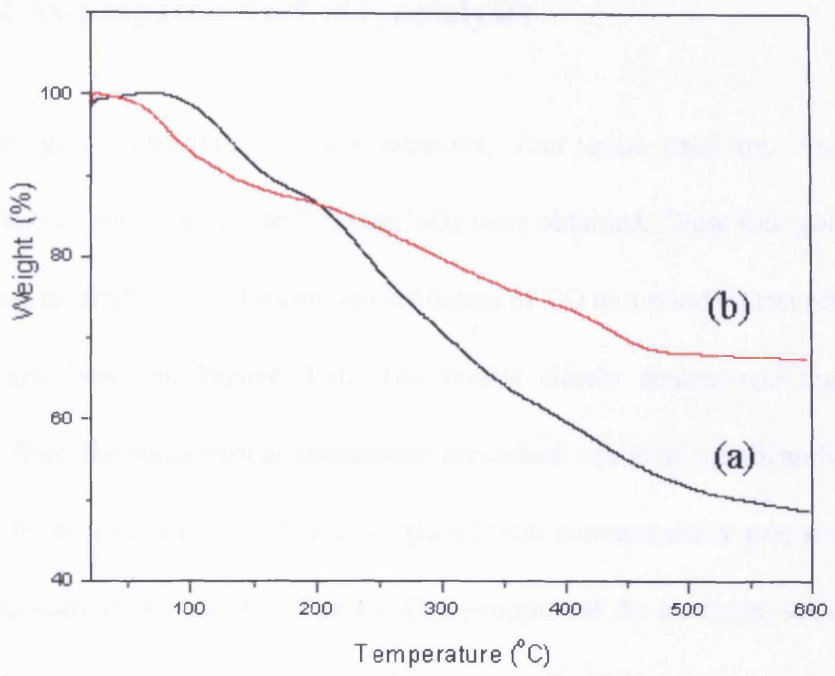

Figure 4.15 TGA analysis of (a) unCe(acac)$_3$ and (b) scCe(acac)$_3$

Based on all the above-mentioned characterizations, it may be concluded that the as-prepared precursors derived from the supercritical process are mainly composed of major amount of carbonates and minor amount of ceria as well as some remaining cerium acetylacetonate. Following calcination, polycrystalline cerium oxides with a hollow structure have been obtained. This suggests that materials prepared by the supercritical antisolvent precipitation process have novel surface structure and composition, which could provide the possibility of preparing supported metal catalysts with good catalytic activity. This hypothesis has been confirmed in our subsequent experiments focusing on preparation of gold catalysts supported on these materials prepared by the supercritical process and testing of their catalytic activity for typically important reactions in the fine chemical industry.

4.3.1.2 As-prepared Au/CeO_2 catalysts

After gold deposition on the supports, four gold catalysts, $Au/scCeO_2$-1, $Au/scCeO_2$-2, $Au/scCeO_2$-3 and $Au/unCeO_2$ were obtained. These four gold catalysts were used as catalysts for the ambient oxidation of CO as a standard test reaction. The results are shown in **Figure 4.16**. The results clearly demonstrate that catalysts derived from the supercritical antisolvent procedure can give significantly enhanced activity by at least a factor of two compared with conventionally prepared Au/ceria materials such as $Au/unCeO_2$. For the CeO_2-supported Au catalysts, $scCeO_2$-2 gave the highest activity and the order of reactivity for CO oxidation is $scCeO_2$-2 > $scCeO_2$-3 > $scCeO_2$-1 > $unCeO_2$.

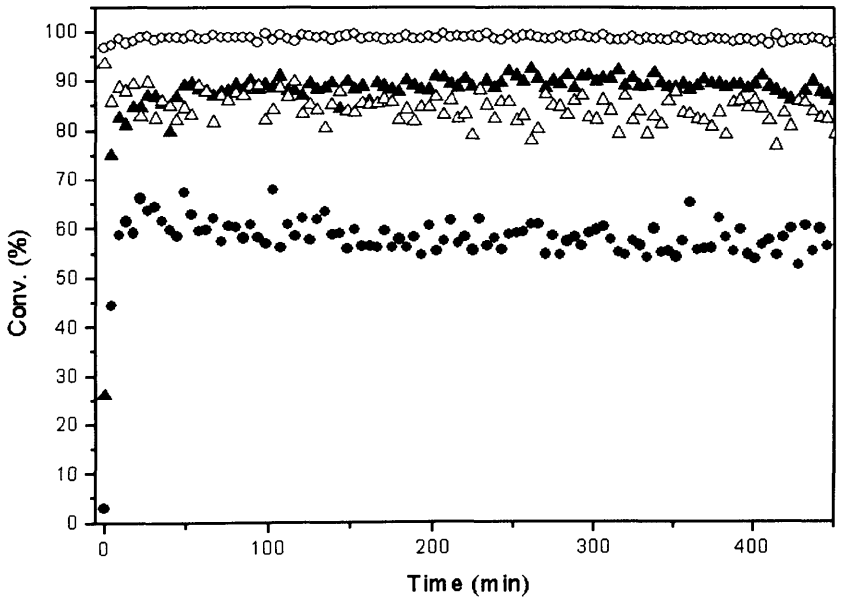

Figure 4.16 Catalytic activities for ambient CO oxidation: $Au/unCeO_2$ (●), $Au/scCeO_2$-1 (△), $Au/scCeO_2$-2 (○), $Au/scCeO_2$-3 (▲). Test conditions: 15mg catalyst, GHSV=90000h^{-1}.

As a comparison, a standard Au/Fe_2O_3 catalyst provided by the World Gold Council was tested in the same condition and this standard Au/Fe_2O_3 catalyst deactivated rapidly as shown by **Figure 4.17**. Indeed, we had to increase the gas flow rate by almost a factor of 5 (448000 h^{-1}) to observe a similar rate of deactivation, as shown in **Figure 4.17** for the catalyst $Au/scCeO_2$-2.

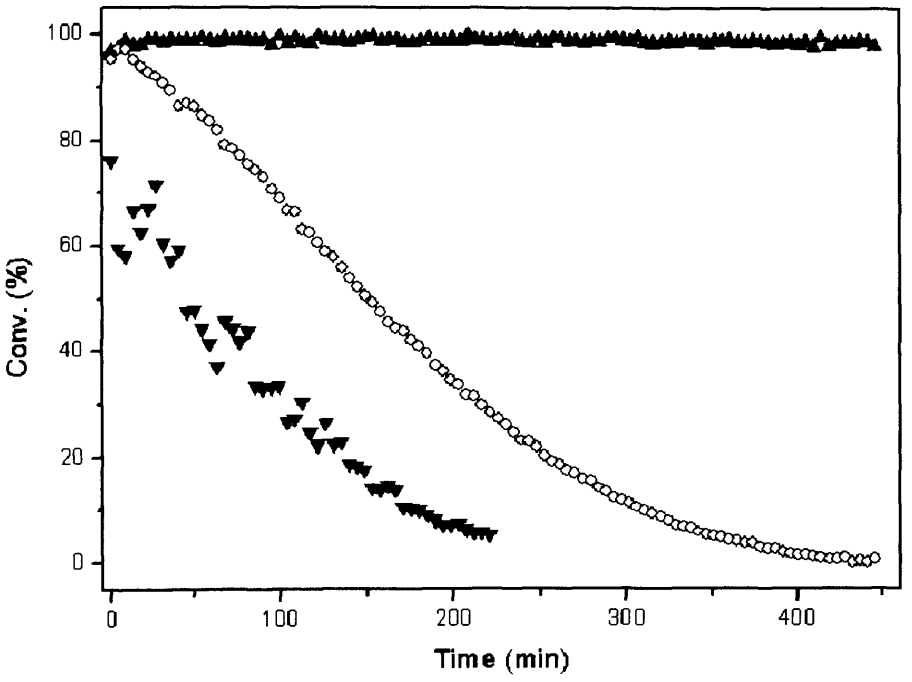

Figure 4.17 Catalytic activities for ambient CO oxidation: 5% Au/Fe_2O_3 (○), the deactivation of $Au/scCeO_2$-2 (▼) using high GHSV (448000h^{-1}) and $Au/scCeO_2$-2 (▲).

To investigate the origin of the effect, detailed characterizations were performed on these as-prepared catalysts. Firstly, XRD analysis was recorded and **Figure 4.18** shows XRD patterns of the four catalysts. As shown by the results, no gold peak can be detected for $Au/scCeO_2$-2, while all the other two $scCeO_2$-supported materials

clearly exhibit gold peaks indicating the presence of Au (111) and Au (220) plane. Therefore, based on these observations, it may be concluded that the size of gold particles may determine the catalytic activities of $scCeO_2$-supported gold catalysts. Of course, Au (111) can also be seen on the XRD patterns of $Au/unCeO_2$. However, the gold peak is relatively weaker than those of $Au/scCeO_2$-1 and $Au/scCeO_2$-3.

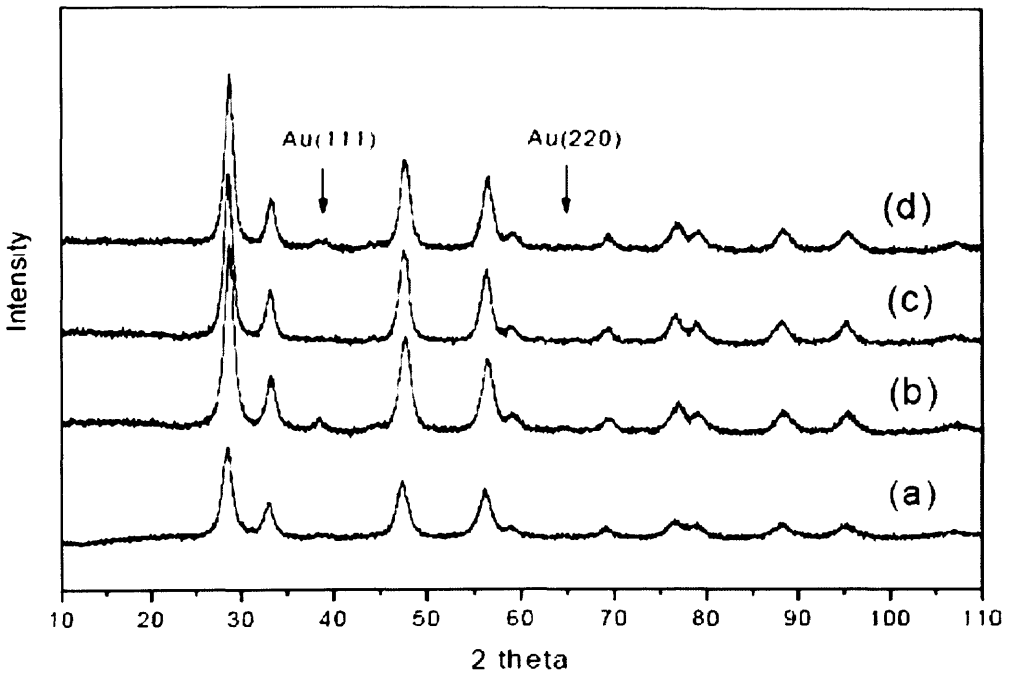

Figure 4.18 XRD patterns of (a) $Au/unCeO_2$, (b) $Au/scCeO_2$-1, (c) $Au/scCeO_2$-2, (d) $Au/scCeO_2$-3.

Detailed transmission electron microscopy and X-ray photoelectron spectroscopy investigations of the CeO_2 samples then have been carried out to further clarify the catalytic activity of the CeO_2-supported gold catalysts. Bright-field TEM micrographs of the catalysts after Au deposition are presented in **Figures 4.19a-d**. A clear difference in the support morphology is shown between the untreated sample (**Figure**

4.19a) and the three supercritically treated samples (**Figure 4.19b-d**). Whereas all the samples prepared using supercritical CO_2 as an anti-solvent displayed polycrystalline spherical agglomerates of particles, the untreated sample was comprised of more irregular and dense agglomerates of facetted CeO_2 crystallites. The gold particles, if present at all, are difficult to discern in such images against the background of the CeO_2 crystallites. This is due to (i) the large atomic number of both gold and cerium atoms, which leads to similar contrast levels in conventional bright-field TEM images and (ii) the expected similarity in size of the Au particles to the primary CeO_2 crystallites within the agglomerates. For example, the 5 nm crystallites visible on the surface of the arrowed sphere shown in **Figure 4.19b-d** cannot be conclusively identified as either Au or CeO_2 particles on the basis of their relative contrast or size.

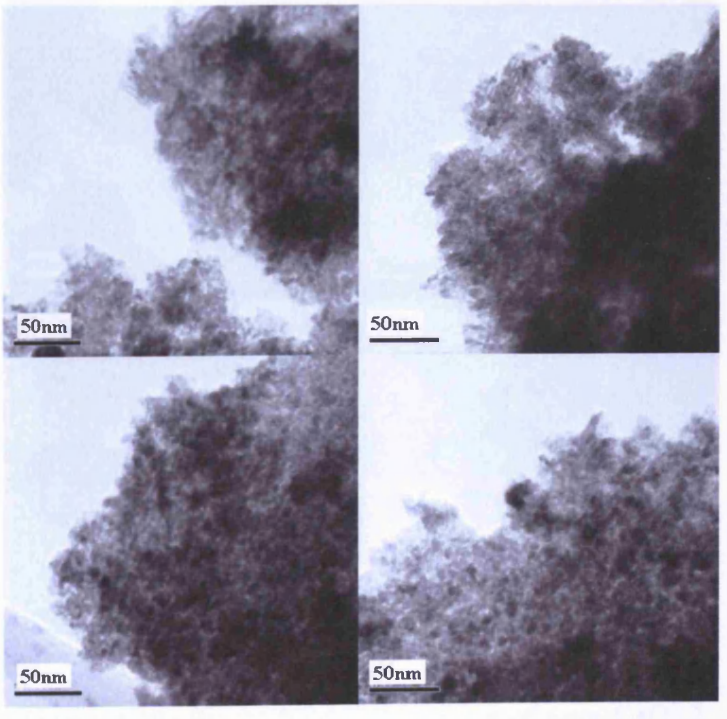

Figure 4.19a Bright-field TEM images of Au/unCeO_2

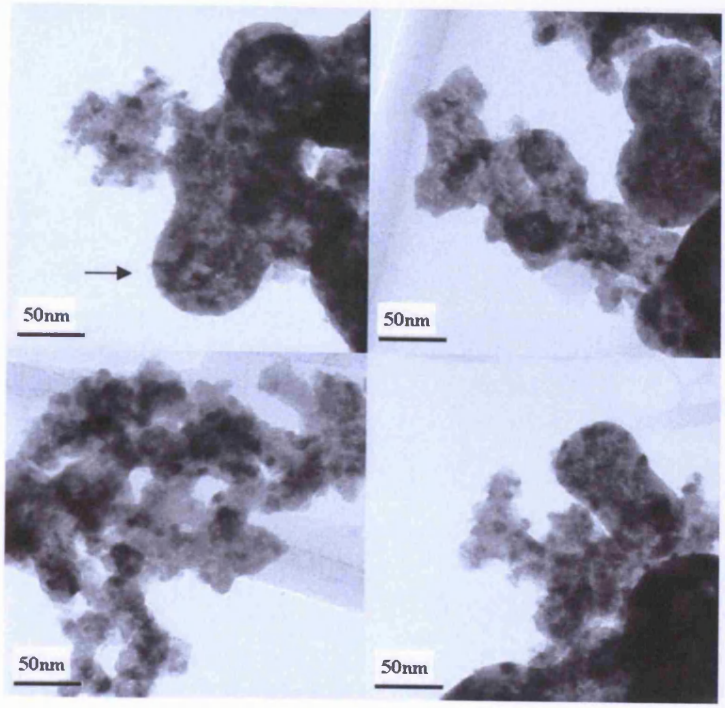

Figure 4.19b Bright-field TEM images of Au/scCeO$_2$-1

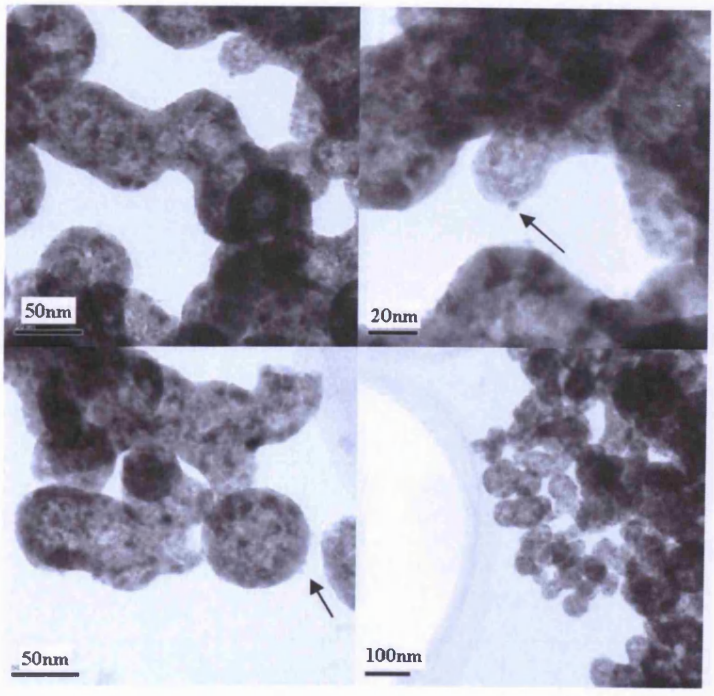

Figure 4.19c Bright-field TEM images of Au/scCeO$_2$-2

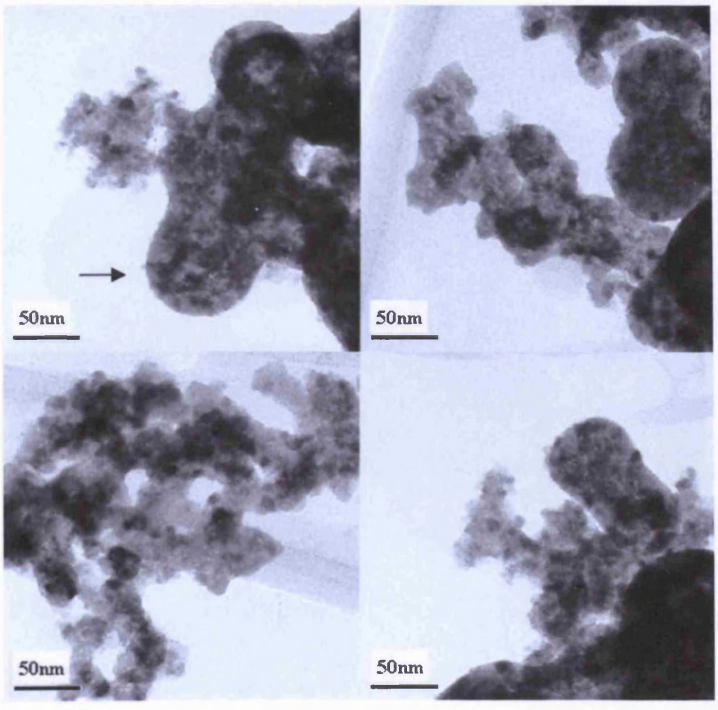

Figure 4.19b Bright-field TEM images of Au/scCeO$_2$-1

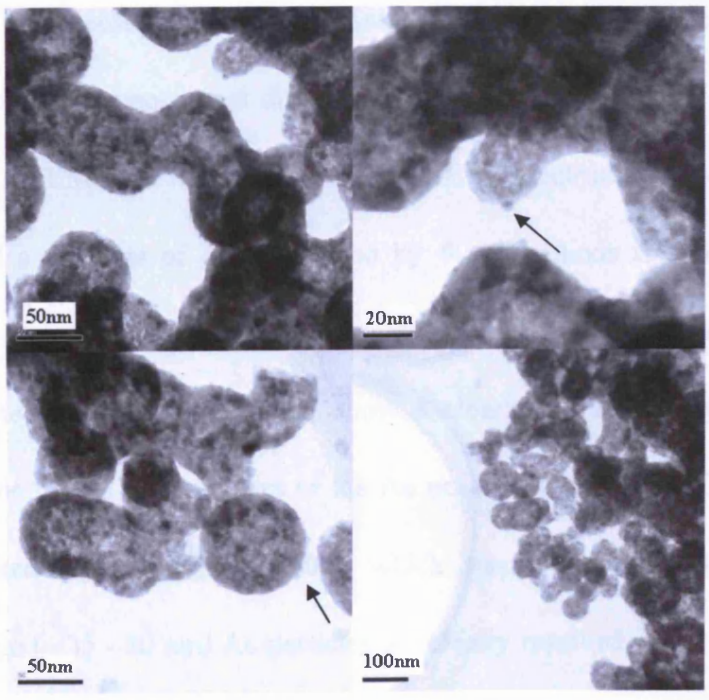

Figure 4.19c Bright-field TEM images of Au/scCeO$_2$-2

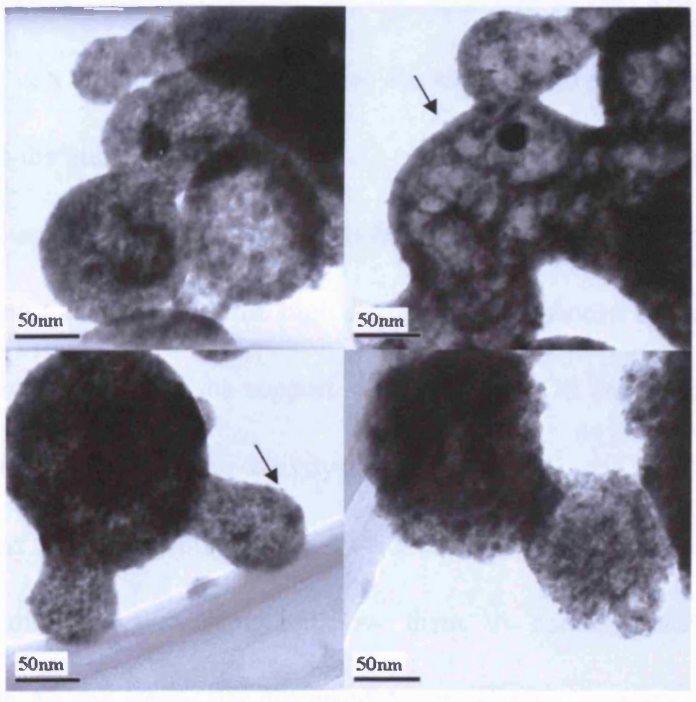

Figure 4.19d Bright-field TEM images of Au/scCeO$_2$-3

Therefore it is necessary to employ an imaging technique that is more sensitive to atomic number and compositional differences to characterize the gold distribution in these samples. STEM-ADF imaging and STEM-XEDS spectrum imaging are ideal for this task, and a montage of data collected by these methods is shown in **Figure 4.20a-d**. The images and x-ray maps, presented in order of increasing catalytic activity as one scans down the page, show a clear correlation between catalytic activity and the degree of dispersion of the Au on the surface of the CeO_2 particles. In the untreated sample (**Figure 4.20a**), which was the poorest catalyst for CO oxidation, large (~ 35 - 80 nm) Au particles are clearly resolved in the Au-M_α XEDS map. This is in stark contrast to the supercritically treated sample Au/scCeO$_2$-2 (**Figure 4.20d**), which was the best CO oxidation catalyst, where no discrete Au

particles at all were observed. Instead, the corresponding Au-M_α XEDS map shows the gold to be very uniformly distributed on the support and maybe even atomically dispersed over the entire surface of the CeO_2 support. This suggests that the highly dispersed Au species on CeO_2 are significantly more active than discrete Au nanoparticles on CeO_2, and that the high dispersion is enhanced by the supercritical CO_2 preparation treatment of the support. The STEM-XEDS data obtained from the catalysts displaying intermediate activity (*i.e.* Au/scCeO_2-1 and Au/scCeO_2-3) also tend to support this correlation. The Au-M_α XEDS maps (**Figures 4.20b and c** respectively) of these two samples show them to contain mixtures of both nanoparticulate Au and atomically dispersed Au in differing proportions. The more catalytically active sample Au/scCeO_2-3 contains a higher fraction of highly dispersed Au species and fewer Au nanoparticles than sample Au/scCeO_2-1, which is catalytically inferior.

Thus, we conclude that the extremely high distribution of fine Au particles on supercritical CeO_2 leads to the high catalytic activity for CO oxidation. The microscopic surface structure of the support does play an important effect on the interaction of gold particles with the support. Consequently, this will give rise to supported gold catalysts with different catalytic activity.

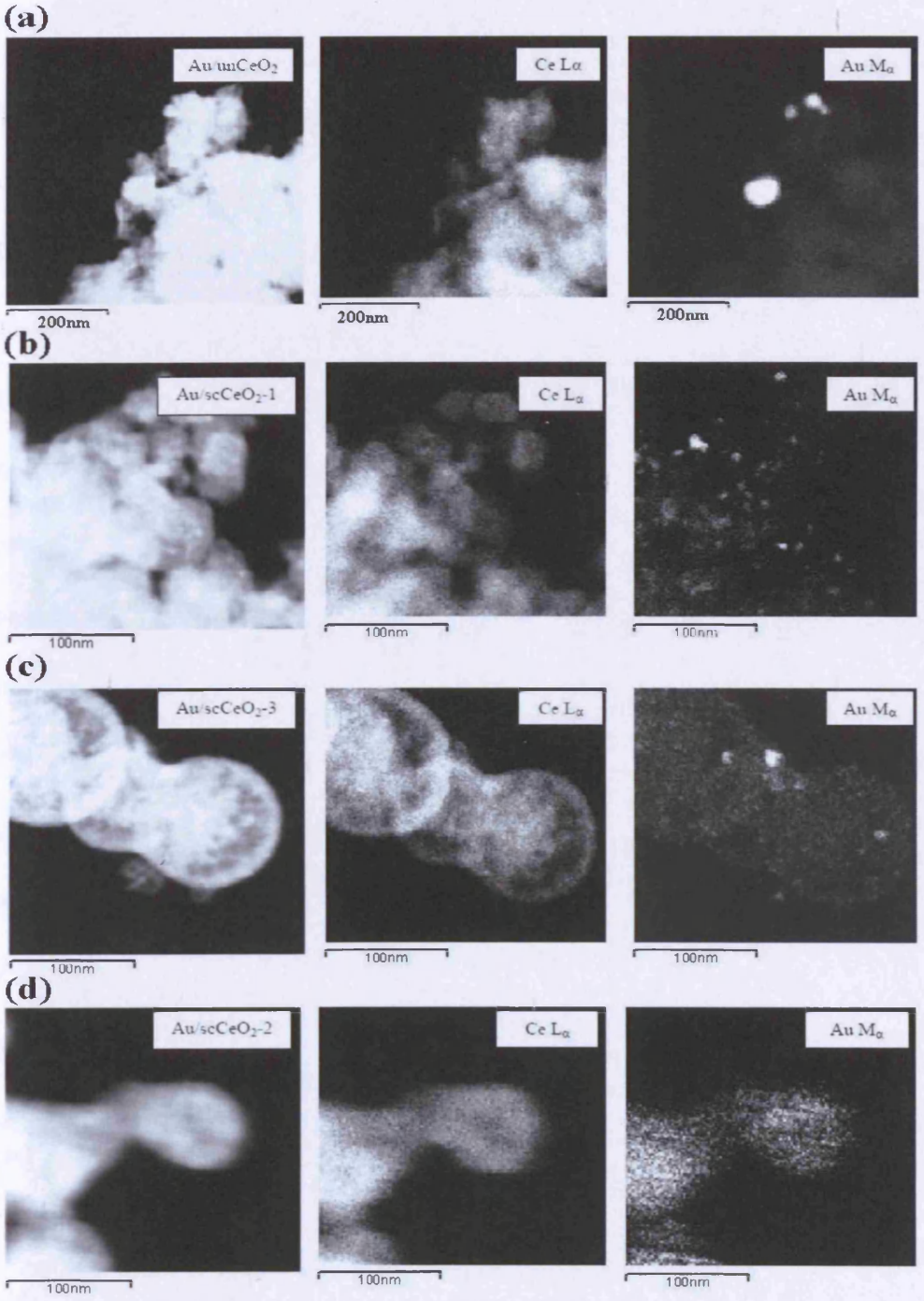

Figure 4.20 STEM-ADF micrographs (left column) and STEM-XEDS spectrum images of Ce-L_α and Au-M_α signals (center and right columns respectively) for Au/unCeO$_2$ (a), Au/scCeO$_2$-1 (b), Au/scCeO$_2$-3 (c) and Au/scCeO$_2$-2 (d). The catalyst samples are ranked in order of increasing activity for CO oxidation as one travels from the top to the bottom in the figure.

X-ray photoelectron spectroscopy revealed that the three catalysts supported on supercritically prepared ceria all exhibit an Au(4f) spectrum characteristic of metallic gold with an Au($4f_{7/2}$) binding energy of 83.7 eV; an example(spectrum a) is shown in **Figure 4.21**. For the gold catalyst supported on ceria prepared by the simple calcination of $Ce(acac)_3$, there are clear signs of two extra components at higher binding energy than the Au^0 peak (spectrum b in **Figure 4.21**). By scaling spectrum a and subtracting it from spectrum b, we generate a difference spectrum which highlights these extra features (**Figure 4.22**). The two components to the difference spectrum have Au($4f_{7/2}$) binding energies of 84.6 eV and 85.9 eV. There are two possible explanations for these features: (i) they arise from a bimodal size distribution of relatively small particles (the Au ($4f_{7/2}$) peak at 83.7 eV would correspond to large gold particles) (ii) they arise from the presence of Au(III) and Au(I) species. Since we have observed an X-ray beam induced transfer of intensity from the feature at 85.9 eV to that at 84.6 eV. We conclude that explanation (ii) is correct, and that Au(III) is reduced to Au(I) under X-irradiation. X-ray induced sintering of Au nanoparticles, which would also be consistent with this observation, is not a likely possibility.

From the XPS results, it is quite interesting to note that the $scCeO_2$-supported gold catalysts only show metallic gold even though they have only been dried and never calcined at high temperature. Both cationic and metallic gold can be detected on $unCeO_2$-supported gold catalyst, and in this case, cationic gold may result in large gold particles appeared on the Au/$unCeO_2$.

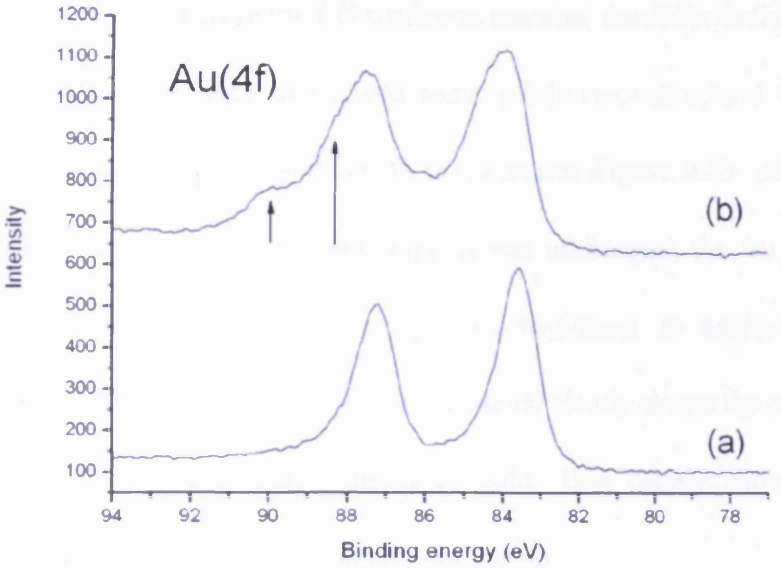

Figure 4.21 Au(4f) spectra for ceria-supported gold catalysts: (a) ceria prepared from $Ce(acac)_3$ using supercritical CO_2 followed by calcination at 400 °C; (b) ceria prepared by calcining $Ce(acac)_3$ at 400 °C. Arrows indicate the presence of two extra components in spectrum (b) compared with spectrum (a).

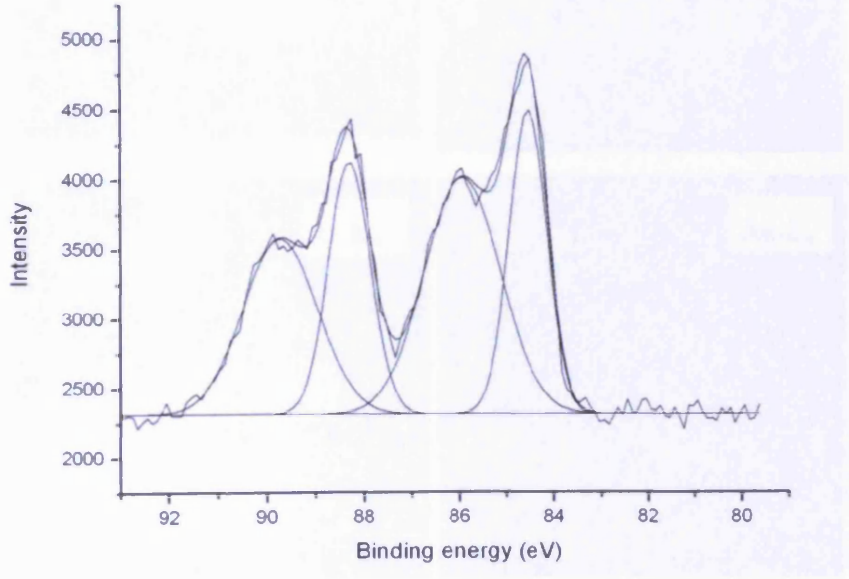

Figure 4.22 Au(4f) difference spectrum obtained by subtracting spectrum (a) from spectrum (b). The difference spectrum has been curve-fitted to quantify the two species present.

After being used to catalyze the CO oxidation reaction, the Au/scCeO$_2$-2 material was reexamined and the material showed some subtle microstructural changes as evidenced by the montage of STEM-XEDS maps shown **Figure 4.23**. Although the morphology of the nanocrystalline CeO$_2$ support was unchanged, the Au which was previously uniformly dispersed shows signs of beginning to agglomerate into sub-5nm particles. The Au-L$_\alpha$ map of the used material clearly shows the co-existence of both nanoparticulate and highly dispersed gold. This clearly shows that the deactivation observed is due to agglomeration of the Au.

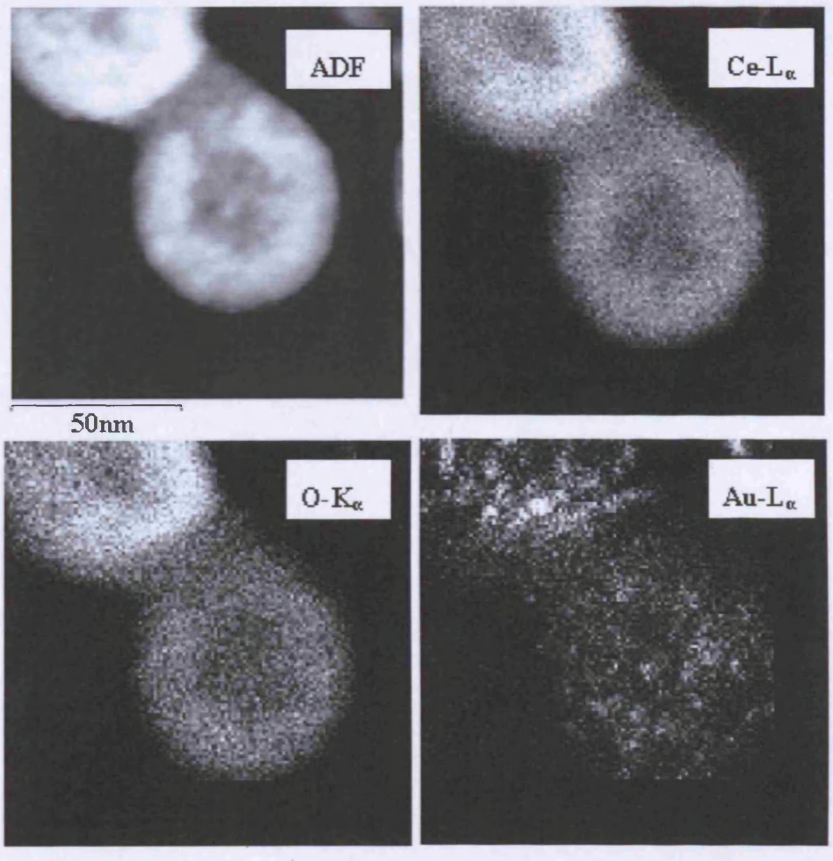

Figure 4.23 STEM-ADF micrographs and STEM-XEDS spectrum images of Ce-L$_\alpha$, Au-M$_\alpha$ and O-K$_\alpha$ signals for used Au/scCeO$_2$-2.

4.3.1.3 Catalytic activity for other reactions using supercritical CeO_2 as a support

To show the catalytic efficacy of the newly prepared supercritically derived CeO_2 support we prepared an Au-Pd alloy catalyst (2.5wt% Au and 2.5wt% Pd) by co-impregnation of $scCeO_2$-2, using aqueous $HAuCl_4$ and $PdCl_2$ and this sample was denoted Au-Pd-$scCeO_2$-2 [15,16].

Initially, we have used this catalyst for the direct synthesis of hydrogen peroxide by the oxidation of molecular hydrogen. Using standard reaction conditions at 2 °C the rate of H_2O_2 synthesis after 30 min reaction was 56 mol H_2O_2/Kg catalyst.h and this is comparable with some of the highest activities reported for this reaction to date using standard TiO_2, Al_2O_3 and Fe_2O_3 supports [21]. Encouraged by this finding, we investigated the use of Au-Pd/$scCeO_2$-2 for the oxidation of a range of alcohols as this is an important reaction for the synthesis of intermediates in the fine chemicals and perfume industries. Two earlier studies have shown that supported metal nanoparticles can be very effective catalysts for the oxidation of alcohols to aldehydes, using O_2 under relatively mild conditions. Kaneda and co-workers [22] found that hydroxyapatite-supported Pd nanoclusters gave very high turnover frequencies (TOFs) for the oxidation of phenylethanol and benzyl alcohol but show limited activity for the oxidation of primary alkyl alcohols, such as octan-1-ol. Corma and co-workers [23] have shown that the addition of Au nanocrystals to nanocrystalline CeO_2 converts the oxide from a stoichiometric oxidant to a catalytic system, with TOFs similar to those

obtained by Kaneda and co-workers [22]. Recently, Hutchings' group have shown that alloying gold with palladium for a TiO_2-supported catalyst gives significantly enhanced activity for alcohol oxidation using a green chemistry approach with O_2 under mild solvent-free conditions [24]. When compared with monometallic supported Au and Pd, the Au-Pd catalysts gave TOFs that are enhanced by a factor of >25. In view of this we have investigated our new 2.5%Au-2.5%Pd/scCeO_2-2 catalyst, which is active for H_2O_2 synthesis, for the oxidation of alcohols under these mild solvent-free conditions. The CeO_2-supported Au-Pd catalysts were initially investigated for the oxidation of benzyl alcohol at 100 °C with O_2 as oxidant in the absence of solvent (**Figure 4.23**). The 5%Au-5%Pd/scCeO_2-2 catalyst was very active for this reaction, and the selectivity to benzaldehyde was *ca.* 91% with minor, amounts of benzyl benzoate (3%), benzoic acid (2%) and toluene (3%). In contrast, the Pd and Au mononometallic catalysts prepared in the same way using the scCeO_2-2 support were much less active and the performance of the catalysts is contrasted in **Figure 4.23**. We also prepared and tested a Au-Pd catalyst prepared using the non-supercritically treated support unCeO_2 and this was found to be significantly less active than the new 2.5%Au-2.5%Pd/scCeO_2-2 catalyst (**Figure 4.24**).

Subsequently, we used the Au-Pd-scCeO_2-2 catalyst for oxidation of a range of alcohols under solvent-free conditions at 160 °C (**Table 4.3**) and it is apparent that this catalyst has high reactivity for a very broad range of alcohols. In particular the rate of oxidation of phenylethanol is about an order of magnitude higher than that reported for Au supported on nanocrystalline CeO_2 prepared using non-supercritical

preparation methodology. [23]

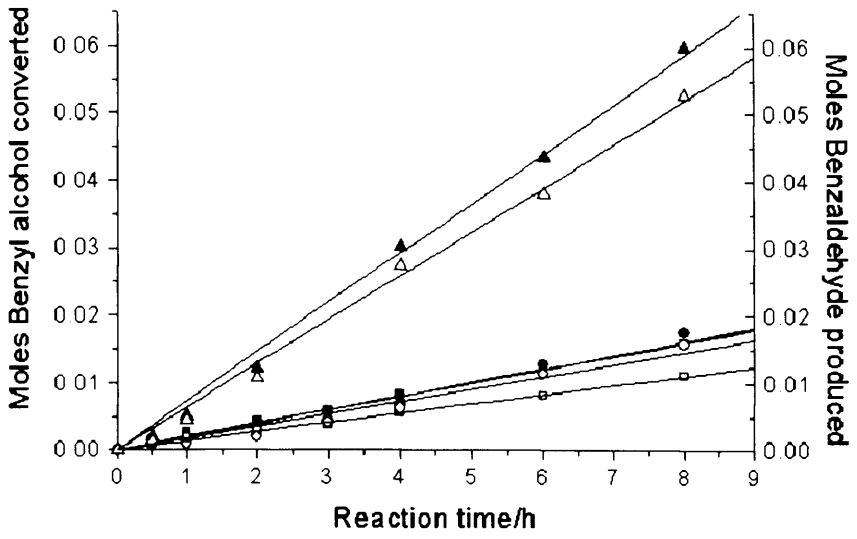

Figure 4.23 Oxidation of benzyl alcohol at 100 °C using solvent free conditions (■) – Au/scCeO-2, (●) – Pd/scCeO-2 and (▲) Au-Pd/scCeO-2; Full symbols refer to mol benzyl alcohol converted, Open symbols refer to mol Benzaldehyde produced.

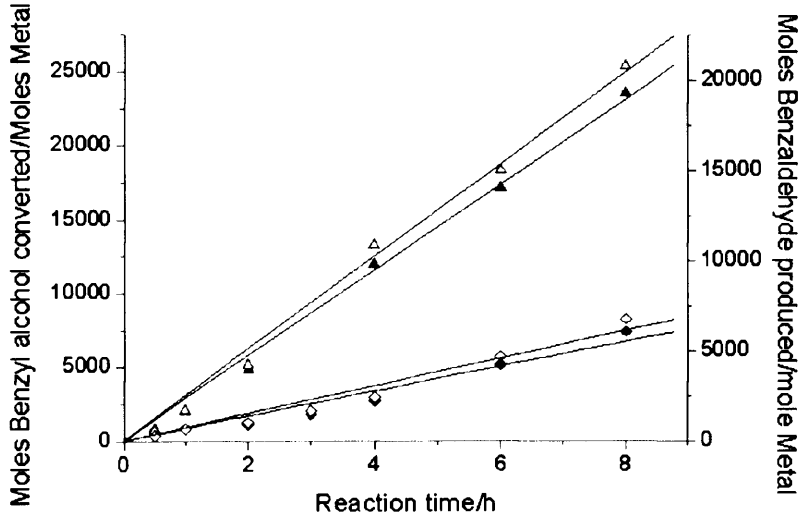

Figure 4.24 Comparison of activity of (▲) Au-Pd/scCeO2 and (◆) Au-Pd/unCeO2; Full symbols refer to mol benzyl alcohol converted/mol metal, Open symbols refer to mol benzaldehyde produced/mol metal.

Table 3 Comparison of the oxidation of alcohols to their corresponding alcohol using 2.5 wt%Au-2.5wt%Pd-scCeO$_2$-2

Alcohol	Reaction Conditions		TOF (h^{-1})[a]
	Temperature (°C)	O_2 Pressure (10^5Pa)	
benzyl alcohol	160	1	17700
butane1,2-diol	160	1	2150
butan-1-ol	160	1	1610
octan-1-ol	160	1	1700
3-phenyl-propan-1-ol	160	1	1700
crotyl alcohol	160	1	19700
phenylethanol	160	1	10500
phenylethanol	160	10	97700

[a] TOF: turnover frequency (mol alcohol converted/mol metal) determined at 30 min reaction time

We investigated the origin of this enhanced activity for the Au-Pd catalysts prepared using scCeO$_2$-2 as a support using STEM-ADF imaging and XEDS mapping. **Figure 4.25a** shows the Au-L$_\alpha$ and Pd-L$_\alpha$ XEDS maps of the Au-Pd/scCeO$_2$-2 catalyst in which both metallic components are observed to be intimately mixed and uniformly dispersed over the nanocrystalline CeO$_2$ support spheres. There is no sign of discrete metallic islands observed, even down to the sub-2nm resolution limit of the XEDS mapping technique. By way of contrast, **Figure 4.25b** shows the Au-L$_\alpha$ and Pd-L$_\alpha$ XEDS maps of the Au-Pd/un-CeO$_2$ catalyst where a large (125nm diameter) Au-Pd alloy particle is clearly visible. Au-Pd alloy particles in the size range 50- 200nm were typical for this material and they all showed a definite tendency to be Au-rich and Pd-deficient. Some weak residual background Pd signal is, however, observed to be

associated with the support suggesting that a small fraction of the Pd is highly dispersed on the CeO_2 platelets. However, it is clear that the supercritically precipitated CeO_2 is able to disperse the metals much more uniformly leading to the enhanced catalytic activity that we observe.

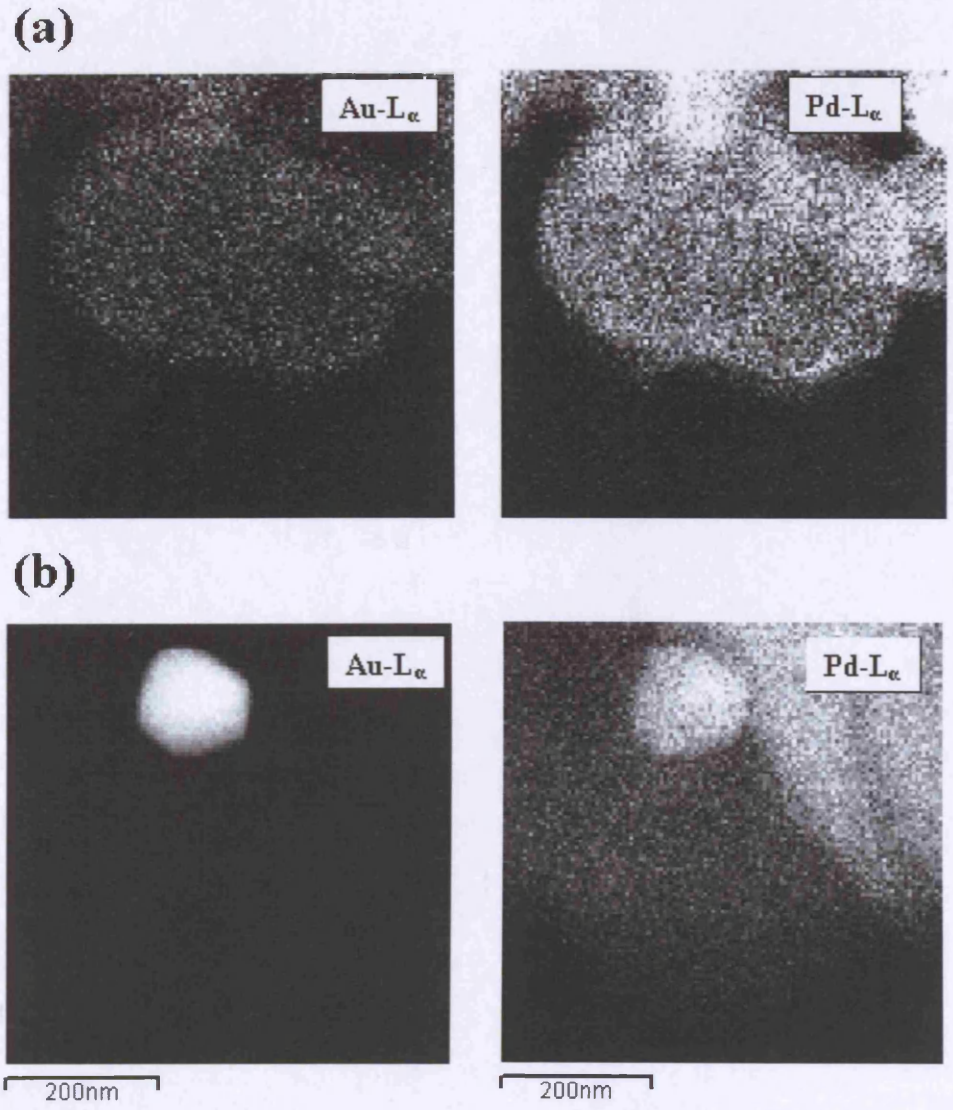

Figure 4.25 STEM-XEDS spectrum images of Au-L_α and Pd-L_α signals for 2.5%Au-2.5%Pd/scCeO_2-2.

4.3.2 Gold supported on TiO_2

4.3.2.1 Precursors and supports

A light yellow powder of the precursor $scTiO(acac)_2$ was obtained from the supercritical antisolvent process at a temperature of 40 °C and a pressure of 110bar. The powder XRD result for the supercritical product is reported in **Figure 4.26**. It is clear to see that the supercritical precursor is completely amorphous, in contrast with the crystalline $TiO(acac)_3$ before supercritical processing. BET surface area measurements indicate that the supercritical precursor has a very high surface area up to *ca.* $160m^2/g$, whereas the titanium salt has a very low surface area of $4m^2/g$.

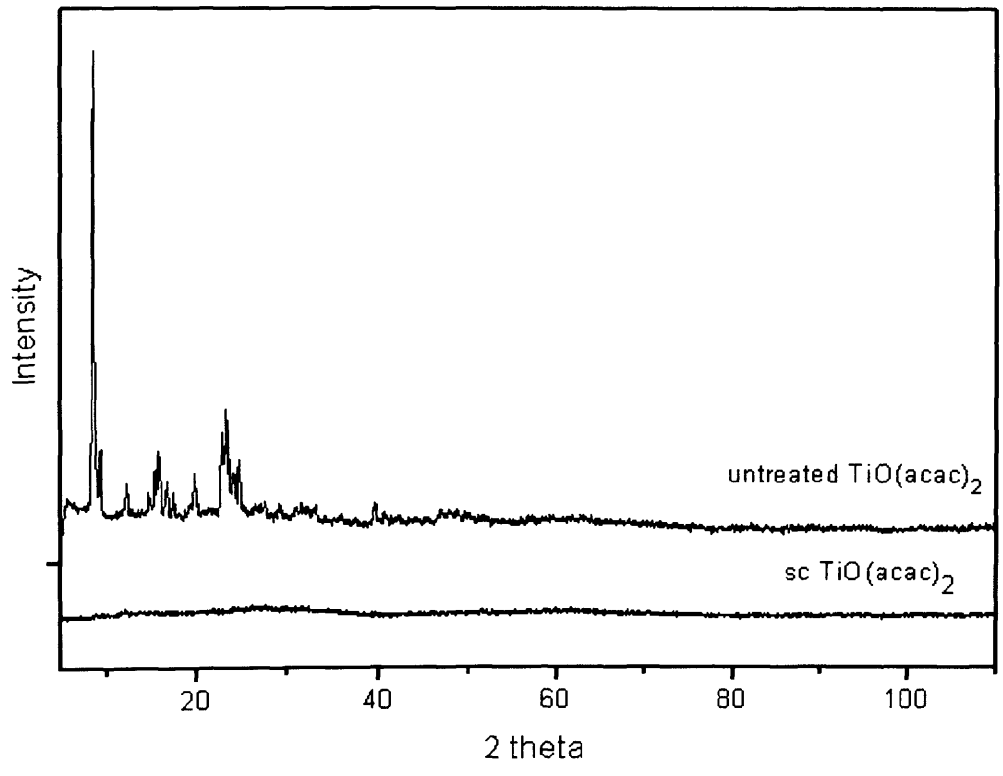

Figure 4.26 XRD patterns of $scTiO(acac)_2$ and the untreated titanium salt

After calcinations, the XRD patterns of both $scTiO_2$ and $unTiO_2$ are the exact same (**Figure 4.27**). Crystalline materials with broad peaks were obtained and, at the same time, only a pure anatase phase can be detected in both of the titanium oxides. In addition, the surface area of $scTiO_2$ dramatically decreased to $35m^2/g$. With respect to $unTiO_2$, its surface area increases a little bit to $8m^2/g$ compared with its non-supercritically treated precursor.

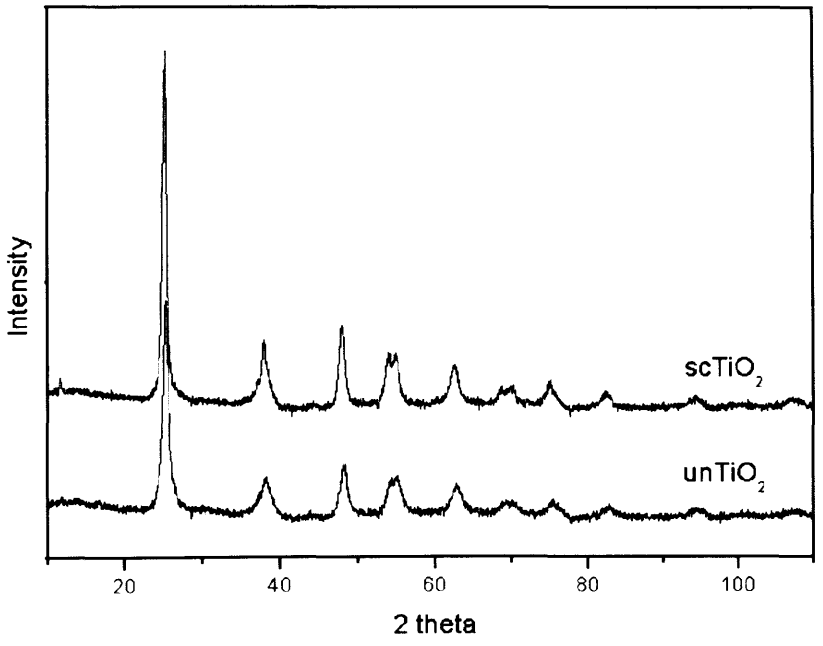

Figure 4.27 XRD patterns of $scTiO_2$ and $unTiO_2$.

The SEM image of the precursor reveals that the individual particles have spherical shape with slight degree of aggregation and the average particle size is around 100 nm (**Figure 4.28a**). Following calcination, the SEM image of $scTiO_2$ (**Figure 4.28b**) indicates the particles have no regular shapes and aggregate with each other greatly. The particle size of the $scTiO_2$ materials is similar to the precursors and

remains around 100nm. As a comparison, SEM images of non-supercritically treated $TiO(acac)_2$ and its corresponding calcined oxides are shown in **Figure 4.29a-b**.These images demonstrate the difference on the surface morphologies of materials before and after the supercritical process.

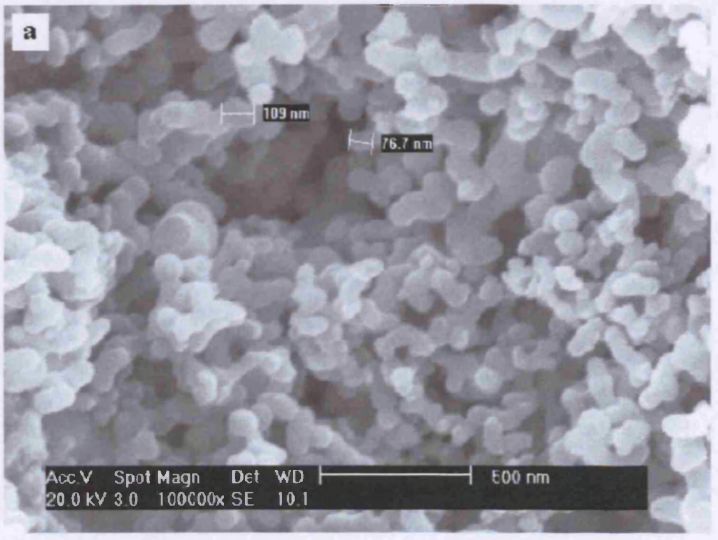

Figure 4.28a SEM images of $scTiO(acac)_2$

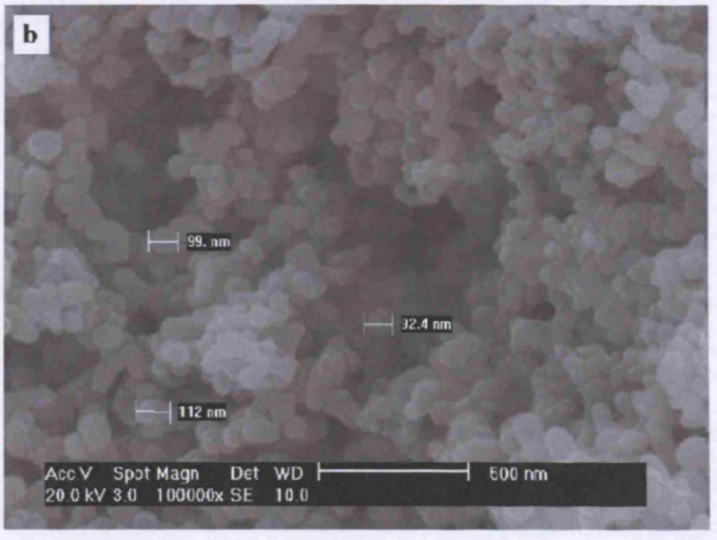

Figure 4.28b SEM images of $scTiO_2$

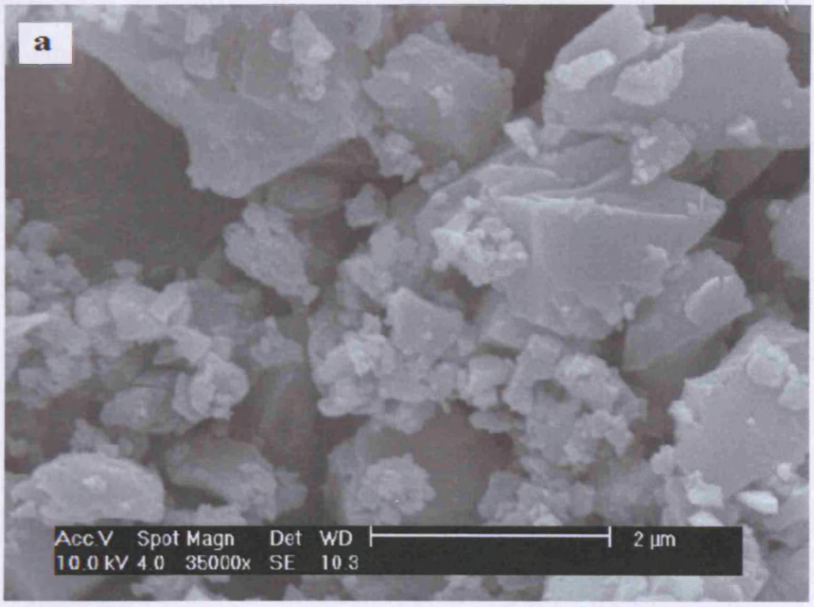

Figure 4.29a SEM images of unTiO(acac)$_2$

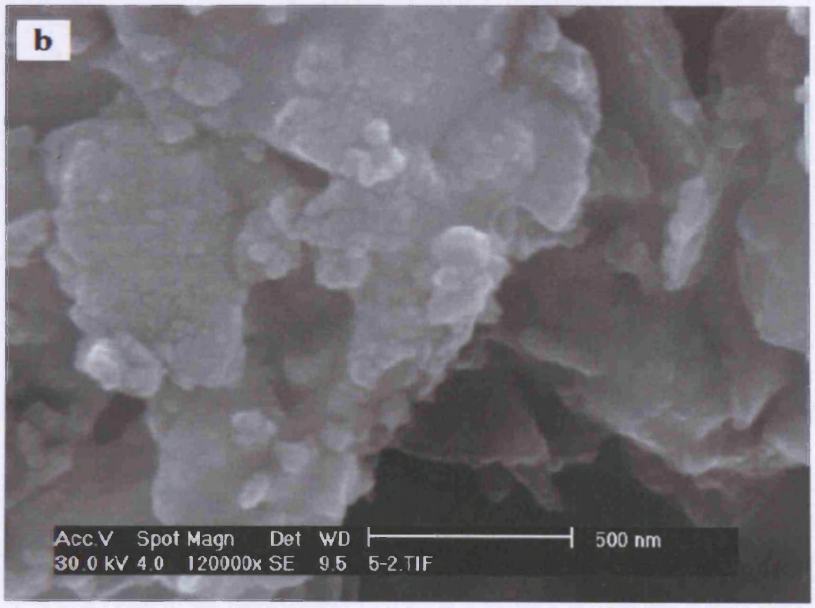

Figure 4.29b SEM images of unTiO$_2$

The FT-IR spectra of the as-prepared precursor and the untreated salt are shown in **Figure 4.30**. The titanium salt has the typical bands of β-diketones, with main peaks at 1603, 1527 and 1385cm^{-1}, corresponding to C=O and C=C stretching vibrations. Meanwhile, the vibration of Ti-O bond can be clearly observed betweeen 1000cm^{-1} and 500cm^{-1}. However, following the supercritical process, scTiO(acac)$_2$ exhibits the characteristics of some basic carbonate salts. The peak at 1585cm^{-1} can be assigned to C=O asymmetric stretching and the peak at 1442 cm^{-1} as a shoulder is assigned to C=O symmetric stretching. In addition, no vibration of the Ti-O bond can be clearly detected in the range of 1000cm^{-1} and 500cm^{-1} which may indicate a change of coordination environment of metal ion. Of course, the characteristics of β-diketones still remain in the supercritically treated material as shown by the spectra.

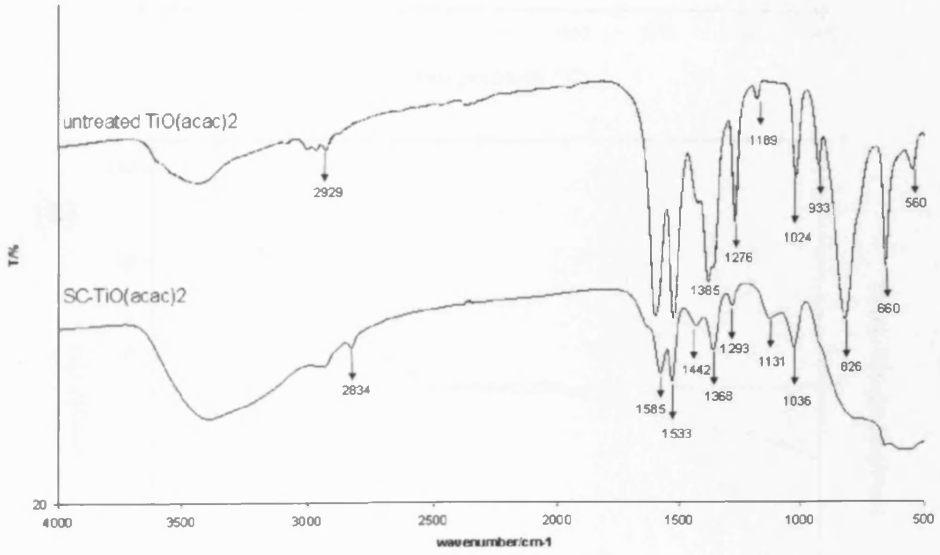

Figure 4.30 IR spectra of scTiO(acac)$_2$ and the untreated titanium salt.

TGA analysis were performed on the as-prepared precursors and the commercial cerium salts. The results as shown in **Figure 4.31** clearly confirm the change of composition before and after supercritical process. For commercial $TiO(acac)_2$, around 45% weight loss can be seen after decomposition over 800 °C, while 70% weight loss is observed on the supercritically treated titanium salts.

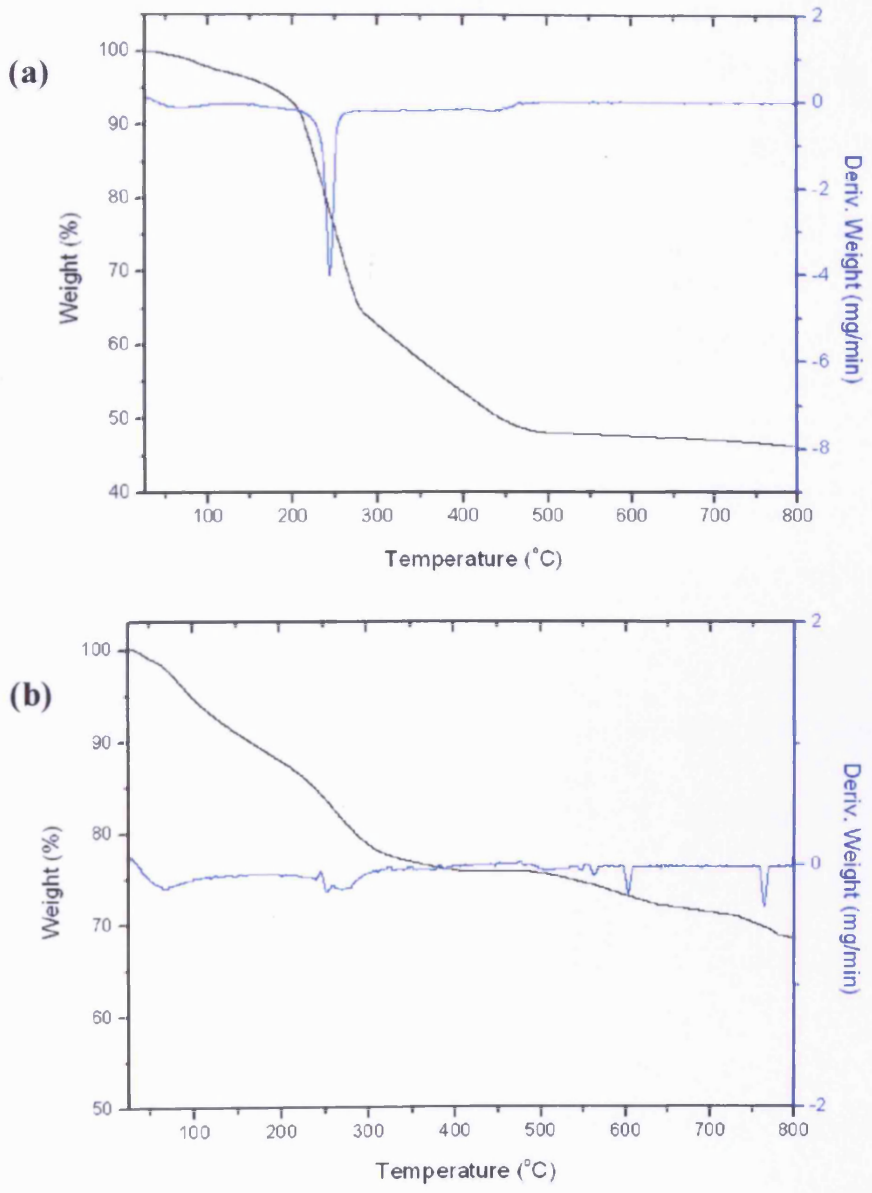

Figure 4.31 TGA analysis on (a) $unTiO(acac)_3$ and (b) $scTiO(acac)_3$

Based on all the above-mentioned characterizations, we concluded that the as-prepared precursors derived from the supercritical process are mainly composed of major amount of carbonates as well as some remaining titanium oxide acetylacetonate. Following calcination, pure anatase titanium oxides with a particle size of around 100nm have been obtained.

4.3.2.2 As-prepared Au/TiO_2 Catalysts

Gold was deposited on the surfaces of the $scTiO_2$ and $unTiO_2$ materials by a deposition-precipitation process. Here we modified the preparation method, that is, the pH value of the slurry was first adjusted to 2~3 from an original pH of 6 by diluted hydrochloric acid before adding $HAuCl_4$. This was found to assist the effective deposition of gold on the two TiO_2 supports, compared with non-modified deposition-precipitation process. The gold loadings of $Au/scTiO_2$, and $Au/unTiO_2$ determined by atomic absorption spectroscopy (AAS) were 0.8 wt% and 1 wt%, respectively.

The catalytic activity of gold catalysts for CO oxidation was tested using a fixed-bed laboratory microreactor. As shown in the **Figure 4.32**, the gold catalyst supported on $scTiO_2$ exhibits extremely high catalytic activity with 100% conversion. In contrast, when gold was deposited on the untreated TiO_2, the conversion of CO oxidation was only about 10%. The results clearly show that the $scTiO_2$ support can greatly improve the catalytic activity of gold nanoparticles. The great improvement in catalytic activity may be due to the unique surface property of $scTiO_2$ from supercritical treating. The mechanism of this enhancement in catalytic activity could be the same as that of $scCeO_2$-supported gold catalysts discussed earlier in this chapter, that is, supercritical treated supports can disperse gold nanoparticles highly and effectively.

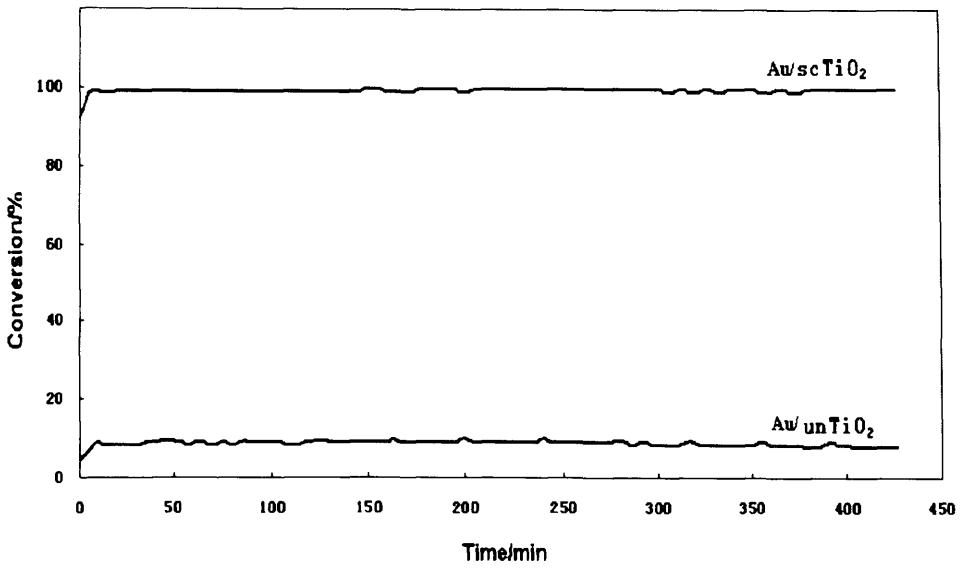

Figure 4.32 Catalytic performances on $Au/scTiO_2$ and $Au/unTiO_2$. Test conditions: 50mg catalyst, GHSV=27000h^{-1}.

In addition, as a comparison, gold catalysts using pure anatase TiO_2 and P25 TiO_2 were tested for CO oxidation under the same conditions. We have found $Au/scTiO_2$ gives a catalytic activity as high as Au/anatase TiO_2 and Au/P25 TiO_2.

Thus, using a supercritical antisolvent precipitation method, we have prepared TiO_2 as a support for gold nanoparticles. The catalytic data on the activity and stability for CO oxidation have shown that gold catalyst supported on this material exhibits much greater catalytic performance than that for gold supported on regular TiO_2 derived from the direct calcination of titanium oxide acetylacetonate.

4.3.3 Gold support on ZnO

4.3.3.1 Precursors and supports

The preparation of ZnO using supercritical CO_2 as an antisolvent has been reported by Reverchon's group[14]. In this work, zinc acetate nanoparticles with high surface area were obtained and it was further calcined to give ZnO nanoparticles. Therefore, this method was adopted in our supercritical system with the control of temperature of 40 °C and the pressure of 110bar, in order to prepare precursors. The preliminary XRD analysis and IR spectroscopy were performed on the as-prepared precursor and calcined oxide. XRD patterns (**Figure 4.33**) showed that an amorphous precursor was produced and after calcination, complete crystalline zinc oxide was obtained. This result is in full agreement with that of Reverchon's work.

The IR spectrum of scZnAc as shown in **Figure 4.34** is a little different from the work reported by Reverchon *et al.* In their work, ZnAc powder produced from supercritical process shows similar characteristics and only minor amount of basic zinc carbonate can be detected. However, in our spectrum typical characteristic peaks of carbonates appearing at 1507, 1399 and 835 cm^{-1} can be detected. Meanwhile, these bands dominate the whole spectrum which means major amount of carbonates have been produced after the supercritical process. Of course, there is also some remaining acetate in the as-prepared precursor because some typical bands of acetate at 1570 and 1021cm^{-1} can still be observed from the spectrum.

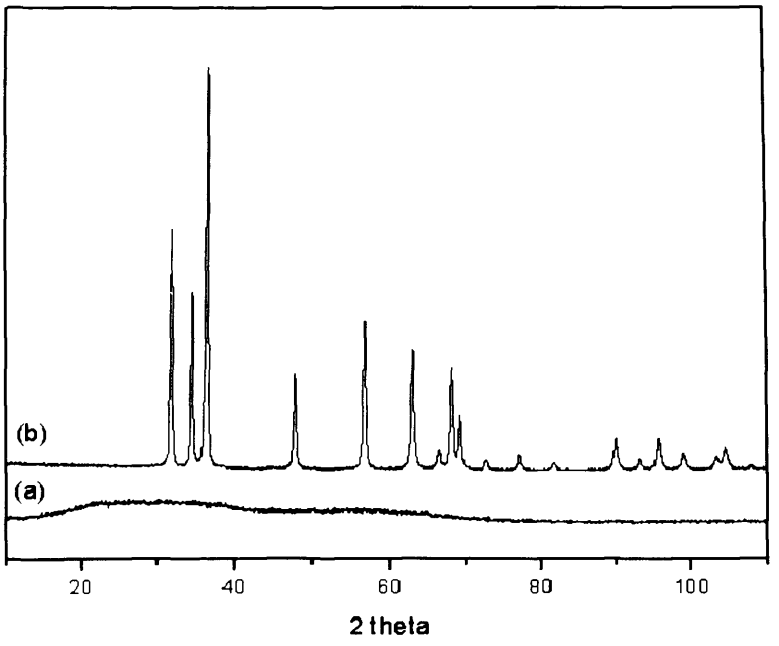

Figure 4.33 XRD spectra of (a) scZnAc and (b) scZnO

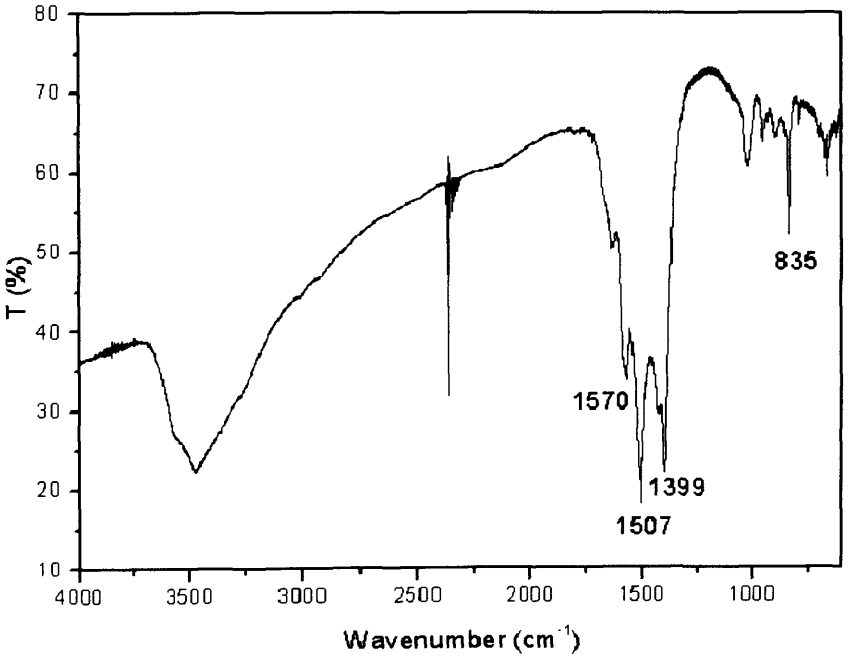

Figure 4.34 IR spectrum of scZnAc

The TGA results (**Figure 4.35**) exhibit a clear change of composition of ZnAc before and after the supercritical process. Around 60% weight loss was observed for scZnAc, which is approximately consistent with the decomposition of zinc carbonate.

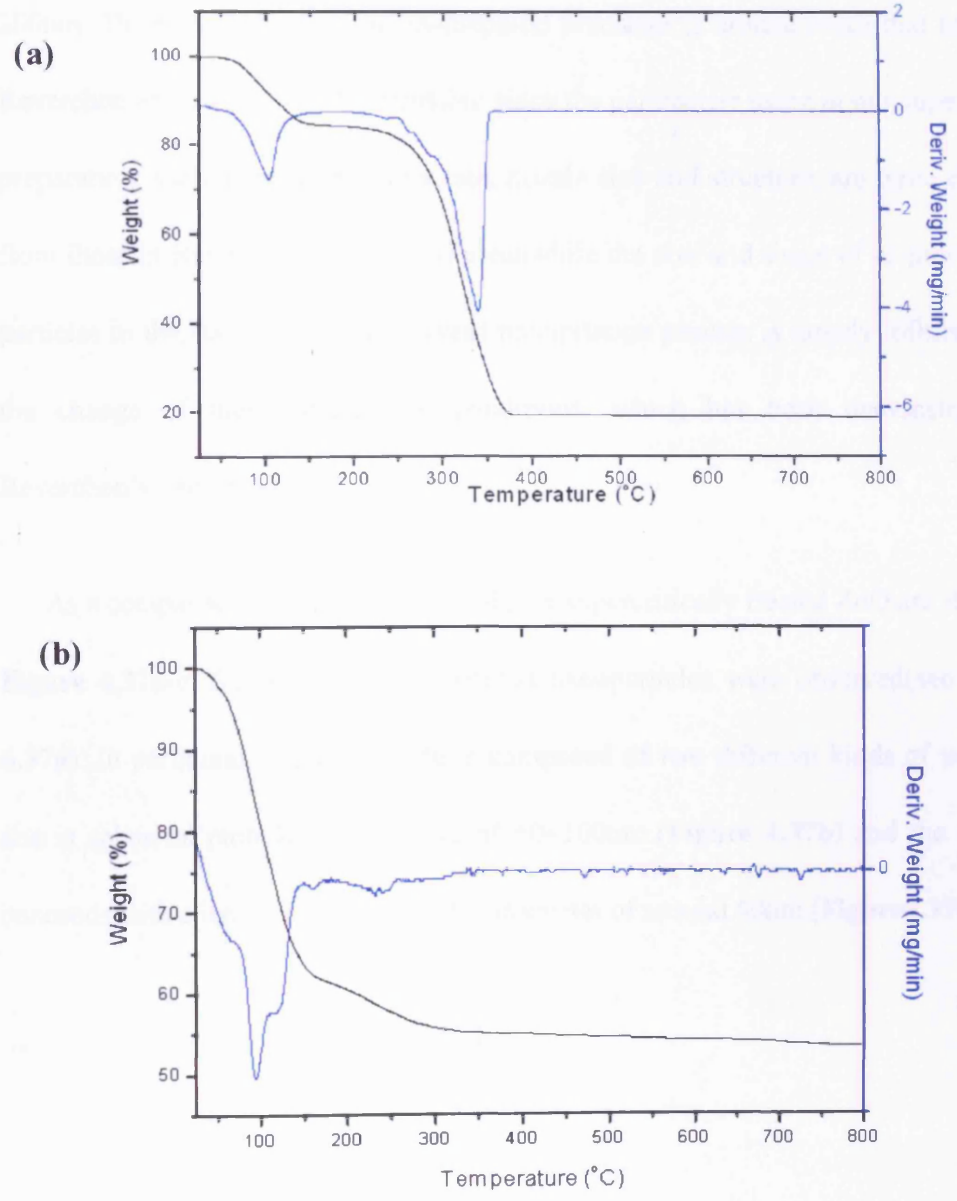

Figure 4.35 TGA analysis on (a) unZnAc and (b) scZnAc

The SEM image of the as-prepared precursor is shown in **Figure 4.36a**. The material has spherical and slightly agglomerate particles with the size of around 200~500nm. After calcination, the whole particles aggregate largely, but are more uniformly distributed (**Figure 4.36b**). The average particle size reduces to around 200nm. The particle size of our as-prepared precursor is around twice that found by Reverchon *et al.* This is understandable since the parameters using in our supercritical preparation, such as pressure, flow rate, nozzle size and structure, are quite different from those in Reverchon's work and meanwhile the size and shape of as-precipitated particles in the supercritical antisolvent precipitation process is largely influenced by the change of these preparation conditions, which has been demonstrated in Reverchon's work [14].

As a comparison, the SEM images of non-supercritically treated ZnO are shown in **Figure 4.37a-c**. Surprisingly, well-defined nanoparticles were observed(see **Figure 4.37a**). In particular, the zinc oxide is composed of two different kinds of particles: one is spherical particles with a size of 50~100nm (**Figure 4.37b**) and the other is nanorods with a length of 500nm with a diameter of around 60nm (**Figure4.37c**).

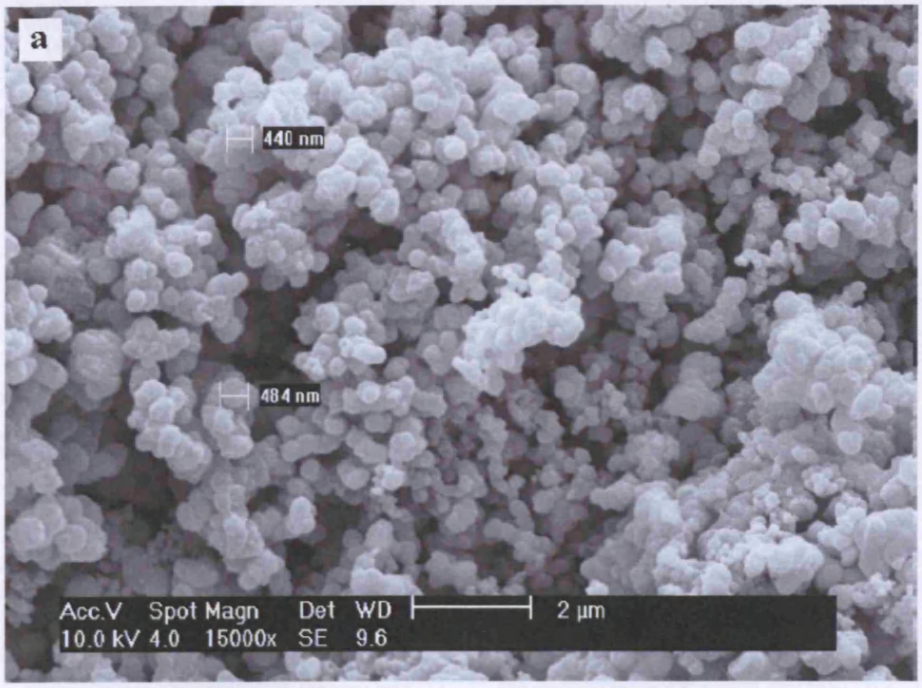

Figure 4.36a SEM images of as-precipitated scZnAc.

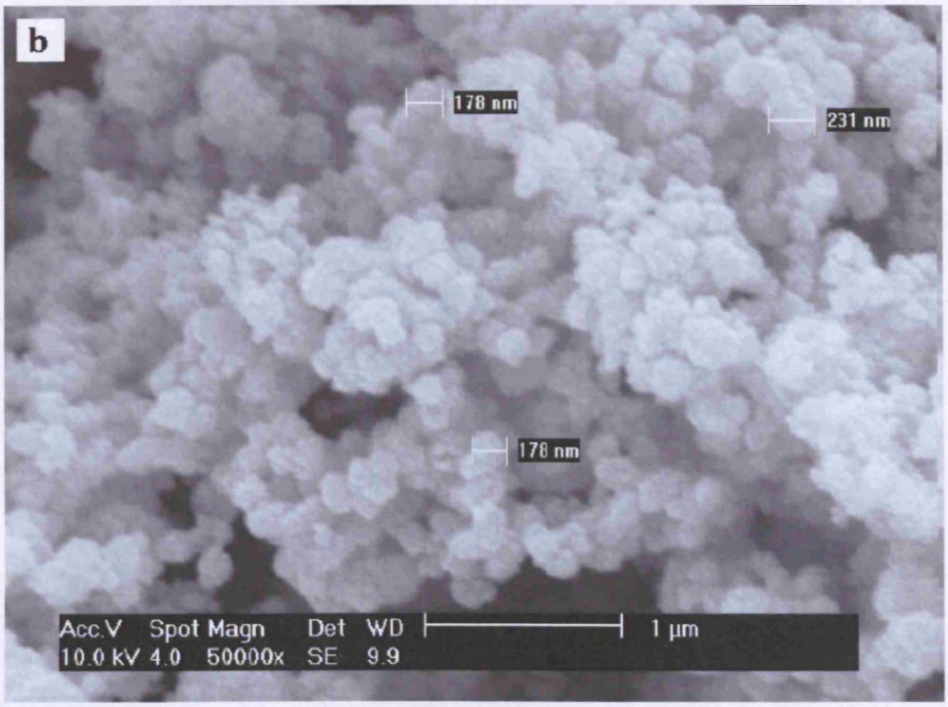

Figure 4.36b SEM images of as-calcined scZnO

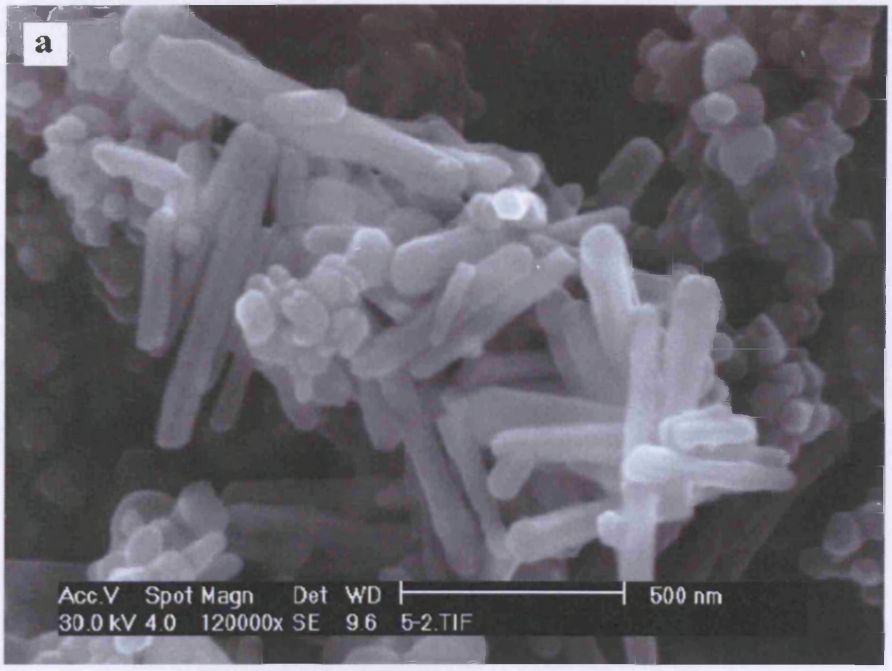

Figure 4.37a SEM images of as-calcined unZnO (nanoparticles and nanorods)

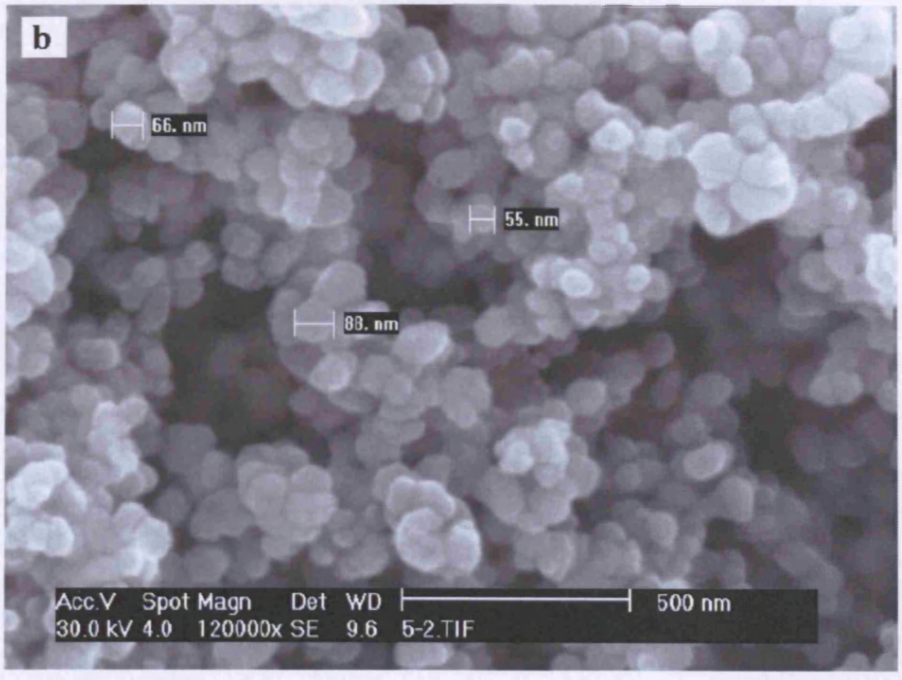

Figure 4.37b SEM images of unZnO with the shape of spherical nanoparticles

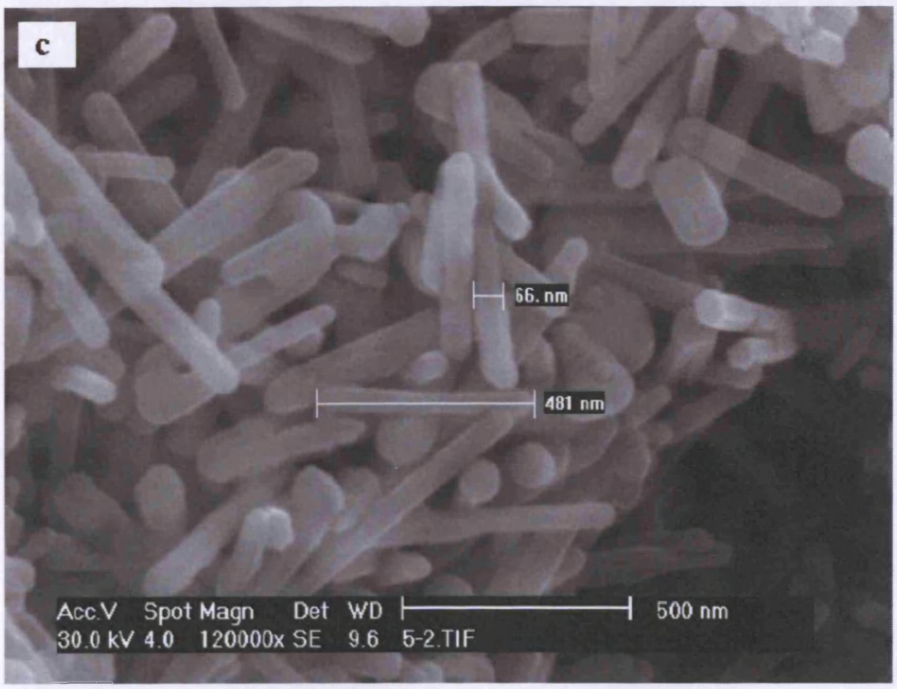

Figure 4.37c SEM images of unZnO with the shape of nanorods

In addition, BET surface areas were tested on the supercritically treated precursor and its calcined oxide. The surface areas of the precursor and the as-calcined oxide are $45m^2/g$ and $32m^2/g$. The decrease of the surface area of as-calcined zinc oxide may be due to the large aggregated nature of particles after calcination at high temperature. With respect to non-supercritically treated zinc oxide, the surface area was found to be $14m^2/g$.

4.3.3.2 As-prepared Au/ZnO

Gold was deposited on scZnO and unZnO by a deposition precipitation method described in **4.2.2.2**. XRD patterns on these two catalysts are shown in **Figure 4.38**. Both of the spectra are quite similar and Au(111) can be observed on both of them.

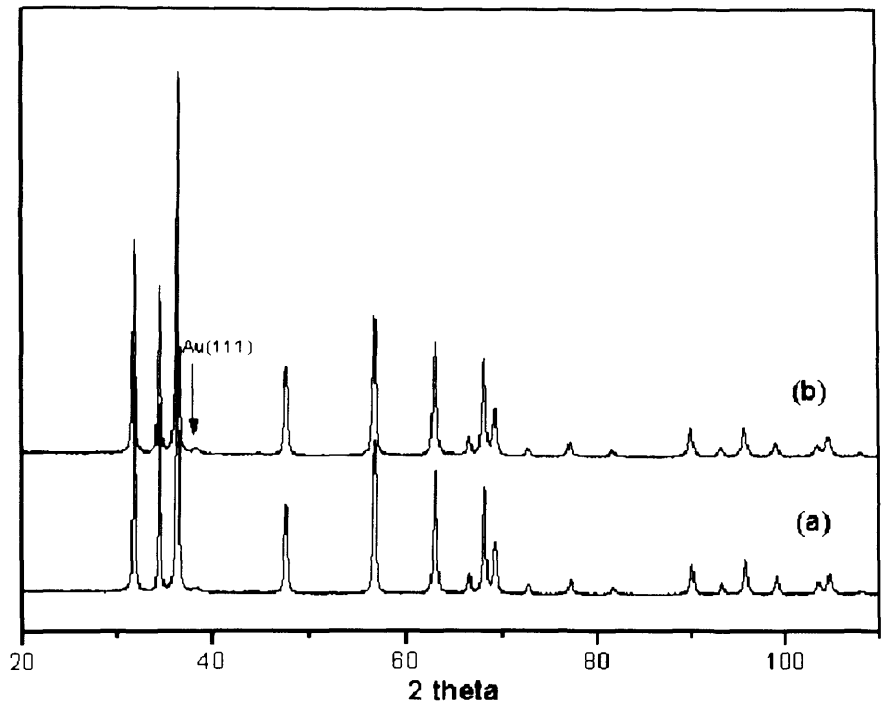

Figure 4.38 XRD spectra of (a) Au/unZnO and (b) Au/scZnO

We have investigated the catalytic performance of these two as-prepared gold catalysts, and the results are shown in **Figure 4.39**. It can be seen that both of the two catalysts show very similar activity for CO oxidation. It is quite surprising that non-supercritically treated ZnO supported gold can give the catalytic activity as high as its supercritical treated counterpart. We consider that its high activity may be attributed to the nanoscaled particle sizes of non-supercritically treated ZnO after calcination; in this case, gold could be highly dispersed in the support and this in turn leads to the high catalytic activity for CO oxidation

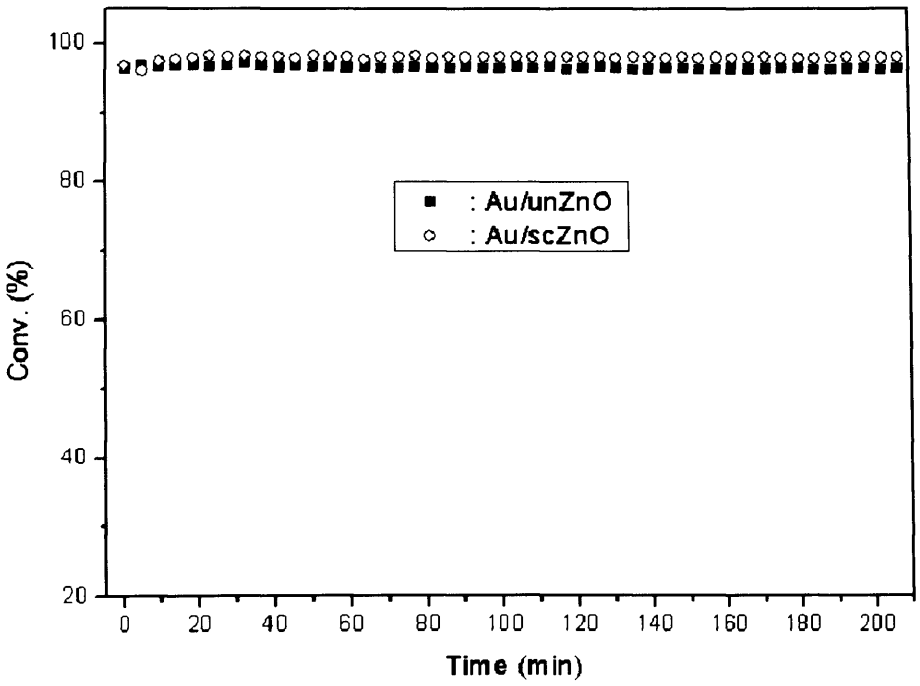

Figure 4.39 Catalytic performances of ZnO-supported gold catalysts. Test conditions: 50mg catalyst, GHSV=27000h^{-1}.

4.4. Conclusion

We have prepared CeO_2, TiO_2 and ZnO using supercritical antisolvent precipitate. These support were applied as supports of gold particles. Based on the above discussions, we have drawn the following conclusions:

(a) When $scCeO_2$ was used as a support for gold and gold palladium nanoparticles, the catalytic data show the activity and stability for CO oxidation of a gold catalyst supported on this material is much greater than that for gold supported on regular CeO_2 derived from the direct calcination of cerium acetylacetonate. In addition, the Au-Pd catalysts supported on CeO_2 prepared using supercritical antisolvent precipitation are amongst the most active catalysts yet reported for the oxidation of alcohols and the direct oxidation of hydrogen to hydrogen peroxide.

(b) In a similar way, when using supercritically treated TiO_2 as a support for gold nanoparticles, the catalytic data show the activity and stability for CO oxidation of a gold catalyst supported on this material is much greater than that for gold supported on regular TiO_2 derived from the direct calcination of titanium oxide acetylacetonate.

(c) When supercritically treated zinc oxide was used as supports for gold particles, the catalytic data show that it can give very high activity for CO oxidation. However, a similar activity from catalysts derived from non-supercritically treated ZnO was also observed. This may be attributed to the nanoscaled nature of non-supercritically treated zinc oxide after calcination, and in turn can make gold particles highly

dispersed on the support. On the other hand, this result also indicates the catalytic activity of our scZnO-supported gold may be enhanced if we can achieve more uniform and smaller particles from supercritical antisolvent precipitation *via* manipulating the different preparation parameters.

In summary, our studies show that using supercritical CO_2 as an antisolvent has significant potential to produce novel supports that can be employed to prepare highly active oxidation catalysts that can be of crucial importance for the design of new green technologies. In particular, using supercritical CO_2 in this way will permit a nitrate-free route to catalytic materials to be realised which will have an enormous positive environmental effect.

References and notes

1 M. Haruta, T. Kobayashi, H. Sano and N. Yamada, *Chem. Lett.*, 1987, **16**, 405.

2 M. Huruta, N. Yamada, T. Kobayashi and S. Lijima, *J. Catal.*, 1989,**115**,301.

3 A. K. Sinha, S. Seelan, S. Tsubota and M. Haruta, *Angew. Chem., Int. Ed.*,2004, **43**, 1546.

4 M. D. Hughes, Y. –J. Xu, P. Jenkins, P. McMorn, P. Landon, D. I. Enache, A. F. Carley, G A. Attard, G J. Hutchings, F. King, E. H. Stitt, P. Johnston, K. Griffin and C. J. Kiely, *Nature*, 2005,**437**,1132.

5 Y. –J. Xu, P. Landon, D. I. Enache, A. F. Carley, M. Roberts. and G. J. Hutchings, *Catal. Lett.* 2005, **101**, 175.

6 P. Landon, J. Ferguson, B. E. Solsona, T. Garcia, A. F. Carley, A. A. Herzing, C. J. Kiely, S. E. Golunski and G J. Hutchings, *Chem. Commun.* 2005, **27**,3385.

7 B. T. Qiao and Y. Q. Deng, *Chem. Commun.* 2003,**17**, 2192.

8 M. M. Schubert, S. Hackenberg, A. C. van Vee, M. Muhler, V. Plzak and R. J. Behm, *J. Catal.* 2001, **197**, 113

9 S. K. Sharkhutdinov, R. Meyer, M. Naschitzki, M. Baumer and H. –J. Freund, *Catal. Lett.* 2003, **86**, 211.

10 S. Arrii, F. Morfin, A. J. Renouprez and J. L. Rousset, *J. Am. Chem. Soc.* 2004,**126**,1199.

11 S. Carrettin, P. Concepcion, A. Corma, J. M. Lopez Mieto and V. F. Puntes, *Angew. Chem., Int. Ed.* 2004, **43**, 2538.

12 J. Guzman and A. Corma, *Chem. Commun.* 2005, 743

13 W. Yan, S. M. Mahurin, Z. Pan, S. H. Overbury, and S. Dai, *J. Am. Chem. Soc.* 2005, **127**, 10480.

14 E. Reverchon, G D. Porta, D. Sannino, P. Ciambelli, *Powder Technology* 1999, **102**, 127-134.

15 Synthesis of H_2O_2 was done by Jennifer K. Edwards in our group.

16 Alcohol oxidation was done by Peter Miedzack and Dan I. Enache in our group.

17 T. Gougousi, D. Barua, E. D. Young and G. N. Parsons, *Chem. Mater.* 2005, **17**, 5093.

18 T. Masui, H. Hirai, Ryo Hamada, N. Imanaka, G Adachi, T. Sakata and H. Mori, *J. Mater. Chem.* 2003, **13**, 622.

19 J. Guzman, S. Carrettin and A. Corma, *J. Am. Chem. Soc.* 2005, **127**, 3286 -3287.

20 J.E. Spanier, R. D. Robinson, F. Zhang, S. –W. Chan and I. P. Herman, *Physical Review B* 2001, **64**, 245407

21 J. K. Edwards, B. Solsona,, P. Landon, A. F. Carley, A. Herzing, C. J. Kiely and G J. Hutchings, *J. Catal.*2005, **236**, 69.

22 K. Mori, T. Hara, T. Mizugaki, K. Ebitani and K. Kaneda, *J. Am. Chem. Soc.* 2004, **126**, 10657.

23 A. Abad, P. Conception, A. Corma and H. Garcia, *Angew. Chemie* 2005, **44**, 4066.

24 D. I. Enache, J. K. Edwards, P. Landon, B. Solsona-Espriu, A. F. Carley, A. A. Herzing, M. Watanabe, C. J. Kiely, D. W. Knight and G J. Hutchings, *Science*, 2006, **311**, 362.

Chapter 5

Conclusion and Future Work

5.1 Conclusion

In this thesis, by using rapid supercritical CO_2 antisolvent precipitation, we have prepared a set of nanoscaled oxide catalyst precursors, which further were calcined to give metal oxides, such as $CuMnO_x$(hopcalite), CeO_2, TiO_2 and ZnO etc. Amongst them, $CuMnO_x$(hopcalite) was used as a catalyst without further modifications, and other single metal oxides were used as supports for gold catalysts. Based on all the works carried out to date, the main conclusions that can be drawn are as follows.

(1) Hopcalite Studies:

Using pure DMSO as a solvent, an amorphous homogenous precursor mainly composed of acetates has been prepared. This precursor has a very high surface area up to *ca.* $300m^2/g$. The material has slightly aggregated quasi-spherical non-faceted particles of relatively uniform size and dimensions (10-20 nm with some particles as large as 50 nm), which are smaller in comparison with those afforded by other precipitation routes. Following calcinations, separated copper nanocrystals supported on manganese oxide (Cu/MnO_x) has been obtained. The preliminary

catalytic data show the intrinsic activity for CO oxidation of the catalyst derived from this precursor is considerably higher than the conventional $CuMn_2O_4$ catalysts prepared by coprecipitation, and also currently available commercial catalysts. The results clearly show that a catalyst with enhanced activity can be prepared without the presence of intimately mixed copper and manganese oxide components.

By using mixed solvents, such as water-ethanol and water-DMF, crystalline heterogeneous precursors have been produced. With the addition of more water to the precursor solution, there appears to be a reaction between the metal acetates CO_2, and H_2O. Therefore, carbonates of the metals are precipitated instead of the acetate composition. Following calcination, less crystalline or even amorphous phase-separated nanostructure final catalysts retain the high surface area, which leads higher catalytic activities than that of the current commercial hopcalite catalysts. Hence, the addtion of water effectively enhances the catalytic performance of as-prepared hopcalite for CO oxidation reaction.

Using 30% H_2O_2 as an oxidizer and ethanol as solvent, catalysts have been prepared as well. All the as-prepared catalysts exhibit higher catalytic activities on CO oxidation when compared to those from solvents in the absence of H_2O_2. However, all the characteristics on these precursors and catalysts showed that similar precursors containing carbonate have been obtained when using H_2O_2-contained solvents.

(2) Supports Studies:

Novel nano-polycrystalline CeO_2 was produced using supercritical antisolvent preparation. When it was used as a support for gold and gold palladium nanoparticles, the catalytic data show that the activity and catalyst lifetime for CO oxidation of a gold catalyst supported on this material is much greater than that for gold supported on regular CeO_2 derived from the direct calcination of cerium acetylacetonate. In addition, the Au-Pd catalysts supported on CeO_2 prepared using supercritical antisolvent precipitation are amongst the most active catalysts yet reported for the selective oxidation of alcohols and the direct oxidation of hydrogen to hydrogen peroxide. This provides a novel route to production of novel supports that can be used for preparation of highly supported nano-crystalline gold catalysts.

Similarly, TiO_2 has been produced by supercritical process. When using it as a support for gold nanoparticles, the activity and stability for CO oxidation of a gold catalyst supported on this material is much greater than that for gold supported on regular TiO_2 derived from the direct calcination of titanium oxide acetylacetonate.

Finally, ZnO was prepared using supercritical process and then was used as supports for gold particles as well. The catalytic data show that it can give very high activity for CO oxidation. Meanwhile, the similar activity derived from non-supercritically treated ZnO was also observed, which may be due to the nanoscaled nature of non-supercritically treated zinc oxide after calcinations. Consequently, the catalytic activity of scZnO-supported gold may be enhanced if

more uniform and smaller particles can be achieved from supercritical antisolvent precipitation *via* manipulating the different preparation parameters.

In summary, these studies have shown that using supercritical CO_2 as an antisolvent has significant potential to produce novel catalysts that can be of crucial importance for the design of new green technologies. In particular, using supercritical CO_2 in this way will permit a nitrate-free route to catalytic materials to be realised which will have an enormous positive environmental effect.

5.2 Future Work

The present work using supercritical antisolvent precipitation so far has obtained promising results. Enhanced catalytic activities can be achieved on the catalysts not only hopcalites but gold catalysts. However, there is still a lot of systematic works needed to be done, which can be summarized as follows:

(a) Literature has shown that many parameters can be manipulated to control the size and the morphology of as-precipitated materials in supercritical antisolvent precipitation process. It is known that the particle size and morphology is very crucial for heterogeneous catalysts since catalytic reactions often occur on the atomic level of the surface of catalysts. Therefore, we can further explore the different T, P, the feeding ratio of the solution and $scCO_2$ and the liquid concentrations. To carrying on the work in this regard will contribute to

optimize the size and surface morphology of as-prepared materials, which in turn decides their catalytic activities.

(b) Further detailed work on the optimization of calcination process needs to be studied since it is well known that calcinations plays a significant effect on the catalyst performance. During the work done in this thesis, we have just performed all the calcination of as-precipitated precursors in static air with the ramp of 10°C. Most likely, catalysts with better performance can be achieved if we explore the different calcination conditions, for example, calcination temperature, atmosphere as well as heating ramp *etc.*

(c) Detailed analysis of TEM and XPS are required for our TiO_2 and ZnO materials so as to completely understand the origin of high catalytic activities of supercritically-treated TiO_2 and ZnO for ambient CO oxidation. This information will effectively contribute to set up the miscroscopic relationship between the structure and activity, which is one of the important goals that current catalysis study is pursuing.

(d) Alonso *et al.* has reported the direct synthesis of TiO_2 from supercritical antisolvent process without thermo-decomposition [1]. This process can be used the preparation of hopcalites and supports in our work in the future. Using ethanol as a solvent, hopcalites, CeO_2, TiO_2 as well as ZnO may precipitate directly if the temperature is set to over 300°C and the pressure is set to over 100 bar. Of course, the SAS apparatus in our experiment firstly needs to be

modified in order to achieve the high temperature.

(e) The SAS apparatus used in this study is a very small-scale supercritical precipitation system. The maximum feeding rate of $scCO_2$ is just 10ml/min which results in the amount of the as-precipitated materials obtained every run is very limited. This induces a great difficulty to the next-step experiments. Moreover, it has been found that the reproduction of this system is not ideal which makes the research more difficult to go further to some extent. Therefore, a large supercritical system is now required. The new supercritical system will give more reliable results to our research. Consequently, this will contribute to develop processes for preparation of catalytic materials that are used for exploring the important catalytic reactions.

References and Notes

1 E. Alonso, I. Montequi, S. Lucas and M. J. Cocero, J of Supercritical Fluids, 2007, **39**,453.